Inhibitors of Alpha-Synuclein Aggregation

_____

A Dissertation

Presented to

the Faculty of the College of Natural Sciences and Mathematics

University of Denver

_____

In Partial Fulfillment

of the Requirements for the Degree

Doctor of Philosophy

_____

by

Jemil Ahmed

November 2022

Advisor: Dr. Sunil Kumar

Author: Jemil Ahmed
Title: Inhibitors of Alpha-Synuclein Aggregation
Advisor: Dr. Sunil Kumar
Degree Date: November 2022

Abstract

Alpha-Synuclein (αS) – a neuronal, disordered, presynaptic protein – aggregates into amyloid fibrils and accumulates in the substantia nigra pars compacta of Parkinson's Disease (PD) patients. The aggregation and accumulation of αS amyloid fibrils leads to death of dopaminergic neurons; a hallmark of PD. Although it's not clear why αS aggregates, prior studies have found that intrastriatal injection of fibril alone is sufficient to cause PD pathology in mouse and non-human primates models. These observations implicate αS as a therapeutic target against PD.

Unfortunately, there are three caveats when attempting to target αS. First, αS is a neuronal protein expressed in the midbrain. A therapeutic agent should be able to cross the Blood Brain Barrier (BBB) and the cell membrane to target αS. Second, αS is intrinsically disordered and dynamic, and most drug design platforms target static tertiary protein structures. Third, it's not clear which sequence domain initiates the aggregation process. αS has 140 residues with the first 90 N-terminal residues typically found in the amyloid core. The specific N-terminus sequence that nucleates aggregation isn't characterized, thus there isn't a known αS region to target.

To address these problem, we prepared and screened a library of small molecule alpha-helical mimetics called 'Foldamers' against αS aggregation. Foldamers fold to a helical conformation and present their functional groups at similar spatial and angular locations to peptide alpha helix, making them great tools for targeting protein-protein

interactions. Our screen identified SK129, an oligoquinoline foldamer that is a potent inhibitor of *in vitro* and *in vivo* αS aggregation as demonstrated in human cells (HEK293 Cells) and *C. elegans* (NL5901, PD model). Then, we tested the hypothesis that SK129 could be binding αS in the sequence that nucleates aggregation. We performed Heteronuclear Single Quantum Coherence NMR experiments and identified sequences 6-12, 15-23, 36-45 and 47-53 as potential binding sites for SK129. We made αS mutants with deletions in the identified sequences – Δ6-12, Δ15-23, Δ36-45 and Δ47-53 – and performed aggregation experiments. Mutants Δ36-45 and Δ47-53 couldn't form amyloid fibrils suggesting these sequences are critical for aggregation.

Additionally, we developed an Oligopyridylamide (OP) based 2-Dimensional Fragment-Assisted Structure-based Technique (2D-FAST) and utilized it to develop a potent inhibitor of αS aggregation – NS163. This molecule was able to prevent cellular αS aggregation in body wall muscle cells (NL5901, *C. elegans* model) and dopaminergic neurons (UA196). NS163 was also able to halt disease progression in post-disease onset PD models.

We also explored the effect polyamines have on αS aggregation. Since one of hallmarks of PD is degradation resistant αS aggregates, we tested if aggregating αS in the presence of different polyamines confers degradation resistance to resulting aggregates. We found αS aggregated with spermine is resistant to enzymatic degradation. Spermine also perturbs the aggregation equilibrium to favor the formation of higher amounts of insoluble protein.

Table of Contents

List of Figures

Chapter 1: Introduction to Parkinson's Disease

1.1 What is Parkinson's Disease?

Parkinson's Disease (PD) is a chronic and progressive neurodegenerative movement disorder first described in 1817 by James Parkinson[1]. In his essay, Parkinson describes a shaking palsy with involuntary resting tremors and decreased muscular power. Since then, additional symptoms have been ascribed to PD like slowness of movement (Bradykinesia), muscular rigidity and postural instability[2]. Non-motor symptoms like constipation, insomnia, depression, anxiety and autonomic dysfunction are also common in PD[3,4].

PD is an age related disorder as 1 % of individuals above 60 years and 3-5 % of people above 85 years suffer from the disease[5]. About 96 % of PD patients experienced disease onset after 50 years of age[5]. PD has a higher prevalence rate in males than females with male-to-female (M: F) ratio of 1.58[5,6]. Population studies based in Europe showed PD has genetic risk factors as individuals with family history of PD are 3 to 4 times likely to develop PD compared to controls [7,8,5]. Non-genetic risk factors have been linked to lifestyle, diet, occupation and environment. For example, dairy intake has been positively associated with PD in men[9,10]. Farming is also a positive risk factor for PD (Odds ratio (OR) = 2.2, $p < 0.05$)[11,12]. Research suggests exposure to agricultural pesticides like paraquat and diquat is a culprit for this association[13].

Recreational use of methamphetamines and synthetic heroin – 1-methyl-4-4 phenyl-1-2-5-6-tetrahydropyridine (MPTP) – increase likelihood of PD up to three times[14]. MPTP is a potent and fast acting inducer of PD symptoms and hospitalization, even as fast as four days after intravenous injection[15]. Malignant melanoma and skin carcinoma increases PD risk by 44 % according to a Danish study with 8090 subjects[16]. Inversely, PD patients are 20.9 times more likely to have non-melanoma skin cancer than the general population[17]. This suggests a common cause for these two diseases.

Similarly, negative risk factors have been identified for PD. Longitudinal studies showed physical activity and exercise reduce the prevalence of PD by 43 %[18]. During physical activity, upregulation of brain derived neurotrophic factor (BDNF) and pro-mitochondrial biogenesis molecule Peroxiosome proliferator-activated receptor γ coactivator 1-α (PGC1α) increase neural plasticity, decreasing likelihood of PD[19]. Drinking black and green tea is also associated with reduced PD risk as they contain epicatechin and epigallocatechin gallate (EGCG)[20]. Non-steroidal anti-inflammatory drugs also reduce PD risk by 45 %, suggesting inflammation is involved in PD pathogenesis[21,22].

1.2 Etiology and Molecular Pathobiology of Parkinson's Disease

In 1912, Friedrich Heinrich Lewy stained serial sections of 25 PD patient brains with eosine (cytoplasmic dye with affinity for proteins) and observed large protein deposits in the dorsal nucleus of the vagus nerve[23]. He observed these deposits were irregularly shaped and having ball-, cord- or serpent-like forms. These structures were later known as lewy bodies (LB) and neurofibrillary tangles. In 1989, in an attempt to create a diagnostic criteria, Gibbs and Lee collected PD brain sections and stained them for LB

and approximately 93.5 % of the PD brains were positive for LB. Other reports showed 70-100 % of clinically confirmed PD patients had LB in dorsal vagal nucleus, sympathetic ganglia, substantia nigra, locus coeruleus, thalamus, cerebral cortex, hypothalamus and nucleus basalis of meynert with striatonigral degeneration [24,25]. In 1993, collaborators from the University of San Diego (UCSD) and University of Tokyo (UTokyo) looked at components of amyloid deposits in Alzheimer's Disease (AD) by boiling AD brain cortex in detergent to disaggregate amyloid deposits. After loading disaggregated peptides into High Pressure Liquid Chromatography (HPLC), they identified Amyloid beta (Aβ), Tau ($\boldsymbol{\tau}$), ubiquitin, ferritin, collagen and two unknown peptides they termed "X" and "Y." They coined the term non-A$\boldsymbol{\beta}$ component of AD amyloid (NAC) to describe these novel peptides. To investigate if NAC peptides X & Y are cross-$\boldsymbol{\beta}$ sheet components of amyloid aggregates or proteins that peripherally associate with amyloid aggregates, the researchers did Immuno-Electron Microscopy (Immuno-EM) and stained amyloid fibrils with anti-X and anti-Y antibodies (antibodies they developed that are specific for these peptides). The two antibodies stained amyloid fibrils verified with Thioflavin S (ThS) - an amyloid fibril dye used in histology. Following the strong evidence that NAC peptides X and Y are components of amyloid fibrils, the researchers made Complementary Deoxyribonucleic Acid (cDNA) of the peptides and screened against human fetal brain λgt11 cDNA library and identified a 14 kilodalton (kDa) protein[26]. A year later, in 1994, Michel Goedert made a similar discovery when he immunoblotted human brain cytosolic extract with the 11.57 monoclonal antibody (a phospho anti-$\boldsymbol{\tau}$ antibody) and discovered two bands in AD brain tissue[27]. Goedert prepared cDNA for the two proteins and screened it against adult human

hippocampal cDNA library and found homology to Synuclein, a neuronal protein identified in 1988, in a species of electric ray called *Torpedo Electoplaques*[28]. Goedert found the proteins he identified were identical to NAC from AD brain. He re-named the 14 kDa proteins from NAC to $\boldsymbol{\alpha}$-Synuclein ($\boldsymbol{\alpha}$S) and $\boldsymbol{\beta}$-Synuclein ($\boldsymbol{\beta}$S)[27].

In the same decade, a report that came out from the National Institute of health (NIH), attempting to identify genetic locus responsible for PD, identified genetic markers in chromosomal location 4q21-23 to aggregate within an Italian Kindred with a history of pathologically confirmed PD (maximal logarithm of likelihood ratio for linkage score, $Z_{max} = 6.00$)[29]. Since $\boldsymbol{\alpha}$S is located in the 4q21-22 region and found in AD brain deposits, it evoked the hypothesis that $\boldsymbol{\alpha}$S could be involved in PD pathogenesis. Thus, an $\boldsymbol{\alpha}$S gene sequence analysis in Italian and Greek family with autosomal dominant inheritance for PD found a G20A mutation that wasn't found in the general population[30]. This mutation results in an A53T mutation in $\boldsymbol{\alpha}$S protein.

Following the genetic association between $\boldsymbol{\alpha}$S and PD, in 1997, Goedert and others raised antibodies against both $\boldsymbol{\alpha}$S and $\boldsymbol{\beta}$S and stained LB's from PD patients. All LB's were positive for $\boldsymbol{\alpha}$S but not $\boldsymbol{\beta}$S. They didn't observe LB's or dense $\boldsymbol{\alpha}$S staining in healthy control brains[31,32]. Interestingly, even though the two groups, Goedert and Takahashi, observed $\boldsymbol{\alpha}$S immunoreactive LB's in pathologically confirmed PD patient brains, the morphology and staining of the LB's were different. Goedert observed round LB's with intense staining in the core and diffuse/light staining at the edge of the LB. Takahashi observed intense staining at the edge of the LB and light staining in the core. Although it's unclear why they observed different LB morphology, it could be due to the

age difference in population, difference in antibody (staining N vs C terminus, staining post translationally modified $\boldsymbol{\alpha}$S) or difference between the stage of disease progression in the patients of the two studies.

Since $\boldsymbol{\alpha}$S was a component of ThS positive LB's and component of A$\boldsymbol{\beta}$ deposits, it raised the hypothesis that $\boldsymbol{\alpha}$S might be an amyloidogenic protein as well. Masliah tested this hypothesis by recombinantly purifying $\boldsymbol{\alpha}$S and testing different conditions to induce aggregation

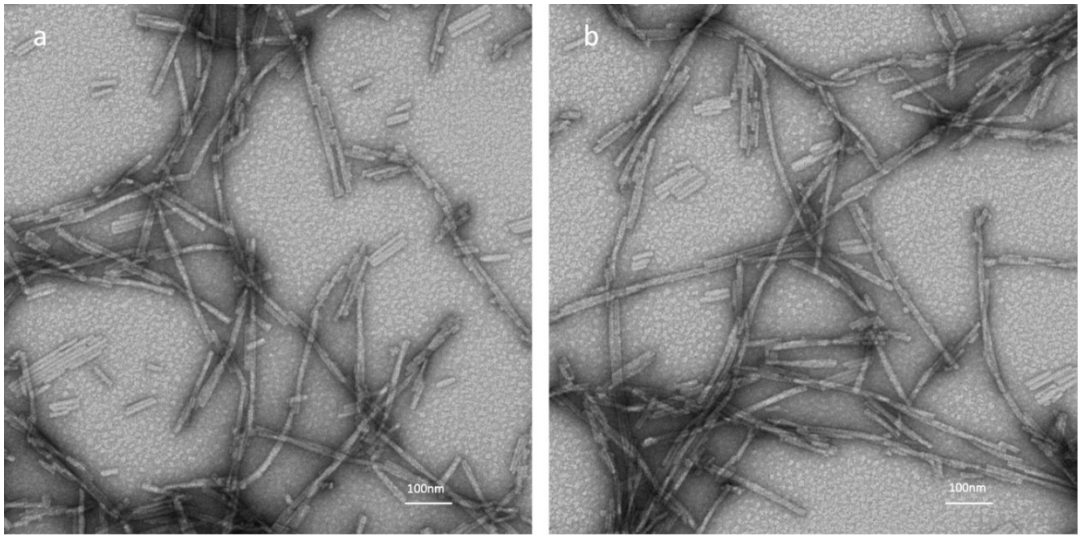

Figure 1.0 a & b) $\boldsymbol{\alpha}$S fibril TEM micrograph taken at 98,000 × magnification and 80.0 eKV.

Masliah found $\boldsymbol{\alpha}$S aggregates spontaneously and forms large insoluble assemblies that stain with ThS (an amyloid dye). He found aggregation can occur at concentrations as low as 10 nM. He also found aggregation happens faster under slightly acidic conditions (pH = 6.9) and 60 ℃[33]. Goedert also found $\boldsymbol{\alpha}$S to aggregate into filamentous structures similar to A$\boldsymbol{\beta}$ and prion protein (figure 1.0)[34].

This prompted Kelly Conway and Peter Lansbury from Massachusetts Institute of Technology (MIT) to look at the biophysical properties of $\boldsymbol{\alpha}$S. They compared the $\boldsymbol{\alpha}$S sequence with that of A$\boldsymbol{\beta}$ and prion protein and found a conserved eight residue long hydrophobic region (Figure 1.1a). They also reported $\boldsymbol{\alpha}$S has an amphipathic N-terminal domain, NAC domain (region of $\boldsymbol{\alpha}$S co-aggregated with A$\boldsymbol{\beta}$ and has high $\boldsymbol{\beta}$-sheet propensity) and an acidic C-terminal domain (figure 1.1b). They observed $\boldsymbol{\alpha}$S has seven repeats of XKTKEGVXXXX throughout the N-terminus domain. Their report shows $\boldsymbol{\alpha}$S is disordered and unstructured based on Circular Dichroism (CD) maximum negative ellipticity minima at 200 nm and Fourier transform Infrared spectroscopy (FTIR) amide I absorption at 1641 cm^{-1}. Change in pH range from 4.5 to 10 didn't change the disordered nature of $\boldsymbol{\alpha}$S nor did salt from 0 M to 2 M range, suggesting $\boldsymbol{\alpha}$S doesn't have ionic interaction stabilized conformation. Adding increasing concentration of urea, a denaturing agent, didn't lower the λ_{max} of the four tyrosine residues in positions 39,125,133 and 136. However, adding SDS induced helical structure. Since the N-terminus of $\boldsymbol{\alpha}$S is amphipathic and shares homology with A$\boldsymbol{\beta}$, a lipid binding peptide, the authors hypothesized $\boldsymbol{\alpha}$S -SDS micelle interaction induced $\boldsymbol{\alpha}$-helical structure[35,36]. Work by others has provided evidence using Nuclear Magnetic Resonance (NMR) and other biophysical methods that $\boldsymbol{\alpha}$S, upon interacting with lipids, adopts $\boldsymbol{\alpha}$-helical conformation[37]. This $\boldsymbol{\alpha}$S- lipid complex is critical for $\boldsymbol{\alpha}$S physiological function and pathological toxicity – which will be discussed later.

Peter Lansbury was also the first to show $\boldsymbol{\alpha}$S aggregates in a nucleation dependent polymerization mechanism by demonstrating the $\boldsymbol{\alpha}$S aggregation profile over time has a sigmoidal shape (figure 1.2)[35,38]. The sigmoidal shape of $\boldsymbol{\alpha}$S aggregation resembles protein crystallization as both processes have a long lag time where a thermodynamically unfavorable nuclei forms – called nucleation[39]. In order for nucleation to occur, the solute concentration (i.e $\boldsymbol{\alpha}$S) has to be above a certain concentration, called critical concentration. Both $\boldsymbol{\alpha}$S aggregation and protein crystallization kinetics can be increased by adding preformed seeds (Figure 1.2), because of this resemblance $\boldsymbol{\alpha}$S nucleation can be modeled using classical nucleation theory (CNT). CNT describes the free energy of nucleation (ΔG_N) as follows:

$$\mu = KT\ ln\ C\ ,$$

$$V = k_v L^3, n = \frac{V}{V_c}$$

$$\Delta\mu = \mu_{\alpha S} - \mu_{\alpha S}^F = kT\ ln\ C_M - kT\ ln\ C_F = kT\ ln\left(\frac{C_M}{C_F}\right)$$

$$\Delta G_N = \sigma A - n\Delta\mu$$

$$\Delta G_N(L) = \sigma k_a L^2 - \frac{k_v}{v_c} L^3 \Delta\mu = \sigma k_a L^2 - \frac{k_v}{v_c} L^3 kT\ ln\left(\frac{C_M}{C_F}\right)$$

To describe nuclei formation, CNT suggests the force driving nuclei formation can be described as the chemical potential (μ) difference between monomeric soluble $\boldsymbol{\alpha}$S and aggregated $\boldsymbol{\alpha}$S. The chemical potential of the monomer and fibril can be described as

a function of concentration (C_M & C_F). The free energy of nucleation (ΔG_N) depends on two factors 1) the nucleating driving force clustering n molecules of $\boldsymbol{\alpha}$S ($n\Delta\mu$) where n can be calculated from volume of nuclei (V) and molecular volume (V_C) and 2) the energy penalty caused by the formation of interphase between the nuclei and solution (σA) here σ is surface energy and A is area of interphase, also written as ($k_a L^2$) [39,40]. This theory is consistent with experimental findings that higher concentration decreases and increase the probability of aggregation while producing small nuclei[41]. The free energy of nucleation can be observed through the energy landscape theory of protein folding, which is a statistical mechanics description of the potential energy surface of protein folding (figure 1.3).

Figure 1.1 a) Sequence similarity between Aβ, αS and PrP fragments is bold and underlined. b) The Amphipathic N-terminus, NAC sequence and the acidic C-terminus are underlined, bolded and italicized. The seven repeats of the 11- amino acid sequence is in color.

With increasing concentration, the kinetics of aggregation also increases according to the transition state theory[40]. The rate of passing through a transition state is proportional to height of the energy barrier (ΔG_N), so the rate of nucleation (J) is

$$J = AC\, exp(\frac{-\Delta G_N}{kT})$$

Where A is the number of nucleation sites, C is frequency of monomer attachment which is proportional to concentration and k is Boltzmann constant. The transition state theory also agrees with experimental results that higher concentrations of $\boldsymbol{\alpha}$S aggregate faster than lower concentrations.

Following nucleation, a process called elongation proceeds where individual $\boldsymbol{\alpha}$S monomers are added to the ends of the nuclei and the fibril gets longer, even upto 6 μm long[41]. Through a dock-lock mechanism, a monomeric $\boldsymbol{\alpha}$S diffuses in solution until it meets a fibril[42]. Then, the monomer interacts with the end of the fibril and through nonspecific hydrophobic interactions, it is temporarily held there[42]. This is called docking. Then the monomer samples β-strand alignment by forming and breaking hydrogen bonds until it's in register with the preformed fibril (PFF)[43]. The final step is called locking and it lengthens the PFF by one monomeric unit at a time. Elongation can be modeled by the classical Arrhenius equation where:

$$k_+ \approx J_{\alpha S}\, exp\left(\frac{-E_a}{kT}\right)$$

k_+ is elongation rate, $J_{\alpha S}$ is diffusion rate of monomeric αS and - E_a is Arrhenius barrier[42].

A third mechanism $\boldsymbol{\alpha}$S fibrils propagate is through secondary nucleation where $\boldsymbol{\alpha}$S monomers interact with the sides of fibrils and use it as a nucleation site, producing more fibrils (figure 1.2). This is considered a very proliferative event in fibril propagation; its probability increases with increasing fibrill mass. The rate of secondary nucleation can be described as follows:

$$r_2 = \frac{N_2(t)}{\int_{t=0}^{t} M(\tau)d\tau}$$

Where r_2 is rate of secondary nucleation, the denominator is the fibril mass during time interval $[t_0, t]$ and the numerator is the cumulative number of secondary nucleation events[44].Once aggregation begins, all three mechanisms take place albeit with different rates (figure 1.4), where secondary nucleation is considered a very proliferative event in fibril propagation; its probability increases with increasing fibril mass[45]

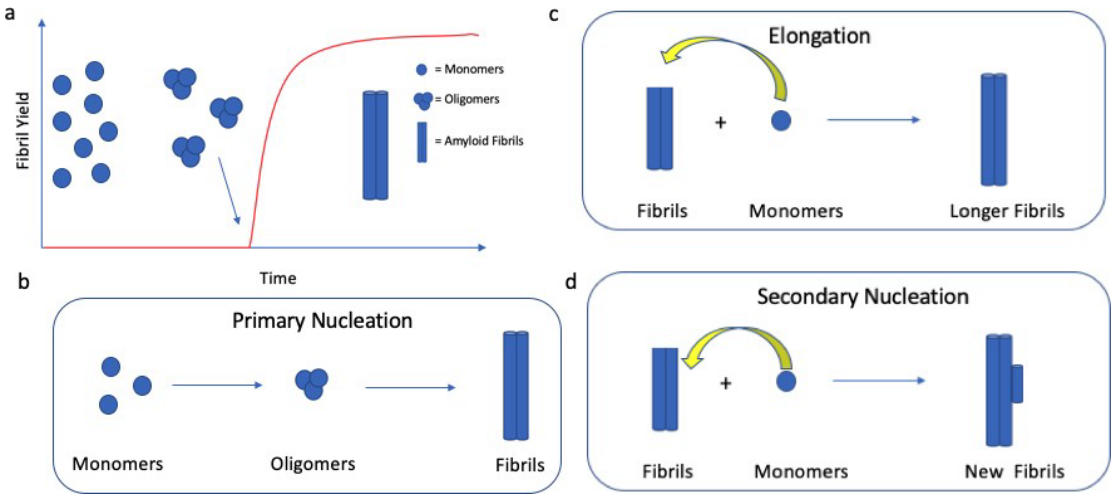

Figure 1.2 a) A plot of amyloid fibril yield vs time showing monomeric αS nucleating to make oligomers which mature to fibrils. b) The process of primary nucleation involving monomeric αS converting to nuclei which can convert to amyloid fibril. c) Monomer αS interact with ends of fibrils and integrate to the existing amyloid lengthening the fibril through a process called elongation. d) Secondary nucleation process where αS gets recruited to the side of a fibril and converts to a new fibril.

1.2.1 αS in the cellular milieu

Alpha Synuclein is located on chromosome 4, 10.7 Kilobases (kb) from the Rep-1 promoter[46]. The transcription factors GATA 1, 2 and (ZSCAN)21 are known regulators of ***α***S[47,48]. The transcribed premature messenger Ribonucleic Acid (mRNA) has six exons and four introns[49]. The translation start codon (ATG) is on exon 2 and the stop codon is on exon 6. After splicing and mRNA processing, the mature mRNA has a 5' untranslated region (UTR) that is rich in GC content (66 %) and thought to make G-Quadruplex (G-q motif), an Iron Regulatory Element (IRE) and an Internal Ribosome Entry Site (IRES). All of these elements help with the constitutive translation of the mRNA. The 3' UTR has many regulatory elements like microRNA (miR) and RNA binding domain (RBD) binding sites. For example, miR 7,153 and 34 can negatively regulate translation while

ELAVL1 and TIAR can positively regulate translation of $\boldsymbol{\alpha}$S (figure 1.5)[50]. As $\boldsymbol{\alpha}$S is constitutively translated, its made at a high concentration – 70-140 μM – accounting for 1 % of the total protein in the cell[41]. This is well above the critical concentration of $\boldsymbol{\alpha}$S (15 μM). Although the cellular $\boldsymbol{\alpha}$S concentration is high, the protein remains soluble in human and mouse brains[51]. Several studies have shown the cellular proteostasis network (chaperones, proteasomes, ubiquitin-proteasome and autophagy-lysosomal system) is sufficient to keep $\boldsymbol{\alpha}$S in the monomeric state[52–54]. The other synuclein proteins (β and γ) which are also expressed in the same cell types as $\boldsymbol{\alpha}$S, can inhibit its aggregation. This discovery came after *in vitro* studies showed, in the presence of βS, $\boldsymbol{\alpha}$S doesn't go through nucleation and secondary nucleation[55].

Additionally, *ex vivo* and *in vivo* experiments verified this finding in neurons and transgenic mouse models[56,57]. Studies in postmortem human brains found healthy brains have ~ 10 fold higher levels of βS than $\boldsymbol{\alpha}$S, conversely in AD and Dementia with Lewy bodies (DLB) brains, the expression patterns is reversed and βS is reduced compared to $\boldsymbol{\alpha}$S[58].

The physiological function of $\boldsymbol{\alpha}$S is still unclear. Studies that knocked out (KO)$\boldsymbol{\alpha}$S in mice have reported minimal physiological changes to the model system suggesting loss of function due to aggregation isn't the pathological cause of PD. Since $\boldsymbol{\alpha}$S localizes to synaptic membranes, it's hypothesized its involved in synaptic function[59]. Several *in vitro* experiments have shown monomeric $\boldsymbol{\alpha}$S induces membrane curvature and converts large vesicles to cylindrical micelles and small vesicles. When the $\boldsymbol{\alpha}$S interacts with vesicles made of neutral and negatively charged lipids, it segregates the negatively charged

vesicles and sequesters them, suggesting its role in membrane biogenesis[60,61]. Further evidence showed $\boldsymbol{\alpha}$S compensates for neurodegeneration caused by the KO of the chaperone Cysteine String Protein $\boldsymbol{\alpha}$ (CSP$\boldsymbol{\alpha}$) – a chaperone with DnaJ domain that facilitates Soluble N-ethylmaleimide-sensitive factor attachment protein receptor (SNARE) assembly[62]. Additionally, $\boldsymbol{\alpha}$S shares sequence homology to $\boldsymbol{\alpha}$-crystalline and small Heat Shock Protein 16 (Hsp16) and can prevent thermally and chemically induced protein aggregation[63,64]. This property extends to $\boldsymbol{\alpha}$S's ability to bind synaptobrevin-2 and chaperone SNARE assembly to facilitate exocytosis and compensate to CSP$\boldsymbol{\alpha}$ loss[65].

Since PD is an aging disorder, changes that occur during aging have been implicated in its initiation and pathology. Alteration in gene replication and expression, mis regulation of RNA transcription, DNA damage, decrease in protein synthesis machinery, increased ribosomal stalling, increase in oxidative stress, increase in cellular senescence, decrease in microbiota diversity, increased inflammation and constitutively active stress response could play a role in PD. For example, during aging, there is proteostatic collapse where BiP (an Endoplasmic Reticulum resident Hsp70) is decreased by ~ 40 % and Hsp70 is decreased by ~ 40 - 50 %[66,67].

Additionally, chaperone mediated autophagy decreases by about ~ 1.7-fold in older organisms[68]. Ubiquitin-proteasome degradation machinery is also compromised during aging resulting in ribosomal stoichiometry imbalance leading to faulty ribosomal assembly and improper protein synthesis[69,70]. During aging, ribosomal stalling increases, destabilizing co-translational proteostasis, resulting in increased aggregation propensity of newly translated peptides[71]. All the aforementioned changes make the aged cell lack

protein folding ability and misfolded protein clearance, increasing the probability of $\boldsymbol{\alpha}$S aggregation.

A xenobiotic causative agent of PD is environmental exposure to metals like Manganese (Mn), Iron (Fe), Aluminum (Al), Mercury (Hg) and Cooper (Cu). Occupational exposure to these metals for 20 years increases PD risk by 2 - 10 fold[72]. The Manganese ion Mn^{2+} can interact with $\boldsymbol{\alpha}$S and induce its transition from liquid phase to solid phase *in vivo* and *in vitro*[73]. The metal also increases exosomal release of $\boldsymbol{\alpha}$S oligomers from dopaminergic neuron and increase the cell-to-cell transmission of $\boldsymbol{\alpha}$S pathology[74]. The effect of Mn^{2+} in PD initiation is well demonstrated, that it's termed Manganism[75].

1.2.2 Structure of αS fibrils

Cryo-EM has elucidated diverse $\boldsymbol{\alpha}$S fibril structures. The structures show many differing features but some of the common features are described below. The fibrils made of wild-type (wt) $\boldsymbol{\alpha}$S have their monomers stacked along a fibril axis. Cryo EM structures typically show two protofibrils symmetric along this axis. The fibrils can have either right-hand or left-hand helix depending on the aggregation conditions. A pitch of 239 nm and periodicity of 60 - 120 nm is typically reported. The two protofibrils are stabilized at the interphase with saltbridges and the monomer stacks are separated by 4.7 Å. Typically, residues 30 - 99 make up the Greek key-like amyloid core where most of the hydrophobicity is concentrated[76].

1.2.3 Prion - like spread of αS fibrils

In late 1900's to early 2000's, Heiko Braak stained brains of PD patients that are at different stages of the disease (early, mid and late) for LB's. He observed early stage PD patients had LB's and $\boldsymbol{\alpha}$S fibrils in their enteric nervous system, olfactory bulb and medulla oblongata. Then, the fibrils spread to the midbrain then to the neocortex. His observation that the enteric nervous system is affected in early stages and the pathology travels to the brain made him hypothesize the pathology could start in the gut, then travel to the brain. This hypothesis is called Braak's hypothesis. Several other reports have demonstrated that $\boldsymbol{\alpha}$S is expressed in the enteric nervous system and during bacterial or viral infection, $\boldsymbol{\alpha}$S is overexpressed and released from neurons into the peritoneal cavity to induce inflammation[77]. Additionally, several experiments injecting $\boldsymbol{\alpha}$S fibrils in mice gut or vein have demonstrated the spread of the aggregates to the brain through the vagus nerve[78].

Initially, the $\boldsymbol{\alpha}$S fibril spreads from gut to the dorsal motor nucleus of the vagus nerve. Then it spreads through the superior axis and travels to raphe nuclei and locus coeruleus. It makes its way to the midbrain into the substantia nigra, where it spreads into anteromedial temporal mesocortex and finally into the neocortex. From the substantia nigra, it can also spread to caudate, putamen and basal ganglia. These findings suggest $\boldsymbol{\alpha}$S fibrils spread through anatomically connected neuron network (figure 1.6). Further evidence for $\boldsymbol{\alpha}$S spreading came PD patients which were transplanted with embryonic neuronal cells and post-mortem staining showed the grafted neurons are positive for LB's[79].

At the cellular level, receptor mediated endocytosis, exocytosis, tunneling nanotubes and exosonal transport are implicated in $\boldsymbol{\alpha}$S fibrils spreading. In a donor neuron, a fibril is loaded on kinesin and anterograde transported from the soma to the axonal terminals (figure 1.7). From the axon terminal, the fibril can cross to the receiving neuron through tunneling nanotubes[80–82]. Other modes of transmission have been identified, particularly through unconventional protein secretion (UPS) mechanisms. One of the UPS' is when the deubiquitiylase protein, ubiquitin-specific protease 19 (USP-19), which can identify misfolded proteins and have chaperone activity, interacts with $\boldsymbol{\alpha}$S fibrils and recruits them to the surface of the ER where they are packaged into late endosomes which fuse with plasma membrane to excrete the fibrils into extracellular matrix. This novel mechanism has been termed misfolding-associated protein secretion (MAPS)[83]. Another mechanism that secretes fibrils involves the Hsp 40 homolog subfamily C member 5 (DnaJC5) together with Hsp 70 places $\boldsymbol{\alpha}$S in vesicles which undergo exocytosis[84].

Additionally, the autophagy-lysosome pathway is heavily involved in $\boldsymbol{\alpha}$S fibril release. A phagophore forms around fibrils and forms into an autophagosome which fuses with the lysosome for degradation. Unfortunately, $\boldsymbol{\alpha}$S fibrils are resistant to degradation and persitist in the lysosome[85]. The lysosome then goes through SNARE- dependent lysosomal exocytosis and dumps the fibrils into the extracellular environment[86].

The fibrils then interact with lymphocyte activation gene 3 (LAG3), Aβ precursor-like protein (APLP1) and α3-Na^+/K^+- ATPase (α3-NKA) receptors on the neuron which facilitate cellular uptake. Once bound, these proteins facilitate clathrin-mediated endocytosis, internalizing the fibril[87]. The internalized vesicles have two fates.

One – they are transported to Multi-Vesicle bodies (MVB) as late endosomes and secreted as exosomes[88]. Two – the $\boldsymbol{\alpha}$S fibril ruptures the endocytic vesicles and escapes into the cytoplasm[89]. Additionally, fibrillar Interaction with Heparan sulfate proteoglycan's (HSPG) induces internalization with pinocytosis. In conclusion, prion spreading takes advantage of amyloid fibril's property to recruit monomeric proteins and cellular excretion and absorption mechanisms.

1.3 Toxicity of fibrils

The $\boldsymbol{\alpha}$S fibrils exert toxicity through the following four mechanisms – membrane disruption, mitochondrial dysregulation, protein sequestration and inflammation. The $\boldsymbol{\alpha}$S oligomers are responsible for many of the mentioned mechanisms. For example, Dobson and De Simone found $\boldsymbol{\alpha}$S oligomers have affinity for negatively charged lipid membranes. Using their positively charged N-terminus (sequence 1-38), oligomers bind membranes at ~ 5 μM affinity and lay on the surface adopting alpha helical structure. This phenomenon is also observed for monomeric $\boldsymbol{\alpha}$S upon membrane interaction[90]. Once the oligomer is in contact, the cross-β sheet rich structure (sequence 70-80) penetrates the membrane and inserts itself into the inner leaflet[91]. This disrupts membrane integrity and causes cellular content to leak out and Ca^{2+} to influx into cytoplasm. The Ca^{2+} influx is associated with increased toxicity and apoptosis[92].

Once the oligomers are taken up by the cell, they interact with the mitochondria and disrupt protein import and general function. Specifically, $\boldsymbol{\alpha}$S bind the mitochondrial translocase of the outer membrane 20 (TOM20), a transmembrane protein that binds cytosolically synthesized mitochondrial proteins and passes them to other membrane

channels (TOM 40 and TIM 23), and competes for substrate binding. This prevents TOM 20s natural substrates (eg. Ndufs3) from translocating into the mitochondria leading to 30-40 % decrease in cellular respiration, ~ 2.2 fold increase in reactive oxygen species (ROS) and mitochondrial depolarization[93]. The interaction between oligomers and TOM 20 is also observed in human postmortem PD and mice brains.

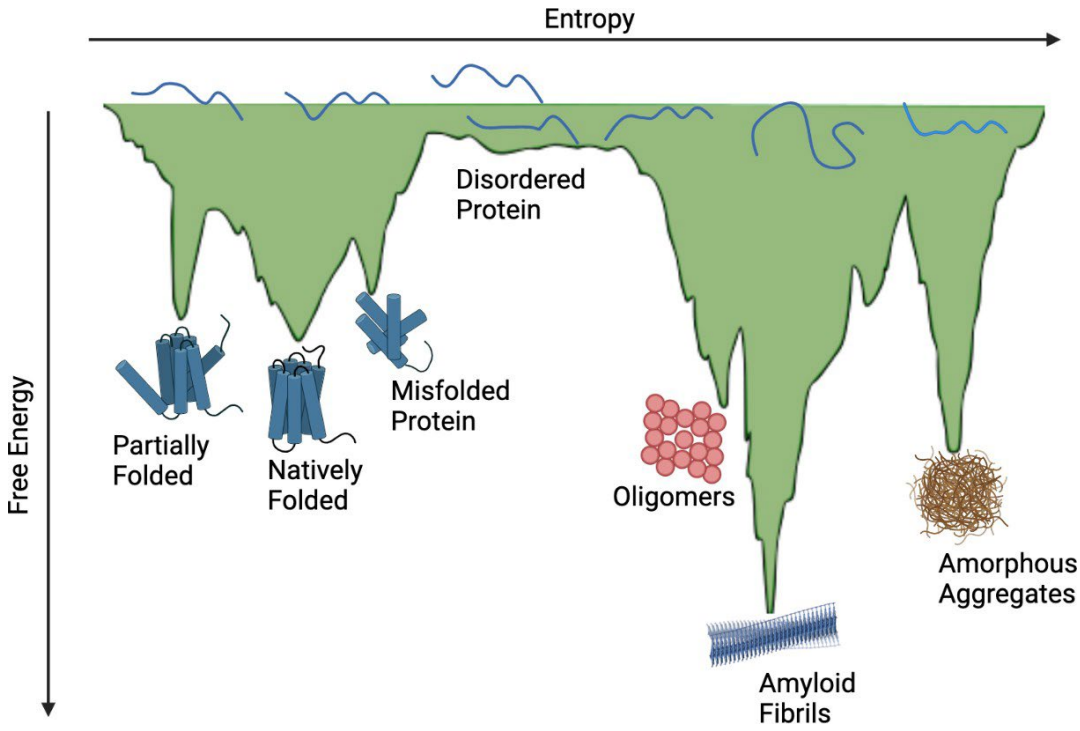

Figure 1.3 Energy landscape of protein folding and amyloid formation. The Y-axis shows free energy of the system as it decreases during intramolecular and intermolecular non-covalent bond formation. The X-axis represents the configurational entropy of the unfolded protein.

During LB formation, $\boldsymbol{\alpha}$S fibrils interact with autophagosomes, ER, golgi, kinesin, dynein and myosin and sequesters them. The sequestration is thought to inactivate cellular ER to golgi trafficking and dysregulation of Rab1a, mislocalization of Atg9 and finally inhibition of autophagy[94–96]. Additionally, BiP, the ER resident Hsp 70 is

sequestered in LB's. This finding is analogous to other reports that oligomers bind Hsp 40 and prevent its interaction with HSP 70. The disrupted interaction between the chaperones inhibits downstream unfolding/refolding mechanism of the HSP system[97].

Inflammation is also considered a neurotoxic event in PD and aging. When neurons secrete $\boldsymbol{\alpha}$S fibrils and oligomers, the aberrant aggregates can recruit and activate microglia through the toll-like receptor 2 (TLR2)[98,99]. This induces inflammation and secretion of Interleukin-6 (IL-6) – a clinical indicator PD severity – IL-17 and Tumor necrosis factor alpha (TNFα)[100,101]. Once TNFα interacts with its receptor TNFRII, they activate the NMDA receptor resulting in Ca^{2+} influx which leads to ERK-dependent neuronal death[102]. Another mechanism TNFα induces cell death is proliferating microglia and activating neuronal phagocytosis[103].

The activation of microglia is also associated with increased levels of inducible Nitric Oxide Synthase (iNOS) which catalyzes the production of nitric oxides and reactive oxygen species, which are cytotoxic[104].

1.4 Therapeutic intervention for Parkinson's disease

The Substantia nigra pars compacta (SNpc) – the anatomical region that shows degeneration during PD – has neurons that innervate to the basal ganglia and interact with the striatum (putamen and caudate). These neurons release dopamine that bind D1 and D2 - dopamine receptors on medium spiny neurons (MSN) activating and inactivating the direct and indirect pathway of movement. The dopaminergic activation of D1- dopamine receptors on MSNs leads to activation and initiation of movement through the direct pathway. Conversely, dopaminergic inactivation of D2 - MNSs leads to deactivation of the indirect pathway (a pathway that inhibits movement) and leads to activation of

movement. Thus, the net effect of the nigrostriatal pathway (SNpc innervation and dopamine release into basal ganglia) is to activate movement[105].

In PD, the death of SNpc neurons leads to lower dopamine levels in the nigrostriatal pathway and reduced effect on MSNs expressing D1 and D2 -dopamine receptors. The consequence of reduced D1 direct pathway activation is impared motor ability[106].

Reduced inactivation of D2 indirect pathway leads to typical parkinsonism like bradykinesia, freezing gate and motor deficits[107,108]. In late 1960, levodopa (a carboxylated precursor of dopamine) was given to advanced PD patients showing promising therapeutic properties. To this day, the levodopa is used in combination with Carbidopa (a peripheral decarboxylase inhibitor) to compensate for the reduced dopamine in the PD brain. Apomorphine – an agonist of D1 and D2 - like receptors – that mimics the effect of dopamine has been relatively successful at managing PD. Deep-brain stimulation (DBS) is another surgical intervention introduced in the 1990's. Using electrodes placed in the ventral intermediate nucleus of the thalamus and globus pallidus internal and applying high frequency electrical stimulation, PD patients experience reduced symptoms and better quality of life[109,110].

Although these approaches are useful, they have five drawbacks. One, these therapeutic approaches treat the symptoms but don't address the loss of dopaminergic neurons or αS aggregation. Two, these treatments don't slow or halt the natural progression of the disease, as the disease progresses, higher Levodopa doses might be required. Three, long term use of levodopa causes levodopa induced dyskinesia and other severe side effects[111]. Four, DBS is a major surgical procedure with unknown mechanism

of action and potential risk of complications like infection, stroke and paralysis. Five, patients often develop resistance to levodopa treatment after several years of use while some patients don't respond to treatment at all[112]. Thus, it's imperative to develop novel therapeutics that address the loss of dopaminergic neurons and halt disease progression.

1.5 Aggregation inhibitors as Parkinson's Disease therapeutics

Although the complete etiology of PD is still unknown, $\boldsymbol{\alpha}$S aggregation and accumulation is central to its pathogenesis. Studies involving Intrastriatal injection of $\boldsymbol{\alpha}$S aggregates in nonhuman primates have definitely shown that fibrils are able to enter neurons, recruit endogenous $\boldsymbol{\alpha}$S, induce lewy pathology and loss of dopaminergic neurons and propagate in a prion like fashion[113,114]. Since $\boldsymbol{\alpha}$S fibrils are sufficient to replicate all the pathological events of PD and parkinsonism in model organism, inhibiting its aggregation is a promising therapeutic option. Thus, I hypothesize, by using small molecule aggregation inhibitors of $\boldsymbol{\alpha}$S, it's possible to modulate the cellular accumulation of $\boldsymbol{\alpha}$S aggregates into LBs and rescue dopaminergic neuron loss.

Several molecules that modulate $\boldsymbol{\alpha}$S *in vitro* aggregation have shown efficacy in mammalian models by inhibiting cellular $\boldsymbol{\alpha}$S aggregation, preserving neurons and preventing parkinsonism[115–117]. There are examples like NPT200-11 that have passed preclinical testing for efficacy and phase I trial for safety[116,118].

1.6 Previously identified αS inhibitors and their limitations

The αS structures that form during aggregation are diverse, thus, there aren't high resolution structural data. So, most of the aggregation inhibitors are identified by screening large molecular libraries instead of rational design. Most of the identified

inhibitors are natural products like biogenic monoamines, polyphenols, phenothiazines, flavonoids, and anthocyanidins (figure 1.8). These molecules are large aromatic compounds that are conjugated and highly oxidized[119]. Although some of these natural compounds are in clinical trials, they have several limitations. For example, Epigallocatechin gallate (EGCG), a green tea extract, is a potent inhibitor of αS aggregation and even has the potential to destabilize fibrils[120,121]. EGCG can easily cross the Blood Brain Barrier (BBB) (Permeability coefficient = $9.31 \pm 0.32 \times 10^{-6}$ cm/s) but it is subject to metabolism by the intestinal bacteria (half-life ~ 3 h) and excreted through the urinary system[122,123]. Thus, only ~ 0.1% of ingested EGCG makes it to the brain[124]. This limited bioavailability is shared by other natural compounds like curcumin. Curcumin, a potent inhibitor of αS aggregation isn't very soluble in water, suffers from poor absorption and ~ 90 % of the ingested compound is excreted through the feces[125].

Two steroid-polyamine conjugates, Trodusquemine (TRO) and Squalamine (SQ), are analogs isolated from sharks and studied extensively for their antimicrobial activity. These cationic steroids insert into the inner leaflet of membranes and reduce its negative charge[126]. They can also destabilize protein membrane interaction[127]. These molecules have shown good anti- αS aggregation properties and have been tested in clinical trials (phase I-III) for safety and efficacy against macular degeneration[128]. Although these molecules are safe according to phase I clinical trial results, SQ can't cross the BBB. On the other hand, TRO can cross BBB, but its ability to displace proteins from cell membranes has created controversy[129]. Even Though the toxic oligomers cause toxicity by interacting with membranes, and TRO can prevent oligomer membrane interaction

preventing toxicity; displacing the monomer from vesicles – its physiological location – can also cause αS's loss of function.

Other therapeutics developed against αS toxicity are S37 peptide and AS69 protein that either bind the fibril core at the ends of the fibril and prevent additional monomeric αS from being added or bind αS monomers and prevent nucleation[130,131]. This approach has limitations because αS fibrils form diverse core structures made up of variable αS sequence and S37 peptide might not work for all amyloid structures. Since S37 is a peptide, it might suffer from proteolytic degradation and have immunoreactivity. The same goes AS69 protein, the protein needs to cross the BBB without being degraded or inducing immune response.

Other well studied potential drugs against PD are NPT100-18A and NPT200-11. They were developed after Molecular Dynamics (MD) simulations showed amino acids 96 to 102 cause dimerization of αS on membranes[132]. The authors speculated inhibiting the dimerization interface could prevent aggregation so they computationally designed inhibitors that target the c-terminus and they found NPT100-18A and NPT200-11 could prevent intracellular αS aggregation[132]. NPT200-11 is in phase II clinical trials and shown to be safe for human use[133]. Unfortunately, the drug didn't show significant improvement in Line 61 PD mouse models. Administering the drug didn't improve grip strength, had little effect on slip and protease resistant αS assemblies[116]. Since many of the inhibitor of αS aggregation mentioned above have limitations, it's imperative to develop other strategies to prevent αS multimerization.

1.7 Foldamers as inhibitors of protein-protein interaction and therapeutics

The nucleation, multimerization and aggregation of αS is initiated and sustained by aberrant protein-protein interactions (PPI). Typically, PPIs have flat and large (1000 - 4000 $Å^2$) interfaces[134]. Thus, PPIs are too large to target with small molecules which are effective against smaller surface area (300 - 1000 $Å^2$) and require a binding cleft[135]. This suggests PPIs aren't amenable to targeting by small molecules. Additionally, hotspots - interactions between non-congruent residues that stabilize the PPIs are commonly found in peptide secondary structures like α- helices and β-sheets. So, peptides and peptide mimetics are used as PPI inhibitors. Synthetic peptide mimetics are more attractive because they aren't sensitive to proteolytic degradation.

The monomeric αS, although disordered, has pre structured motifs that can exchange between α-helical and disordered structures[136]. Once aggregation commences, the intermediate structures – oligomers – are populated with ~ 47 % α-helix and ~ 29 % β -sheet structures. Proto-fibril contain more β-sheet structure at ~ 54 % and lower α - helical structure at ~ 37 %[137]. Mature fibrils contain ~ 66 % β-sheet structure and almost no disordered regions. This goes to show how important secondary structures are at stabilizing the different ordered conformations of amyloid intermediates. Since the αS aggregation process and toxic intermediates are stabilized by intermolecular protein-protein (PPI) interaction between secondary structures, we hypothesized disrupting the PPIs between the secondary structures, could prevent αS aggregation.

For the reasons mentioned above, we turned to a class of peptide mimetic small molecules called Foldamers. Foldamers are short polymers that adopt conformationally

folded structures in aqueous solution and are stabilized by noncovalent interactions between non-adjacent monomers[138]. We polymerized pyridyl and quinoline monomeric units to construct oligopyridyl (OP) and oligoquinoline (OQ) foldamer libraries to screen against αS aggregation. Both type of foldamers mimic α-helical topology but in different ways. Oligopyridyls are structurally stabilized by hydrogen bonds and conformationally restrained and don't have rotational freedom. When OP foldamers are superimposed with α-helix turns, the OP functional groups overlap with *i*, *i* + 3/ 4 and *i* + 7 side chains form the helix. OQs on the other hand can fold into a helix due to π-stacking and hydrogen bonding and Once folded, they present functional groups that can interact with α-helical side chains at *i* and *i* + 3/ 4.

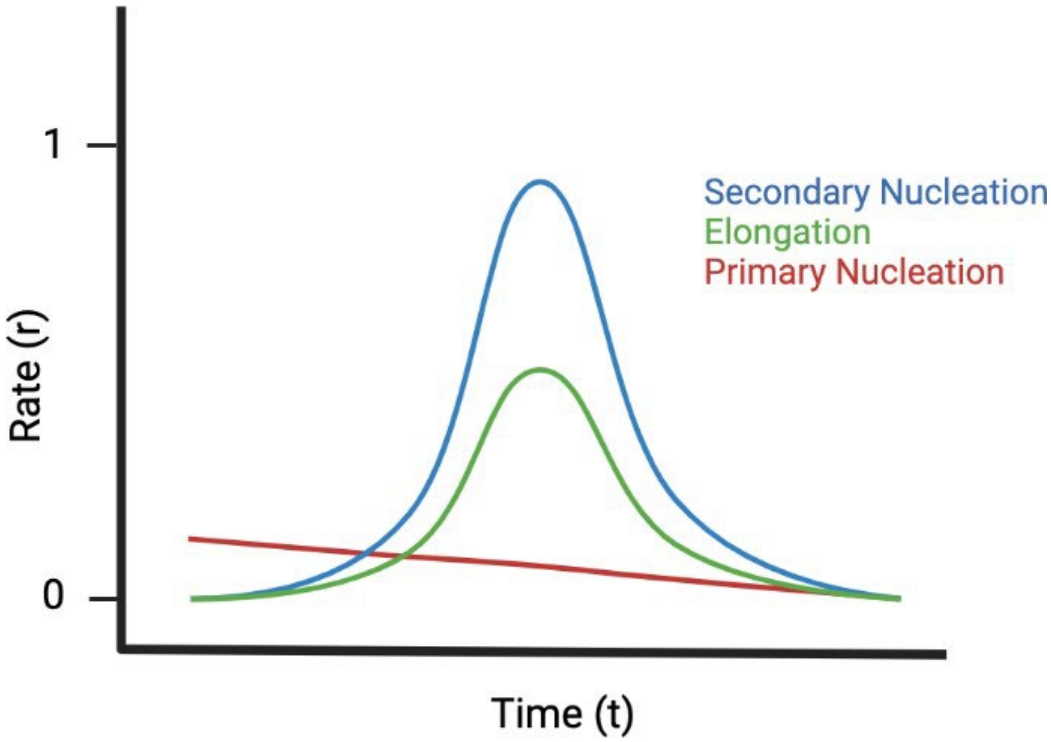

Figure 1.4 shows the rate of fibril proliferation as a function of time. At time = 0, elongation and secondary nucleation don't proceed and primary nucleation is the

predominant process. As fibrils form and proliferate, the rate of primary nucleation decreases and elongation and secondary nucleation increase. Fibril proliferation proceeds through secondary nucleation more than elongation.

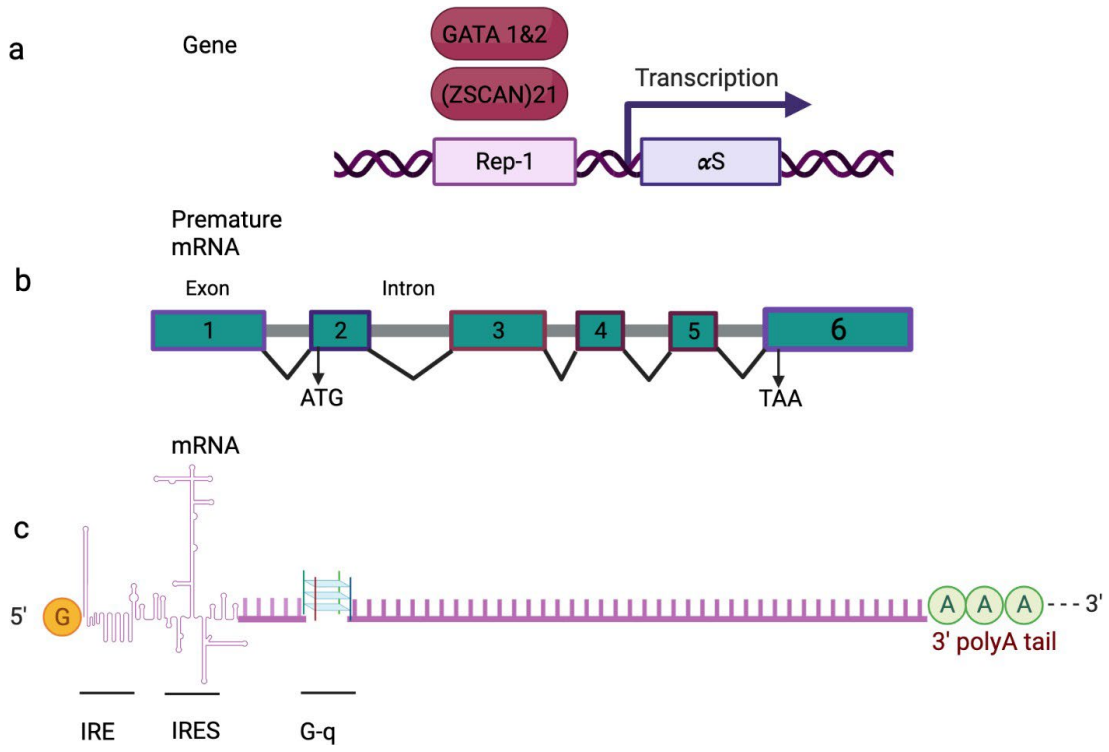

Figure 1.5 a shows the transcription factors and promoter region that regulate αS transcription. b shows the pre-mature mRNA with exons 1 - 6 and 5 introns. c represents the mature mRNA with 5' cap, G-quadruplex, internal ribosomal entry site, iron regulatory element and poly A tail.

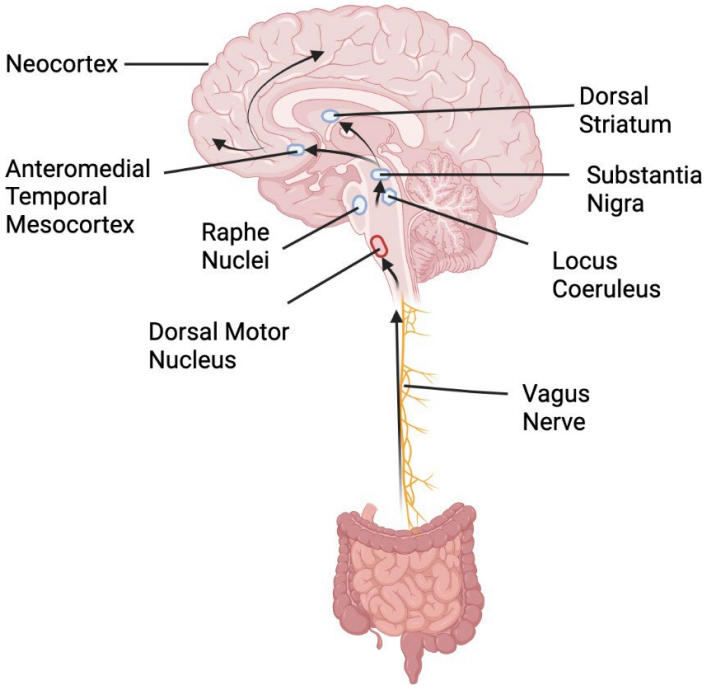

Figure 1.6 shows anatomically connected neurons and brain regions that αS fibrils spread, starting from the gut to the basal ganglia and neocortex.

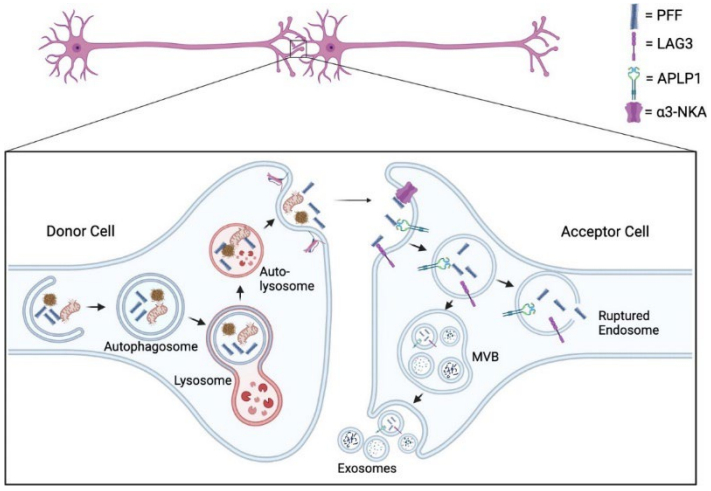

Figure 1.7 shows cellular mode of αS fibril transfer where a donor cell secrets αS fibrils into the synaptic cleft and an acceptor cell internalizes the amyloids into its cytoplasm through endocytosis.

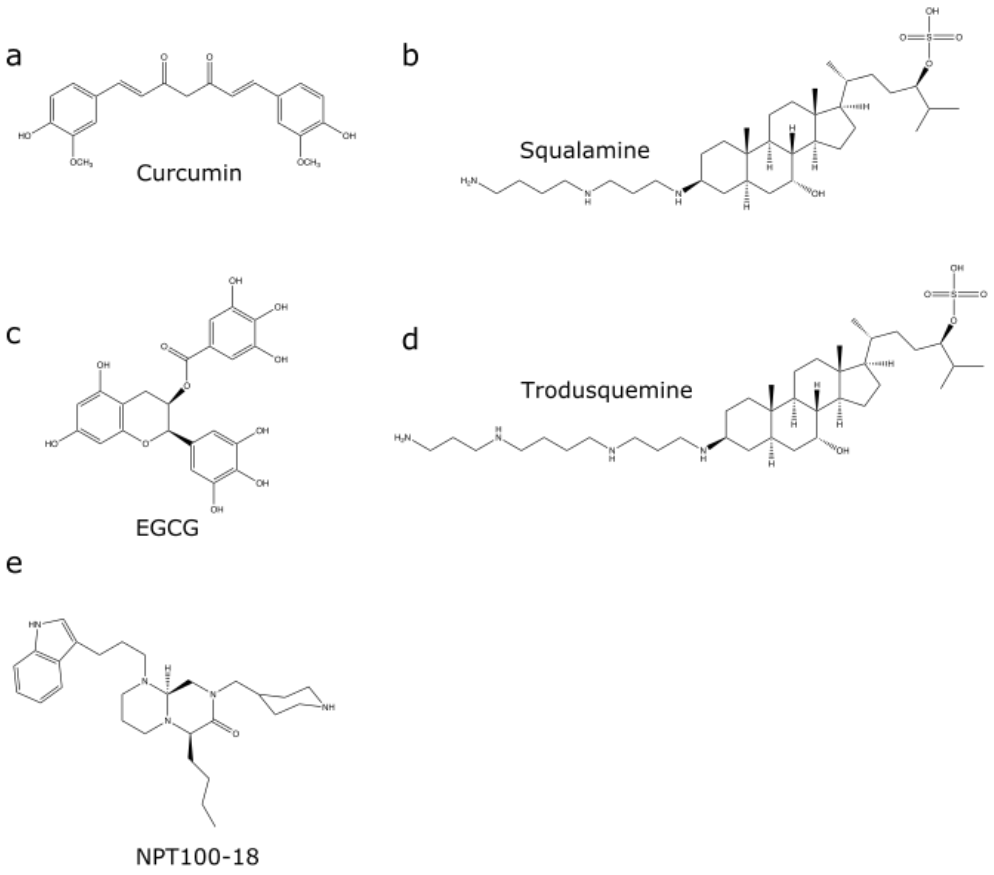

Figure 1.8 shows molecules that have potent anti-aggregation potential against αS. E shows NPT100-18 redrawn from Wrasidlo *et al*[132].

Chapter 2: Foldamers reveal and validate therapeutic targets associated with toxic α-synuclein self-assembly

2.1 Introduction

Alpha-Synuclein (αS) is a neuronal protein expressed at high levels in dopaminergic neurons and it is believed to be implicated in the regulation of synaptic vesicle trafficking and recycling, and neurotransmitter release. The misfolding of αS leads to its self-aggregation, which is a pathological hallmark of PD[139]. Therefore, modulation of αS aggregation is a promising therapeutic intervention for PD. The identification and specific targeting of sequences or domains that initiate αS aggregation could promise potent antagonism of the αS self-assembly. A few small molecules have been shown to inhibit αS aggregation, however, limited atomic-level understanding is available of the ligand-αS interaction, which restricted the further optimization of the antagonists against αS aggregation. More importantly, limited progress has been made in the identification of factors that are associated with αS aggregation, e.g., αS sequences that initiate aggregation. Mutation studies enable the identification of αS sequences/domains that are important for aggregation[140]. However, no study has been directed to validate these αS sequences as novel targets. Here, we have utilized a foldamer-based approach in tandem with a mutation study that allowed the identification and validation of αS sequences as key therapeutic targets that are essential for the initiation of αS aggregation.

Foldamers are dynamic ligands with the ability to mimic the topography and the chemical space of the secondary structure of proteins[141,142]. The diversity of chemical space can be conveniently tuned in foldamers, an essential property for the optimization of interactions with targets. Various foldamers, including Oligoquinoline (OQ)-based and photo responsive prion-mimics have been shown to modulate the self-assembly of islet amyloid polypeptide, Aβ peptide, and αS whose aggregation is associated with type 2 diabetes (T2D),Alzheimer's disease (AD), and PD respectively[143,144].

We have utilized OQs to gain mechanistic and therapeutic insights into αS aggregation. Using an array of biophysical, cellular, in vivo assays and mutation studies, we have identified SK-129, a potent antagonist of αS aggregation in both in vitro and in vivo PD models. A Two-dimensional (2D) NMR-based-based atomic-level investigation enabled the identification of the binding sites of SK-129 on αS, which are validated using fluorescent polarization and mutation studies. More importantly, we have identified αS sequences as novel targets that are essential for the initiation of the aggregation. We have also validated αS sequences by targeting them with OQs and rescued PD phenotypic readouts in cellular, neuronal, and in vivo PD models. SK-129 is a potent antagonist of the αS seeds catalyzed aggregation of αS monomer. The activity of SK-129 against the αS seeds catalyzed aggregation is confirmed using distinct αS seed polymorphs generated from the recombinant αS and extracted from the substantia nigra of the post mortem brain of PD patient. The antagonist activity of SK-129 is also confirmed in a novel HEK cell-based intracellular assay for the αS seeds catalyzed aggregation of intracellular monomeric αS. Overall, SK-129 interacts at the N-terminus of αS monomer, induces or stabilizes an aggregation incompetent helical conformation, and modulates both denovo

aggregation and the αS seeds catalyzed aggregation. We used a chemical tool to identify and validate αS sequences with structural insights that are essential for the aggregation and associated with PD phenotypes. The study will have significant mechanistic and therapeutic implications, which will aid in expediting treatments for PD.

2.1 Methods

2.2.1 Expression and Purification of Proteins

The proteins, WT αS, Δ6-12 αS, and Δ47-53 αS were expressed and purified from the periplasm according to previously described protocol[145,146]. Briefly, the WT αS sequence cloned into pET11 vector (Addgene, Watertown, MA), Δ6-12 αS and Δ47-53 αS cloned in pET-21a(+) (GenScript Biotech, Piscataway, NJ) were chemically transformed into *Escherichia coli* BL21(DE3) cells. Transformed cells were grown at 37 °C and shook at a rate of 200 rounds per minute (rpm) until the O.D. (optical density) reached a value of 0.8. Protein expression was induced by adding isopropyl β-D-thiogalactoside (IPTG) at a final concentration of 1 mM. The induced cells were kept shaking at 200 rpm at 37 °C for 5 h. Cells were then collected by centrifugation (8217×g at 4 °C for 10 min) and resuspended in an osmotic shock buffer (30 mM Tris pH 7.2, 30% sucrose, 2 mM EDTA) and stirred for 15 min, similar to the reported protocol[145]. Subsequently, cells were collected again from the osmotic shock buffer by centrifugation (7177 × *g* for 10 min at 4 °C) and reconstituted in cold Milli-Q water and stirred for another 10 min. A solution of 5 mM MgCl2 was added and stirred cells for an additional5 min. Cells were removed by centrifugation at 5635 × *g* for 10 min and the solution was boiled at 95 °C for 15 min for further purification.

The resulting protein precipitate was centrifuged (6000 × *g* for 20 min) and loaded on Bio-Scale Macro-Prep High Q ion-exchange column (Bio-Rad, Hercules, CA) (20 mM Tris pH 8.0, 25 mM NaCl, 1 mM EDTA). The protein was eluted with a high salt buffer (20 mM Tris pH 8.0, 1 M NaCl, 1 mM EDTA). The purified protein was buffer exchanged and concentrated in Milli-Q water using amicon ultra 3 K filters (MilliporeSigma, Burlington, MA). The concentration was determined using NanoDrop One ($\varepsilon_{280} = 5960\ M^{-1}\ cm^{-1}$) and lyophilized, then stored at −80 °C. Mutants Δ15-23 αS and Δ36-45 αS cloned into pET-21a(+) were transformed into T7 Express Iq competent cells. The cells were grown, induced, and collected as described above. The cell pellet was reconstituted in IEX A buffer (20 mM Tris pH 8.0, 25 mM NaCl, 1 mM EDTA) and boiled for 20 min at 95 °C. The insoluble fraction was removed by centrifugation at 6000 × *g* for 20 min and the soluble fraction was loaded on Bio-Scale Macro-Prep High Q ion-exchange column and purified as described above. The purified proteins (WT and mutants) were characterized using mass spectrometry (Mass spec facilities at the University of Colorado, Anschutz Medical Campus, CO and the University of Illinois at Urbana-Champaign mass spec facility, IL, Fig. 2.1-2.5) and the purity was confirmed with SDS-PAGE (Fig. 2.6).

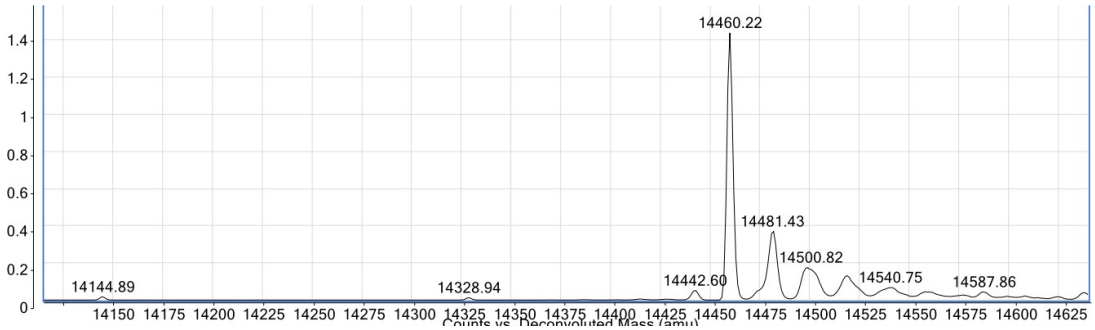

Figure 2.0 ESI-MS spectrum of αS1. Theoretical mass = 14460.2, Observed mass = 14460.2.

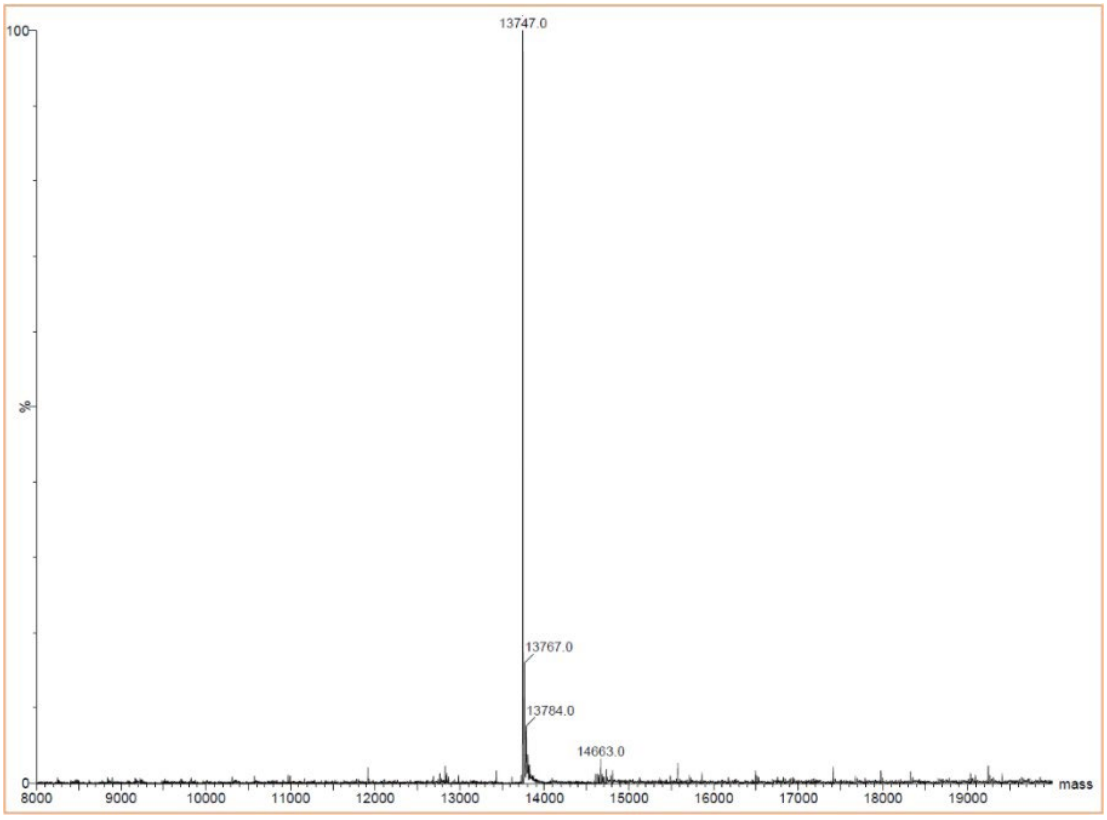

Figure 2.1 ESI-MS spectrum of αS1. Theoretical mass = 13,747.3, Observed mass = 13,474.0

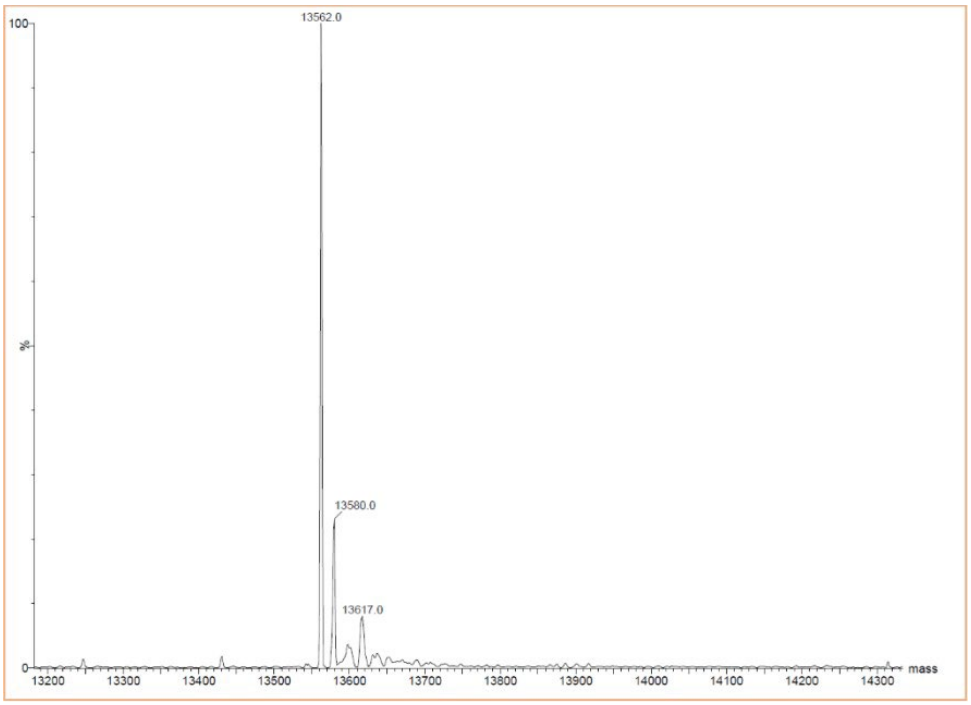

Figure 2.2 ESI-MS spectrum of αS2. Theoretical mass = 13,562.1, Observed mass = 13,562.0

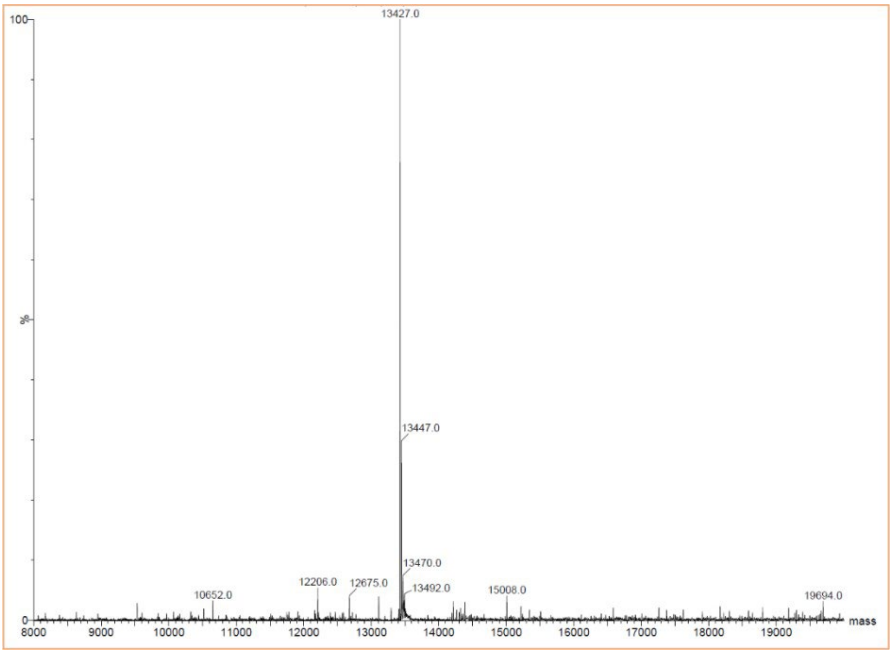

Figure 2.3 ESI-MS spectrum of αS3. Theoretical mass = 13,426.9, Observed mass = 13,427.0

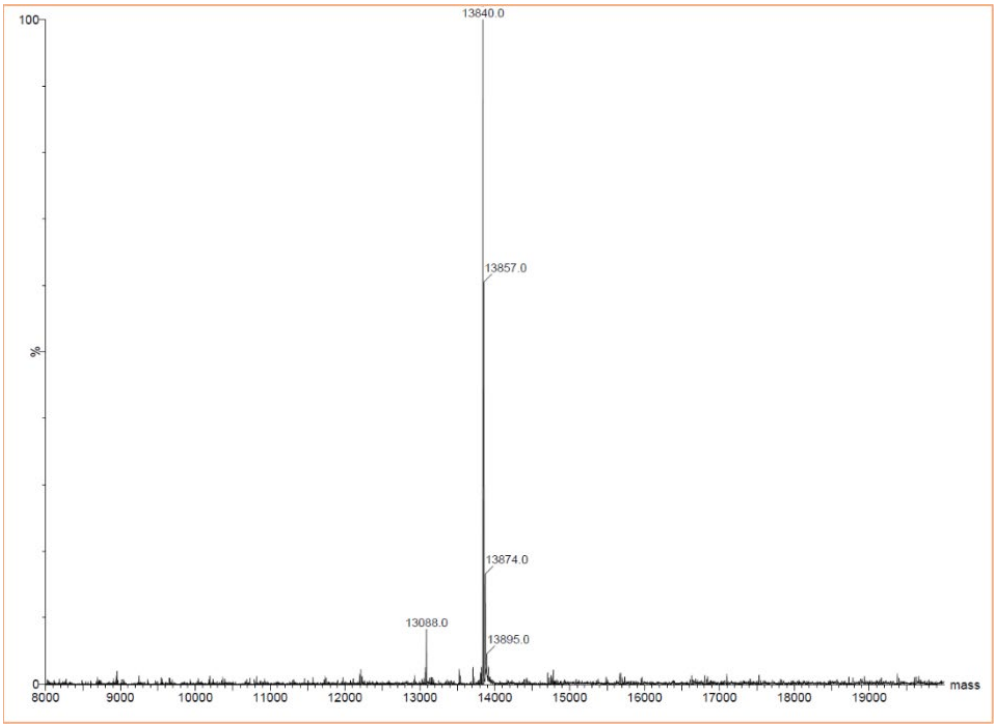

Figure 2.4 ESI-MS spectrum of αS4. Theoretical mass = 13,840.4, Observed mass = 13,840.0

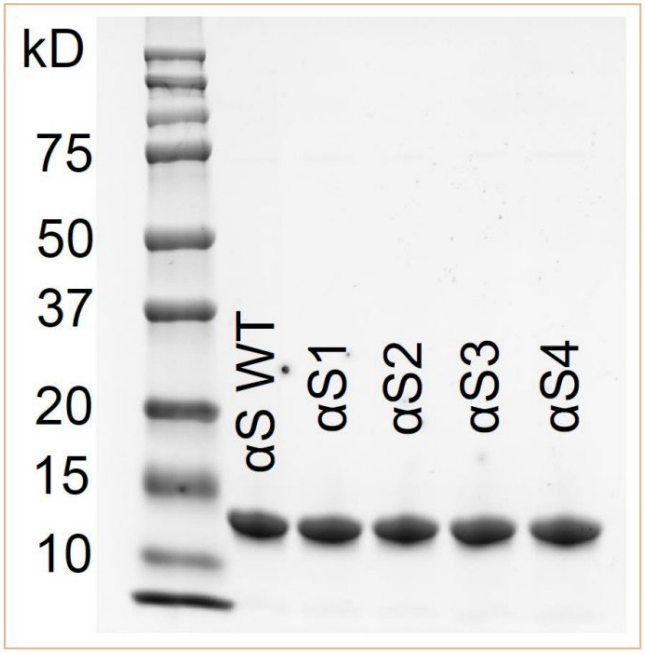

Figure 2.5 SDS-PAGE of WT αS and various αS mutants, αS1, αS2, αS3, and αS4 that have deleted residues 6-12, 15-23, 36-45, and 48-53, respectively.

2.2.2 ThT-based aggregation kinetic assay

The aggregation kinetics of αS was monitored using ThT fluorescence assay (λex = 450 nm and λem = 485 nm). To study the aggregation kinetics of αS, the ThT dye at a final concentration of 50 μM was added to 100 μM αS solution in the aggregation buffer (1 x PBS buffer) with and without various concentrations of SK-129 in a Costar black 96–well plate (Corning Inc., Kennebunk, ME). The small molecules were dissolved in dimethyl sulfoxide (DMSO; final DMSO concentration = 0.5%, v/v). The final volume in each well was 140 μL. The plate was incubated at 37 °C with 16 min shaking (434 rpm) and 44 min without shaking in an Infinite M200PRO plate reader (Tecan, Männedorf, Switzerland) and fluorescence was recorded after every hour. We used two methods to quantify the effect of molecules on the aggregation of αS; either we have reported the *t*50 (time required to reach 50% fluorescence of ThT), which was extracted by fitting the ThT curve as a sigmoidal fit or the absolute ThT fluorescence intensity was reported. ThT-based aggregation kinetics were conducted three times and the reported *t*50 (with or without ligands) is an average of three separate experiments. In the second method, we determined the final ThT fluorescence intensity for the aggregation of αS/Aβ42(with or without ligands) as an average of three separate experiments. In this method, proteins (αS/Aβ42) were aggregated in the absence and presence of various ligands at the indicated molar ratios similar to the above-mentioned conditions. The experiments were conducted three separate times and the reported ThT intensity was an average of three separate experiments. The ThT intensity was reported as relative intensity where the highest and lowest intensity were used from the protein sample and the control (ThT, DMSO, and buffer conditions only), respectively. The concentration of

DMSO was kept constant (1%, v/v) in protein (αS/Aβ42), control, and molecule solutions. The aggregation kinetics of WT αS and αS variants were monitored and was carried out with a slightly modified protocol. A 100 μM monomeric WT αS/ αS variants solution (200 μL, in 1x PBS buffer) was placed into a ThermoMixer (Eppendorf, Hamberg, Germany) and shook for five days at a rate of 14,000 rpm and 37 °C. The aggregation of proteins was monitored at the indicated times (See the main manuscript). For each data point, a 5 μL protein solution (from 100 μM stock solution) was pipetted and diluted to a total of 100 μL (in 1x PBS buffer). To this solution, ThT dye (5 μM from a stock solution of 1 mM in 1x PBS buffer) was added and the solution was mixed well. The solution was transferred to a 96-well black plate and the ThT fluorescence intensity was measured using a 96-well plate reader. A solution of ThT dye in 1x PBS buffer was used as a control. For each protein (WT αS and αS variants), the ThT experiment was conducted in triplicate.

Seed-catalyzed αS aggregation assay was performed similarly to a previously described protocol[147]. Briefly, 100 μM monomeric WT αS solution (200 μL, in 1x PBS buffer) was placed into a ThermoMixer (Eppendorf, Hamberg, Germany) and shook for five days at a rate of 14,000 rpm and 37 °C. The solution was sonicated for 10 min and used as αS seeds. The seed-catalyzed aggregation of WT αS/ αS variants was performed by adding αS seeds (10% seeds, αS in monomeric concentration, v/v) into 140 μL of fresh 100 μM WT αS/ αS variants solution and aggregation was started with constant shaking at a rate of 14,000 rpm and 37 °C. The aggregation of proteins was monitored at the indicated times (See the main manuscript) using the above-mentioned method.

The ThT aggregation assay for each protein (WT αS and αS variants) in the presence of SK-129 was carried out the above-mentioned method. SK-129 (from 10 mM stock solution in DMSO) was added at an equimolar ratio (1% DMSO, v/v) to the proteins at the start of the aggregation experiment. The concentration of DMSO was kept constant (1%, v/v) in protein (WT αS and αS variants), control, and protein+molecule solutions. The kinetic profiles of protein aggregation were processed using OriginPro software (Version 9.1). Kinetic curves were fit using a built-in sigmoidal fit in the OriginLab.

2.2.3 Large unilamellar vesicles preparation

The LUVs were prepared from a powder of 1,2-dioleoyl-sn-glycero-3-phospho-L-serine (sodium salt) (DOPS, Avanti Polar Lipids, Alabaster, AL). The powder was hydrated in 1x PBS buffer and vortexed for 15 min to make a 20 mM mixture of DOPS. The mixture of lipid in buffer was passed 21 times through a mini extruder (Avanti Polar Lipids, Alabaster, AL) using a polycarbonate membrane (Pore diameter = 100 nm, Avanti Polar Lipids, Alabaster, AL). The sizes of liposomes were confirmed using dynamic light scattering. The liposomes were used within a week of their preparation in various experiments.

2.2.4 Circular dichroism spectroscopy

The CD experiments were carried out on a JASCO J-1100 instrument. To study the kinetics of αS aggregation, a freshly prepared solution of 100 μM (or 70 μM) αS in 1x PBS buffer was used. The CD spectra were recorded from 260 nm to 195 nm at 0.5 nm intervals with 15 s averaging time and an average of three repeats. The αS solution was then aggregated at 37 °C with constant shaking (1400 rpm) for 7 days. The aggregated

solution of αS was diluted to run the CD spectra. Similar CD experimental conditions were used to study the aggregation kinetics of various αS variants. To monitor the effect of SK-129 on αS aggregation, similar conditions were used in the presence of SK-129, except a solution of 1:1 molar ratio of SK-129: αS was used for CD experiments. The CD experiment in lipid membrane conditions was carried out with a solution of 30 μM αS in 375 μM LUVs (100 nm, DOPS) in the absence and presence of 30 μM SK-129. The CD spectrum of SK-129 was also recorded, which does not show any strong signal in the region of 190–260 nm and no interference was observed with SK-129 CD signal intensity. All CD experiments were conducted one time and the CD experiments between αS and SK-129 (or LUVs, DOPS) were conducted at different stoichiometric ratios and a consistent trend of the change in the CD signals was observed as a function of stoichiometric ratios (of αS and SK-129/DOPS, LUVs), which supports the reproducibility of the data.

2.2.5 αS and LUV titration

The binding affinity between αS and LUVs was determined according to previously described methods[148]. Briefly, 300 μL of a 40 μM αS solution in PBS buffer was placed in a 1 mm pathlength Quartz cuvette (Hellma, Plainview, NY) and the CD spectra was recorded at 30 °C, 1 nm data pitch and 1 nm band width using a Jasco-1100 CD spectrometer (Jasco, Easton, MD). Subsequently, increasing concentrations of LUV's (100 nm, DOPS) were titrated into the αS solution and mixed well before recording the CD scan. After each titration, 5 min was waited until the next measurement. The change in the CD signal (at wavelength = 222 nm) was plotted against the molar ratio LUVs to

αS. The plot was fitted using one binding site model according to the earlier used methods[148].

2.2.6 Transmission Electron Microscopy

A solution of αS (600 μM) was incubated in 1x PBS buffer (150 mM NaCl, 2.7 mM KCl, 8 mM Na2HPO4, and 2 mM KH2PO4) in the absence and presence of SK-129 at an equimolar ratio at 37 °C and with constant shaking at 1200 rpm for 72 h. The aliquots (5 μL) of the solutions were applied on glow-discharged carbon-coated 300-mesh copper grids for 2 min and dried using tissue paper. The copper grids were negatively stained for 60 sec with uranyl acetate (0.75%, w/v). The micrographs were taken on an FEI Tecnai G2 Biotwin TEM at 80 kV accelerating voltages. The TEM experiments were repeated three times ($n = 3$) independently to ensure the reproducibility of the data.

2.2.7 SDS-PAGE analysis

The solution of αS (100 μM) in the absence and presence of SK-129 were prepared in the aggregation buffer (20 mM NaCl, 20 mM NaPi, pH 6.5) and kept at 37 °C and constant shaking at 1200 rpm until the aggregation of αS plateaued (four days). The solutions were separated into soluble and insoluble fractions of αS by centrifugation at 22,000 × g for 20 min. Afterwards, 2 x Laemmli protein sample loading buffer (Biorad, Hercules, CA) was added to the fractions and boiled at 95 °C for 5 min and ran on a 12% Mini-PROTEAN precast protein gel (Biorad, Hercules, CA). In addition, we also quantified SDS-PAGE gel band intensities using ImageJ software. The gel-based experiments were repeated three times ($n = 3$) independently to ensure the reproducibility of the data.

2.2.8 αS fibril extraction from brain matter

Fixed brain tissues were obtained from the Carroll A. Campbell, Jr. Neuropathology Lab (CCNL) brain bank at the Medical University of South Carolina (Dr. Steve Carroll, Director) and from Dr. Greg Gerhardt's laboratory at the University of Kentucky. The seeds were extracted from the postmortem brain by following a published protocol with a slight modification[149]. The brain was sliced in 1 cm slabs as soon as possible to avoid long postmortem intervals and fixed free-floating in a solution of 4% paraformaldehyde in 1x PBS buffer (4% paraformaldehyde in 1x PBS buffer). All brain tissues used in the study had a postmortem interval (PMI) of less than 12 h. Following fixation, tissue was transferred to a cryoprotectant solution (30% glycerol, 30% ethylene glycol, and 40% 1x PBS buffer, v,v) and kept at −20 °C until dissection. A total of Sixteen brain regions were dissected after fixation and processed for neuropathological diagnosis of PD according to a published protocol[149]. A diagnosis was conducted, which included staining with H & E, Bielshowsky's silver stain, as well as p-Tau, Amyloid-β, and αS immunohistochemistry. From the total tissue amount, ~100 mg of fixed *substantia nigra* tissue was homogenized using a Bio-Gen PRO200 Tissue Homogenizer (PRO Scientific Inc., Oxford, CT) in 1x PBS buffer (10%, w/v). The homogenate was centrifuged at a rate of 19,000 × *g* for 12 min. The supernatant was discarded, and the pellet was homogenized again in 1 x PBS buffer supplemented with Triton-X 100 (1%, v/v). The solution was centrifuged (19,000 × *g* for 12 min) to remove soluble components and the pellet was reconstituted in 1 x PBS buffer with 1% Triton X-100 (v,v) and stored at −80 °C prior to use in various experiments.

2.2.9 Preformed misfolded amplification assay

The PMCA was performed according to the previously described method[150]. A lyophilized αS powder was dissolved in 1x PBS buffer to a final concentration of 90 µM. Subsequently, 60 µL of the 90 µM αS solution was placed in 200 µL Polymerase Chain reaction (PCR) tubes and the mixture was subjected to 24 h cycles of 1 min shaking (1200 rpm) and 29 min incubation at 37 °C. Every 24 h, 1 µL of PMCA incubated sample was transferred to a fresh soluble monomeric αS solution, which was repeated for five days. For the preparation of PMCA samples of αS in the presence of SK-129, the samples were prepared by adding SK-129 to maintain a molar ratio of 1:1 (αS:SK-129). Control samples were prepared with an equal volume of DMSO (0.9%) as used in the case of SK-129. All experiments were performed in triplicates.

For the PMCA assay for αS seeds extracted from PD brain, we have used similar conditions to αS seeds from recombinant αS with slight modification. The αS seeds extracted from PD brain were added at 5% (v/v) to freshly prepared monomeric αS solution (60 µL and 90 µM) and the assay was carried out as described above for the recombinant αS seeds where we used a 1 µL solution for each cycle for up to five cycles.

2.2.10 Proteinase K digestion

A 50 µg/ml solution of PK (IBI Scientific, Dubuque, IA) in the digestion buffer (10 mM Tris pH 8.0, 2 mM CaCl2) was diluted 10 times into 30 µL of PMCA solutions and incubated for 30 min at 37 °C. Subsequently, the sample was diluted 2 times in SDS Protein Gel Loading Dye 2 × (Quality Biological, Gaithersburg, MD) and loaded on Mini-PROTEAN TGX Stain-Free Protein Gel (BioRad, Hercules, CA). The gel was

stained with Fairbanks staining method and then imaged using ChemiDoc MP (BioRad, Hercules, CA).

2.2.11 Primary rat hippocampal neuron culture

Pregnant Sprague Dawley Rats (72-85 days old, mixed male and female) were purchased from Charles River Laboratories (Strain Code 400) and maintained at the University of Denver Animal facility (AAALAC accredited). All animal protocols and experiments were approved by the University of Denver Animal Care and Use Committee.

The rat embryos (both male and female) at embryonic day 18 were used to prepare the primary neurons according to previously published protocol[151]. After removing all the meninges, the hippocampi were isolated from the fetal rat brain and kept in the dissection solution (1x HBSS, 10 mM HEPES buffer, 5 µg/mL Gentamicin, pH 7.3, Thermo Fisher Scientific, Waltham, MA). The hippocampi were minced and treated in the dissection solution containing 20 U/ml Papain (Worthington Biochemical Corp., Lakewood, NJ) and triturated in 50 µg/ml Dnase I (Sigma-Aldrich, St.Louis, MO). The isolated cells were plated on 1 mg/mL Poly-L-Lysine (Sigma-Aldrich, St.Louis, MO) coated µ-slide eight-well plate (Ibidi, Munich, Germany) at 200,000 cells/mL in neuron plating medium, which includes Minimum Essential Media (MEM)(Thermo Fisher Scientific, Waltham, MA) supplemented with 5% FBS (Thermo Fisher Scientific, Waltham, MA) and glucose (Sigma-Aldrich, St.Louis, MO). After neurons adhered, the neuron plating medium was replaced with Neurobasal media (Thermo Fisher Scientific, Waltham, MA) with 0.3 C GlutaMAX (Thermo Fisher Scientific, Waltham, MA) and 1 X

B-27 (Thermo Fisher Scientific, Waltham, MA) and neurons were maintained at 37 °C and 5% CO2(g).

The fiber solution made from brain seeds via PMCA assay (5the cycle) in the absence and presence of SK-129 were added to the primary culture neurons in the eight-well plate. The seeds were added at a concentration of 1 μM (αS in monomer concentration) on DIV 10 (days in vitro). The primary cultured neurons were incubated with various conditions for DIV 21 before carrying out experiments, including lactate dehydrogenase (LDH) release assay and immunocytochemistry.

2.2.12 LDH assay

The LDH assay was performed on the primary neurons treated with various conditions and incubated for 21 DIV. The release of LDH was measured using a Cytotox 96 Non-Radioactive Cytotoxicity Assay kit (Promega, Madison, WI) by following the instructions provided by the manufacturers. After the neurons were incubated with various conditions for DIV 21, the media was collected from the wells (300 μL). The media for each condition (50 μL/each well) was transferred to a flat-bottom 96-well cell culture plate (Costar, Kennebunk, ME). To this media solution, 50 μL of the Cytotox reagent was added to make it a total of 100 μL solution and mixed gently with a pipette. The absorbance of the media in the wells was measured at 490 nm using a 96-well plate reader.

2.2.13 Immunocytochemistry

The primary neurons treated under various conditions in a μ-slide eight-well plate were washed three times with an ice-cold 1x PBS buffer and fixed with 4% paraformaldehyde for 10 min at room temperature (RT). Afterward, neurons were

permeabilized with PBST buffer (0.15%, v/v, Triton-X 100 in 1x PBS buffer) for 10 min and blocked with 5% Bovine serum albumin (BSA) in PBST buffer. Subsequently, the fixed primary neurons were stained with various primary antibodies including, LB biomarkers, αS-pS-129 (stains phosphorylated residue 129 of αS), p62 (stains autophagosome vesicles), and TOM20 (stains mitochondria) and ThS, a dye that specifically stains αS aggregates. All primary antibodies were diluted to a ratio of 1:1000 (v,v) in a 5% BSA solution in the PBST buffer. The primary neurons were incubated with the primary antibodies overnight at 4 °C and then washed five times with the PBST buffer. The primary neurons were then incubated with secondary antibodies (dilution to a ratio of 1:1000 (v,v) in a 5% BSA solution in the PBST buffer) for 1 h at RT. Afterward, the eight-well plate was washed with 1x PBS buffer (three times) to remove any excess of the antibodies. Subsequently, the cells were stained with 300 µL/well of Thioflavin S in the PBST buffer (1%, w/v) (Sigma-Aldrich, St. Louis, MO) for 10 mins and washed five times with PBST buffer and then used for confocal imaging. The primary and secondary antibody specifications are included in the Reporting Summary (Antibodies section).

2.2.14 Confocal imaging of neurons

The eight-well plate with neurons treated under different conditions was fixed and stained with various biomarkers were then imaged using confocal microscopy. The confocal imaging was performed on an Olympus Fluoview FV3000 confocal/2-photon microscope, using a 20×Plan-Apo/1.3 NA objective with DIC capability. The confocal images of the primary neurons were then processed using the OlympusViewer in ImageJ processing software. The confocal imaging experiments were repeated four times independently to ensure the reproducibility of the data.

2.2.15 Fluorescence polarization titration

All Fluorescence Polarization (FP) experiments were conducted on a Varian Cary Eclipse fluorometer (Agilent, Santa Clara, CA) equipped with a polarizer. The stock solutions of αS, 1 mM or 100 μM in 1x PBS buffer, were serially added into a solution of 10 μM SK-129F (300 μL in 1x PBS buffer) while stirring in a quartz cuvette (Fireflysci, Staten Island, NY). All FP measurements were conducted in triplicates in 20 mM Tris, 100 mM NaCl, pH 7.2 at 20 °C. The excitation and emissions wavelengths were set at 490 nm and 520 nm, respectively. Each titration was equilibrated for five min before measurements were taken for the next addition of αS solution. The addition of αS solution was continuous until no more change in the FP signal was observed. Similar conditions were used for the titration of various αS mutants and Aβ42 peptide against SK-129F. A stock solution of Aβ42 (1 mM or 100 μM in 1x PBS buffer on ice) was sequentially added to a solution of 10 μM SK-129F (300 μL in 1x PBS buffer) until no more change in the FP signal was observed. The polarization of each point was calculated using Eq. 1:

$$FP = \frac{I_{\parallel} - I_{\perp}}{I_{\parallel} + I_{\perp}}$$

Where $I\parallel$ is fluorescence intensity parallel to the excitation plane and $I\perp$ is fluorescence intensity perpendicular to the excitation plane. The plot between the relative change in the FP signal against the concentration of the protein (αS/ Aβ42) was fit using one site binding model and *K*d between SK-129F and αS (αS mutants/Aβ42) was extracted from the fit. For displacement titration, a 10 μM SK-129F solution was

saturated with 10 mole equivalents of αS (300 µL in 1x PBS buffer). To this solution, a stock solution of SK-129 (1 mM or 10 mM) was serially added to displace SK-129F from the αS-SK-129F complex. The solution of SK-129 was continuously added until no more change in the FP signal was observed. A plot between the relative change in the FP signal against the concentration of SK-129 was fit using a one-site competitive binding model and Kd between SK-129 and αS was extracted from the fit.

2.2.16 Parallel artificial membrane permeability assay

A parallel artificial membrane permeability assay (PAMPA) Kit (BioAssay Systems, Hayward, CA) was used to measure the membrane permeability of SK-129 according to the manufacturer's protocol. Briefly, a 4% lecithin solution (LS) was prepared in dodecane and solubilized with constant sonication for 20 min. Then, 5 µL of LS was placed on the donor plate membranes. A 300 µL 1x PBS buffer was applied to the acceptor plate. The solutions of SK-129 and various permeability controls (Highly soluble, medium soluble and low soluble) molecules were added to donor plates (200 µL and 500 µM). The donor plate was placed in the acceptor plate and incubated at RT for 18 h. Then the solutions were removed from the acceptor plate and placed in a clear-bottom 96-well plate (Corning Inc., Corning, NY) and absorbance was recorded at 360 nm for SK-129 and 275 nm for standards. The permeability was calculated using Eq. 2:

$$P_e = C \times -\ln\left(1 - \frac{OD_A}{OD_E}\right) \text{cm/s}$$

Where the permeability rate C is 7.72 × 10−6, ODA is the absorbance of acceptor solution and ODE is absorbance of equilibrium standard.

2.2.17 MTT assay

An MTT assay was conducted to assess the effect of SK-129 on the cytotoxicity mediated by αS aggregation in SH-SY5Y cells. The cells were cultured in phenol red-free Dulbeco's Modified Eagle Medium (DMEM) with 10% Fetal Bovine Serum (FBS) and 1% penicillin-streptomycin (Pen/strep) at 37 °C and 5% CO2(g). The cells were plated in a clear, flat bottom 96-well cell culture plate (Costar, Kennebunk, ME) using a density of 10,000 cells per well with more than 90% cell viability. After incubating for 24 h, the media was aspirated, and 100 µL of fresh OptiMEM (Fisher Scientific, Pittsburgh, PA) was added, which contains the aggregated solution of 25 µM of αS in the absence and presence of various ligands at various stoichiometric ratios. The samples were then incubated for an additional 24 h at 37 °C and 5% CO2(g), followed by the addition of MTT dye (10 µL per well, prepared in 1x PBS buffer, 5 mg/mL). The plates were covered in aluminum foil and incubated again for 3 h. The solution in each well was carefully removed without disturbing the formazan crystals and replaced with 100 µL of DMSO to dissolve the formazan crystals. Subsequently, the plate was shaken in a 96-well plate reader for 5 min before measuring the absorbance at 570 nm. The cell viability was reported on a scale of 100%, using the control wells with regular media as 100% viability and the wells with 10% DMSO (v/v) as 0% viability.

2.2.18 αS transfection using Lipofectamine 3000

The Lipofectamine solution (Lipofectamine+P3000 reagent, Thermo Fisher Scientific, Waltham, MA) was diluted to a ratio of 1:20 (v,v) in the OptiMEM (Fisher Scientific, Pittsburgh, PA) media. Simultaneously, the αS fiber solution (Stock solution

conc. = 100 μM) was diluted in OptiMEM media to the desired conc. used for each assay. The αS fiber solution was sonicated for 10 min at r.t., followed by the addition of the Lipofectomine solution (in the OptiMEM media) at 1:1 ratio. Subsequently, this solution was incubated for another 10 min and then added to the HEK cells media with a dilution factor of 10 (10 μL of the combined αS fiber solution+Lipofectomine solution, in 90 μL HEK cells media).

2.2.19 Confocal imaging of HEK cells

The HEK cells expressing αS-A53T-YFP or αS-YFP (200,000 cells/mL) were plated in a μ-slide eight-well plate (Ibidi, Gräfelfing, Germany) (300 μL/well) and incubated at 37 °C and 5% CO2 (g), and allowed to adhere to the plate for 24 h in complete media (DMEM, 10% FBS, 1% pen/strep). After 24 h, the media was aspirated and 300 μL of OptiMEM containing αS fibrils, 0.125 μM and 7.5 μM of the PD brain sample (PMCA, 5th cycle) and recombinant protein in the presence of Lipofectamine 3000, respectively were added. The plate was incubated for 48 h after the addition of fibers. The HEK cells were treated for 1 h with a mixture of Hoechst 33342 dye solution (3 μL/well from 1 mg/mL solution in 1x PBS buffer) and wheat germ agglutinin alexa fluor 633 conjugate (3 μL/well from 1 mg/mL solution in 1x PBS buffer) to stain nuclei and the plasma membrane, respectively of the cells. The HEK cells were washed with the 1x PBS buffer (four times) to remove excess traces of dyes and used for the live-cell confocal imaging. The confocal imaging was performed on an Olympus Fluoview FV3000 confocal/2-photon microscope, using a 20×Plan-Apo/1.3 NA objective with DIC capability. The confocal images of the HEK cells were processed using the Olympus Viewer in ImageJ processing software.

Similar conditions were used to monitor the effect of SK-129 on the aggregation of αS in HEK cells. A solution of 100 μM αS was aggregated for seven days in 1x PBS buffer in the absence and presence of SK-129 at an equimolar ratio. The fibers of αS in the absence and presence of SK-129 in the presence of Lipofectamine 3000 were used in HEK cells. For PD brain samples, the PD brain seeds were used in the PMCA assay with fresh αS sample in the absence and presence of SK-129 at an equimolar ratio. The PMCA samples from the fifth cycle in the absence and presence of SK-129 were used for the HEK cells. The confocal imaging experiments were repeated four times independently to ensure the reproducibility of the data.

2.2.20 Fluorescence activated cell sorting

For flow cytometry experiments, the HEK cells expressing αS-A53T-YFP or αS-YFP proteins (200,000 cells/mL) were treated with different conditions (αS fibrils with and without SK-129 in the presence of Lipofectamine 3000), fixed, and stained with Proteostat dye as described in the previous method. The HEK cells were analyzed by flow cytometry using the Sony cell sorter (SH800, San Jose, CA) using a 488 nm laser and 525/50 FL2 (YFP) and 600/60 FL3 (Proteostat dye) filters. The gating was created based on the fluorescence intensity of the control cells (No αS fibrils) without seeding. For each sample, 10,000 cells were counted, analyzed, and plotted using Cell Sorter Software (Version 1.7, LE-SH800 Series, Sony, San Jose, CA). To further quantify the inclusions in HEK cells treated with different conditions, the histograms were divided into two parts on the x-axis. The x-axis represents the Proteostat signal intensity in HEK cells, which was detected in a single channel with 600/60 FL3 (Proteostat dye) filters. The flow cytometry experiments were conducted one time each for HEK cells expressing

αS-A53T-YFP or αS-YFP proteins. A similar trend was observed on the intracellular aggregation of both proteins (αS-A53T-YFP or αS-YFP) facilitated by exogenously added αS fibers in the absence and presence of SK-129. These results support the reproducibility of the data form the flow cytometry experiments.

2.2.21 2D HSQC NMR

Two-dimensional 1H-15N HSQC NMR experiments were performed on a 600 MHz Bruker instrument equipped with a triple resonance HCN cryoprobe. Uniformly labeled 15N-αS (>95% purity from SDS-PAGE) was purchased from rpeptide (Bogart, GA). One mg of αS powder was dissolved in 970 µL of milli-Q water (0.2 µM filter) to make a final concentration of 70 µM in 1x PBS buffer, which was eventually taken into another buffer of 20 mM NaPi, pH 6.4. The αS solutions were divided into 350 µL aliquots, lyophilized, and stored at −80 °C until further use. The concentration of each aliquot was determined spectroscopically at 280 nm using an extinction coefficient of 5960 M−1cm−1. The 2D HSQC NMR experiments were carried out in 20 mM NaPi, pH 6.4, and by maintaining a solution ratio of 90:10 (H2O:D2O) at 15 °C. For each 2D HSQC NMR experiment, a freshly prepared solution of 15N-αS was used and the experiments were carried out at 15 °C to avoid potential complications from the amyloid formation. For the HSQC experiment in the presence of SK-129, a stock solution of 10 mM SK-129 was prepared in DMSO (pure, HPLC grade). Under the NMR conditions used here, αS was exclusively found in the monomeric state. For HSQC NMR in the presence of SK-129, a fresh solution of 15N-αS was prepared at a concentration of 70 µM (350 µL) in the presence of 70 µM and 140 µM concentration of SK-129 (stock solution of 10 mM in DMSO). The solution was mixed well before starting the HSQC NMR experiments. The 15N-αS

sample was diluted to 0.8% in the presence of SK-129 at an equimolar ratio. For 1H-15N HSQC NMR experiments, data for the 1H and 15N frequencies were acquired using 1024 and 512 points, respectively. Apodization was achieved in the 1H and 15N dimensions using a sine square function shifted by 90°. The 2D HSQC NMR spectra were processed and analyzed using the MestReNova (Version 12.0.4) software. The peak heights were used to calculate the change in the intensity of amide backbone peaks of 15N-αS residues were analyzed manually using MestReNova (Version 12.0.4) software. The reported values are the ratio of the change in the intensity peaks of amide backbone peaks of 15N-αS residues in the absence and presence of SK-129 at various stoichiometric ratios.

For the lipid membrane conditions in HSQC NMR, a fresh solution of 15N-αS was prepared at a concentration of 70 μM (350 μL) in the presence of 1 mM DOPS (100 nm, LUVs) for 2D HSQC NMR. All the conditions were exactly similar to HSQC conditions used earlier, including buffer, temperature, and HSQC NMR parameters. The peak heights were used to calculate the change in the intensity of amide backbone peaks of 15N-αS residues were analyzed manually using MestReNova (Version 12.0.4) software.

To check the effect of SK-129 on the lipid membrane-bound 15N-αS, a complex was formed between 70 μM 15N-αS and 1 mM DOPS (100 nm, LUVs). To this solution, SK-129 (70 μM) was added (10 mM stock solution in DMSO) and the solution was mixed gently before running the HSQC NMR experiment. All the conditions were exactly similar to the HSQC conditions used earlier, including buffer, temperature, and HSQC NMR parameters.

All NMR experiments were conducted one time and the NMR experiments between αS and SK-129 were conducted at different stoichiometric ratios and a consistent trend of the chemical shift volume change in the amide peaks was observed as a function of stoichiometric ratios (of αS and SK-129), which supports the reproducibility of the data.

2.2.22 C. elegans maintenance

The PD strain (NL5901), the control strain (N2, Bristol), and *Escherichia coli (E. coli)* OP50 were obtained from the Caenorhabditis Genomics Center (CGC, Minneapolis, MN). Standard conditions were used to maintain the worms at ~23 °C on nematode growth media (NGM) agar plates (60 mm), including *E. coli* OP50 (a uracil requiring mutant of *E.coli* with 0.5 optical density, O.D.) used as a food source for *C elegans*[152]. Stocks of N2 and NL5901 strains of *C. elegans* were cultured and maintained in accordance with the previous protocol[153]. NGM media, M9 buffer, and OP50 food for *C elegans* were prepared according to previous protocols[152,153]. M9 buffer was used for the preparation of liquid media for this experiment. The buffer was prepared by dissolving 3 g of potassium dihydrogen phosphate (KH2PO4), 6 g of sodium hydrogen phosphate (Na2HPO4), and 5 g of sodium chloride (NaCl) in 1 L of Milli-Q water. The M9 buffer was autoclaved for 47 min and subsequently, 1 mL of 1 M magnesium sulfate (MgSO4) was added to the buffer, and it was stored at RT for making the liquid media

2.2.23 C. elegans motility assay

The assay was carried out based on a previous protocol with slight modifications[154]. On day one, N2 and NL5901 strains were synchronized through the bleaching process involving egglay and the incubation of the eggs at an ambient temperature (~23 °C) on a solution of 3 mL NGM media in 60 mm culture plates (CytoOne, USA Scientific, Ocala, FL). The plates were seeded with 300 µL OP50 at an O.D. of 0.5 for 30 h. Simultaneously, a solution of 15 µM SK-129 (Stock solution concentration = 10 mM in DMSO) was made in M9 buffer and added to two sterilized 35 mm NGM solid media plates (Fisher Scientific, Pittsburgh, PA). The plates were already containing 2 mL of NGM solid media and 75 µM Fluorodeoxyuridine (FUDR) to prevent offspring in the worms. On day two, M9 buffer was used to transfer the worms from 60 mm NGM plates into 35 mm FUDR and SK-129 containing solid media plates (Fisher Scientific, Pittsburgh, PA) and incubated up to day three on these plates. On day four, liquid media was prepared according to the previous protocol with some modifications including 67.28% (v/v) of M9 buffer, 0.018% (75 µM) of FUDR solution (v/v), 0.1% of 1 M magnesium sulfate (v/v), 0.1% of 1 M calcium chloride (v/v), 2.5% of 1 M potassium phosphate solution (pH 6, v/v), and 30% of 0.5 OD600nm OP50 (v/v)[153]. A total of 100 worms were transferred using a worm pick into each liquid media plate, including N2, NL5901 in the absence and presence of SK-129. For each experiment, two plates were used for each condition. For the NL5901 strain, the solution conditions were the same in the absence and presence of SK-129, except that SK-129 was present in one condition (15 µM SK-129, stock solution concentration = 10 mM in DMSO). On day five, motility assay was conducted for worms under different conditions in duplicate using a

WMicroTracker Arena plate reader (Phylumtech, Argentina) at ~23 °C for 1 h per day over a period of 12 days. Before each run, the plates were gently tapped for 30 sec to enable the worms to become active in the liquid media. A total of 20 activity scores were collected per strain per condition over 1 h on each day. For each condition, at least two technical replicates and three biological replicates were used. The data to extract the mean and s.e.m. (n = 3 independent experiments) was processed using GraphPad Prism (Version 9.3.1) software.

2.2.24 C. elegans confocal imaging

The worms from the NL5901 strain were treated in the absence and presence of SK-129 (15 µM SK-129, stock solution concentration = 10 mM in DMSO) as described in the paralysis experiment. The worms (days of adulthood = 8 days) were placed in a 20 mM solution of sodium azide for 5 min. Simultaneously, a glass coverslip was prepared with a drop of 2% agarose pad on it. Subsequently, the worms were mounted with a coverslip on a 2% agarose pad. The worms were visualized on an Olympus Fluoview FV3000 confocal/2-photon microscope, using a 20× (or 40×) Plan-Apo/1.3 NA objective with DIC capability. The confocal images of the worms were processed using the OlympusViewer in ImageJ processing software. The system acquires a series of frames at a specific Z-axis position (focal plane) using a Z-axis motor device. For each experiment, at least 15 worms were used, and the inclusions were counted manually, and each condition consisted of at least four independent experiment

2.3 Results

2.3.1 Biophysical characterization of foldamers with αS

The OQs with carboxylic acid and hydrophobic side chains have been shown to modulate the self-assembly of amyloid proteins by specifically targeting sequences that are rich in positively charged and hydrophobic side chain residues[144,155]. Therefore, we utilized an established library of OQs with carboxylic acid and various hydrophobic groups as side chains (Figure 2.7 a-c). The library was screened against αS aggregation using a Thioflavin T (ThT) dye-based amyloid assay[156]. The aggregation kinetics of 100 μM αS (in 1x PBS buffer) was characterized by a sigmoidal curve with a t_{50} (time to reach 50% fluorescence) of ~ 38.1 ± 1.8 h. The screening led to the identification of SK-129 as the most potent antagonist of wild type (WT) αS (and αS mutants, αSA30P and αSA53T) aggregation at equimolar and sub-stoichiometric ratios (Figure 2.7 c-d and Supplementary Figure 2.8 a-b). SK-129 inhibits αS aggregation under both de novo and lipid membrane conditions at an equimolar ratio (Figure 2.9 a), which was also validated by transmission electron microscopy (TEM) images in the absence (Figure 2.9 b) and presence of SK-129 (Figure 2.9 c). The antagonist activity of SK-129 for αS aggregation was also analyzed using SDS-PAGE (Supplementary Figure 2.10). A solution of 100 μM αS was aggregated for four days in the aggregation buffer (20 mM NaCl, 20 mM NaPi, pH 6.5) in the absence and presence of SK-129 at an equimolar ratio. Subsequently, the αS solutions were centrifuged to separate αS aggregates from the soluble αS. Afterward, the samples were boiled at 95 °C for 5 min. to disassemble αS aggregates and examined them using sodium dodecyl sulfate–polyacrylamide gel electrophoresis (SDS-PAGE)

(figure 2.10). In addition, we also quantified SDS-PAGE gel band intensities using ImageJ software (Figure 2.10 b-c). In the absence of SK-129, αS was predominantly detected in the insoluble fraction (αS aggregates) (Supplementary Figure 2.10 a-b). In marked contrast, in the presence of SK-129, αS was predominantly detected in the soluble fraction (αS monomer) (Figure 2.10 a & c). These results clearly demonstrate that SK-129 is a potent inhibitor of αS aggregation.

The antagonist activity of SK-129 is predominantly a consequence of the side chains. Among analogs (with varying hydrophobicity), SK-129 was the most potent antagonist of αS aggregation (Figure 2.7 e,f and Figure 2.11), which indicates that moderate hydrophobicity at positions 1 and 3 is required to achieve the optimal activity. The positioning of the side chains was important for SK-129's activity as scrambling of side chains led to significantly diminished activity (Figure 2.7 f). The antagonist activity of SK-129 was much better than Epigallocatechin Gallate (EGCG), a potent antagonist of αS aggregation[121]. Gel shift assay shows that SK-129 potently inhibits αS aggregation; however, higher-order toxic oligomers ($n > 5$) were observed in the presence of EGCG (Figure 2.12).

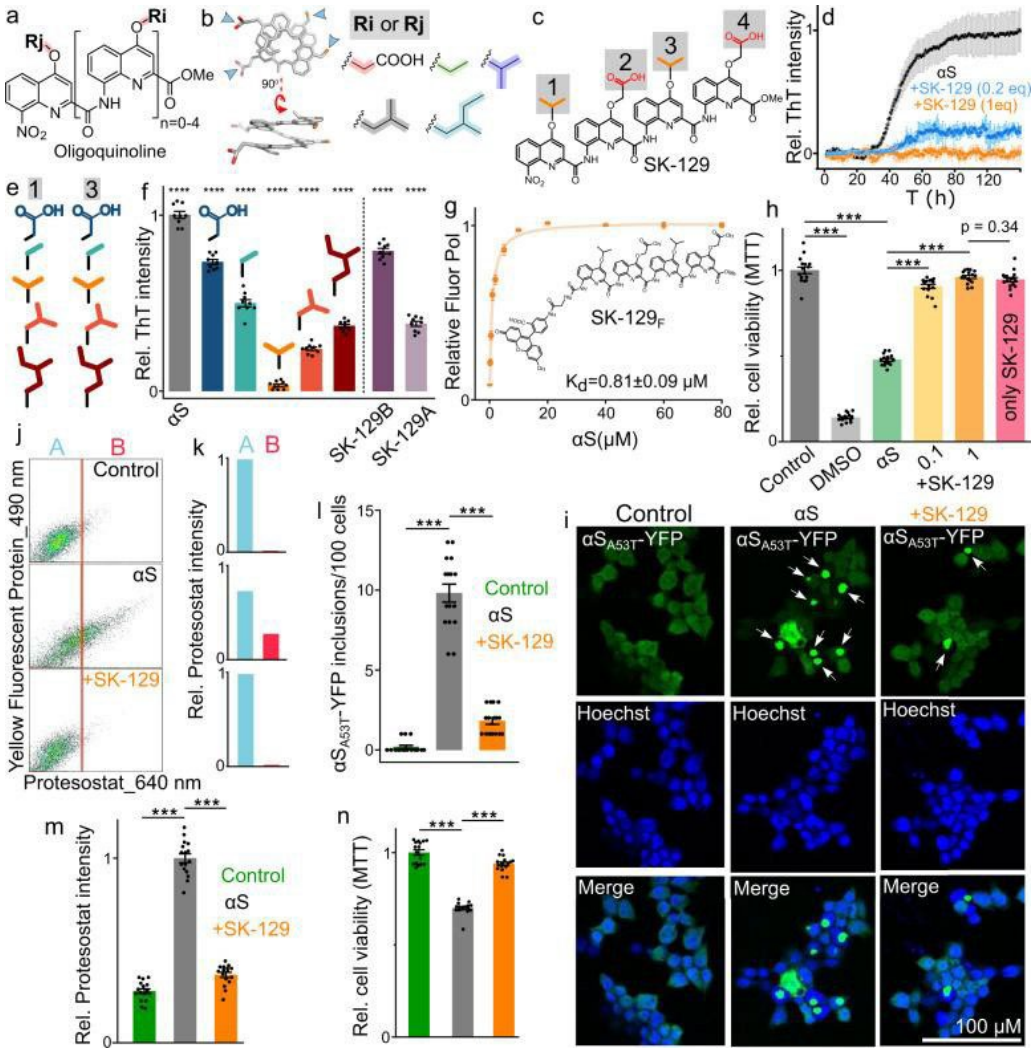

Figure 2.6 a The generic chemical structure of the OQ with Ri and Rj are the side chain surface functionalities. The side and top view of the crystal structure of OQs and the surface functionalities are represented by arrows. The OQs with the indicated side chains (Ri and Rj) were used in the study. c Chemical structure of SK-129 and the four side chains were indicated from 1 to 4. d The average of ThT-dye fluorescence-basedaggregation profile of 100 μM αS in the absence and presence of SK-129 at the indicated molar ratios. The data were expressed as mean and the error bars report the S.D. (n = 3 independent experiments). e The chemical structures of the side chains at position 1 and 3 of various analogs of SK-129. f The antagonist activities of the analogs (100 μM) ofSK-129 against 100 μM αS aggregation. The data were expressed as mean and the error bars report the s.e.m. (n = 3 independent experiments and each n consisted of 3 technical replicates). g The fit for the FP titration curve to determine the binding affinity between 10 μM SK-129F and αS. The chemical structure of SK-129F is shown as well. The data were expressed as mean and the error bars report the s.d. (n = 3 independent experiments). h The statistical analysis of the relative viability of SH-SY5Y cells when

treated with the aggregated solution of 10 μM αS in the absence and presence of SK-129 at the indicated molar ratios. The data were expressed as mean and the error bars report the s.e.m. ($n = 4$ independent cell toxicity experiments and each n consisted of 4 technical replicates). i Confocal images of HEK cells treated with the aggregated solution of 7 μM αS in the absence and presence of SK-129 at an equimolar ratio. Inclusions ofαSA53T-YFP = white arrows, Hoechst (blue), merge = Hoechst and αSA53T-YFP. j The flow cytometry-based analysis of HEK cells treated with the aggregated solution of 7 μM αS in the absence and presence of SK-129 at an equimolar ratio. The x-axis represents αSA53T-YFP aggregates containing cells that are stained with Proteostat dye($\lambda = 640$ nm) and the y-axis represents the total number of cells with YFP ($\lambda = 490$ nm). k Columns A and B represent the relative % of HEK cells without and with αSA53T-YFP aggregates, respectively. l The number of αSA53T-YFP inclusions when HEK cells were treated with the aggregated solution of 7 μM αS in the absence and presence of SK-129 atan equimolar ratio. A total of 100 HEK cells were examined to count the number of inclusions at four different locations in the eight-well plate for each experiment and it was repeated in four independent experiments. The relative intensity of Proteostatdye-stained aggregates of αSA53T-YFP inclusions (m) and relative viability (n) of HEK cells treated with the aggregated solution of 7 μM αS in the absence and presence ofSK-129 at an equimolar ratio. The data (for l–n) were expressed as mean and the error bars report the s.e.m. ($n = 4$ independent HEK cells-based experiments and each n consisted of four technical replicates). The statistical analysis was performed using one-way analysis of variance (ANOVA) with Tukey's multiple comparison test.*$p < 0.05$, **$p < 0.01$, ***$p < 0.001$.

Next, we determined the binding affinity of SK-129 using fluorescence polarization (FP) titration between a fluorescent analog of SK-129 (SK-129F) (Figure 2.11) and αS, which yielded a *K*d of 0.81 ± 0.09 μM (Figure 2.7 g) and a binding stoichiometry of 1:1 (αS:SK-129F) (Figure 2.13). The complex of SK-129F-αS was used for a displacement titration with SK-129, which yielded a *K*d of 0.72 ± 0.06 μM (Figure 2.14). More importantly, SK-129F (SK-129F-αS complex) could be used as a novel tool for a high throughput assay to screen and identify high-affinity ligands for αS. Also, SK-129 is a very specific antagonist of αS aggregation. The *K*d of SK-129 for Aβ42 was more than 15-fold higher than αS (Figure 2.15 a). Corroborating this specificity, SK-129 did not show any noticeable effect on Aβ aggregation (Figure 2.15 b).

The aggregation of αS is associated with toxicity, therefore, we tested the efficacy of SK-129 on the neuroblastoma SH-SY5Y cell line. The aggregation of αS was carried out in the absence and presence of SK-129 at an equimolar ratio, and the solutions were tested in SH-SY5Y[157]. The viability of SH-SY5Y cells decreased to 48 ± 3% upon exposure to 10 μM αS for 24 h; which was rescued to 91 ± 4% and 97 ± 4% in the presence of SK-129 at molar ratios of 1:0.1 and 1:1 (αS:SK-129), respectively (Figure 2.7 h). The rescue of toxicity by SK-129 in SH-SY5Y cells was similar at higher concentrations of αS (25 μM and 50 μM) (Figure 2.16). To confirm that SK-129 did not generate seed-competent structures during the inhibition of αS aggregation, we utilized two HEK cell lines, which stably express YFP-labeled WT αS (αS-YFP) and a familial mutant, A53T (αS-A53T-YFP)[147,158]. Both HEK cells have been shown to template endogenous monomeric αS-A53T-YFP (αS-YFP) into fibers when transfected with αS fibers with lipofectamine 3000 (Figure 2.7 i), which is detected by intracellular fluorescent puncta (Figure 2.7i, white arrows). αS was aggregated in the absence and presence of SK-129 at an equimolar ratio and the HEK cells were treated with αS fibers (7 μM in monomeric αS) for 24 h. A very small number of inclusions (αS-A53T-YFP or αS-YFP) were observed in the presence of SK-129 (Figure 2.7i). The inclusions (αS-A53T-YFP) were quantified by confocal microscopy (Figure 2.7 i,l), flow cytometry (intracellular inclusions stained with ProteoStat dye, Figure 2.7j,k), and a 96-well plate reader (using ProteoStat dye, Figure 2.7 m), which were alleviated significantly in the presence of SK-129. The viability of HEK cells improved from 68% to 94% (αS aggregated solution in the presence of SK-129), which was determined using the (3-(4,5-dimethylthiazol-2-yl)-2,5-diphenyltetrazolium bromide) (MTT) reduction-based

cytotoxicity assay (Figure 2.7 n). We used all the above-mentioned techniques to assess the antagonist activity of SK-129 on the aggregation of WT αS in HEK cells as well (Figure 2.17). SK-129 was equally effective in inhibiting aggregation and cytotoxicity in HEK cells that were expressing intracellular αS-YFP, which was confirmed with confocal imaging (Figure 2.17 a), flow cytometry (Figure 2.7 b-d), ProteoStat dye-based quantification of intracellular inclusions (Figure 2.17 e,f), and MTT based cytotoxicity assay (Figure 2.17 g).

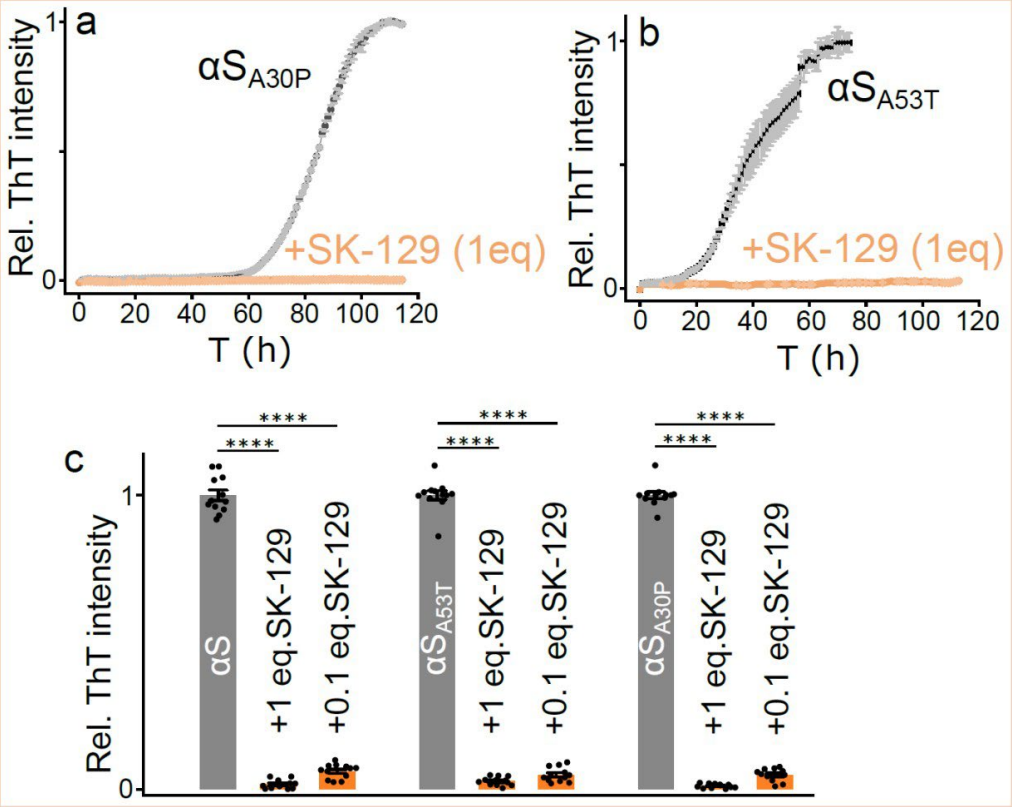

Figure 2.7 The antagonist effect of SK-129 on the aggregation profile of various mutants of αS. The aggregation kinetic profiles of 70 μM αSA30P (a), and 70 μM αSA53T (b) in the absence (light black curve) and presence (orange curve) of SK-129 at an equimolar ratio. c, Statistical analysis of the ThT intensity change for WT αS and various αS variants in the absence and presence of SK-129 at the indicated stoichiometric ratios. The ThT intensity was measured after 120 h of aggregation of WT αS and various αS variants

in the absence and presence of SK129. The aggregation kinetics were conducted three times and the reported change in ThT intensity for various conditions is an average of three separate experiments and the error bars are the s.d.'s for three sets of experiments. For experiment a and b, data were expressed as mean and the error bars report the S.D. (n = 3 independent experiments). For experiment c, the data were expressed as mean and the error bars report the s.e.m. (n = 4 independent experiments and each n consisted of 3 technical replicates). The statistical analysis was performed using ANOVA with Tukey's multiple comparison test. *p<0.05, **p<0.01, ***p<0.001, ****p<0.0001.

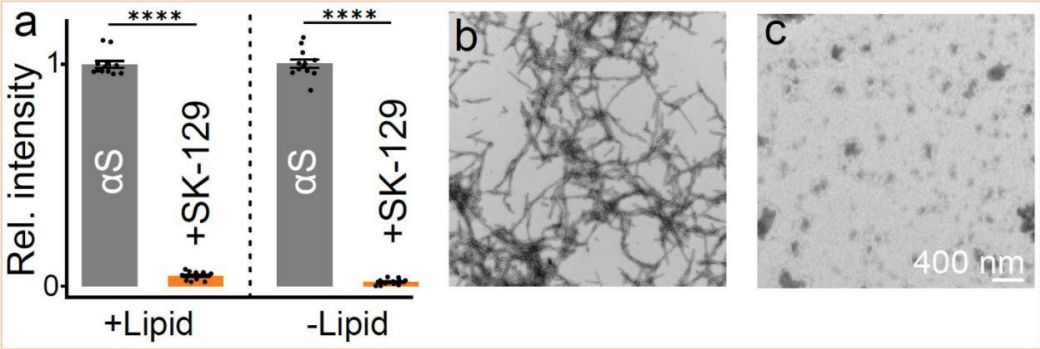

Figure 2.8 a, The graphical representation of the ThT intensity of the aggregation of 70 μM αS and 35 μM αS under de novo conditions and in the presence of LUVs (875 μM, 100 nm, DOPS), respectively in the presence of SK-129 at an equimolar ratio. The ThT intensity of the lipid-free and lipid-catalyzed aggregation of αS was monitored after 7 days. Negatively stainedTEM images of the aggregation of 70 μM αS in the absence (b) and presence (c) of SK-129 at an equimolar ratio after four days. The data were expressed as mean and the error bars report the s.e.m. (n = 4 independent experiments and each n consisted of 3 technical replicates). The statistical analysis was performed using ANOVA with Tukey's multiple comparison test. *p<0.05, **p<0.01, ***p<0.001, ****p<0.0001.

2.3.2 Identifying SK-129 binding site on αS

The N-terminal domain spanning residues 1–90 plays a significant role in αS aggregation[159,160]. Therefore, we hypothesized that SK-129 could be interacting with the N-terminus of αS for the potent inhibition of αS aggregation. We utilized 2D heteronuclear single quantum coherence NMR spectroscopy (2D HSQC NMR) for atomic-level insight into the binding site of SK-129 on αS. We collected the HSQC NMR of 70 μM 15N-1H-uniformly labeled αS in the absence and presence of SK-129 at an

equimolar ratio (Figure 2.18 a-e) and compared the signal intensity of the amide peaks. The total changes in the intensity in the presence of SK-129 suggest that the binding site of SK-129 is toward the N-terminus of αS, more specifically SK-129 interacts and changes the conformation of four αS sequences, including 6-12, 15-23, 36-45, and 48-53. The binding sites of SK-129 on αS contain lysine and hydrophobic residues; therefore, we propose that the carboxylic acid and the propyl side chains of SK-129 are involved in binding interactions with lysine and hydrophobic residues of αS.

2.3.3 Effect of SK-129 on αS conformation

The NMR study also suggests that SK-129 induces α-helical conformation in αS. The intensity changes of αS residues in the presence of large unilamellar vesicles [0.875 mM, LUVs, 100 nm, DOPS, 1,2-dioleoyl-sn-glycero-3-phospho-l-serine (sodium salt)] were similar to those influenced by SK-129 at a higher molar ratio (1:2, αS:SK-129) (Figures 2.19 - 2.20). As αS samples α-helical conformations in the presence of LUVs[59,160], we postulated that αS forms an α-helical conformation in the presence of SK-129. We utilized circular dichroism (CD) to study the interaction of αS with SK-129. The conformation of 35 μM αS transitioned from random coil to β-sheet in 7 days (Figure 2.18 f); however, the conformation of αS switched from random coil to α-helix and stayed in the same conformation in the presence of SK-129 at an equimolar ratio (Figure 2.18 g). We posit that the antagonist activity of SK-129 against αS aggregation is a consequence of the direct interaction with the N-terminus and the induction or stabilization of an α-helical conformation in αS. SK-129 behaved similarly under lipid catalyzed αS aggregation. SK-129 was a potent antagonist of LUVs catalyzed αS

aggregation (Figure 2.9). The CD spectra of 30 μM αS switched from an α-helix to a β-sheet conformation via an α-helical conformation in the presence of LUVs (375 μM, 100 nm, DOPS, Figure 2. 21 a). In marked contrast, αS remained in an α-helix conformation in the presence of LUVs and SK-129 at an equimolar ratio (Figure 2.21 b). However, there was a decrease in the CD intensity of α-helix upon the addition of SK-129, which suggests that SK-129 might be competing against the lipid membrane for αS. We utilized a CD study to determine the K_d between αS and LUVs (DOPS, 100 nm), like previously published work[148,159]. A CD titration was carried out between 40 μM αS and an increasing conc. of DOPS (molar ratio, 1:160, αS:DOPS), which yielded a $K_d > 5$ μM ($K_d = 7.2 \pm 2.5$ μM, Figure 2.22). The K_d between αS and DOPS was higher than the K_d between SK-129 and αS (0.72 ± 0.06 μM), which indicates that the binding affinity of SK-129 is higher than DOPS for αS. Consequently, αS should favor binding to SK-129 than DOPS, when SK-129 is added to the complex of αS + DOPS. Our CD data support this claim as the addition of SK-129 to the αS + DOPS complex resulted in a decrease in the CD signal intensity of the DOPS bound αS.

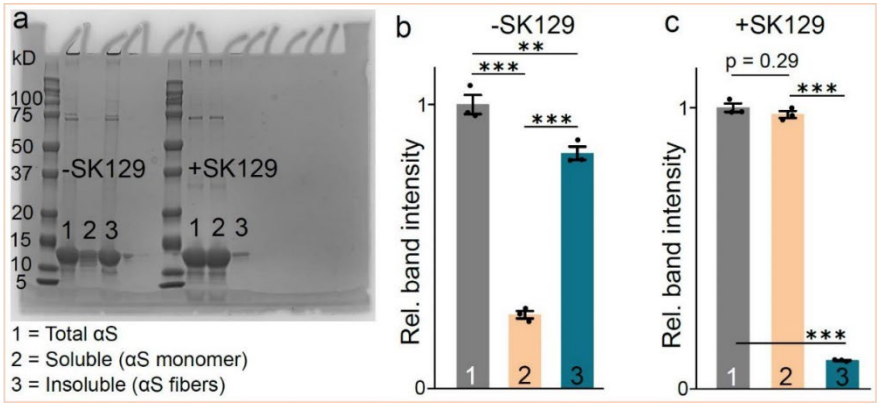

Figure 2.9 SDS-PAGE gel analysis of 100 μM αS aggregation for four days in the absence and presence of SK-129 at an equimolar ratio in the aggregation buffer (20 mM NaCl, 20 mM NaPi, pH 6.5). a, The SDS-PAGE gel showing the Coomassie-stained αS,

including total protein (1), soluble fraction (2), and insoluble fraction (3). The αS aggregation was tested in the absence and presence of SK-129 at an equimolar ratio. The reference of the masses (in kD) is shown on the left side of the gel. b, The statistical analysis of the relative band intensities of the total αS (1), the soluble fraction (2), and the insoluble fraction (3) of αS. c, The statistical analysis of various forms of αS in the presence of SK-129 at an equimolar ratio (αS:129, 1:1). The aggregation kinetics of αS in the absence and presence of SK-129 and the gel shift assays were conducted three times and the reported relative band intensities for various αS fractions is the mean of three separate experiments. The data were expressed as mean and the error bars report thes.e.m. (n = 3 independent experiments). The statistical analysis was performed using ANOVA with Tukey's multiple comparison test. *$p<0.05$, **$p<0.01$, ***$p<0.001$. The quantification of the band intensity of gels for all the independent experiments was conducted in parallel using matched conditions. Source data are provided as a Source Data file

Under these conditions, SK-129 does not form any micelle structures, as confirmed with the TEM images (Figure 2.23). Overall, the data suggest that SK-129 specifically interacts with αS and competes with the LUVs for αS and inhibits the aggregation of lipid catalyzed aggregation.

Collectively, our data from CD and NMR suggest that the conformation of αS remains in the α-helical state in the presence of SK-129 for the whole time course of the experiments. The data also indicate that αS was not completely displaced from lipid membranes in the presence of SK-129 and the lipid catalyzed aggregation of αS was wholly inhibited by SK-129. Our CD and NMR data suggest that the inhibition of the membrane-catalyzed aggregation of αS might be a consequence of the competition of αS between lipid membranes and SK-129. A recent study has suggested that one of the main therapeutic strategies could be the inhibition of αS aggregation on lipid membranes without completely displacing αS from lipid membranes[129]. The native function of αS is partly facilitated by its interaction with lipid membranes and the complete displacement of αS from lipid membranes could be detrimental to its function and might promote

neuropathology. A natural product, Squalamine, was able to inhibit the membrane-potentiated αS aggregation and rescued cytotoxicity by completely displacing αS from lipid membranes[161]. However, SK-129 was able to inhibit the aggregation of αS without completely displacing it from lipid membranes, which is evidenced by the intact α-helical conformation of αS in the presence of SK-129 under lipid membrane conditions.

We also employed HSQC 2D-NMR to gain molecular insights into the mode of action of SK-129 on lipid membrane catalyzed aggregation of αS and the overall effect of SK-129 on the membrane bound-αS complex. SK-129 (140 μM) was added to the complex of 15N αS:LUVs (70 μM: 875 μM) and the intensity changes of the amide peaks from this NMR (Figure 2.24) were compared with the amide peaks of the NMR from the αS:SK-129 complex (Figure 2.19) and the αS:LUVs complex. The addition of SK-129 to the αS-LUVs complex leads to the dissapperance of various amide peaks in the NMR spectrum (Figure 2.24). If SK-129 was able to completely displace αS from the LUVs, this NMR spectrum should have been similar to the NMR spectrum of the αS-SK-129 complex (Figure 2.19 a). However, the NMR spectrum was not similar to that of the αS-SK-129 complex or the αS-LUVs complex. The NMR spectrum was a combination of the NMRs of αS-SK-129 and αS-LUVs complexes, which suggests an interchange of αS between SK-129 and LUVs (Figure 2.24). The NMR also suggests that SK-129 did not completely displace αS from the LUVs. Our study demonstrates that SK-129 was able to inhibit membrane catalyzed αS aggregation without completely displacing αS from lipid membranes. The study suggests that SK-129 is likely not interfering with the native function of αS, which is partly facilitated by the interaction of αS with the lipid membranes.

To further confirm the binding sites of SK-129 on αS, we carried out a mutation study by systematically removing residues 6-12, 15-23, 36-45, or 48-53 from WT αS denoted as αS1, αS2, αS3, and αS4, respectively (Figure 2.25). The mutants were expressed and characterized using SDS-PAGE (Figure 2.6) and mass spectrometry (Figure 2.1 - 2.5). The FP-based binding affinity of SK-129F for αS1 and αS2 mutants was 3–4-fold weaker (than WT αS) and very weak for both αS3 (~8 fold) and αS4 mutants (>10 fold, Figure 2.25). We posit that SK-129 has multiple binding sites on αS with varying binding affinities or that the main binding site spans residues 36–53, and the intensity change of residues 6–12 and 15–23 is a consequence of the conformational switch in αS.

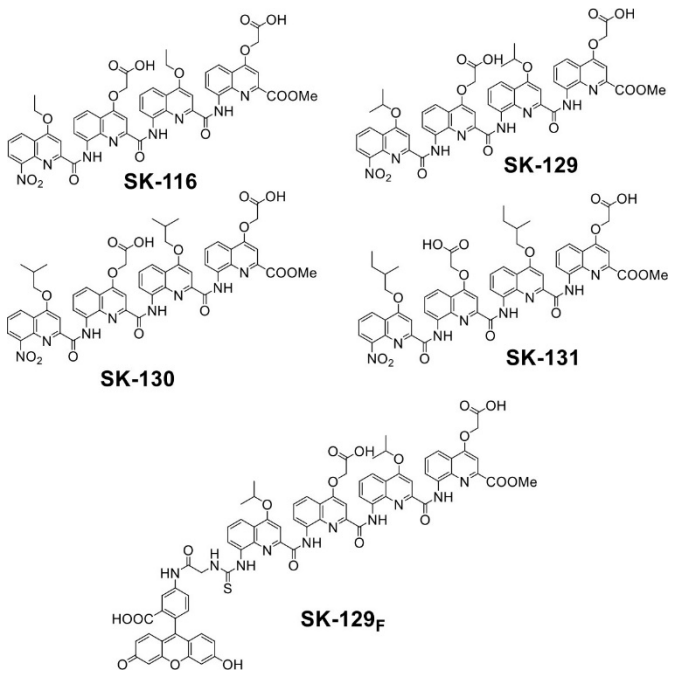

Figure 2.10 The chemical structures of various OQs used in the study.

2.3.4 αS sequence critical for de novo aggregation

SK-129 inhibits aggregation by interacting with four αS sequences; therefore, we hypothesize that these sequences might be essential to initiate αS aggregation. Therefore, we investigated the effect of these sequences on αS aggregation. Mutants αS3 and αS4 did not aggregate under our conditions via ThT and TEM (Figure 2.25 a, i, j, n, o and Figure 2.26), and their CD spectra were random-coil (Figure 2.18). Mutants αS1 and αS2 aggregated with t_{50}'s 3–4-fold higher than WT αS (Figure 2.25 a, f, g and Figure 2.26). The morphology of αS1 fibers was similar to WT αS (Figure 2.25); however, αS2 fibers were amorphous. Both WT αS and αS1 sampled β-sheet conformation (Figure 2.25 p, q); however, αS2 did not have the characteristics of a β-sheet conformation.

We also investigated the role of these αS sequences on the seed-catalyzed aggregation of αS. The WT αS seeds (10% monomer concentration) accelerated 100 μM αS aggregation by decreasing the t_{50} of WT αS (28.3 ± 2.2 h), αS1 (84.1 ± 3.6 h), αS2 (72.1 ± 3.4 h) to WT αS (8.9 ± 0.2 h), αS1 (14.0 ± 0.6 h), αS2 (21.6 ± 0.7 h) (Figure 2.25 u-y and Figure 2.27). The αS seeds did not template and aggregated mutants αS3 and αS4 (Figure 2.25 x-y and Figure 2.27), which suggests that the deleted sequences in αS3 and αS4 might be involved in seed catalyzed aggregation. SK-129 wholly suppressed the seed-catalyzed aggregation of WT αS, αS1 and αS2 (Figure 2.25 u-w and Figure 2.27) at an equimolar ratio. These experiments show that the sequences affected by SK-129 are important for αS aggregation.

The antagonist activity of SK-129 on αS aggregation was also assessed using a protein misfolding cyclic amplification (PMCA) technique. The PMCA technique is used

to cyclically amplify the aggregation of proteins from a small quantity and diverse species and it also generates robust seeds via a nucleation-dependent polymerization model[162,163]. In the PMCA assay, αS fibers are amplified for five cycles using αS monomer and seeds from the previous cycle. Additionally, αS seed polymorphs from different sources differ in mediating PD phenotypes[162]. Therefore, we utilized two αS seed polymorphs, including recombinant αS seeds and αS seeds extracted from the substantia nigra of a PD brain and a control brain (post mortem condition) and used them in the PMCA assay (Figure 2.28 a). The Lewy bodies (LBs)-like structural features in the substantia nigra of the PD brain were confirmed using immunostaining (bluish/black, black arrows) (Figure 2.28 c). We did not observe any LBs-like structural features in the control brain (Figure 2.28 b). The aggregates of αS were extracted from the PD brain using a published protocol[147].

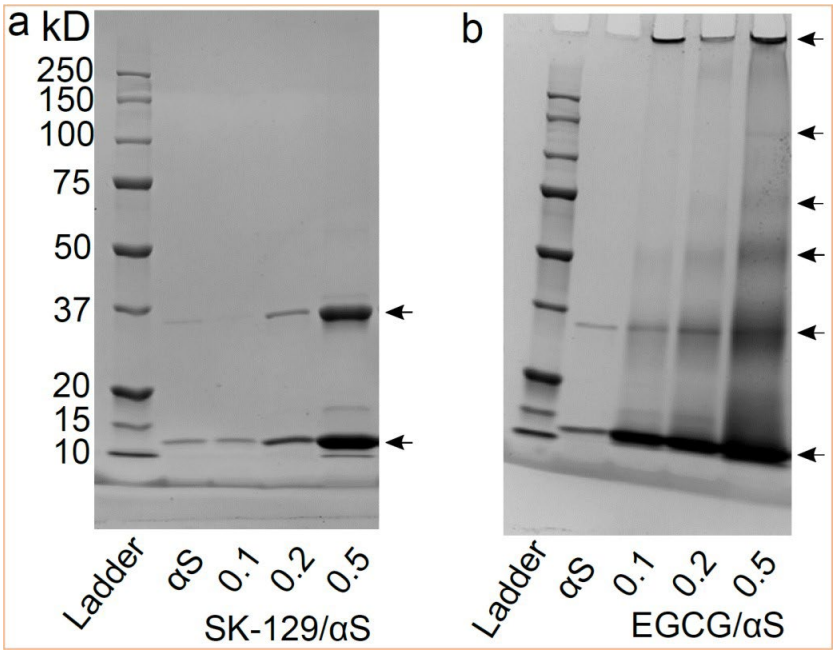

Figure 2.11 Gel-shift images of αS (70 μM) incubated in the absence (lane 2) and presence of SK-129 (a) and EGCG (b) at sub-stoichiometric ratios (0.1, 0.2, 0.5 mol eq.) for 7 days at 370C with constant shaking. The solutions of αS in the absence and

presence of ligands were centrifuged and the supernatant was used for the gel shift assay. The arrows indicate the formation of various αS structures. The gel shift assay of the supernatant of the αS aggregated solution resulted in a very small amount of monomer because most of the protein converted into fibers. Most of the αS was found in the supernatant as a monomer and a dimer in the presence of SK-129; however, higher-order oligomers were observed in the presence of EGCG. The most toxic states of αS are considered to be the higher-order oligomers (n>5) and SK-129 efficiently inhibits their formation.

The αS aggregates were extracted and confirmed from the PD brain using TEM (Figure 2.28) and western blot (Figure 2.28). In marked contrast, no aggregates of αS were detected after extraction from the control brain as confirmed by TEM (Figure 4 d). Both samples from the control brain and the PD brain were assessed for their ability to seed and accelerate the aggregation of αS monomers. No noticeable change was observed in the t_{50} or the total ThT intensity for αS aggregation in the presence of the control brain sample. The t_{50} for αS aggregation was 67.4 ± 12.2 h and 62.1 ± 3.4 h in the absence and presence of the control brain sample, respectively (Figure 2.29 a, b)). In marked contrast, both t_{50} (22.7 ± 5.4 h) and ThT intensity (~4 fold) for αS aggregation were significantly enhanced in the presence of the PD brain sample (Figure 2.29 a, b). Clearly, the αS seeds from the PD brain sample template and significantly accelerate αS aggregation via seed catalyzed mechanism. The PMCA assay sample (cycle 5) of the control brain extract was not PK (proteinase K) resistant (Figure 2.28 f) and it was also not effective at templating αS-A53T-YFP monomer into inclusions in HEK cells (Figure 4 h). However, the sample (cycle 5) from the PD brain was PK resistant (Figure 2.28 f) and it was also effective at templating αS-A53T-YFP monomer into inclusions in HEK cells (Figure 2.28 i, k). The inclusions and toxicity increased gradually up to four days in the presence of the seeds from PD brain sample (Figure 2.28 i, k ,l). Under the biological condition used, the

control HEK cells were healthy up to 4 days and therefore, we decided to restrict our study up to 4 days.

2.2.5 Effect of SK-129 in ex vivo models of αS seed catalyzed aggregation

We next investigated the effect of SK-129 at preventing seed-catalyzed aggregation from PD brain samples. The sample (cycle 5) of PD brain extract in the presence of SK-129 was neither aggregated nor PK resistant (Figure 2.28 a). Also, we observed a lower number of inclusions and improved cell viability for up to four days (Figure 2.28 j-l). We observed similar behavior of the PMCA sample (cycle 5) from recombinant αS seeds in the absence and presence of SK-129 at an equimolar ratio (figure 2.30). The PMCA assay for recombinant αS leads to an abundance of αS fibers (Cycle 5), confirmed with high ThT signal (figure 2.30 f), TEM image (figure 2.30 d), PK resistance (figure 2.30 b, white arrows), high number of inclusions from confocal imaging (figure 2.30 g-i), high ProteoStat dye signal (figure 2.30 j), and much higher cytotoxicity (figure 2.30 k) in HEK cells. In contrast, there was no formation of αS fibers for the PMCA assay (Cycle 5) in the presence of SK-129 at an equimolar ratio as confirmed by low ThT intensity (figure 2.30 f), TEM image (figure 2.30 e), no PK resistance (figure 2.30 c, orange arrows), very low number of inclusions from confocal imaging (figure 2.30 g, i), low ProteoStat dye signal (figure 2.30 j) and rescue of cytotoxicity in HEK cells (figure 2.30 k).

To further confirm the antagonist activity of SK-129 on the seed catalyzed aggregation of αS in the presence of the PD brain extract, we employed a more physiologically relevant model based on the primary rat hippocampal neurons[94]. Using primary hippocampal neurons, an αS aggregation-based seeding model has been recently

developed that recapitulates the key events of aggregation, seeding, and maturation of inclusions that partly mimic the features of LB-like structures[94]. We incubated primary culture neurons for a total of 31 days, including a 10 day of incubation period, followed by the addition of PMCA samples (+PD or PD + SK-129) and incubation for another 21 days. The reported total incubation time (in literature) for the primary culture neurons was much shorter (maximum time = 21 days)[94]; however, we incubated the primary culture neurons for a total of 31 days. The reason for the longer incubation time for the primary neurons in the presence of the PD sample was because we did not observe any significant intracellular aggregation and neurotoxicity at shorter incubation times in the presence of the PD sample. The difference in the incubation time (literature vs our experiment) required to induce neurotoxicity in the primary culture neurons was likely due to the difference in the αS fibril polymorphs of our experiment and the literature sample. It has been shown earlier that different αS fibril polymorphs could differ in templating αS aggregation and inducing toxicity[164]. At 31 days of incubation time, we observed both aggregation and significant neurotoxicity in the primary culture neurons in the presence of PD fibrils. The primary culture neurons treated with the PD sample (figure 2.28 m) were stained after 31 days and they were stained positive for αS-pS-129 (phosphorylated residue 129 in WT αS) (red color) and ThS (blue color), a dye that specifically binds protein aggregates (figure 2.28 m). In addition, these aggregates were stained positive and colocalized for p62 (autophagosome vesicles) and TOM20 (mitochondria) as well (figure 2.28 m) and the aggregates were most likely colocalized in the cytoplasmic region of the neurons as suggested by others as well[94]. Our confocal imaging data corroborate well with the earlier published work[94]. The data suggest that αS

inclusions recruit and sequester various organelles, proteins, and membranous structures, like the published work[165]. The staining profile of the primary neurons was very similar for both the control and PD fibrils+SK-129 conditions. We did not observe any colocalization of αS-pS-129 with p62, TOM20 in both the control and PD + SK-129 conditions (figure 2.28 m, +PD + SK-129). Also, no staining of αS-pS-129 was observed with ThS dye for both the control and PD + SK-129 conditions (figure 2.28 m). We observed mild staining and diffusion of αS-pS-129 in both the control and PD + SK-129 conditions; however, we did not observe any colocalization of αS-pS-129 with any other biomarker, including ThS dye . The partial staining of αS-pS-129 is likely due to the longer incubation time (31 days) for the primary culture neurons in our experimental conditions, which might have contributed to some neurotoxicity and the mild staining of αS-pS-129. We used lactate dehydrogenase (LDH) release assay to determine the neurotoxicity of the primary culture neurons in the presence of PD fibrils (±SK-129). We observed very high neurotoxicity (~8-fold higher than control) in primary neurons in the presence of the PD sample. In marked contrast, similar to the control sample, we did not observe any significant neurotoxicity in the presence of PD + SK-129 condition (figure 2.28 n).

To further validate these results, we use an HEK cells-based model, which expresses endogenous monomeric αS-A53T-YFP. In the presence of PD fibrils, both P62 and αS-pS-129 colocalized in the aggresome of αS inclusions in HEK cells after 24 h (figure 2.31). The αS inclusions were localized in the cytoplasmic region of the HEK cells as suggested by others as well[85]. Our results corroborate well with the earlier published work with HEK cells (figure 2.31 a b). In marked contrast, in the presence of

PD fibrils+SK-129 condition, we detected a significantly smaller number of colocalization of P62 and αS-pS-129 in the aggresome of αS inclusions (figure 2.31 a, b). In addition, we carried out the MTT reduction-based cytotoxicity assay for the HEK cells in the presence of PD fibrils. The cell viability of HEK cells decreased to 50.5 ± 5.4% in the presence of PD fibrils (figure 2.31 c). However, in the presence of PD fibrils+SK-129 condition, the cell viability increased to 85.6 ± 7.8%. Using primary culture neurons and HEK cells, we have shown that various proteins, including P62 and αS-pS-129 colocalize in the aggresome of αS inclusions and mediate toxicity in the presence of PD fibrils. In the presence of PD + SK-129 condition, we observed a significant decrease in the colocalization of P62 and αS-pS-129 in the aggresome of αS inclusions and rescue of the toxicity in HEK cells and primary culture neurons.

2.3.6 Effect of SK-129 in *in vivo* models

The antagonist activity of SK-129 against αS aggregation was tested in vivo using a *C elegans*-based PD model (NL5901). The ability of SK-129 to efficiently permeate cell membranes was confirmed by the parallel artificial membrane permeation assay (Figure 2.32 a) and confocal microscopy (using SK-129F, Figure 2.32 b). The NL5901 strain is a well-established PD model that expresses WT αS-YFP in the body wall muscle cells and PD phenotypic readouts include a gradual increase in inclusions (αS-YFP) in body wall muscle cells and a decline in motility during aging (Figure 2.32 c and e-g)[163]. The NL5901 strain was treated with 15 μM SK-129 at the larval stage and incubated with and without SK-129 for 9 days. The inclusions (αS-YFP) were counted manually using confocal microscopy. We observed a high number of inclusions (~33 inclusions/*C elegans*) (Figure 2.32 c, e) ; however, there was a substantial decline in inclusions in the

presence of SK-129 (~8–9 inclusions/*C elegans*) (Figure 2.32 d, e), suggesting that SK-129 permeates the body wall muscle cell membrane and inhibits αS aggregation (Figure 2.32 d, e). The motility rate of the NL5901 strain decreases during the aging process because of αS inclusions. We utilized a newly developed

WMicroTracker ARENA plate reader to measure the locomotion (overall activity counts) of NL5901 in the absence and presence of SK-129[154,166]. The overall activity of NL5901 displayed a gradual decline in the activity in comparison to the WT model of *C elegans* (N2) (Figure 2.32 f, g and Supplementary Figure 2.33); however, NL5901 treated with 15 μM SK-129 at the larval stage resulted in a significant improvement in the overall activity (Figure 2.32 f, g and Figure 2.33). The overall activity of NL590 treated with SK-129 was closer to the N2 strain (Figure 2.32 f, g and Figure 2.33).

2.3.7 Effect of SK-129 on intracellular αS seed catalyzed aggregation

SK-129 was a very potent antagonist of in vitro seed catalyzed aggregation of αS, both in cellular and primary culture neuronal models. However, in these models (cellular and neuronal), the solutions of αS aggregates (±SK-129) were prepared extracellularly and then introduced to the cells or neurons to determine their ability to template the monomeric αS. Here, we aim to determine the antagonist activity of SK-129 against the seed catalyzed aggregation of αS in a novel intracellular assay using HEK cells. In this assay, the seeds of αS will be introduced to the HEK cells, followed by the introduction of SK-129 to the cells. This assay will test the antagonist activity of SK-129 against the seed catalyzed aggregation of αS in an intracellular manner. To develop this assay, first, we assessed the total time required by αS seeds for the internalization into HEK cells.

The HEK cells (expressing αS-A53T-YFP) were exposed to αS seeds (0.125 μM) extracted from PD brain for various time points (0.5, 4, 8, 12, and 24 h), washed the cells, and incubated for a total of 24 h. The formation of αS inclusions was noticeable within 4 h of the treatment of cells with αS seeds. The number of inclusions were comparable (~20 inclusions/100 cells) in the case of 8, 12, and 24 h treatment of cells (Figure 2.32 h, i), which suggests that αS seeds were completely internalized in cells within 8 h. The antagonist activity of SK-129 against the intracellular seed catalyzed aggregation of αS was measured using the HEK cells treated with αS seeds for 8 h. A solution of SK-129 (10 μM) was added to HEK cells that were already treated with αS seeds (0.125 μM) for 8 h, followed by the incubation for an additional 16 h (total 24 h) (Figure 2.32 j). There was an abundance of inclusions in the absence of SK-129 after 24 h (~19 inclusions/100 cells, Figure 2.32 i); however, a low number of inclusions (~1–2 inclusions/100 cells) were observed in the presence of SK-129 (Figure 2.32 jj). We also observed a gradual increase in inclusions in the presence of αS seeds for up to 4 days. However, in the presence of SK-129, a low number of inclusions was observed for up to 4 days (2–3 inclusions/100 cells, Figure 2.32 i, j). In addition, we also observed a gradual decrease in the cell viability of HEK cells treated with PD samples from day one to four (Figure 2.28). In marked contrast, the cell viability was significantly higher up to four days in the presence of SK-129 (Figure 2.32 k). The data clearly suggest that SK-129 is a potent antagonist of both intracellular de novo αS aggregation and the seed catalyzed aggregation of αS.

2.4 Discussion

αS aggregation is one of the causal agents in PD pathologies, making it an enticing therapeutic target. However, the atomic-level understanding of the sequences that initiate αS aggregation is limited; therefore, strategies that identify aggregation-prone αS sequences could have significant therapeutic implications in the treatment of PD. We used OQs as a multipronged approach to investigate αS aggregation on a molecular level and to identify targets that are essential for the initiation of αS aggregation.

The study led to the identification of SK-129 as a potent inhibitor of de novo aggregation of αS under both in vitro and in vivo PD models. The data suggest that SK-129 stabilizes αS in an helical conformation by specifically interacting with distinct αS sequences towards the N-terminal of αS. We propose that SK-129 inhibits the aggregation of αS by either modulating the conformation of monomeric αS into aggregation incompetent helical structure or SK-129 stabilizes the intermediate conformation of αS and inhibits the aggregation and rescue toxicity functions.

Deletion of the binding sites of SK-129 (αS sequences) from WT αS completely abolished the de novo and seed-catalyzed aggregation of αS. We postulate that the identified αS sequences are essential to initiate the aggregation and could be considered as novel therapeutic targets for the potent inhibition of αS aggregation. In groundbreaking findings, Eisenberg and Radford groups have identified αS sequences that initiate aggregation and they are in close proximity to the αS sequences identified from our study[159,167]. More importantly, we have also validated these αS sequences by targeting

them with foldamers, which led to the complete inhibition of αS aggregation and rescue of PD phenotypes in both in vivo and in vitro PD models. Our data suggest that the aggregation-prone αS sequences are potentially sampling helical conformation during αS aggregation; therefore, the design of helical mimetics complementing the chemical fingerprints of the helical conformation of αS sequences could lead to effective antagonism of αS aggregation and rescue of PD phenotypes.

We demonstrated that the binding sites of SK-129 (αS sequences) that initiate the de novo αS aggregation are also important for the seed-catalyzed aggregation of αS. The seed catalyzed aggregation requires the interaction of αS fibers with αS monomers to accelerate the aggregation. We have shown that SK-129 inhibits the seed catalyzed aggregation of αS. We surmise that the mode of action for SK-129 is a consequence of the interaction of SK-129 with the monomeric αS (towards N-terminal) and the conversion of the latter into a fiber-incompetent conformation, which consequently inhibits the seed catalyzed aggregation of αS. SK-129 was also a potent antagonist of de novo aggregation of αS (*C elegans* PD model) and seed catalyzed aggregation of αS (HEK cells) in the intracellular models. Based on our data, we propose that SK-129 permeates the membrane, interacts with the intracellular monomeric αS, and modulates both the de novo aggregation of αS (*C elegans*) and the seed catalyzed aggregation of αS (HEK cells). A similar mode of action has been displayed by affibodies, which interact with monomeric αS and modulate it into a β-hairpin conformation. Similar to SK-129, the affibodies were potent inhibitors of both the de novo aggregation of αS and the seed catalyzed aggregation of αS[131].

Our atomic-level study suggests that SK-129 regulates the aggregation of αS under both de novo (lipid free) and lipid membrane conditions by binding to N-terminal sequences of αS, which are in close vicinity to the binding sites of molecular chaperones (secB)[168]. Our NMR and CD data under de novo and lipid membrane conditions suggest that SK-129 regulates αS aggregation by shifting the equilibrium toward non-aggregating and potentially functional αS, similar to molecular chaperones. The chaperones have been shown to interact with the N-terminal region of αS and shift the conformational equilibrium towards the functional membrane-bound αS to maintain the cellular homeostatic balance 60. SK-129 was able to inhibit the aggregation (de novo and lipid membrane conditions) and it was very effective in rescuing PD phenotypes in various cellular and in vivo PD models. If SK-129 was only able to inhibit αS aggregation and has interfered with the native function of αS, we would not have observed a significant rescue of toxic functions in various biological systems from PD phenotypes. Collectively, our data suggest that SK-129 potently inhibits αS aggregation without interfering with the native function of αS.

The modulation of αS aggregation by affibodies and molecular chaperones could be an attractive therapeutic intervention for PD; however, proteins/peptides are limited with poor cell permeability and poor enzymatic and conformational stability in biological milieus. Similarly, SK-129 has demonstrated chaperone/affibody-like ability to manipulate αS aggregation and it was able to efficiently rescue PD phenotypes in both in vitro and in vivo PD models. The intracellular antagonist activity of SK-129 in various PD models suggests that it possess good pharmaceutical properties, including good cell permeability, enzymatic stability, and structure stability because all of these properties are

required for its activity against intracellular αS aggregation. The OQs have been previously shown to maintain potent antagonist activity against their therapeutic targets and demonstrated good cell permeability, structure stability, and enzymatic stability in the biological milieu. A PD mouse model-based study is underway to further assess the pharmaceutical properties and the antagonist activity of SK-129 against PD phenotypes. We are using a well-established mouse model of PD (αSA53T transgenic line M83)[169]. This mouse model has been studied extensively because it mimics the PD pathologies. Using this model, we will be able to assess the pharmacokinetics and pharmacodynamics properties of SK-129. Also, the mouse model study will be used to assess the ability of SK-129 to cross the blood–brain barrier. The mouse model study will be used to assess the antagonist activity of SK-129 against PD phenotypes. In addition, the PD mouse model will be treated with PD fibrils in the absence and presence of SK-129. The study will be used to assess the effect of SK-129 on the spreading and propagation of PD phenotypes facilitated by PD fibrils. We are optimistic that the pharmaceutical properties and the antagonist activity of SK-129 can be further optimized without sacrificing its overall conformation. The side chain functionalities of SK-129 scaffold can be conveniently modified synthetically without disturbing its overall conformation for further optimization of activity, which is often challenging with proteins/peptides. Additionally, the C- (COOMe of SK-129) and N-terminus (-NO2 of SK-129) of SK-129 can also be modified to tune various pharmaceutical properties, including solubility and permeability etc. These manipulations in the chemical structure of SK-129 will not significantly alter its antagonist activity as we have seen with a fluorescent analog of SK-129 (SK-129F), which has almost similar affinity to SK-129 against αS.

To the best of our knowledge, this is the first report that simultaneously led to the identification and validation of the chemical fingerprints of key sequences, which initiate αS aggregation and the targeting of these sequences completely abolishes αS aggregation.

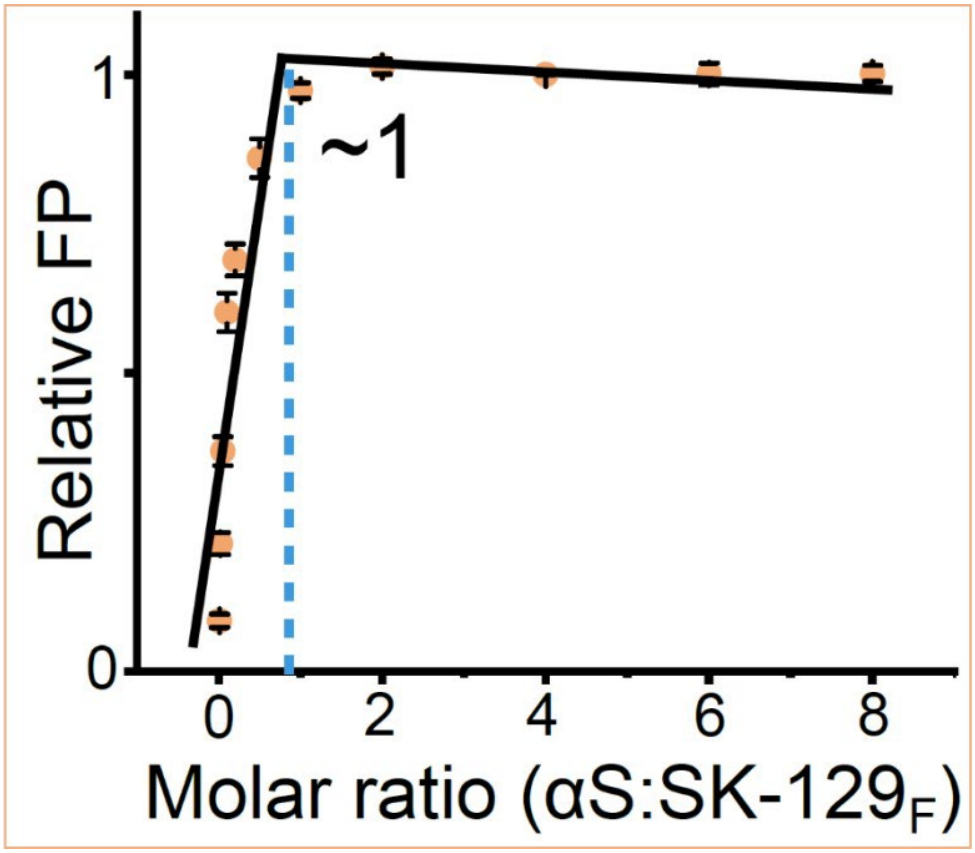

Figure 2.12 The plot between the relative FP and the molar ratio (αS:SK-129F), which is extracted from the FP titration between 10 μM SK-129F and increasing concentrations of αS. The binding stoichiometry of SK-129F against αS was determined by fit using two linear equations. The intersection of two equations lead to the binding stoichiometric ratio between αS and SK129F. The fluorescence polarization titrations between SK129F and αS were conducted three times and each point in titrations was the average of three data points. The reported error bars are the s.d.'s for three independent experiments (n = 3 independent experiments).

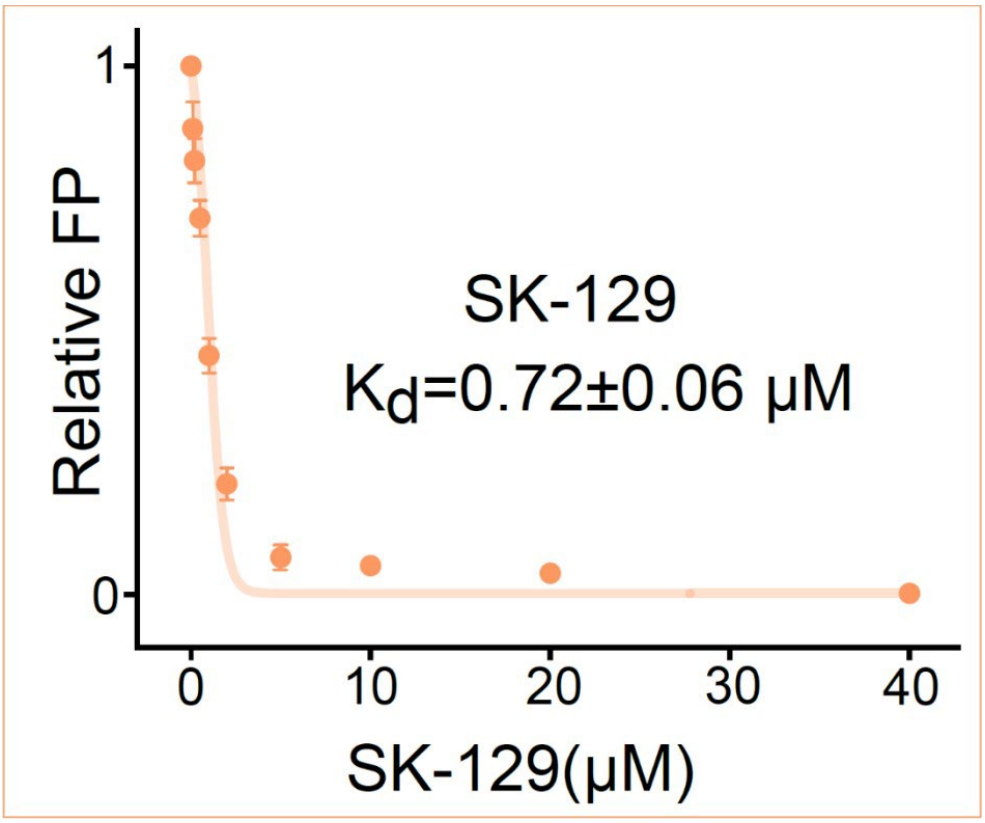

Figure 2.13 A competitive FP titration between a preformed saturated solution of αSSK-129F (100 μM: 10 μM) and SK-129 to determine the binding affinity betweenSK-129 and αS. SK-129 was serially added to a saturated solution of αS-SK-129F until no more change in the FP was observed. The plot between the related change in the FP against the concentration of SK-129 was fit using a competitive one binding site model to determine the binding affinity between SK129 and αS. The Kd ' s for SK-129 andSK-129F against αS were 0.72±0.06 and 0.80±0.06, respectively, which suggests that the fluorescein tag on SK-129F has a slight effect on the binding affinity of SK-129 against αS. The fluorescence polarization titrations between SK129 and the preformed saturatedcomplex of SK129F-αS were conducted three times and each point in titrations was the average of three data points. The reported error bars are the s.d.'s for three independent experiments (n = 3 independent experiments).

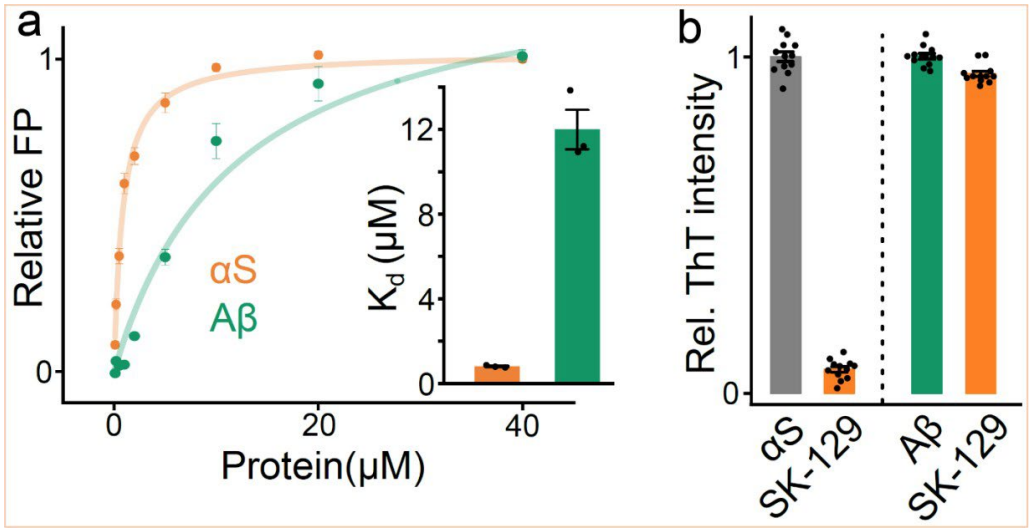

Figure 2.14 a, The curves and graphical representation (inset) of the comparison of FP-based binding affinities of SK-129F against αS and Aβ. The reported error bars are the s.d.'s for three independent experiments (n = 3 independent experiments). b, The comparison of the antagonist activity of SK-129 against the aggregation of 70 μM αS and 15 μM Aβ at an equimolar ratio. The final ThT intensity was monitored after one and four days for Aβ and αS, respectively. The data were expressed as mean and the error bars report the s.e.m. (n = 4 independent ThT aggregation experiments and each n consisted of 3 technical replicates).

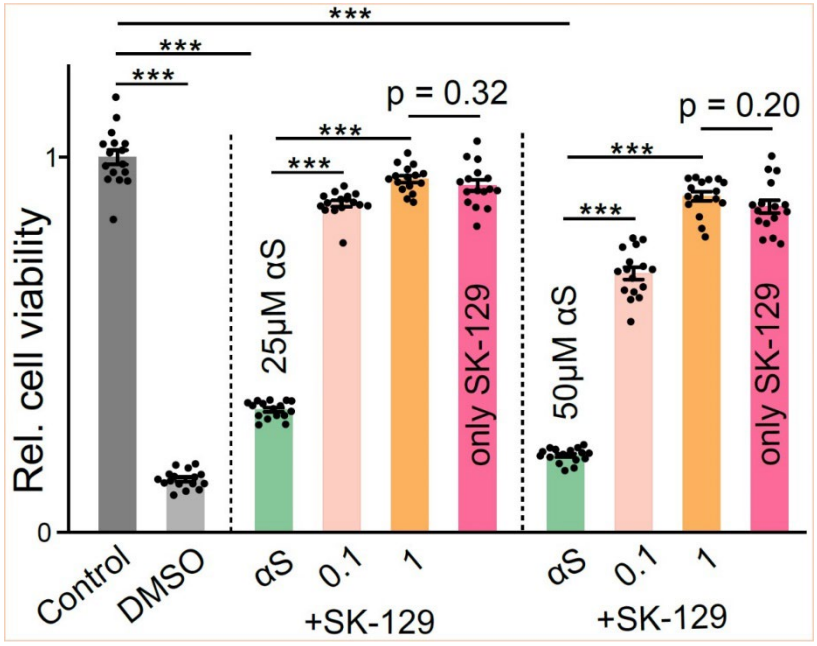

Figure 2.15 The statistical analysis of the relative viability of SH-SY5Y cells in the presence of the indicated concentrations of αS and the αS-SK-129 complex (the

aggregated state) at the indicated molar ratios using the MTT assay. For the relative viability the highest and lowest cell viability are used from the control (1 × PBS buffer) and DMSO, respectively. The inherent toxicity of SK-129 in SH-SY5Y was also monitored at the indicated concentrations. The data were expressed as mean and the error bars report the s.e.m. (n = 4 independent cell viability experiments and each n consisted of 4 technical replicates). The statistical analysis was performed using ANOVA with Tukey's multiple comparison test. *p<0.05, **p<0.01, ***p<0.001.

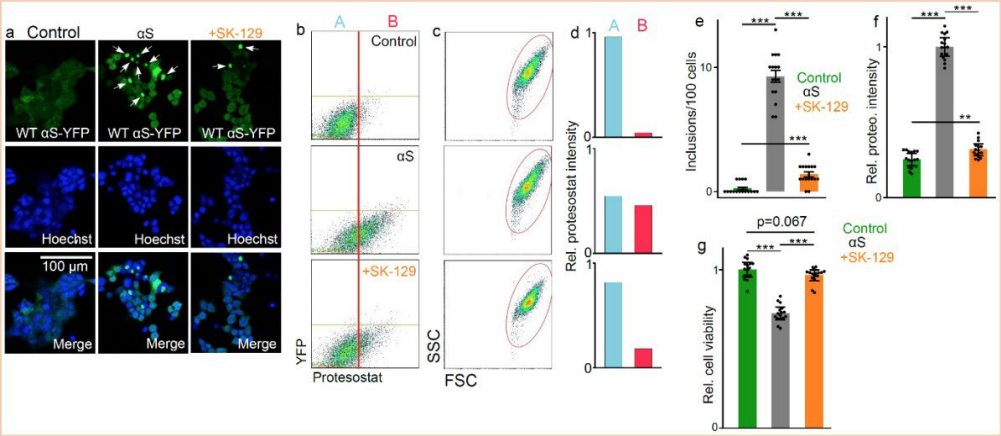

Figure 2.16 The effect of αS fibers on the HEK cells (αS-YFP) in the absence and presence of SK-129. a, The confocal images of the HEK cells (expressing endogenous WT αSYFP) treated with the control (1 × PBS buffer), 7 µM αS (the aggregated state), and 7 µM αS-SK129 complex (the aggregated state). The WT αS-YFP inclusions are indicated with white arrows. The images show the staining of HEK cells with Hoechst dye (blue) and the merge is the combination of the Hoechst and YFP signals. scale bar, 100 µm. The represented FACS dot plots (b) and gated plots (c) of the flow cytometric analysis of HEK cells treated with the indicated conditions. The x-axis representsαS-YFP aggregates containing cells stained with Proteostat dye (x-axis = Forward scatter, FSC) and the Y-axis represents the YFP signal intensity (y-axis = Side scatter, SSC). d, A and B represent the relative % of HEK cells without and with αS-YFP aggregates, respectively. e, The number of inclusions in HEK cells observed for the indicated conditions. Relative intensity of ProteoStat-stained aggregates (f) and relative viability(g) of HEK cells under the indicated conditions. A total of 100 HEK cells were examined to count the number of inclusions at 4 different locations in the 8-well plate for eachexperiment and it was repeated in 4 independent experiments. The data (e,f,g) were expressed as mean and the error bars report the s.e.m. (n = 4 independent experiments for e,f,g and each n consisted of 4 technical replicates). The counting of inclusions (e) was carried out for four different experiments and for each experiment 100 cells were counted from at least four different locations. The statistical analysis was performed using ANOVA with Tukey's multiple comparison test. *p<0.05, **p<0.01, ***p<0.001.

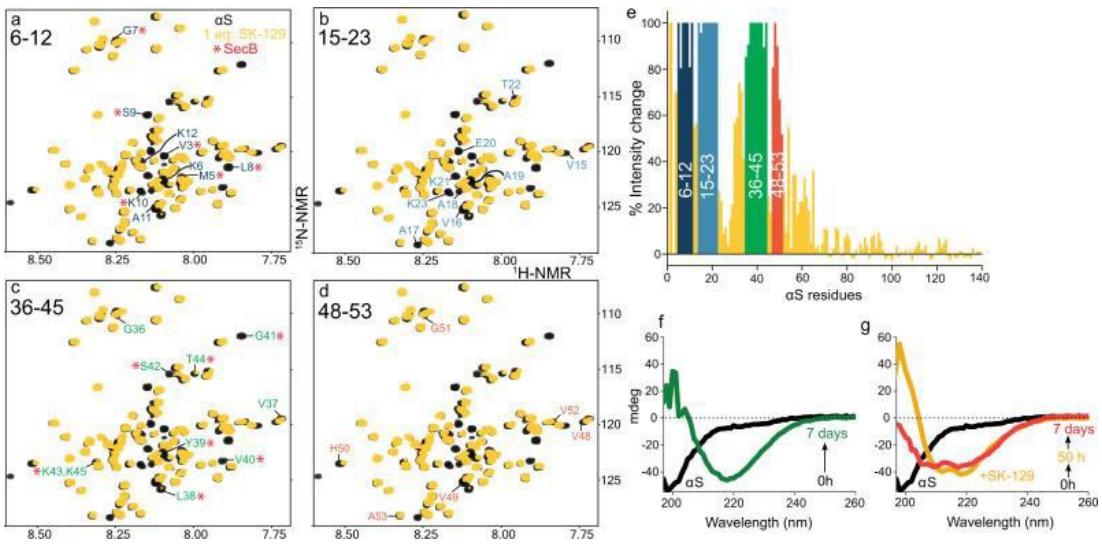

Figure 2.17 Overlay of 2D HSQC (1 H, 15N) NMR spectra of 70 µM uniformly 15N-labeled αS in the absence (black) and presence (yellow) of SK-129 at an equimolar ratio. The largest attenuation in the volume of the backbone amide residue NMR signals are highlighted and assigned, which includes αS segments from 6–12 (a), 15–23 (b), 36–45 (c), and 48–53 (d). The change in the volume of amide backbone residue peaks of αS was compared between SK-129 and a molecular chaperone SecB (*, red) and the pronounced changes were observed in segments 6–12 (a) and 36–45 (b). e Graphical presentation of the changes in the chemical shifts of the backbone amide residue peaks of 15N-labeled αS (70 µM) in the presence of SK-129 at an equimolar ratio. The colored sequences are the potential binding sites of SK-129 on αS. CD-based characterization of the aggregation kinetics of 35 µM αS in the absence (f) and presence (g) of SK-129 at an equimolar ratio. The spectra were recorded for 7 days.

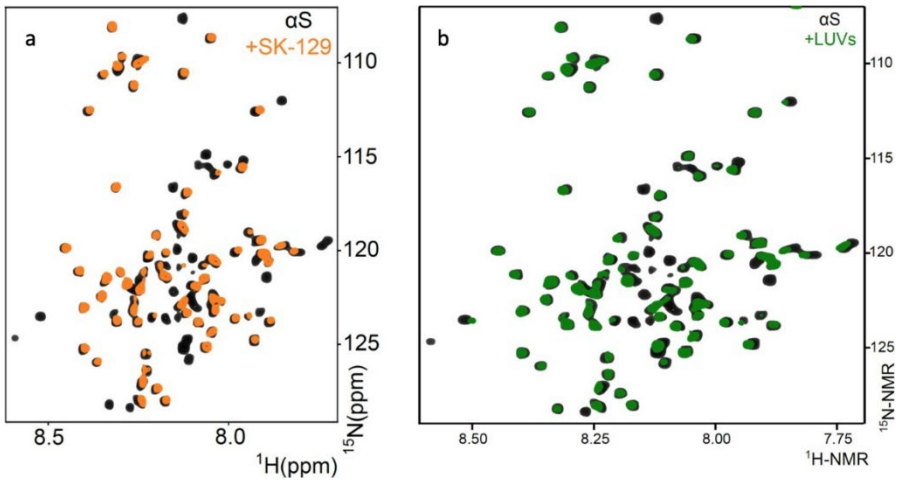

Figure 2.18 a Overlay of two-dimensional HSQC (1H, 15N) NMR spectra of 70 µM uniformly 15N-labelled αS in the absence (black) and presence (yellow) of 140 µM SK-

129. The HSQC NMR experiment conditions were exactly similar to the HSQC NMR spectrum at an equimolar ratio (SK-129: αS). b Overlay of two-dimensional HSQC (1H, 15N) NMR spectra of 70 µM uniformly 15N-labelled αS in the absence (black) and presence (green) of 875 µM LUVs (100 nm, DOPS). The HSQC NMR experiment conditions were similar to the HSQC NMR spectrum at an equimolar ratio (SK-129: αS)

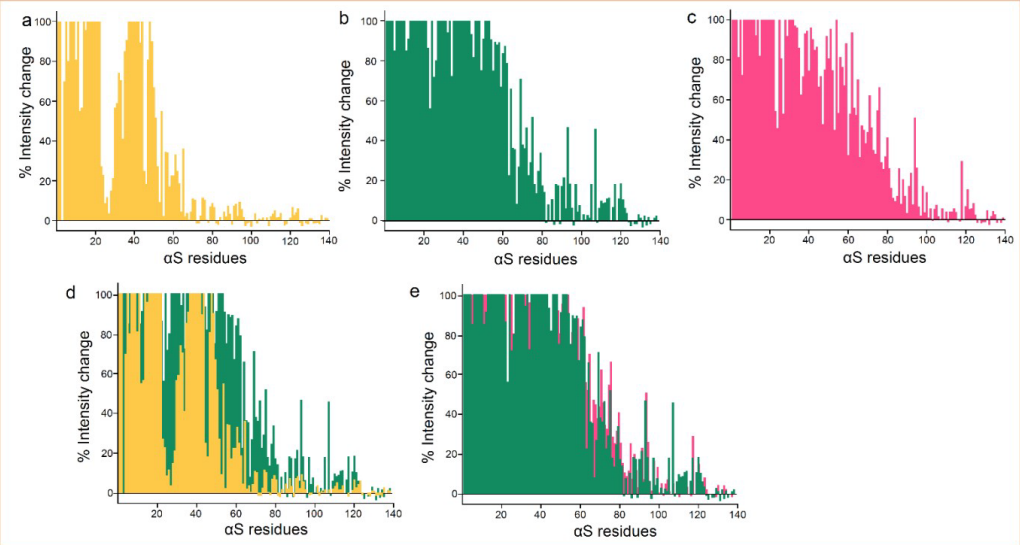

Figure 2.19 Comparison of the binding interaction between SK-129 and αS, and αS and LUVs using HSQC NMR spectroscopy. Graphical presentation of the intensity changes of the backbone amide peaks of 15N-labeled αS (70 µM) in the presence of 70 µM (a) and 140 µM (b) SK-129, and LUVs (875 µM, 100 nm, DOPS) (c). d, overlay of the intensity changes of the backbone amide peaks of 15N-labeled αS (70 µM) in the presence of 70 µM (orange) and 140 µM (green) SK-129. e, overlay of the intensity changes of the backbone amide peaks of 15N-labeled αS (70 µM) in the presence of 140 µM SK-129 (green) and 875 µM LUVs (red).

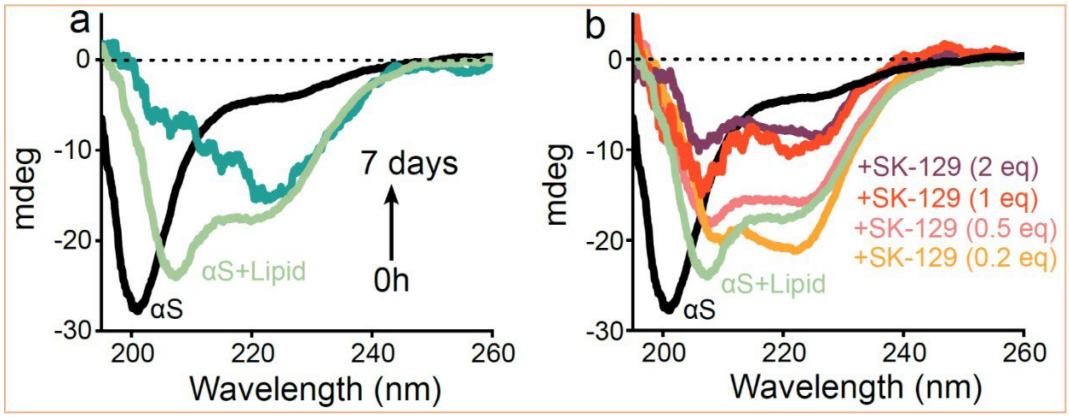

Figure 2.20 CD-based characterization of the effect of SK-129 on lipid-catalyzed aggregation kinetics of αS. a, Time-dependent CD spectra of 30 μM αS in the absence (black) and presence of LUVs (375 μM, 100 nm, DOPS) for 7 days. b, CD spectra of 30 μM αS in the presence of LUVs (375 μM, 100 nm, DOPS) and SK-129 under indicated stoichiometric ratios after 7 days.

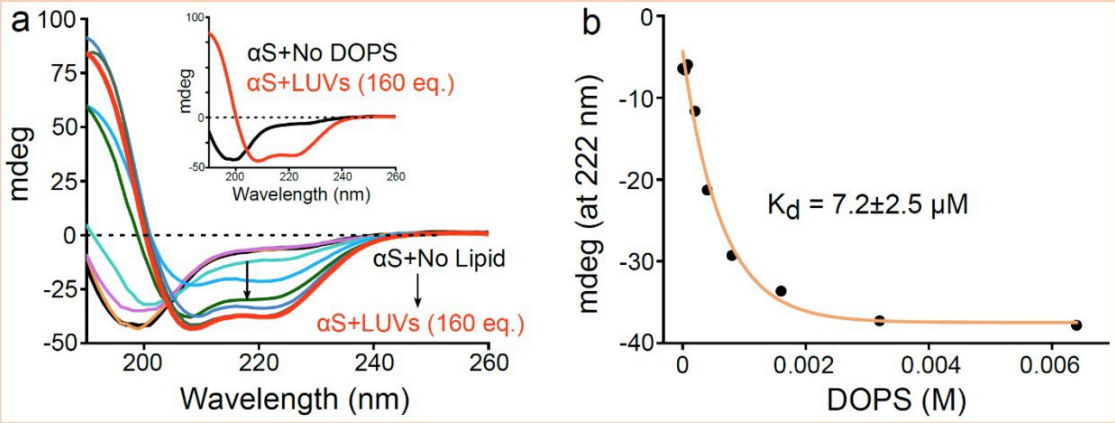

Figure 2.21 CD-based binding characterization of αS and lipid membranes. a, Far UV CD-spectra of 40 μM αS in the absence and presence of LUVs (100 nm, DOPS) at the indicated molar ratios (from 1 to 160, αS:LUVs). (Inset) Far UV CD-spectra of 40 μM αS in the absence (black) and presence of LUVs (100 nm, DOPS) at a mola ratio of 1:160 (αS:LUVs). b, A plot between the change of CD signal intensity (at wavelength = 222 nm) as a function of the concentration of lipid membranes (DOPS, 100 nm, LUVs). Data were fitted using a single-step binding site model to yield the binding constant between αS and LUVs.

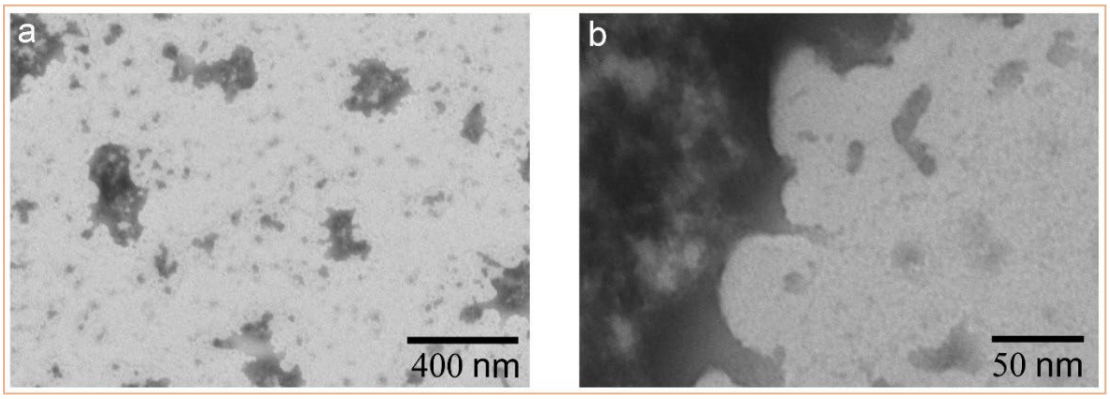

Figure 2.22 The negatively stained-TEM images at 400 nm (a) and 50 (b) scales of the aggregation of 35 µM αS in the presence of LUVs (875 µM, 100 nm, DOPS) in 20 mM NaCl, 20 mM NaPi, pH 6.5 in the presence of SK-129 at an equimolar ratio after seven days.

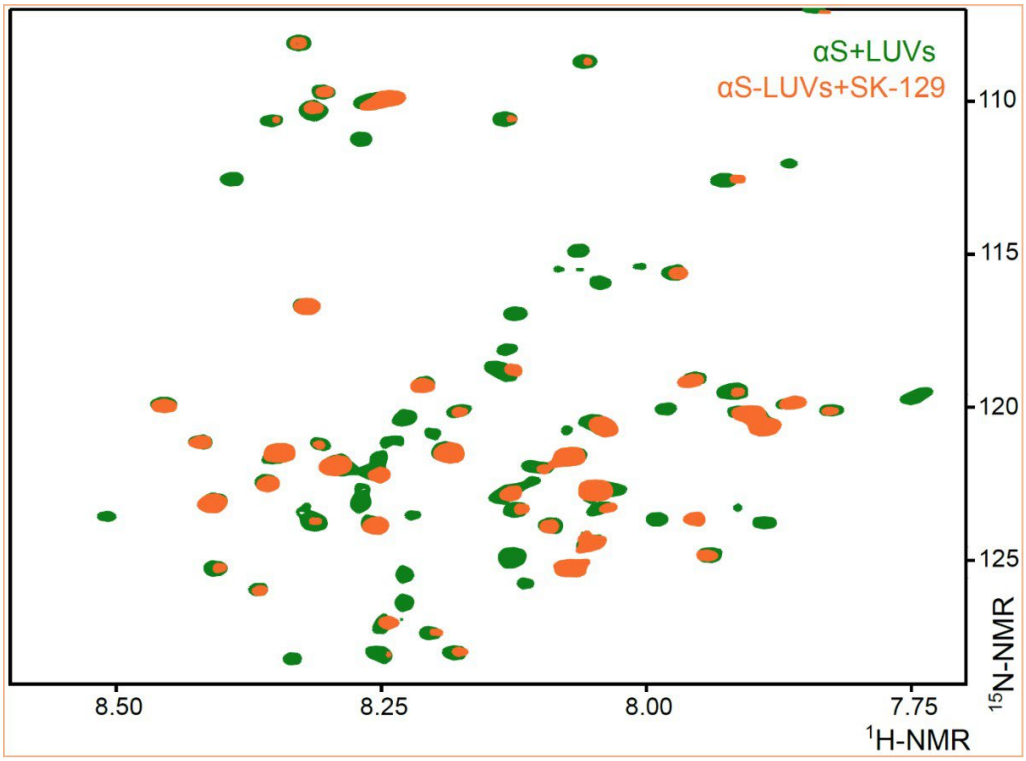

Figure 2.23 Overlay of two-dimensional HSQC (1H, 15N) NMR spectra of 70 µM uniformly 15N-labeled αS (+LUVs, 875 µM, 100 nm, DOPS) in the absence (green) and presence (orange) of 140 µM SK-129. The HSQC NMR experiment conditions were exactly similar to the HSQC NMR spectrum at an equimolar ratio (SK-129:αS).

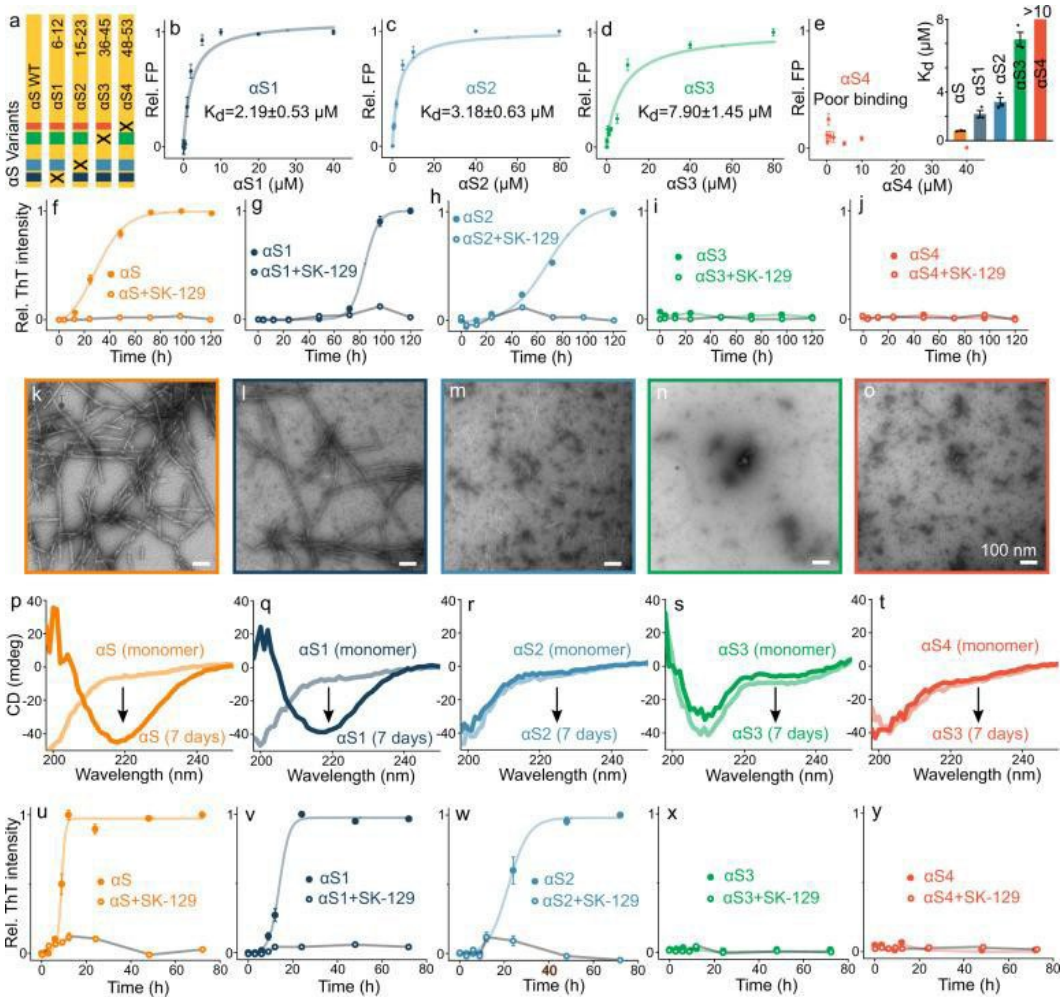

Figure 2.24 a A schematic of the design of αS variants where "x" represents the deleted sequence from the WT αS. b–e The fits for the FP titrations to determine the binding affinities between 10 μM SK-129F and αS variants (inset). The data were expressed as mean and the error bars report the S.D. (n = 3 independent experiments). f–j ThT fluorescence-based aggregation kinetic profiles of 100 μM αS variants in the absence (closed circle) and presence (open circle) of SK-129 at an equimolar ratio. The circles represent the average ThT intensity of three different experiments. The data were expressed as mean and the error bars report the S.D. (n = 3 independent experiments). k–o TEM images of αS variants (100 μM) after aggregating them for seven days. p–t CD spectra of monomeric (light color, monomer) and the aggregated (dark color, 7 days) states of αS variants (35 μM). The same aggregated samples of αS variants were used for both CD and TEM images. u–y Aggregation profiles of 100 μM αS variants catalyzed by preformed fibers of WT αS (10 μM in monomeric unit) in the absence (close circle) and presence (open circle) of SK-129 at an equimolar ratio. The data were expressed as mean and the error bars report the S.D. (n = 3 independent experiments).

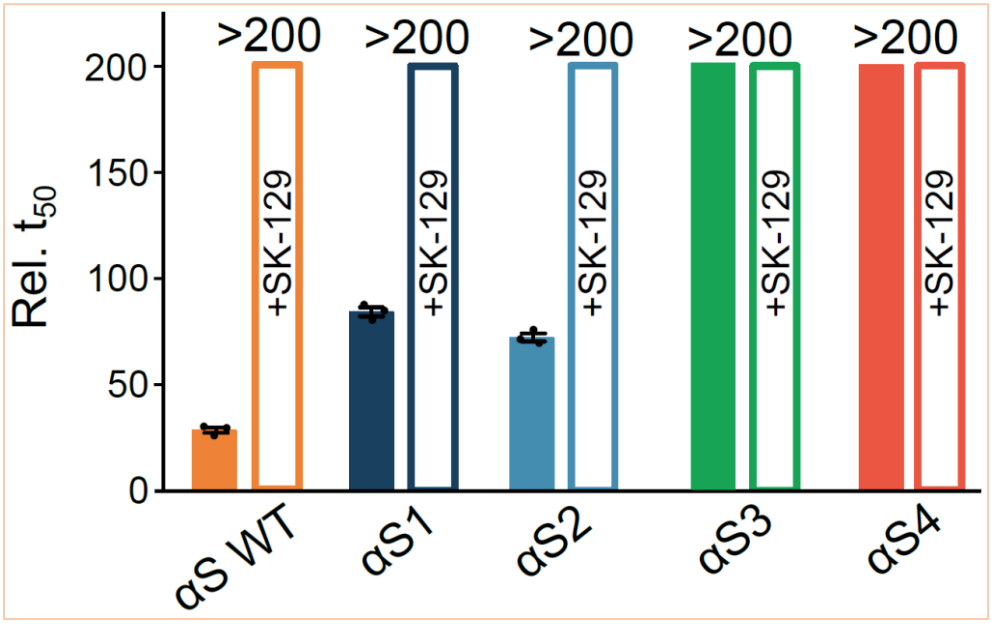

Figure 2.25 Comparison of t50's (The time required to reach 50% fluorescence intensity of ThT) for the aggregation of 100 μM WT αS and αS mutants in the absence (filled bar) and presence of SK-129 (open bar) at an equimolar ratio. The aggregation kinetics of various proteins were conducted three times (n = 3 independent experiments) and the reported t50 for various proteins is the mean of three separate experiments and the error bars report the s.e.m. (n = 3 independent experiments).

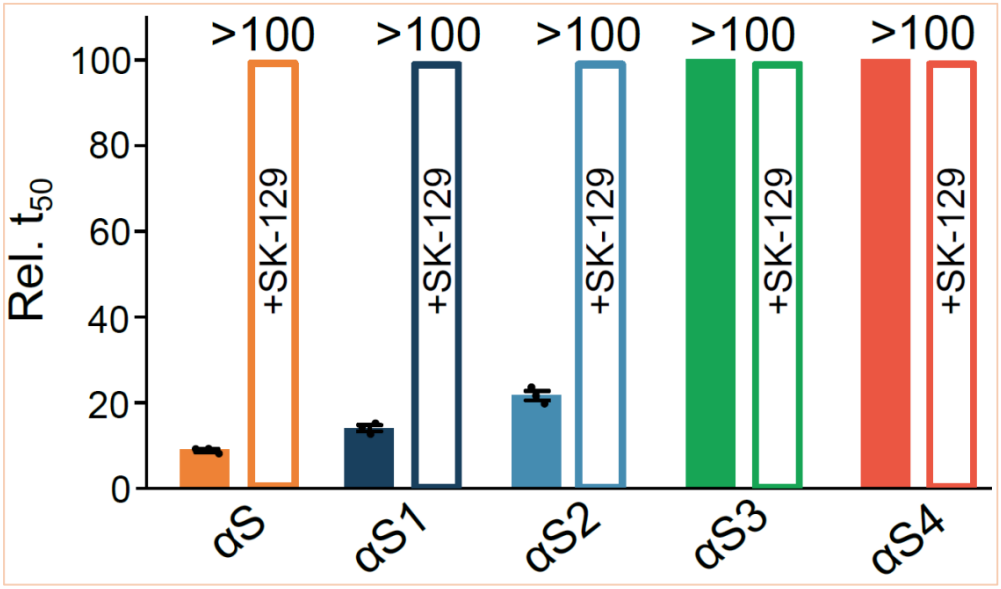

Figure 2.26 Comparison of t_{50}'s (The time required to reach 50% fluorescence intensity of ThT) of seed catalyzed (seeds= WT αS, 10% in monomer concentration of αS)

aggregation of 100 µM WT αS and αS mutants in the absence (filled bar) and presence of SK-129 (open bar) at an equimolar ratio. The aggregation kinetics of various proteins were conducted three times (n = 3 independent experiments) and the reported t50 for various proteins is the mean of three separate experiments and the error bars report the s.e.m. (n = 3 independent experiments).

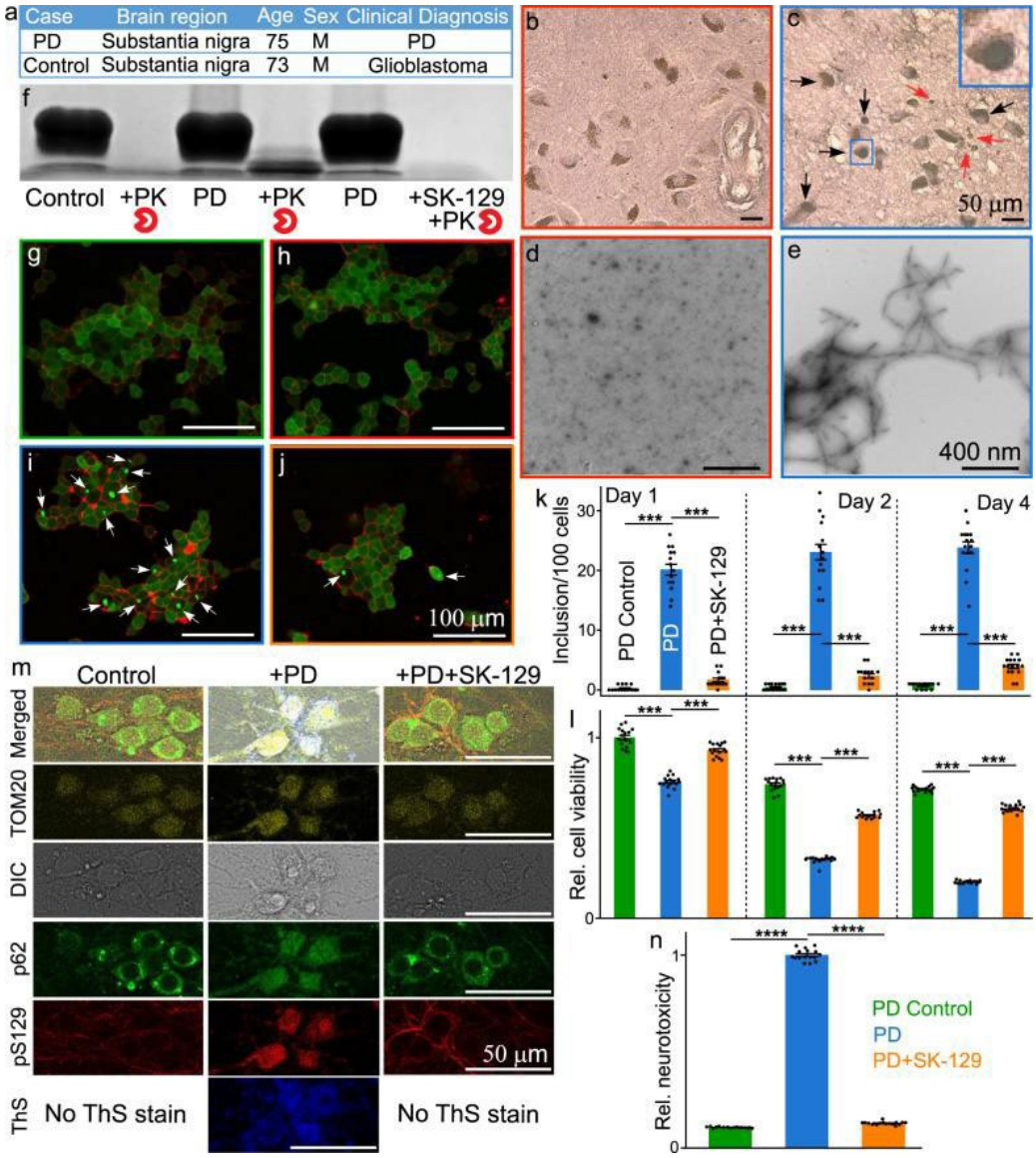

Figure 2.27 a The demographic and clinical information of the human brain tissues. Neuromelanin (brown) and αS immunostaining (LBs-like structure, bluish/black, black arrows, inset) in substantia nigra neurons from control (b) and PD (c) post mortem brain. Degenerating neurons and the extracellular neuromelanin debris from dying neurons (red

arrows) were also visible. The hollow spaces in the PD brain demarcate cell loss. (Inset) A zoom in view of LB-like structure. TEM images of the αS seeds extracted from the control (d) and PD brains (e). f The αS stained western blot of the PMCA sample from the fifth cycle of the control and PD brain extracts after treatment with PK in the absence and presence of SK-129. Confocal images of HEK cells after treatment with control (g), control (h), and PD (i) brain extracts from PMCA sample (fifth cycle) and in the presence of SK-129 (j) at an equimolar ratio (j). The number of inclusions (k) and relative viability (l) of HEK cells in the presence of PMCA samples (fifth cycle) from PD brain extracts under the indicated conditions. A total of 100 HEK cells were examined to count the number of inclusions at four different locations in the eight-well plate for each experiment and it was repeated in four independent experiments. The data (for k, l) were expressed as mean and the error bars report the s.e.m. (n = 4 independent HEKcells-based experiments and each n consisted of 4 technical replicates). m Confocal imaging of primary neurons treated with PMCA samples (fifth cycle) of control and PD brain extracts in the absence and presence of SK-129 at an equimolar ratio for 21 days. The primary neurons were stained with various markers, including LB biomarkers (pS129 and p62), mitochondria marker (TOM20), and aggregate staining ThS dye. n Under matched conditions (to m), the neurotoxicity of primary neurons was measured using the LDH assay. The data were expressed as mean and the error bars report thes.e.m. (n = 4 independent LDH experiments and each n consisted of four technical replicates). The data were expressed as mean and the error bars report the s.e.m. (n = 4 independent experiments and each n consisted of four technical replicates). The statistical analysis was performed using ANOVA with Tukey's multiple comparison test. *p < 0.05, **p < 0.01, ***p < 0.001, ****p < 0.0001.

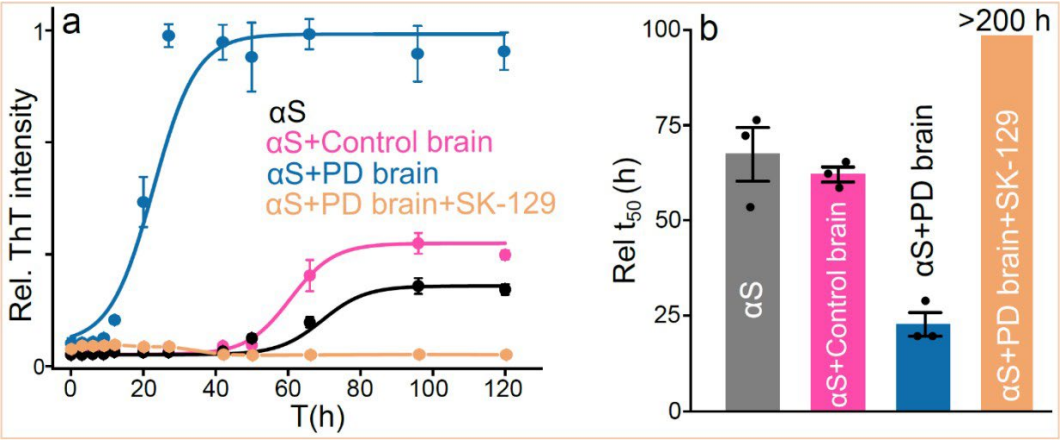

Figure 2.28 a, The aggregation profile of 70 μM αS (black) catalyzed in the presence of the control brain sample (pink) and the PD brain sample (fibers, blue) in (1 × PBS buffer). The aggregation profile of 70 μM αS catalyzed by PD brain samples in the presence of SK-129 at an equimolar ratio (orange). b, Comparison of t50's (The time required to reach 50% fluorescence intensity of ThT dye) for the aggregation profiles indicated in 'a'. The aggregation kinetics of various conditions were conducted three

times (n = 3 independent experiments) and the reported t50 for various conditions is the mean of three separate experiments and the error bars report the s.e.m. (n = 3 independent experiments).

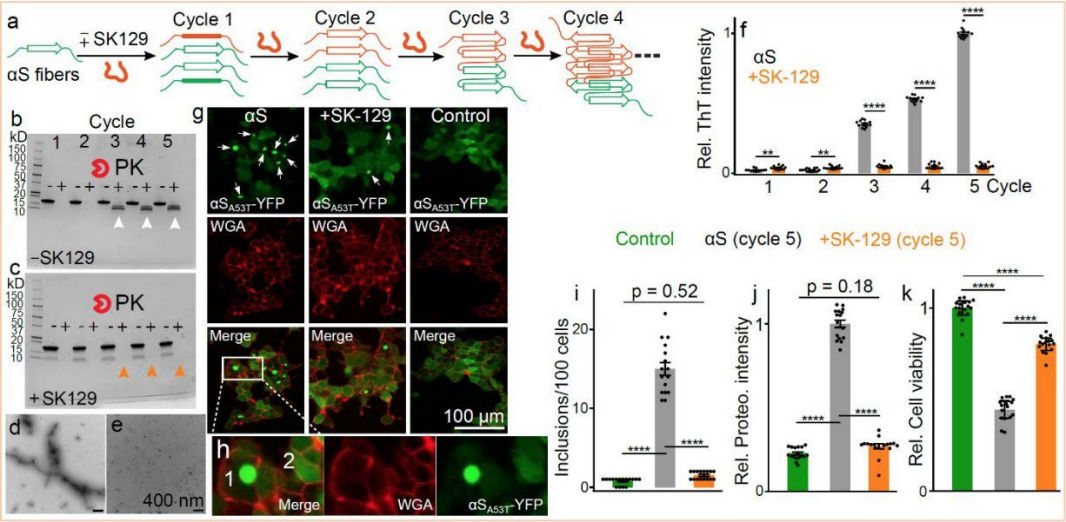

Figure 2.29 a, Schematic of the protein misfolding cyclic amplification (PMCA) assay. In the first step, the preformed fibers of αS (1 μM in monomer conc.) were used to template αS monomer (20 μM) in the absence and presence of 20 μM SK-129. The solutions were incubated at 37 0C with constant shaking for 2 days. In the second step, 1/10 volume of the solutions (±SK129) was used to template αS monomer. The process was repeated for five cycles. The Bis-tris gels of PMCA samples from cycle first to fifth in the absence (b) and presence (c) of SK-129. The -ve and +ve signs indicate the amplified samples in the absence and presence of PK, respectively. The arrows indicate the effect of PK on the PMCA samples from the indicated cycles. TEM images of the PMCA samples from the fifth cycle in the absence (d) and presence (e) of SK-129. f, The relative ThT intensity of various PMCA samples in the absence (black bar) and presence (orange bar) of SK-129, before treating the samples with PK. The data were expressed as mean and the error bars report the s.e.m. (n = 4 independent PMCA experiments and each n consisted of 3 technical replicates). g, The representative images of HEK cells after treatment with PMCA samples from the fifth cycle under the indicated conditions. The αSA53T-YFP inclusions are indicated by white arrows. The green color images are due to the intracellularly expressed αSA53TYFP and the red colored images are due to the staining of HEK cell membranes by wheat germ agglutinin (WTA). h, The zoom-in version of the difference in an intracellular αSA53T-YFP inclusion (1) and the homogenous distribution of αS-A53T-YFP (2). i, The number of αSA53T-YFP inclusions/100 HEK cells observed in the presence of PMCA samples from the fifth cycle under the indicated conditions. A total of 100 HEK cells were examined to count the number of inclusions at 4 different locations in the 8-well plate for each experiment and it was repeated in 4 independent experiments. The data were expressed as mean and the error bars report the s.e.m. (n = 4 independent confocal imaging experiments and each n consisted of 4 technical

replicates). j, The relative intensity of ProteoStat dye stained αSA53T-YFP aggregates in HEK cells treated with the PMCA sample from the fifth cycle in the absence and presence of SK-129 for 24 h. The data were expressed as mean and the error bars report the s.e.m. (n = 4 independent ProteoStat based experiments and each n consisted of 4 technical replicates). k, The relative viability of HEK cells treated with the indicated conditions for 24 h determined using the MTT-reduction toxicity assay. The data were expressed as mean and the error bars report the s.e.m. (n = 4 independent cell viability experiments and each n consisted of 4 technical replicates). The counting of inclusions in HEK cells was carried out for four different experiments and for each experiment, 100 cells were counted from at least four different locations in an 8-well plate. The statistical analysis was performed using ANOVA with Tukey's multiple comparison test. *$p<0.05$, **$p<0.01$, ***$p<0.001$, ****$p<0.0001$

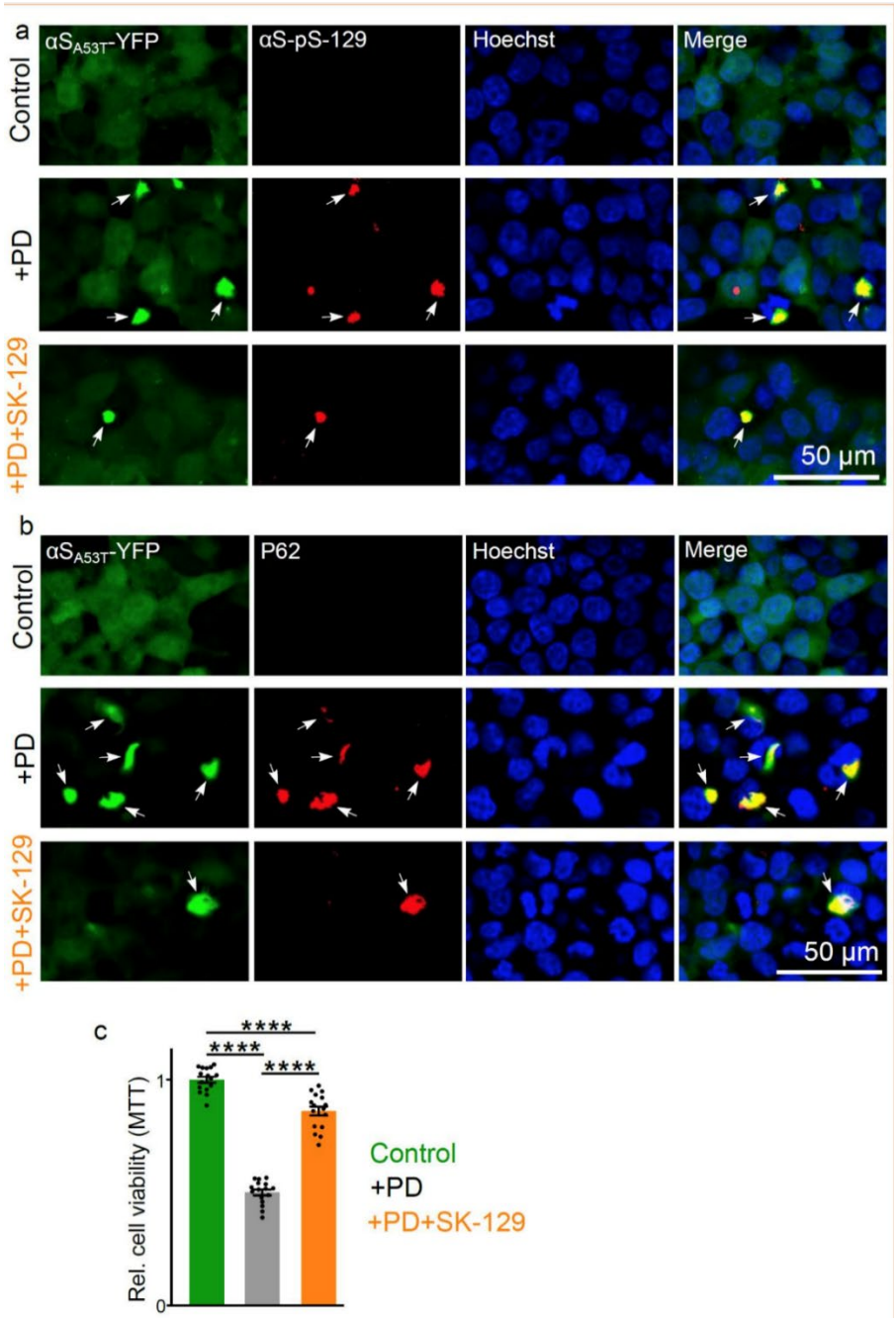

Figure 2.30 Effect of SK-129 on the PD fibrils catalyzed aggregation of αS templated by PMCA technique. a, The representative confocal images of HEK cells after treatment with PMCA samples from the PD and control brain. The green color images are due to the intracellularly expressed αSA53T-YFP. The αSA53T-YFP inclusions, αS-pS-129, and DAPI are represented by green, red, and blue colors. The αSA53T-YFP inclusions are indicated by white arrows. b, The αSA53T-YFP inclusions, P62, and DAPI are

represented by green, red, and blue colors. The αSA53T-YFP inclusions are indicated by white arrows. c, The statistical analysis of the relative viability of HEK cells treated with the indicated conditions for 24 h determined using the MTT-reduction toxicity assay. The data were expressed as mean and the error bars report the s.e.m. (n = 4 independent cell viability experiments and each n consisted of 4 technical replicates). The statistical analysis was performed using ANOVA with Tukey's multiple comparison test. *p<0.05, **p<0.01, ***p<0.001, ****p<0.0001.

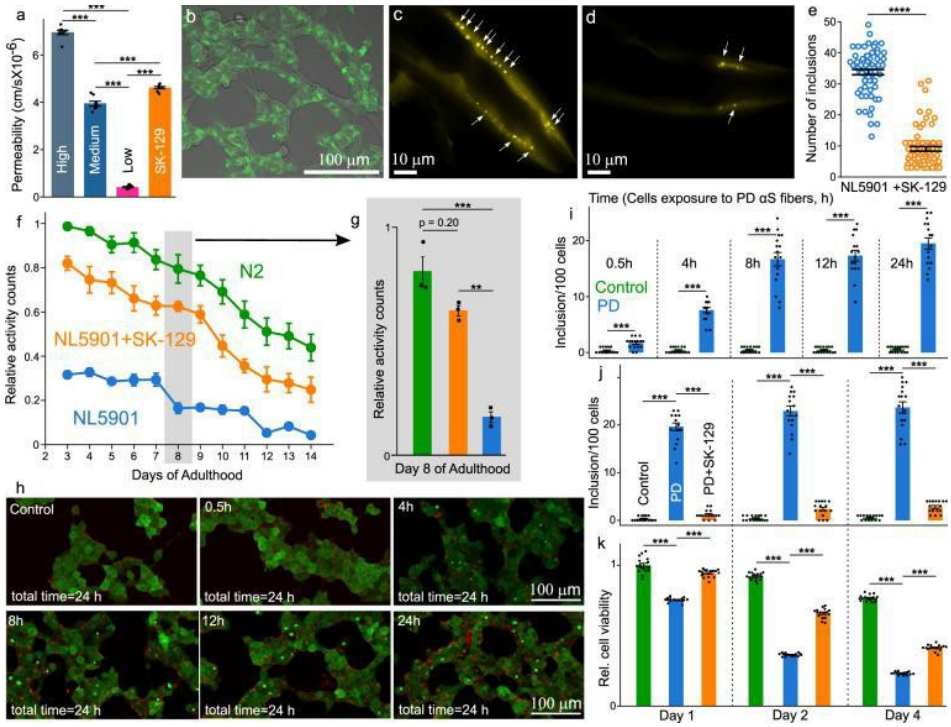

Figure 2.31 Assessment of cell permeability of SK-129 using PAMPA (a) and confocal microscopy (b). Confocal image of SH-SY5Y cells after treatment with 100 nM SK-129F for 15 h. The data were expressed as mean and the error bars report the s.e.m. (n = 4 independent experiments and each n consisted of two technical replicates). Confocal images (c, d) of αS-YFP inclusions (white arrows) in muscle cells of NL5901 (days of adulthood = 8 days) in the absence (c) and presence (d) of 15 µM SK-129. e The number of inclusions for experiment 'c, d' for NL5901 worms in the absence and presence of SK-129 (days of adulthood = 8 days). The data were expressed as mean and the error bars report the s.e.m. (n = 4 independent experiments and each n consisted of at least 15 technical replicates). f The relative activity counts for 14 days of adulthood of N2 and NL5901 in the absence and presence of 15 µM SK-129. g A graphical representation with statistical analysis of the relative activity counts of N2 and NL5901 in the absence and presence of 15 µM SK-129 for day 8 of the adulthood. The data were expressed as mean and the error bars report the s.e.m. (n = 3 independent experiments and each n consisted of two technical replicates). h Confocal images and number of inclusions (i) of HEK cells incubated with PMCA sample from control and PD brain extract for indicated times. The

HEK cells were washed after incubating them with the PMCA sample for various amounts of time. The number of inclusions (j) and relative viability (k) of HEK cells when they were incubated with the PMCA sample from PD brain extract for 8 h followed by washing, and further incubating HEK cells up to 4 days. A total of 100 HEK cells were examined to count the number of inclusions at four different locations in the eight-well plate for each experiment and it was repeated in 4 independent experiments. The data i–k were expressed as mean and the error bars report the s.e.m. (n = 4 independent experiments and each n consisted of four technical replicates). The statistical analysis was performed using ANOVA with Tukey's multiple comparison test. *p < 0.05, **p < 0.01, ***p < 0.001, ****p < 0.0001.

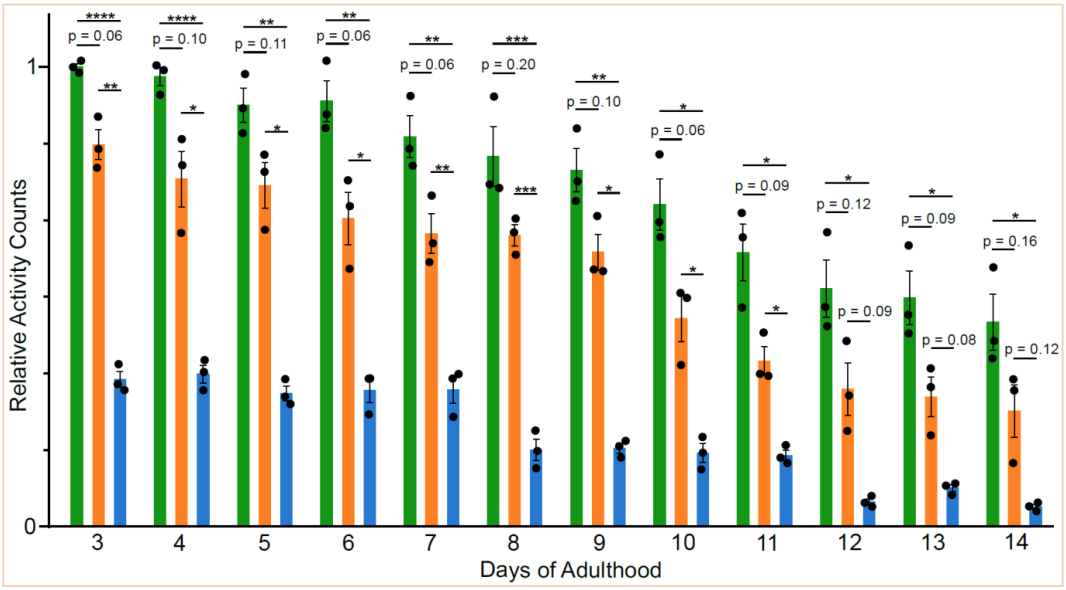

Figure 2.32 The statistical analysis of the comparison of relative activity counts of the control strain (N2) and NL5901 in the absence and presence of 15 µM SK-129 was measured for 14 days of adulthood. The readings were taken for 1 h and for each reading, 100 worms were used for each condition. A total of 100 worms were used for each experiment and the reported relative activity counts is the mean of three independent experiments and the error bars report the s.e.m. (n = 3 independent experiments). The statistical analysis was performed using ANOVA with Tukey's multiple comparison test. *p<0.05, **p<0.01, ***p<0.001, ****p<0.0001.

Chapter 3: A 2D Fragment-Assisted Protein Mimetic Approach to Rescue α-Synuclein Aggregation Mediated Early and Post-Disease Parkinson's Phenotypes

3.1 Introduction

Aberrant protein-protein interactions (aPPIs) are associated with a plethora of pathological conditions, including infectious diseases, cancer, neurodegenerative diseases, and amyloid diseases[170,171]. Consequently, modulation of aPPIs is considered to be a promising therapeutic intervention toward various pathologies. The pathological aPPIs are mediated via specific chemical interactions that often sample dynamic and transient conformations, which spread over large and hydrophobic surfaces[172]. One such example is the aggregation of αS, which is a neuronal protein expressed at high levels in DA neurons in the brain and implicated in the regulation of synaptic vesicle trafficking and recycling and neurotransmitter release[28]. The aggregation of αS is associated with the impaired dopaminergic neurons, which is a pathological hallmark of PD. Therefore, one of the potential disease-modifying therapeutic strategies for PD is the modulation of αS aggregation[116]. A few small molecules have been shown to inhibit αS aggregation[173]; however, some of them have complex chemical structures, which might limit their ability for synthetic tuning and further optimization of the antagonist activity against αS aggregation. Also, protein mimetics have been identified to inhibit αS aggregation; however, the chemical space on them was limited and there was no systematic optimization carried out against αS aggregation[174]

Moreover, most of these ligands were not tested against PD phenotypes in DA neurons in *in vivo models* to further assess their therapeutic potential. Therefore, ligands with the ability to manipulate aggregation with a large chemical space and having the tendency for systematic optimization of the antagonist activity could lead to potent antagonism of αS aggregation.

Oligopyridylmides (OPs) are a class of synthetic protein mimetics that have been shown to manipulate the aggregation of multiple proteins, including islet amyloid polypeptide, Aβ peptide, and mutant p53, which are associated with type 2 diabetes (T2D), Alzheimer's disease (AD), and cancer, respectively[175,176]. OPs have a large surface area and synthetically tunable side-chain functionalities that can complement the topography and side-chain residues of proteins such as those present at the interfaces of aPPIs during protein aggregation[175]. However, the OP library used in the screening to identify antagonists of protein aggregation was moderate in size (~30 OPs) with limited chemical diversity (~10 side chains), which may have precluded the opportunity for the optimization of the antagonist activity of OPs against the aggregation of various amyloid proteins[177]. There were several limitations with the previous method to generate OP libraries with larger chemical space to identify antagonists for the aggregation of proteins, including tedious synthesis with several chromatography steps (Figure 3.0) and pre-synthesized and screened OPs, which lacked a systematic optimization against the dynamic and transient nature of protein aggregation surfaces.

We have developed a novel 2D-FAST by combining fragment and structure-based techniques into the OP scaffold in order to systematically optimize the

antagonist activity against αS aggregation (Figure 3.0 B, C). The fragment-based approach has emerged as a promising method for drug discovery to identify high-affinity ligands against various pathological targets, including aPPIs[178,179]. The OP is an ideal scaffold for the fragment-based approach because the antagonist activity of OPs against their biological targets have been shown to increase with increasing side chains (monopyridyl<dipyridyl<tripyridyl)[180]. In 2D-FAST, the 2D consist of the side chains and the number of pyridyls groups in OPs (Figure 3.0 C). There are several novel features of our 2D-FAST for OPs, including (1) Use of common precursors for the elongation of OP from mono- to di- to tri- pyridyl synthesis; (2) Use of a chromatography-free amide coupling method for the elongation of the backbone chain; (3) Introduction of a large chemically diverse library of side chains on OPs with no column chromatography for most of the products; (4) Use of a fragment-based approach for systematic optimization of the antagonist activity of OPs against αS aggregation.

Using the synthetic 2D-FAST and an array of biophysical and cellular assays, we have identified NS132 as the most potent antagonist of *de novo* and fibers catalyzed aggregation of αS. NS132 was able to wholly inhibit αS aggregation, even at a substoichiometric ratio (αS:NS132, 1:0.2). In contrast, the peptidomimetic approaches without the novel features of our 2D-FAST, have identified ligands that require 5-100 fold molar excess to inhibit the aggregation of αS[181]. This observation highlights the novel aspects of our 2D-FAST approach, which entails a systematic fragment-based screening of a very large chemical space against αS aggregation that allows the identification of a very potent antagonist. A structure-activity relationship demonstrated that the side chains of NS132 are essential for its antagonist activity. The HEK

cells-based assays demonstrated that NS132 potently rescues cytotoxicity and inhibits the formation of intracellular inclusions. The 2D HSQC NMR study demonstrates that NS132 interacts with specific sequences of αS, which have been previously suggested to be the key aggregation-prone sequences[159]. The study also led to the synthesis of an analog of NS132 (NS163, Figure 3.1) with improved cell permeability without sacrificing the antagonist activity against αS aggregation. The antagonist activity of NS163 and NS132 was tested against αS aggregation-mediated PD phenotypes in two *C. elegans* PD models. Both ligands (NS163 and NS132) were very effective in rescuing various PD phenotypes in two *C. elegans* PD models, including neuroprotective effect against degeneration of DA neurons, motility recovery, improved food sensing behavioral deficits, increased dopamine synthesis, and reduced ROS level. Moreover, the OPs were very effective in rescuing further progression of PD phenotypes in DA neurons when administered in a post- disease-onset PD model, a model that mimics the current therapeutic intervention strategies, where the treatment starts during post-diagnosis of PD.

Overall, we have developed a novel 2D-FAST and demonstrated its utility in the identification of potent antagonists of αS aggregation, a process that is associated with PD. We have used a comprehensive study to establish the synthetic protein mimetic-based 2D-FAST approach and identified potent ligands, which were very effective in rescuing αS aggregation mediated PD phenotypes in physiologically relevant PD models.

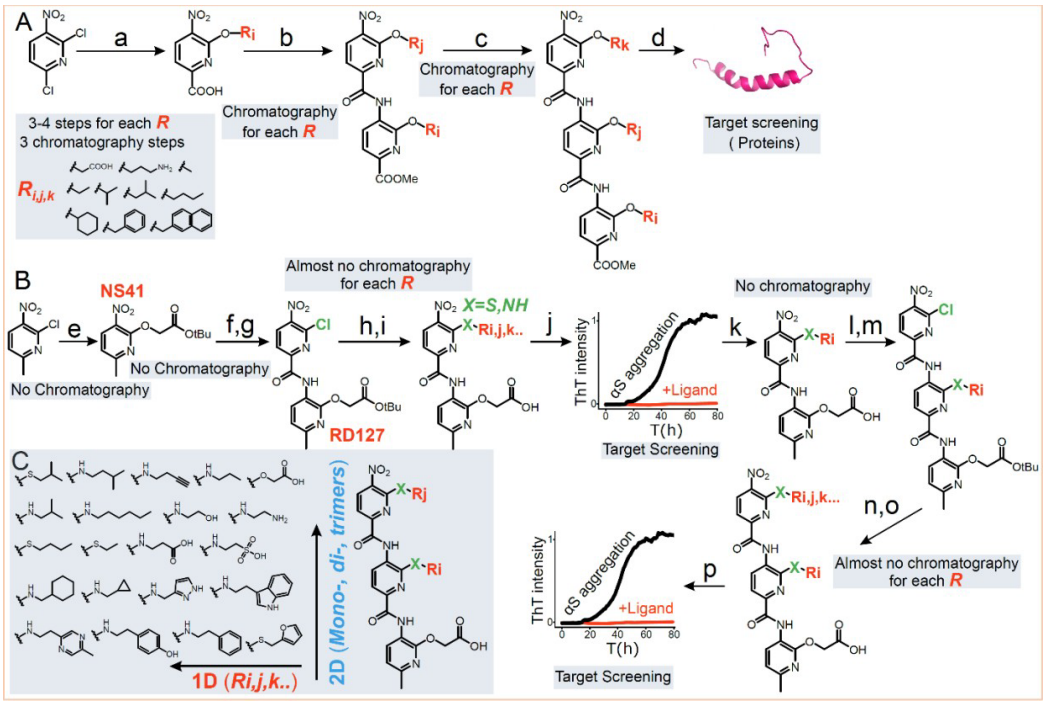

Figure 3.0 A schematic for the comparison of the old method (A) and the novel 2D-FAST (B). **a**, Synthesis of the monopyridyls with various side chains (Ri,j,k). (**Inset**) The chemical structures of the side chains on OPs. **b-d**, A flowchart for the synthesis of dipyridyls and tripyridyls and their testing against various biological targets. **e**, *Tert*-Butyl 2-hydroxyacetate, NaH (60% dispersion in mineral oil), toluene, 50 min. at 0 °C, then 5 h at r.t. **f**, **l**, Pd/C, H2 (g), EtOAc, 3 h at r.t. **g**, 6-chloro- 5-nitropicolinic acid, DCM (anhydrous), triethylamine, thionyl chloride, 0 °C to r.t., 45 min. **h**, Primary amine/thiol, DIPEA, DCM, 3 h at r.t. **i**,**o**, TFA, DCM, TES, 3h, r.t. **j**, Screening of the dipyridyls against αS aggregation using high throughput ThT kinetic aggregation assay. **k**, The identification of the most potent dipyridyl antagonist of αS aggregation (X-Ri on the second side chain of the dipyridyl). **m**, triethylamine, 6-chloro-5-nitropicolinoyl chloride, THF (anhydrous) 0 °C to r.t., 40 min. **n**, Primary amine, DIPEA, DCM, 3 h at r.t. **p**, Screening of the tripyridyls against αS aggregation using ThT kinetic aggregation assay. **C**, The representation of the 2D-FAST approach.

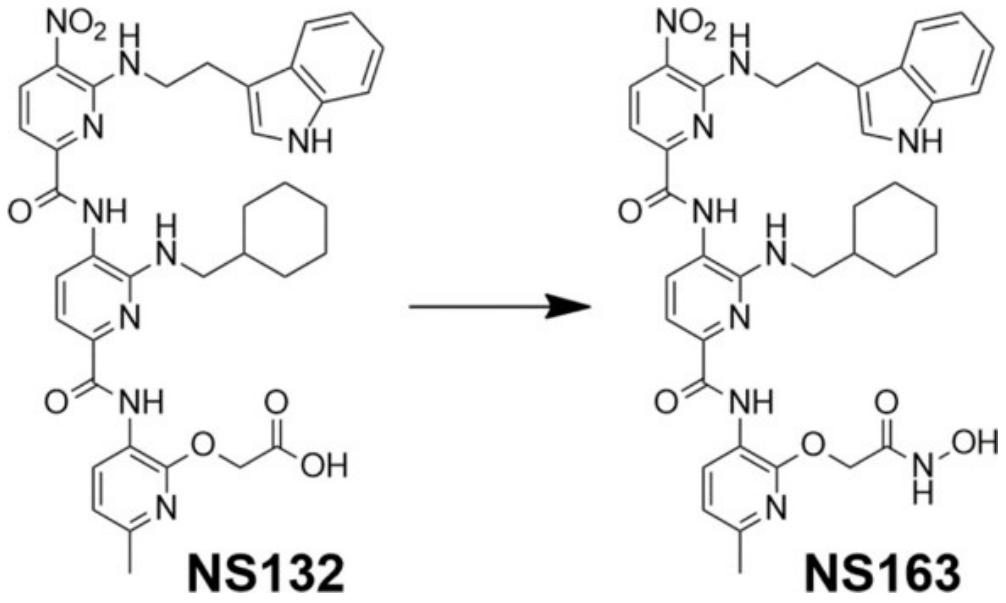

Figure 3.1 Synthesis of NS163. Reagents and conditions: Carbonyldiimidazole (CDI), tetrahydrofuran (THF, anhydrous), stir 1 h at r.t., hydroxylamine hydrochloride, 20 h, r.t.

3.2 Methods

3.2.1 Protein Expression and Purification

The plasmid construct pET11-αS (Addgene, Watertown, MA) was chemically transformed into competent BL21(DE3) cells and plated on ampicillin selection plate. A single colony was used to inoculate a 5 mL starter culture which was kept overnight at 37 °C while shaking at 200 rpm. The following day, the starter culture was used to inoculate 4 L of autoclaved Luria Broth (LB). The culture was incubated at 37 °C and shaken at 200 rpm until the optical density (OD600nm) reached 0.8. Then, protein expression was induced for 5 h by adding isopropyl β-D-thiogalactoside (IPTG) at a final 1 mM concentration. Cells were then harvested by centrifugation at 7,000 rpm and 4 °C for 15 min. αS purification was carried out using a previously described Osmotic Shock protocol[145]. Briefly, harvested cells were resuspended in Osmotic Shock Buffer (30 mM

Tris pH 7.2, 30% sucrose, 2 mM EDTA) and stirred for 15 min at 4 °C. The cells were centrifuged again at 12,000 rpm for 10 min at 4 °C and resuspended in cold Milli-Q H2O. The cell suspension was spiked with MgCl2 at a final 5 mM concentration. The suspension was stirred for an additional 5 min and centrifuged at 6,000 rpm for 10 min to remove cells. The supernatant was boiled at 95 °C for 15 min to precipitate proteins other than αS. The resulting precipitate was removed by centrifugation at 6000xg for 20 min and the solution was loaded on Bio-Scale Macro-Prep High Q ion-exchange column (Bio-Rad, Hercules, CA) equilibrated with 20 mM Tris pH 8.0, 25 mM NaCl, 1 mM EDTA, and αS was eluted using 20 mM Tris pH 8.0, 1 M NaCl, 1 mM EDTA. Pure fractions were collected, buffer exchanged to Milli-Q water using Amicon ultra 3K filters(MilliPoreSigma, Burlington, MA), before lyophilizing and storing the dried protein at -80 °C.

3.2.2 Aggregation Kinetics Measurement

Aggregation Kinetics were measured according to a previously described protocol[174]. Briefly, 100 μM αS solutions (250 μL, with or without ligands) were prepared in phosphate buffer saline (PBS, 137 mM NaCl, 2.7 mM KCl, 8 mM Na2HPO4, 2 mM KH2PO4, pH 7.3). The solutions were placed in a ThermoMixer (Eppendorf, Hamberg, Germany) at 37 °C with constant shaking at 1300 rpm (rpm). At different time points, 5 μL aliquots of each αS solution were added to 95 μL PBS containing 50 μM Thioflavin T (ThT) dye in a Costar black 96 well plate (Corning Inc., Kennebunk, ME). ThT fluorescence intensity was measured (λ_{ex} = 450 nm and λem = 490 nm) on an Infinite M200PRO plate reader (Tecan, Männedorf, Switzerland), and plotted against time to give a sigmoidal curve typical of amyloid aggregation. For the single point ThT aggregation,

100 μM αS, in the absence and presence of ligands, was aggregated under the described conditions and the ThT fluorescence was reported at 96 h. The reported ThT intensity values are the average of each experiment conducted in triplicate, with the error bars representing the standard deviations or standard error of the mean (sem) as described in the main manuscript.

3.2.3 Spin-down assay

An αS solution (100 μM) was prepared in PBS with or without ligands and shaken (13,000 rpm, 37 °C) until the fluorescence plateaued, as observed using the ThT aggregation assay, indicative of the aggregation of αS as a control. The solutions were separated into soluble and insoluble fractions by centrifugation at 22,000 × g for 20 min. The fractions were diluted in 2×Laemmli protein sample loading buffer (Bio-rad, Hercules, CA), boiled at 95 °C for 5 min, and ran on a 12 % Mini-PROTEAN precast protein gel (Bio-rad, Hercules, CA). The gel was visualized using ChemiDoc MP Imaging System (Bio-rad, Hercules, CA) and band intensity was quantified using Image Lab image acquisition and analysis software (Bio-rad, Hercules, CA). Densitometry values were averaged from three technical replicates and reported with the error bars representing their standard deviations.

3.2.4 Transmission Electron Microscopy (TEM)

Transmission Electron Microscopy was used to visualize protein assemblies after aggregation experiments as previously described[174]. Briefly, aliquots (5 μL) of αS solutions (with or without ligands) were applied on glow- discharged carbon-coated 300-mesh copper grids for 2 min and dried using Kimwipes (Kimberly-Clark, Irving, TX). The copper grids were negatively stained for 1 min with uranyl acetate (0.75 %,

w/v). The micrographs were taken on an FEI Tecnai G2 Biotwin TEM at 80 kV accelerating voltages.

3.2.5 Isothermal Titration Calorimetry (ITC)

The ITC experiments were performed in a NANO-ITC (TA Instruments, New Castle, DE). For each ITC experiment, a solution of 250 μM NS132 in PBS was serially titrated (2 μL injections every 10 sec via rotary syringe, stirring speed at 300 rpm) into a sample cell containing 350 μL of 15 μM αS in the same buffer conditions at 300 sec intervals. The heat associated with each injection was calculated by integrating each heat burst curve using NanoAnalyze software (TA Instruments, New Castle, DE). The associated heat for each injection of NS132 in αS solution was corrected by subtracting heat resulting from the titration of NS132 into buffer (in 1 × PBS) under identical conditions. The corrected heat values were plotted as a function of the molar ratio of NS132 to αS and the plot was fitted using a one binding site independent model available in NanoAnalyze software. The fitting was carried out using 10,000 iterations in the software without any data constraints during the fitting. The ITC titrations were conducted in triplicate and the reported thermodynamic parameters were calculated as an average of three independent experiments.

3.2.6 Protein Misfolding Cyclic Amplification Assay (PMCA)

The PMCA assay was performed according to a previously described protocol[174]. Briefly, an αS solution (100 μM) was prepared in PBS and 60 μL of the solution was placed in a 200 μL Polymerase Chain Reaction (PCR) tube and the mixture was subjected to five 24 h cycles of 1 min shaking (1200 rpm) and 29 min incubation at 37

°C. Every 24 h, 1 µL of αS solution was passaged to seed 60 µL of fresh soluble monomeric αS solution. The seeding cycle was repeated for five days, after which the ThT signal was measured for all five passages. For the preparation of PMCA samples of αS in the presence of NS132, a molar ratio of 1:1 (αS:NS132) was maintained. All experiments were performed in triplicate. The reported ThT intensity values are the average of three separate experiments with the error bars representing the standard deviations.

3.2.7 Proteinase K Digestion of PMCA Samples

A Protease K (PK) solution at 50 µg/mL (IBI Scientific, Dubuque, IA) in digestion buffer (10 mM Tris, pH 8.0, 2 mM CaCl2) was diluted (0.1 eq.) into 30 µL of PMCA solution (with or without NS132) and incubated for 30 min at 37 °C. Subsequently, the samples were diluted (1:1, v/v) in SDS Protein Gel Loading Dye (2 ×) (Quality Biological, Gaithersburg, MD) and loaded on Mini-PROTEAN TGX Stain-Free Protein Gel (BioRad, Hercules, CA). The gel was stained using the Fairbanks staining method and imaged using ChemiDoc MP (BioRad, Hercules, CA).

3.2.8 Parallel Artificial Membrane Permeability Assay (PAMPA)

The permeability of various ligands was assessed with a PAMPA kit (BioAssay Systems, Hayward, CA) according to manufacturer's instructions. Briefly, 4 % lecithin solution (LS) was prepared in dodecane and 5 µL was applied to the donor plate membrane. Then, 300 µL PBS was added to the acceptor plate. Subsequently, 200 µL of ligand solutions (500 µM) and various permeability standards (high, medium, and low,

$$P_e = C \times -\ln\left(1 - \frac{OD_A}{OD_E}\right) \text{ cm/s}$$

500 μM) were added to the donor plate membrane. The donor plate was placed in the acceptor plate and incubated at r.t. for 16 h. The solutions were then moved from the acceptor plate into a clear-bottom 96-well plate (Corning Inc., Corning, NY) and absorbance was recorded at 360 nm for various ligands and 275 nm for permeability standards. The permeability was calculated using Eq. 1 below, where the permeability rate, *C,* equals 7.72×10^{-6}, *ODA* is the absorbance of the acceptor solution, and *ODE* is the absorbance of the equilibrium standard.

3.2.9 Heteronuclear Single Quantum Coherence (HSQC) NMR Spectroscopy

A solution of ^{15}N αS was prepared by resuspending 1 mg of uniformly labeled ^{15}N αS (rpeptide, Bogart, GA) in 1 mL Milli-Q water to yield a 70 μM αS solution in 20 mM Tris-HCl pH 7.4, 100 mM NaCl. The protein was buffer exchanged to Milli-Q water, lyophilized, and stored at -80 °C. For the preparation of NMR experiments, the lyophilized ^{15}N αS powder was dissolved in the NMR buffer (300μL, 20 mM NaPO pH 6.4, 5% D2O, v/v) to make a final concentration of 70 μM. The protein concentration was confirmed with a NanoDrop One (Thermo Scientific, Waltham, MA) at 280 nm using an extinction coefficient of 5960 $M^{-1}cm^{-1}$. The solutions were transferred into Shigemi BMS-005 NMR tube (Shigemi, Tokyo, Japan) and the two-dimensional ^{1}H-^{15}N HSQC NMR experiments were performed on a 600 MHz Bruker Avance Neo (CU Anschutz, NMR core facility, CO) instrument equipped with a triple resonance HCN cryoprobe. Data was collected at 12 °C on Topspin 4.9.0 software (Bruker, Billerica, MA). The HSQC spectra were recorded using a data matrix consisting of 1024 (t_2, ^{1}H) × 160 (t_1,

^{15}N) complex points. Resonance assignments were determined utilizing a previous publication[136] and the data analysis was performed using MestReNova software.

For the HSQC experiments titrating NS132 into ^{15}N αS, the same experimental conditions were used as above. Incrementally, NS132 was added to a single ^{15}N αS solution, mixed, kept at r.t. for 10 min and HSQC was recorded under the conditions stated above. For HSQC experiments containing pre-formed fibrils (PFF) of αS, 5.4 eq. of PFF solution (500 μM) was added to monomeric ^{15}N αS solution, and the spectra were recorded as previously stated.

3.2.10 Preparation of Lipofectamine solution

The Lipofectamine solution was made fresh for each transfection to avoid possible denaturation of reagents in a stored stock solution. For each transfection protocol, the total volume of lipofectamine solution required is equivalent to 30 % of the total volume of αS/lipofectamine solution needed. The solution was made by mixing OptiMEM media (Thermo Fisher Scientific, Waltham, MA), Lipofectamine, and P3000 reagents (Invitrogen, Carlsbad, CA) at a ratio of 50:1:1 (v/v/v), homogenized, and incubated at r.t. for 20 min. To prepare a 5 μM αS/Lipofectamine solution, 250 μL of an aggregated solution of αS (100 μM) was diluted with OptiMEM to a final volume of 3.5 mL and sonicated for 10 min. Subsequently, the Lipofectamine solution (1.5 mL) was combined with the αS protein solution for a total volume of 5 mL. The resulting solution (5 μM) was homogenized and added into their respective wells for transfection of cells.

3.2.11 MTT Assay

This assay was performed based on a previous protocol with slight modifications[174]. Unless stated otherwise, the density of Human Embryonic Kidney (HEK) cells (Generous gift by Prof. Mark Diamond' lab) expressing αSA53T- YFP was 150,000 cells/mL for each experiment. The HEK cells were plated (100 µL/ well) and incubated (24 h, 37 °C, 5% CO2) in a Costar 96-well transparent plate (Corning, Kennebunk, ME) with complete DMEM (Thermo Fisher Scientific, Waltham, MA) supplemented with 10% FBS (Hyclone, Logan, UT) media containing 1% penicillin/streptomycin (Life Technologies Corporation, Grand Island, NY). The cell solution was replaced with OptiMEM (Life Technologies Co., Grand Island, NY) containing an αS aggregated solution in the absence and presence of NS132 at an equimolar ratio, containing the lipofectamine solution. A solution of MTT dye (10 µL, 5 mg/mL in PBS) was added to each well and the plate was covered with aluminum foil and incubated for 3 h. Afterward, the solution was carefully aspirated out without disturbing the formazan crystals, and replaced with DMSO (100 µL/well). The crystals were dissolved with gentle shaking of the plate, and subsequently, the absorbance was measured at 570 nm using an Infinite M200 Pro Plate Reader (Tecan, Grŏdig, Austria). For all MTT assays, four biological replicates were performed and each biological assay consisted of four technical replicates.

3.2.12 ProteoStat-Dye Assay

HEK cells (αSA53T-YFP) were plated in 35 mm dishes (Celltreat, Pepperell, MA) with a density of 300,000 cells/dish. The cells were then transfected with αS fibrils (aggregated in the absence and presence of NS132 at an equal molar ratio) using

lipofectamine and incubated for 24 h. The Petri dishes were checked for puncta using an Axio Observer Microscope (Carl Zeiss Microscopy, Göttingen, Germany) before measuring intracellular aggregation using the PROTEOSTAT Protein Aggregation Assay Kit (Enzolifesciences, Farmingdale, NY). The media containing dead cells was then transferred into 15 mL Falcon tubes (Corning Science Mexico, Tamaulipas, Mexico). Subsequently, a solution of Detachin (Genlantis, San Diego, CA) was added to detach the live cells, which were then transferred into their respective 15 mL Falcon tubes. After the cells were transferred, the solution was centrifuged for 10 min, and the detachin was aspirated out and replaced with 500 µL PBS. The resulting cell pellets were then homogenized, transferred into an autoclaved 1.7 mL microcentrifuge tube, and counted to normalize the data. The microcentrifuge tubes were then centrifuged for 5 min at 4000 rpm and 4 °C (unless stated otherwise, centrifugation parameters remained the same throughout the assay). The process was repeated two more times with 500 µL PBS to properly wash the cell pellets and remove any excess of detachin or FBS media. The cells were treated with 4% paraformaldehyde (Electron Microscopy Sciences, Hatfield, PA), homogenized, and incubated on ice for 30 min. The tubes were then centrifuged for 5 min, the paraformaldehyde solution was replaced with 100 µL PBS, and centrifuged for another 5 min. The 100 µL PBS was replaced with 500 µL PBS containing 0.15% (v/v) Triton X-100 (Oakwood Chemical, Estill, SC), homogenized, and incubated on ice for 20 min. The tubes were then centrifuged again, and the supernatant was replaced with 100 µL PBS. Following another round of centrifugation, the supernatant was replaced with 375 µL PBS containing the ProteoStat buffer (10%, v/v) and ProteoStat Dye (1%, v/v), according to the manufacturer's guidelines. The cell solutions were homogenized,

protected from ambient light, and incubated at r.t. for 20 min. The tubes were centrifuged, and the dye solution was replaced with 400 μL PBS. The cell solution was homogenized and equally aliquoted into the desired number of wells in a Costar 96-well flat black plate and fluorescence was measured (λ_{ex} = 550 nm, λem = 600 nm) on an Infinite M200 ProPlate Reader. For each condition, four biological replicates were performed, each consisting of three technical replicates.

3.2.13 Immunofluorescence staining and confocal imaging

The HEK cells were plated (300 μL/well) in a μ-slide 8-well plate (Ibidi, Gräfelfing, Germany) and incubated (24 h at 37 °C and 5% CO2). The cells were then transfected with αS fibrils aggregated in the absence and presence of NS132, using lipofectamine and incubated for 24 h as previously described. The transfection was confirmed by the appearance of puncta within the plated cells using an Axio Observer microscope. The cells were then fixed with 4% paraformaldehyde for 10 min and subsequently washed with PBS (3×). The paraformaldehyde was then replaced with PBS containing 0.15% Triton X-100 for 10 min and washed with PBS (3×). A PBS solution containing 1% (w/v) BSA (Thermo-Fischer Scientific, Rockford, IL) and 0.1% (v/v) Tween-20 (Sigma-Aldrich, St. Louis, MO) was added and incubated at r.t. for an additional 30 min then washed with PBS (3×). Next, the cells were stained with anti-α-Synuclein Phospho Ser129 (phosphorylated αS at serine residue 129) mouse antibody (BioLegend, San Diego, CA) for 1 h and washed with PBS (3×). The cells were then treated with Donkey anti-mouse tagged with Alexa Fluor Plus 647 secondary antibody (Invitrogen, Rockford, IL) for 1 h and washed with PBS (3×). Lastly, the cell nuclei were stained with DAPI (Cayman Chemical Company, Ann Arbor, MI) for 10 min

and washed with PBS (2×). Confocal imaging was conducted on an Olympus Fluoview (FV3000 confocal/2-photon microscope). The images produced by the confocal microscope were analyzed on OlympusViewer in ImageJ processing software.

3.2.14 Culture methods for *C. elegans* strains

The N2 (wild-type *C. elegans* Bristol strain), NL5901 (*C. elegans* model of PD), and *Escherichia coli* OP50 (*E. coli*, a uracil requiring mutant) strains were obtained from Caenorhabditis Genomics Center (Minneapolis, MN). UA196 strains ([sid-1(pk3321);baIn33(Pdat-1::sid-1,Pmyo-2::mCherry);(Pdat-1::a-syn, Pdat-1::GFP)]) was generously donated by the laboratory of Dr. Guy Caldwell (Department of Biological Science, The University of Alabama, Tuscaloosa, AL, United States)[182]. The worms were maintained at standard conditions on nematode growth media (NGM) agar in 60 mm plates (CytoOne, Ocala, FL) using *E. coli* OP50 as the food source. NGM agar plates, M9 buffer (3 g KH2PO4, 6 g Na2HPO4, 5 g NaCl, 1 mL 1 M MgSO4, milli-Q H2O to 1 L), Chemotaxis (CTX) media plates (2% Agar, 5 mM KH2PO4, 1 mM CaCl2, and 1 mM MgSO4), CTX buffer (5 mM KH2PO4, 1 mM CaCl2, and 1 mM MgSO4) and OP50 solution at 0.5 OD600nm were prepared using previous protocols.

3.2.15 Motility assay for *C. elegans* (N2, NL5901 and UA196)

The motility assay was conducted based on previously described protocols with slight modifications[174]. On day one, N2 and NL5901 strains were synchronized using the bleaching process, involving egglay and incubation of the eggs (23 °C, 30 h) on a solution of NGM in 60 mm culture plates (CytoOne, Ocala, FL) with OP50 (350 µL, 0.5 OD600nm) as a food source. On day two, the worms were transferred (using M9 buffer) to 35 mm NGM plates (CellTreat Scientific, Pepperell, MA) containing 75 µM

Fluorodeoxyuridine (FUDR; to prevent worm reproduction and ensure that equal ages of worms were used for the experiment) and ligand (NS132 and NS163, 50 μM) and incubated at r.t. for 24 h (up to day four). On day three, fresh stock of OP50 was prepared by diluting 1 μL of OP50 in 5 mL of LB Miller media (Neogen, Lansing, MI) and incubated in a shaking incubator (Eppendorf, Hamburg, Germany) at 37 °C and 200 rpm for ~ 24 h. On day four, liquid media was prepared with 67.28 % (v/v) of M9 buffer, 0.018 % (75 μM) of FUDR solution (v/v), 0.1 % of 1 M magnesium sulfate (v/v), 0.1 % of 1 M calcium chloride (v/v), 2.5 % of 1 M potassium phosphate solution (pH 6, v/v), and 30% of 0.5 OD_{600nm} OP50 (v/v). The experiment was carried out using a sterile 24 well plate (CellTreat Scientific, Pepperell, MA) containing liquid media (500 μL/well). The three conditions included: (1) N2 worms (positive control), (2) NL5901 worms (untreated, negative control) and (3) NL5901 worms treated with the ligands (50 μM NS132 and NS163). A total of 50 worms per well were manually transferred into a 24 well plate and incubated at r.t. for 24 h. On day four, before conducting each motility assay, the 24 well plate was mechanically tapped for about 30 sec to make the worms more active in the liquid media. The assay was started on day four where 20 activity scores per well were collected using the WMicroTracker ARENA plate reader (Phylumtech, Santa Fe, Argentina) at 23 °C for 1 h per day over a 14-day period. For each condition, four biological replicates were performed and each biological replicate consisted of two technical replicates. For each condition, the data were expressed as mean and the error bars report the s.e.m. (n = 4 independent experiments and each n consisted of a minimum of two technical replicates). The motility rate experiment was

repeated for the UA196 strain (in the absence and presence of NS132 and NS163 at 50 μM) following the same conditions and protocol as used for the NL5901 strain.

3.2.16 Motility assay for *C. elegans* in the presence of dopamine and ligands

The motility assay was conducted for UA196 and N2 worms in the absence and presence of Dopamine (2 mM, treated on day two) and ligand (50 μM NS163, treated on day two) using the previous protocols[174]. The six worm conditions for this experiment included: (1,2) N2 in the absence and presence of Dopamine (2 mM), (3) UA196 (negative untreated control), (4) UA196 treated with 2 mM Dopamine, (5) UA196 treated with ligand (50 μM NS163), and (6) UA196 treated with both Dopamine (2 mM) and ligand (50 μM NS163). The worms were treated with NS163 and/or dopamine on day two and the motility assay was conducted as described in the previous section 3.2.17 Confocal microscopy of early stage treated *C. elegans* with ligands

The NL5901 worms in the absence and presence of ligands (50 μM NS132 or NS163 treated on day two) were used for this experiment under conditions identical to the motility assay. At least 10 worms per condition were transferred to a cover slide containing an anesthetic (40 mM sodium azide), and mounted on a glass microscope slide containing 2 % agarose pads for imaging. The images of the worms were collected using an Olympus Fluoview FV3000 confocal/2-photon microscope (40 x Plan-Apo/1.3 NA objective with DIC capability) from day five through day nine (for NL5901 strain) and processed using the OlympusViewer in ImageJ software. The inclusions of aggregated αS (in the muscle cells of NL5901 strain) were manually counted (10 worms per condition) for the five-day imaging period. For UA196 strain, the confocal imaging of the worms was conducted on day 3, day 5, day 10, and day 15. For each condition, three biological

replicates were performed and at least 10 technical replicates were used for each biological replicate. The data were expressed as mean and the error bars report the s.e.m. (n = 3 or 4 independent experiments and each n consisted of a minimum of ten technical replicates).

3.2.18 Confocal imaging of a post-disease onset PD model of UA196 worms

The UA196 worms were synchronized by bleaching and transferred into FUDR plates as described in the previous section. For this experiment, the UA196 worms were treated with 50 µM ligands (NS132 or NS163) on day five and then incubated at r.t. Confocal imaging was performed with worms immediately prior to treatment with the ligand on day five. The confocal imaging of UA196 worms was then performed on day 10 and day 15 in the absence and presence of ligands. For each condition, three biological replicates were performed and at least 10 technical replicates were used for each biological replicate. The data were expressed as mean and the error bars report the s.e.m. (n = 3 or 4 independent experiments and each n consisted of a minimum of ten technical replicates).

3.2.19 Chemotaxis Assay for *C. elegans* in the presence of ligands

The assay was performed in CTX solid media 35 mm plates (CellTreat Scientific, Pepperell, MA). The UA196 (treated and untreated with 50 µM ligands on day two) and N2 worms were prepared similar to the motility assay conditions as described above. Three CTX 35 mm plates (for the N2, treated and untreated UA196 strains) were divided into four equal quadrants designated A and C (the left diagonal quadrant), B and D (the right diagonal quadrant). A solution of *E coli* (attractant) was placed at ~ 0.4 cm from the

edge of quadrants B and D and ethanol (10 µL, repellant) was placed at ~ 0.4 cm from the edge of quadrants A and C. The solutions in the quadrants were allowed to dry for about 1 h at r.t. to develop the gradient. CTX buffer (1 mL) was used to transfer adult worms from the 35 mm plates (in the absence and presence of ligands) for each condition in sterile 1.7 mL microcentrifuge tubes (Eppendorf, Hamburg, Germany). The worm solution was centrifuged for 10 sec using a mini-Vortex mixer (VWR, China) to allow the worm pellets to settle at the bottom of the microcentrifuge tubes. The supernatant solution was aspirated out and replaced with CTX buffer. This buffer exchange step was conducted three times to ensure that the worms are re-suspended in only 100 µL of CTX buffer. After homogenizing the worm solution, 10 µL of the worm solution was transferred into a blank solid media 35 mm plate and the number of worms were counted under an Olympus microscope (SZ- 6145, Waltham, MA) in triplicate. A worm suspension was then prepared with the CTX buffer containing 50 worms/10 µL. Approximately 50 worms were transferred to the center of the CTX plate, and the lids were covered with parafilm (Bemis Company, Inc., Neenah, WI). Subsequently, the worm activity was monitored using a WMicroTracker ARENA plate reader (Phylumtech, Santa Fe, Argentina) at ~23 °C for 2 h. The report was generated using MapPlot option on the plate reader. Three biological replicates of this experiment were performed. The experiment was conducted for the UA196 worms (in the absence and presence of ligands) and N2 worms on day three and day 10 of the aging process. For each condition, three biological replicates were performed and at least two technical replicates were used foreach biological replicate. The data were expressed as mean and the error bars report

the s.e.m. (n = 3 independent experiments and each n consisted of two technical replicates).

3.2.20 Measurement of the ROS level in UA196 worms

A fluorescent probe 2',7'-dichlorofluorescein diacetate (H2DCFDA) was used to measure the intracellular ROS based on previously established protocols with slight modifications[154]. The UA196 worms were synchronized and treated with ligands (NS163 and NS132, 50 μM) on day two as described in the previous sections. On day eight, the worms were transferred into 1.7 mL microcentrifuge tubes using M9 buffer (1 mL). The samples were centrifuged for 2 min at 2,500 rpm and 20 °C. Subsequently, 0.8 mL of the supernatant was discarded. After, homogenizing the worm pellet in the remaining solution, 10 μL of the suspension was placed onto a glass slide for counting using an Olympus microscope (SZ-6145, Waltham, MA) in triplicate. The worm solution was then diluted with M9 buffer to approximately 50 worms/10 μL. Each well of a Costar 96-well black plate (Corning, Kennebunk, ME) contained M9 buffer (40 μL), worm solution (10 μL), and H2DCFDA (50 μL, 50 μM in DMSO). For the vehicle, 50 μL of M9 buffer and50 μL of H2DCFDA reaction solution were placed in the wells (as a control). Subsequently, the Costar 96-well plate was gently shaken for 30 sec at r.t. and the fluorescence intensity was quantified (λ_{ex} = 485 nm and λ_{em} = 530 nm) at multiple time points (0 to 120 min) using the Infinite M200 Pro Plate Reader.

For confocal imaging, the same UA196 worms used for running the ROS quantification, were transferred into different 35 mm NGM plates, air-dried using the fume hood, and transferred to a cover slide containing an anesthetic (40 mM sodium

azide), and mounted on a glass microscope slide containing 2% agarose pads for imaging as described previously.[13] This experiment consisted of three biological replicates and each biological replicate consisted of three technical replicates. The data were expressed as mean and the error bars report the sd's (n = 3 independent experiments and each n consisted of three technical replicates).

3.2.21 Measurement of intracellular ROS in a post-disease onset PD model

The UA196 worms were synchronized by bleaching and transferred into FUDR treated plates as described in the previous sections. On day five, the quantification of ROS level was conducted as described in the previous section. Subsequently, the UA196 worms were treated with ligands (NS132 and NS163, 50 μM) on day five and then incubated at r.t. for three days. On day eight, the quantification of ROS level was carried out for UA196 worms in the absence and presence of ligands. This experiment consisted of one biological replicate and four technical replicates. This experiment consisted of three biological replicates and each biological replicate consisted of three technical replicates. The data were expressed as mean and the error bars report the sd's (n = 3 independent experiments and each n consisted of three technical replicates).

3.3 Results

3.3.1 Design and Synthesis of the 2D-FAST for OPs.

Foldamers with carboxylic acid functional groups as side chains have been shown to effectively modulate αS aggregation and they partly mimic the topography of OPs[183]. Also, OPs with a minimum of two side chains (in dipyridyls) have been shown to achieve moderate antagonist activity against protein aggregation[184]. Therefore, for the 2D-FAST,

we synthesized a library of dipyridyls with the carboxylic acid functional group as the first side chain and appended diverse chemical side chains on the second pyridyl position (Figure 3.0 B). The 2-chloro-6-methyl-3-nitropyridine was used as a precursor to synthesize the nitro *tert*-butyl protected carboxylic acid monopyridyl (NS41, Figure 3.0 e) using our novel chromatography free method. Subsequently, we synthesized the chloro-dipyridyl using a newly developed chromatography-free amide coupling in our lab (RD127, Figure 3.0 f,g, and Figure 3.2), which was used as a common precursor to synthesize a library of dipyridyls with diverse side chains using primary amines/thiols via a one-pot reaction (Figure 3.0 h). All reactions went to completion and a large number of dipyridyl products did not require column chromatography as the excess primary amines/thiols were evaporated on rotovap or lyophilizer. However, a few dipyridyls required column chromatography to separate them from the starting material side chains because of their very high boiling point (7 out of 21 dipyridyls required column, Figure 3.2) 3.3.2 Biophysical characterization of OPs against the aggregation of αS

The dipyridyl library was screened against the aggregation of 100 μM αS (in 1 × PBS buffer) at an equimolar ratio using Thioflavin T (ThT) dye-based aggregation assay (Figure 3.0 j). The screening led to the identification of NS55 as the most potent antagonist as it was able to completely suppress the aggregation of αS (Figure 3.3 a-d), reflected by a low ThT fluorescence signal. The inhibition of αS aggregation by NS55 was also confirmed by transmission electron microscopy (TEM) images, which show an abundance (Figure 3.3 e) and no (Figure 3.3 f) αS fibers in the absence and presence of NS55, respectively. Next, we used NS55 (dipyridyl) as a precursor to synthesize and generate a tripyridyl library because we have shown that tripyridyls are better antagonists

than dipyridyls for various amyloid proteins[184]. Surprisingly, all OP dimers synthesized using primary thiols were agonists of αS aggregation; therefore, we did not pursue primary thiols for the synthesis of tripyridyl. We used similar synthetic steps to generate tripyridyls as we used to generate dipyridyls (Figure 3.0 l-o, and Figure 3.0). All reactions went to completion and most of the tripyridyls products did not require column chromatography (6 out of 15 tripyridyls required column, Figure 3.2).

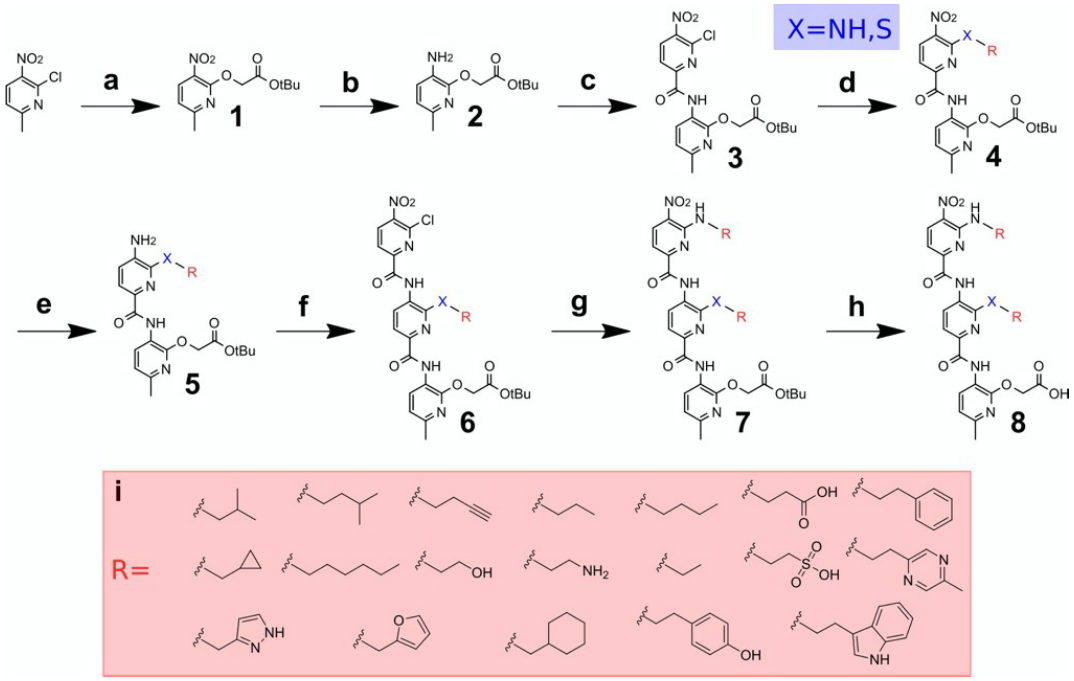

Figure 3.2 General Synthesis of Ops using 2D-FAST. **a**, *tert*-Butyl 2-hydroxyacetate, NaH (60% dispersion in mineral oil), toluene, 50 min at 0 °C, then 5 h at room temperature (r.t.) **b,e**, Palladium on activated carbon (Pd/C), H2 (g), ethyl acetate (EtOAc), 3 h at r.t. **c**, 6-chloro-5-nitropicolinic acid, dichloromethane (DCM, anhydrous), triethylamine (TEA), thionyl chloride 0 °C to r.t., 45 min. **d,g**, Primary amine/thiol, N,N- Diisopropylethylamine (DIPEA), DCM 3 h at r.t. **f**, TEA, 6-chloro-5-nitropicolinoyl chloride, THF (anhydrous) 0 °C to r.t., 40 min **h**, Triethylsilane (TES):trifluoroacetic acid (TFA) (1:1), DCM, 3-6 h at r.t. **i**, Chemical structures of various side chains appended on the dipyridyls and tripyridyls.

The screening of tripyridyls against αS aggregation at an equimolar ratio using ThT assay led to the identification of NS132 as the most potent antagonist (Figure 3.0 p, 2g-i). The absence of αS fibers in the presence of NS132 was also confirmed by TEM images (Figure 3.3 j,k). Both dipyridyl (NS55) and tripyridyl (NS132) were very effective inhibitors of αS aggregation at an equimolar ratio; however, NS132 was a far more effective antagonist than NS55 at a substoichiometric ratio of 1:0.5 (αS:ligand) and NS132 was almost equally effective at 1/5 of the conc. of NS55 in inhibiting the aggregation of αS (αS:ligand, Figure 3.3 l), reflected by SDS-PAGE (Sodium dodecyl sulphate– polyacrylamide gel electrophoresis) and ThT assay (Figure 3.4 a,b). For SDS-PAGE analysis, a solution of 100 μM αS was aggregated for four days in the absence and presence of NS55 and NS132 at various substoichiometric ratios (αS:ligand, 1:0.5, 1:0.1). Subsequently, the αS solutions were centrifuged to separate soluble and insoluble fractions, which were analyzed by SDS-PAGE (Figure 3.3 l). In the case of NS132, αS was predominantly detected in the soluble fraction at a substoichiometric ratio (αS:ligand, 1:0.5). In marked contrast, in the case of NS55, a significant amount of αS protein was found in the insoluble form (αS:ligand, 1:0.5). The soluble and insoluble amounts of αS were comparable when the concentration of NS132 was 5-fold less than NS55 (Figure 3.3 l). Collectively, both the ThT assay and SDS-PAGE analysis demonstrate that NS132 is a far better antagonist than NS55 of αS aggregation. These results highlight the validity of our 2D- FAST, where we were able to identify NS132 (tripyridyl) as a better antagonist than NS55 (dipyridyl) of αS aggregation.

To confirm that the side chains of NS132 are essential for its antagonist activity, we used various analogs of NS132 and compared their antagonist activity for αS

aggregation. The ThT signal of αS aggregation was decreased from 1.0 to 0.80, 0.30, and 0.07 in the presence of NS132-P (Protected COOH group), NS122 (Chloro side chain), and NS132 at an equimolar ratio, respectively (Figure 3.3 m-n). The SDS-PAGE analysis also validated the ThT results, suggesting that NS132-P was a poor antagonist of αS aggregation (Fig. 3.4 c-f). Collectively, both ThT assay and SDS-PAGE analysis demonstrate that NS132 is a far better antagonist than NS132- P and NS122 and the side chains are important for the antagonist activity of NS132 against αS aggregation. Under matching conditions of the ThT aggregation assay, we did not observe any significant quenching of the ThT fluorescence signal by NS132 (Figure 3.5). We also characterized the binding interaction between αS and NS132 using the isothermal calorimetry titration (ITC) (Figure 3.3 o). The ITC titration yielded the dissociation constant (K_d) of 1.81 ± 0.33 μM with a binding stoichiometry of 1:1 (αS:NS132). We utilized two-dimensional heteronuclear single quantum coherence NMR spectroscopy (2D NMR HSQC) to gain insights into the binding site of NS132 on αS. We collected the HSQC NMR of 70 μM ^{15}N-^{1}H-uniformly labeled αS in the absence (Figure 3.3 p, red) and presence of NS132 (Fig. 3.3 p, blue) and compared the signal intensity of the amide peaks. In the presence of NS132, we observed noticeable changes in the amide peaks for specific residues toward the N-terminus, indicative of the interaction and binding site of NS132 on αS, especially residues 10-20, 36-43, and 50,55,59 (Figure 3.3 q). The binding sites of NS132 have been suggested to be the essential sequences for αS aggregation and these sequences have been considered to be the potential therapeutic targets for the effective inhibition of αS aggregation and associated PD phenotypes[159]. Our study supports the hypothesis that the targeting of these sequences will effectively inhibit αS aggregation.

To confirm that NS132 did not generate fiber-competent cytotoxic structures during αS aggregation inhibition, we utilized a well-established model of HEK293 cells, which stably express YFP-labeled αS-A53T mutant (αS-A53T-YFP)[147]. The endogenous monomeric αS-A53T- YFP have been shown to template into fibers when transfected with exogenously added αS fibers in the presence of Lipofectamine 3000 (Figure 3.3 r,s). The aggregation of endogenous monomeric αS-A53T-YFP into fibers can be detected by the intracellular fluorescent puncta (Figure 3.3 r,s). A solution of 100 μM αS was aggregated in the absence and presence of NS132 at an equimolar ratio for four days. The resulting solutions of αS fibers (5 μM in monomeric αS, ±NS132) were introduced to HEK cells in the presence of Lipofectamine 3000 for 24 h. In contrast to the control (no fibers), we observed a significant number of fluorescent inclusions in the presence of αS fibers (Figure 3.3 r,s, white arrows, αS-A53T-YFP), which was a consequence of the templating of endogenous monomeric αS-A53T-YFP by the exogenously added αS fibers. The αS inclusions were localized in the cytoplasm of HEK cells as shown by others[147]. In addition, we also observed that the αS-pS-129 protein (Phosphorylated αS at residue 129) colocalized in the aggresome of αS inclusions in HEK cells (Figure 3.3 r, red). Moreover, we observed the colocalization of the autophagy adaptor protein, p62, in the aggresome of αS inclusions in HEK cells (Figure 3.3 s, red). The autophagy machinery regulates many vital cellular processes and its impairment due to αS aggregation can lead to PD and other neurodegenerative disorders[85]. In marked contrast, in HEK293 cells transfected with aS aggregated in the presence of NS132, there was a significant decrease in the intracellular αS-A53T-YFP inclusions (Figure 3.3 r, + αS+NS132). We also quantified the inclusions (αS-A53T-YFP) using a novel

ProteoStat dye-based high throughput 96-well plate reader-based assay recently developed in our lab[174]. The ProteoStat dye-based intensity of HEK cells treated with αS fibers was ~ 4-5 fold higher than the control (no fibers) (Fig. 3.3 t). In marked contrast, we did not observe a significant difference in the ProteoStat intensity of HEK cells treated with αS fibers+NS132 and the control conditions. Both proteins, including αS-pS-129 and p62 have been shown to be key pathological biomarkers for the formation of Lewy body like aggregates[165]. The presence of both proteins in the inclusions suggests that these inclusions mimic some features of Lewy-body like structures that are important events in inducing cytotoxicity in HEK cells. Therefore, we used HEK cells to test the cytotoxicity of the aggregated solution of αS in the absence and presence of NS132 (Figure 3.3 u). The viability of HEK cells was measured using the (3-(4,5-dimethylthiazol-2-yl)-2,5- diphenyltetrazolium bromide) (MTT) reduction based assay. The viability of HEK cells decreased to 52 % in the presence of the aggregated solution of αS; however, the viability of HEK cells was improved to 85% in the presence of the αS aggregated solution with an equimolar ratio of NS132 (Fig. 3.3 u). This data suggest that NS132 doesn't promote the formation of seed competent αS assemblies and the higer order aggresome.

3.3.3 Antagonist effect of OPs against fibers catalyzed aggregation of αS

In addition to the spontaneous accumulation of αS via *de novo* aggregation, another crucial mechanism for inducing pathology in PD is αS fibers catalyzed aggregation of αS[185]. Therefore, we monitored the effect of NS132 on the αS fibers catalyzed aggregation of αS. The aggregation of 100 μM αS monomer in the presence of preformed αS fibers (20%, monomer eq.) resulted in the acceleration of monomeric αS

aggregation, reflected by a significant increase in the ThT signal after 20 h (Fig. 3.6 a). The αS fibers catalyzed aggregation of αS was wholly suppressed by NS132 at an equimolar ratio as evidenced by significantly lower ThT signal (Fig. 3.6 a). The antagonist activity of NS132 was also assessed on more robust αS fibers generated using the protein misfolding cyclic amplification (PMCA). In the PMCA assay, the fibers of αS are amplified for five cycles using αS monomer and αS fibers from the previous cycle. The ThT intensity for αS aggregation via PMCA assay increases significantly after cycle two and the intensity stays consistent up to cycle five (Fig. 3.6 b, grey bar). Additionally, PMCA samples (from αS aggregation) from cycle three to cycle five were PK (proteinase K) resistant (Fig. 3.6 c, white arrow), which indicates these αS fibers are very robust and non-degradable after cycle three (Fig. 3.6 c). In marked contrast, in the presence of NS132 at an equimolar ratio, we did not observe any significant change in the ThT intensity up to cycle five (Fig. 3.6 b, orange bar). More importantly, the PMCA assay samples of αS aggregation in the presence of NS132 from cycle three to cycle five were completely degraded by PK treatment (Fig. 3.6 d, orange arrow). The data suggest that NS132 interacts with αS and generates off-pathway fiber-incompetent structures, which are easily degradable with PK treatment. To further validate that NS132 generates fiber incompetent structures from the fiber catalyzed aggregation, we utilized HEK cells that stably express αS-A53T- YFP. The solutions of αS aggregation in the absence and presence of NS132 from the PMCA cycle five (2 μM in monomeric αS, ±NS132) were introduced to the HEK cells in the presence of Lipofectamine 3000 for 24 h. In contrast to the control (no fibers) (Fig. 3.6 e, control), we observed a significant number of inclusions in the presence of αS fibers (Fig. 3.6 e, white arrows, αS-A53T- YFP). In

addition, we also observed the colocalization of αS-pS-129 in the aggresome of αS inclusions in HEK cells (Fig. 3e, αS-pS-129, red). In contrast, in the presence of the PMCA assay sample from cycle five (+NS132), there was a significant reduction in the number of αS inclusions (Fig. 3.6 e, +NS132). The ProteoStat intensity of inclusions in HEK cells treated with the PMCA sample from cycle five was ~ 2-3 fold higher than the control condition (no fibers) (Fig. 3.6 f). In marked contrast, we observed a significantly lower ProteoStat intensity in the presence of the PMCA sample from cycle five in the presence of NS132 (Fig. 3.6 f). Clearly, NS132 was a potent antagonist of the fibers catalyzed aggregation of αS and it generates fiber incompetent off-pathway structures.

We also employed 2D NMR HSQC for atomic-level insights into fibers catalyzed aggregation of αS and its inhibition by NS132. It has been suggested that the negatively charged flexible C- terminal tail of αS (in fibers) interacts and recruits the positively charged N-terminal segment of αS (in monomer) during the fibers catalyzed aggregation of αS (Fig. 3g)[186]. We have also shown that NS132 specifically interacts with the N-terminal residues of αS. Therefore, we hypothesize that NS132 will be able to inhibit the interaction of αS (monomer) with αS fibers, which is suggested to be the prerequisite interaction to initiate the seed-catalyzed aggregation of αS. We incubated preformed fibers of αS with 70 μM ^{15}N-^{1}H-uniformly labeled αS monomer and used HSQC NMR to characterize the kinetics of fibers catalyzed aggregation of αS on a molecular level. The total changes in the intensity of the amide peaks of ^{15}N αS monomer in the presence of αS fibers suggest that the binding interaction was predominantly toward the N-terminus of αS (Fig. 3.6 h,i); more specifically, αS fibers interact specifically with four αS sequences, including 3-23, 40- 45, 49-59, and 75-84 (Fig. 3.6 h,i). Also, there was an

induction of a secondary structure in the αS monomer, indicated by the spreading of the amide peaks toward the ^{1}H resonances (Fig. 3.6 i, green). At 40 h, more pronounced changes were observed in the location and intensity of the amide peaks of αS monomer, suggesting a much stronger interaction with αS fibers and further induction of a secondary structure in ^{15}N-^{1}H-αS monomer (Fig. 3.6 j). In marked contrast, no significant change in the amide peaks of ^{15}N-^{1}H-uniformly labeled αS monomer was observed in the presence of NS132 at an equimolar ratio (Fig. 3.6 k). Even after 40 h, there were fewer and smaller changes in the amide peaks of ^{15}N-^{1}H-uniformly labeled αS monomer in the presence of NS132 (Fig. 3.6 l). The NMR study suggests that NS132 inhibits the αS monomer-αS fibers interaction by potentially interacting at the N-terminal of αS. Clearly, NS132 is a potent inhibitor of fibers catalyzed aggregation of αS.

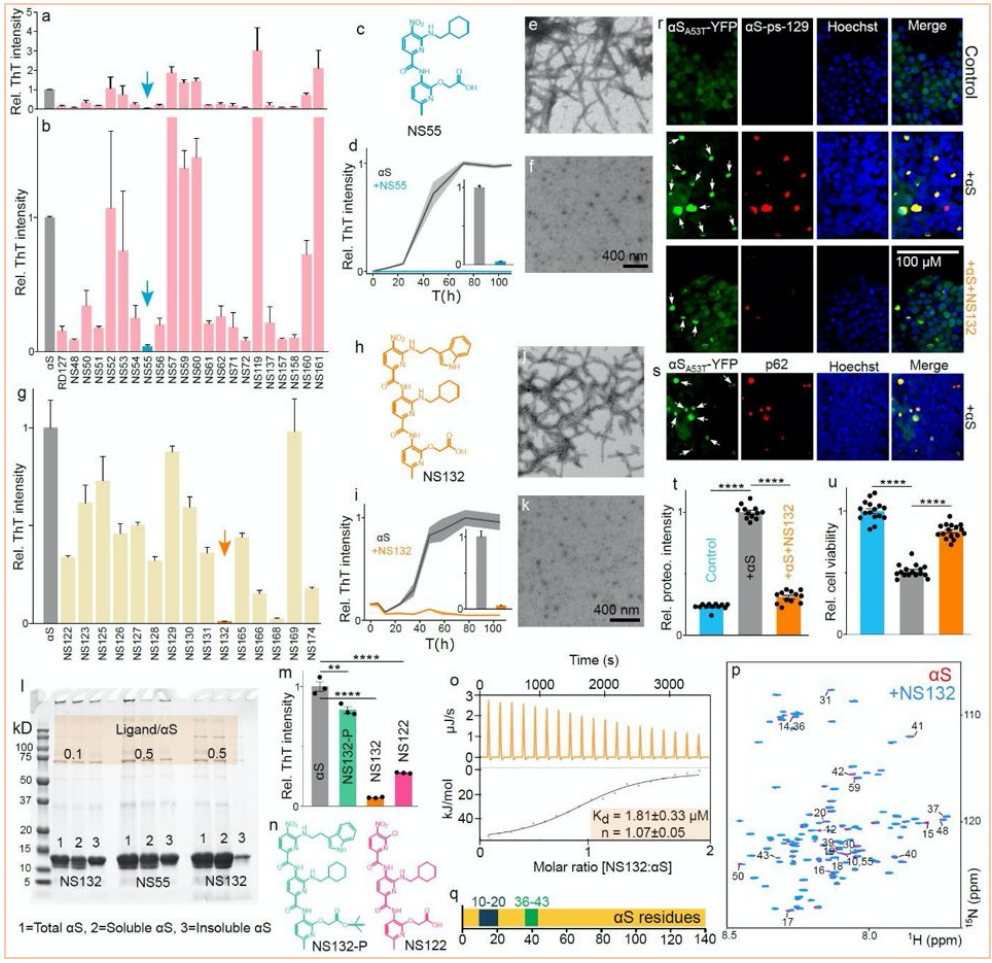

Figure 3.3 **a**, The graphical representation and zoom in version (**b**) of the ThT intensity of 100 μM αS aggregation for four days in the absence and presence of dipyridyls and tripyridyls (**g**) at an equimolar ratio. The arrow indicates the most potent antagonist of αS aggregation. **c**, The chemical structure of NS55 and NS163 (**h**). The aggregation profile (**d**) and TEM image of 100 μM αS in the absence (**e**) and presence (**f**) of NS55 at an equimolar ratio. (Inset) The ThT intensity of 100 μM αS aggregation after four days in the absence and presence of NS55 at an equimolar ratio. **i**, The aggregation profile and TEM image of 100 μM αS in the absence (**j**) and presence (**k**) of NS132 at an equimolar ratio. (Inset) The ThT intensity of 100 μM αS aggregation after four days in the absence and presence of NS132 at an equimolar ratio. **l**, SDS- PAGE gel analysis of 100 μM αS aggregation after four days in the absence and presence of NS55 and NS132 at the indicated molar ratios. **m**, The ThT intensity of 100 μM αS aggregation after four days in the absence and presence of the indicated ligands (chemical structures, **n**) at an equimolar ratio.**o**, The ITC thermogram for the titration of a solution of NS132 into αS where heat burst curves (upper panel) and the corrected injection heats (lower panel). **p**, Overlay of 2D HSQC (^{1}H, ^{15}N) NMR spectra of 70 μM uniformly ^{15}N-labelled αS in the absence (red) and presence (blue) of NS132 at an equimolar ratio. **q**, The potential binding site of

NS132 on αS, represented by blue and green boxes. **r,s**, Confocal images of HEK cells treated with the aggregated solution of 5 μM αS in the absence and presence of NS132 at an equimolar ratio. Inclusions of αSA53T-YFP = white arrows, Hoechst = blue, αS-ps-129 = red, p62 = red (**s**), merge = Hoechst, αS-ps-129, and αSA53T-YFP. **j**, Confocal images of HEK cells treated with the aggregated solution of 5 μM αS. Inclusions of αSA53T-YFP = white arrows, Hoechst = blue, p62 = red, merge = Hoechst, p62, and αSA53T-YFP. The relative intensity of Proteostat dye-stained aggregates of αSA53T-YFP inclusions (**k**) and relative viability (**l**) of HEK cells treated with the aggregated solution of 5 μM αS in the absence and presence of NS132 at an equimolar ratio. The ThT experiments were conducted three times and the reported change in the ThT intensity was an average of three separate experiments. The cell viability or Proteostat assays were conducted with at least four biological replicates and four technical replicates for each biological replicate. The data were expressed as mean and the error bars report the s.e.m. (n = 3 to 4 independent experiments and each n consisted of three technical replicates). The statistical analysis was performed using ANOVA with Tukey's multiple comparison test. *$p < 0.05$, **$p < 0.01$, ***$p < 0.001$.

3.3.4 Effect of OPs on intracellular αS aggregation in a *C. elegans* PD model.

Next, we investigated the antagonist activity of NS132 against αS aggregation in a well-established *C. elegans* PD model. The *C. elegans* models have been extensively used to study the underlying mechanisms and therapeutic interventions for neurodegenerative diseases associated with protein aggregation because of the short lifespan (2-3 weeks), tractability to genetic manipulation, distinctive behavioral and neuropathological defects, and high degree of genetic relevance compared to humans. We utilized NL5901 worms, which express αS-fused yellow fluorescent protein (αS-YFP) in the body wall muscle cells[174]. The PD phenotypic readouts in the NL5901 worms include a gradual increase in inclusions (αS-YFP) in body wall muscle cells and a decline in motility during the aging of the worms . To act as a potent antagonist of aS aggregation in *C. elegans* model, NS132 should permeate the cell membrane of the body wall muscle cells of *C. elegans*. We used the parallel artificial membrane permeation assay (PAMPA) to test the cell permeability of NS132 and compare it with various

PAMPA standards of cell permeabilities (Fig.3.7 a). The cell permeability of NS132 was lower in comparison to the PAMPA medium standard (Fig. 3.7 a), which was most likely a consequence of the COOH functional group. We have also shown that COOH is a very important side chain for the antagonist activity of NS132 against αS aggregation (NS132 vs NS132-P). We surmise that we may underachieve the overall antagonist effect of NS132 against αS aggregation in *C. elegans* due to its less than moderate cell permeability. Therefore, to enhance the cell permeability without sacrificing the antagonist activity of NS132, we synthetically replaced the carboxylic acid with hydroxamic acid (NS163, Fig. 3.7 a,b), which is considered to be one of the most common and successful carboxylic acid isosteres in the pharmaceutical industry and has shown higher cell permeability than the former[64]. The cell permeability of the hydroxamic acid analog (NS163) was higher than NS132 (Fig. 3.7 a,b). NS163, similar to NS132, was a potent antagonist of αS aggregation, confirmed by ThT assay (Fig. 3.7 c) and TEM images (Fig. 3.8). Clearly, the PAMPA assay, ThT assay, and TEM demonstrate that we have improved the cell permeability of NS132 without sacrificing the antagonist activity against αS aggregation. Subsequently, we tested the antagonist activity of NS163 against αS aggregation-mediated PD phenotypes in NL5901 worms. The NL5901 worms were treated with 50 μM NS163 on day two, followed by incubation at r.t. for one day before assessing the effect of NS163 on PD phenotypes. We observed a gradual increase in the number of inclusions from day five (~15 inclusions/worms) to day eight (~34 inclusions/worms) and a slight decrease on day nine (~32 inclusions/worms), suggesting a saturation in the number of inclusions after day eight in the animals (Fig. 3.7 d,e, white arrow). In marked contrast, there was a substantial decline in the number of

inclusions in the presence of NS163 from day five (~4 inclusions/worms) to day nine (~2 inclusions/worms) (Fig. 3.7 d,g). We also observed a decrease in the number of inclusions in the presence of NS132 (lower effect than NS163), despite its lower cell permeability (Fig. 3.7 d,f). As we predicted earlier, the cell permeability of NS132 was lower than NS163, which is the likely reason for the lower effect of NS132 (Fig. 3.7 d,f). The motility rate of the NL5901 worms decreases during the aging process due to an increase in αS aggregation, which impairs the muscle cells. We utilized the WMicroTracker ARENA plate reader to measure the motility rate of NL5901 worms in the absence and presence of NS163[166]. We observed a significant decline in the activity of NL5901 worms in comparison to the control worms (N2, healthy *C. elegans* strain) (Fig. 3.7 h,i). In marked contrast, the NL5901 worms treated with NS163 on day two resulted in a significant improvement in the motility rate (Fig. 3.7 h,i). The *C. elegans*-based study suggests that NS163 permeates the body wall muscle cell membrane of the worms and inhibits αS aggregation. NS132 also demonstrated an increase in the motility rate of NL5901 worms, albeit with a less pronounced effect than NS163 (Fig. 3.9).

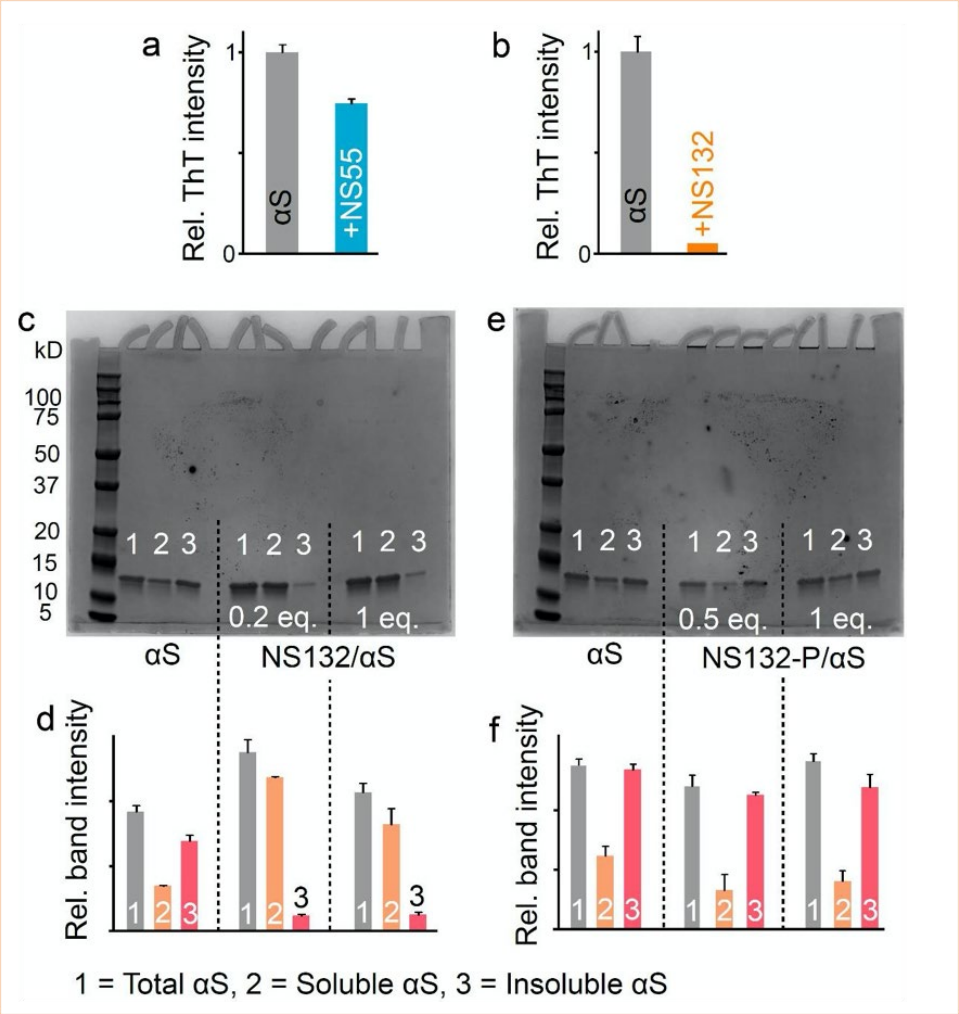

Figure 3.4 **a**, The graphical representation of the ThT intensity of 100 µM αS aggregation for four days in the absence and presence of NS55 (**a**) and NS132 (**b**) in 1 × PBS at substoichiometric ratio (for NS55, αS:ligand, 1:0.5, and for NS132, αS:ligand, 1:0.1,). **c**, Representative SDS-PAGE gel images and band intensities of 100 µM αS aggregation for four days in the absence and presence of NS132 (**c,d**) and NS132-P (**e,f**) at the indicated molar ratios. The ThT experiments were conducted three times and the reported change in the ThT intensity was an average of three separate experiments. The gel shift assay experiments were conducted three times and the reported intensity changes were an average of three separate experiments. The data were expressed as mean and the error bars report the standard deviation (s.d.) (n = 3 independent experiments and each n consisted of three technical replicates).

3.3.5 Effect of OPs on the degeneration of DA neurons in a *C. elegans* PD model

The aggregation of αS is associated with the neurodegeneration of DA neurons, which is a pathological hallmark of PD. We have also shown that NS163 rescues αS aggregation-mediated PD phenotypes in the body wall muscle cells of *C. elegans* worms. Next, we investigated the neuroprotective effect of NS163 on αS aggregation-mediated degeneration of DA neurons in a well-established *C. elegans* PD model (UA196)[187]. The UA196 worms express both human αS and GFP in DA neurons under the control of the dopamine promoter genotype (Pdat-1::GFP; Pdat-1::α-SYN). The expression and aggregation of αS in six DA neurons that are located within the anterior region of worms lead to progressive neurodegeneration characteristics during the aging of UA196 worms. This strain has been used to gain insights into the PD-associated mechanisms and to assess the neuroprotective effect of ligands against αS aggregation[188]. The DA neurons in UA196 worms degenerate from day three to day 15, represented by a gradual decline in the GFP fluorescence in DA neurons shown by others as well (Fig. 3.10 a-g)[188]. The number of DA neurons decreased from 6 (day three) to 1 (day 15) in UA196 worms (Fig. 3.10 b-g). In marked contrast, the % loss of six intact DA neurons in UA196 worms was 95%, 87%, and 78% on day five, 10, and 15, respectively, after treatment with 50 μM NS163 on day two (Fig. 3.10 h-k). The degeneration and subsequent loss of DA neurons is a consequence of αS aggregation during the aging of worms (Fig. 3.10 d-f). The % decline in the total DA neurons in UA196 worms was 72%, 36%, and 23% after five, 10, and 15 days, respectively (Fig. 3.10 k, blue). In contrast, in NS163 treated UA196 worms, the % loss of the total number of DA neurons was <5% even up to 15 days (Fig. 3.10 k, red). The data suggest a remarkable neuroprotective

effect of NS163 as a significant number of DA neurons were intact up to day 15 (Fig. 3.10 h-k). Other reported ligands were not able to achieve such a remarkable neuroprotective effect against αS aggregation mediated degeneration of DA neurons in *C. elegans* PD model even at 1 mM concentration[70]. Under matched conditions, NS132 also displayed a very good neuroprotective effect on the degeneration of DA neurons in UA196 worms, confirmed by confocal imaging (Fig 3.11 a-f). The neuroprotective effect of NS163 was better than NS132, indicated by a higher number of healthy neurons (Fig. 3.10 k, Fig. 3.11 f), most likely due to the former's better ability to permeate the cell membranes.

3.3.6 Effect of OPs on the motility rate of UA196 worms

The degeneration of DA neurons has been directly linked with the loss of motor functions resulting in slow motility rate[174]. Therefore, we assessed the motility rate of UA196 in the absence and presence of NS163 using WMicroTracker ARENA plate reader (Fig. 3.10 o,p). There was a significant decline in the motility rate of the UA196 worms (Fig. 3.10 o,p, blue) during the aging process in comparison to the control worms (Fig. 3.10 o,p, N2, green). In marked contrast, the motility rate of UA196 worms treated with 50 μM NS163 (day two) was significantly improved during the aging process. The improvement in the motility rate is likely due to the rescue of the degeneration of DA neurons by NS163. NS132 also displayed a neuroprotective effect; therefore, we also assessed its effect on the motility rate of UA196 worms. Under matched conditions to NS163, we observed a noticeable rescue of the motility rate of UA196 worms in the presence of NS132 during the aging process (Fig. 3.12). The effect of NS163 was better than NS132 in rescuing the motility rate of UA196 worms.

3.3.7 Effect of OPs on the ROS level in UA196 worms.

One of the causal agents associated with the etiology of PD is the generation of ROS, which oxidizes lipids, proteins, and DNA[188]. The neurodegeneration in UA196 worms due to αS aggregation leads to the production of intraworm ROS. The ROS level was determined using a fluorescent probe (CM-H2DCFDA), which reacts with intraworm ROS level in UA196 worms (day eight) and produces a green fluorescent signal, whose intensity increases up to 2 h (Fig. 3.13 a,c)[154]. In marked contrast, UA196 worms treated with 50 μM NS163 (on day two) displayed a significant decrease in the intracellular ROS level on day eight (Fig. 3.13 b,c). The signal intensity was very similar for the dye sample and UA196 worms treated with NS163 (Fig. 3.13 c). The data suggest that the decrease in the ROS level in UA196 worms in the presence of NS163 is a consequence of the rescue of degeneration of DA neurons. Similarly, in the presence of NS132, the ROS level was low in UA196 worms (Fig. 3.14 a). It has been shown earlier that the GFP signal in DA neurons does not interfere significantly with the detection of the ROS level by the green fluorescent dye because of the weak signal of the former in comparison to the later

3.3.8 Effect of OPs on Behavioral deficits in UA196 worms.

It has been shown that the lack of dopamine synthesis in DA neurons in *C. elegans* leads to behavioral deficits, like food sensing behavior[189]. The DA neurons in UA196 worms degenerate over time, which leads to a decrease in the amount of dopamine and NS163 rescues the degeneration of DA neurons. Therefore, we hypothesized that NS163 would be able to rescue behavioral deficits of UA196 worms. We used a chemotaxis assay to assess the effect of NS163 on the behavioral deficits of

UA196 worms. In this assay, a petri dish is divided into four quadrants where two opposite quadrants were treated with a toxic chemical (ethanol, repellent) or food (*E. coli*, movement deterrent) for worms[190]. For each experiment, 50 worms were placed at the center of the dish and ethanol (red dots) and *E. coli* (green dots) were placed at the polar ends of the petri dish (Fig. 3.13 e). We used the ARENA plate reader to measure the chemotaxis index (CI) over time with values from -1.0 to +1.0. The kinetics of the CI index over time was generated based on the time spent by worms in ethanol or *E. coli* quadrants. The kinetics of the CI over time was monitored on day three for 2 h for various worms, including N2 (Fig. 3.13 f), UA196 (Fig. 3.13 f), and UA196+50 μM NS163 (Fig. 3.13f). The kinetic data for the CI suggest that all the worms spent most of their time in the *E. coli* quadrants reflected by a value of ~1 during the course of 2h (Fig. 3.13 f). None of the worms displayed behavioral deficit on day three (Fig. 3.13 f). All the DA neurons in UA196 worms on day three were intact (Fig. 3.10 b,g,k); therefore, we anticipate a similar behavioral response of UA196 (Fig. 3.13 f) and N2 (Fig. 3.13 f) worms. In marked contrast, on day 10, the kinetics of the CI of UA196 did not display any preference for ethanol or *E. coli* for the whole time course of the experiment (Fig. 3.13 g,h, Movie S6). The lack of preference of UA196 worms is due to the behavioral deficits caused by the decrease in dopamine as a result of the degeneration of DA neurons. However, the UA196 worms treated with NS163 strongly favored *E. coli* (Fig. 3.13 g,i) than ethanol, similar to the control worms (Fig. 3.13 g,j, Movie S5), indicated by the chemotaxis indices. Clearly, NS163 was able to rescue the behavioral deficits of UA196. Similarly, NS132 was also able to rescue behavioral deficits in UA196 worms under the matched conditions to NS163 (Figure 3.15).

3.3.9 Effect of OPs on the dopamine level in UA196 worms

We have shown that a decrease in the motility rate in UA196 worms is a consequence of the loss of DA neurons, which is potentially associated with a substantial decrease in dopamine synthesis. Therefore, we hypothesized that the motility rate could be enhanced by administering dopamine in UA196 worms. The 2 mM dopamine treated UA196 worms displayed a much higher motility rate during the aging process (Fig. 3.13 l). In marked contrast, we did not observe any significant difference in the motility rate for 50 μM NS163 treated UA196 worms in the absence and presence of 2 mM dopamine (Fig. 3.13 m). We observed similar behavior for the N2 worms (to UA196+NS163) in the presence of 2 mM dopamine (Fig. 3.13 k). The data suggest that the improvement in the motility rate of the dopamine treated UA196 worms is the compensation for the decrease in the dopamine synthesis due to the loss of DA neurons. However, we did not observe any change in the motility rate for N2 and NS163 treated UA196 worms because of the intact DA neurons and dopamine synthesis.

3.3.10 Effect of OPs in a post-disease onset PD model.

NS163 had shown a remarkable neuroprotective effect against the degeneration of DA neurons in UA196 worms, when it was added on day two to UA196 worms. However, the effect of NS163 has not been tested in a post-disease onset PD model. For PD, most of the current therapeutic intervention strategies predominantly rely on the post-disease-onset model and the treatment occurs after the diagnosis of PD[191]. Also, during the post-disease onset of PD, the aggregation of αS is facilitated by multiple mechanisms, including the *de novo* αS aggregation, fibers catalyzed αS aggregation, and prion-like spread of αS fibers. Moreover, we have identified that NS163 is a potent

inhibitor of both the *de novo* (Fig. 3.3 g-m) and the fiber catalyzed αS aggregation (Figure 3.16). Therefore, we envision that NS163 will be effective in rescuing the degeneration of DA neurons in the post-disease onset model of PD in UA196 worms. We have already shown that the DA neuron loss in UA196 worms was 28%, 67%, and 78% after five, 10, and 15 days, respectively (Fig. 3.10 m,n). It has been suggested that ~30% neuronal loss or day four timepoint of adulthood (total five days) in *C. elegans* is considered a post-disease-onset PD model[191]. Therefore, we chose day five of the UA196 worms as the post-disease onset PD model, where 28% of the total DA neurons were degenerated (Fig. 3.10 m,n). The UA196 worms were treated with 50 μM NS163 on day five and the number of healthy DA neurons was counted on day 10 and day 15 (Fig. 5l-n). NS163 was very effective in rescuing the degeneration of DA neurons as we did not observe any further loss of DA neurons in the presence of NS163 (Fig. 3.10 l-n). The effect of NS163 was also tested on the intraworm ROS level in the post-disease model of *C. elegans*. The ROS level of UA196 worms was measured on day five, followed by the addition of 50 μM NS163 and the ROS level was assessed on day eight in the absence and presence of NS163 (Fig. 3.13 d). In UA196 worms, the ROS level increased from day five to day eight due to the increase in the degeneration of DA neurons mediated by αS aggregation (Fig. 3.13 d). However, the ROS level was significantly decreased in UA196 worms treated with NS163 (Fig. 3.13 d). Clearly NS163 is a potent ligand in rescuing degeneration of DA neurons (and ROS level) when added to a post-disease onset PD model. Similarly, NS132 was also effective (less than NS163) in rescuing degeneration of DA neurons in a post-disease onset PD model, characterized by confocal imaging and the number of healthy neurons (Fig. 3.17 a-h). Additionally, NS132 was also

very effective in decreasing the ROS level when added on day five to UA196 worms (Fig. 3.14 b). It is a remarkable finding that NS163 and NS132 are able to rescue PD phenotypes in a post-disease onset PD model. Most of the ligands reported in the literature rescue PD phenotypes when added in the early stages of PD models, which does not mimic the clinical landscape for the current therapeutic interventions that rely on the post-diagnosis of PD.

Our data suggest that NS163 and NS132 are potent inhibitors of αS aggregation both *in vitro* and *in vivo* models. NS163 and NS132 displayed potent efficacy to rescue PD phenotypes in a DA neuron *C. elegans* PD model, including degeneration of DA neurons, impaired motility rate, decreased dopamine synthesis, behavioral deficits, and increased ROS level. More importantly, OPs were very effective in rescuing PD phenotypes in a post-disease onset model. Overall, we have developed a novel technique to identify potent ligands with tremendous therapeutic potential for the treatment of PD.

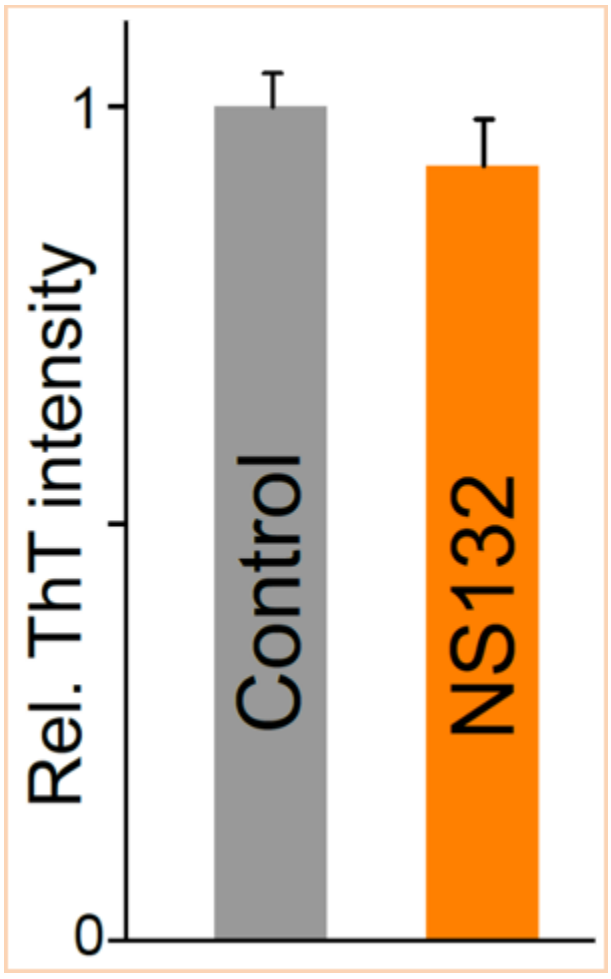

Figure 3.5 The comparison of the fluorescence intensity of the ThT dye (50 μM) in the absence and presence of NS132 (100 μM) in 1 × PBS. The ThT experiments were conducted three times and the reported change in the ThT intensity was an average of three separate experiments. The data were expressed as mean and the error bars report the s.d. (n = 3 independent experiments and each n consisted of three technical replicates).

3.4 Discussion

The aPPIs are elusive targets as they are of pathological significance and their modulation approaches are directly linked to the discovery of lead therapeutics. One of the most effective approaches to modulate aPPIs is the design of synthetic protein mimetics with diverse chemical space, which can complement the sequence and structural topography of aPPI's interfaces. OPs are a class of synthetic protein mimetics

that imitate the secondary structure of proteins and have been shown to modulate the aggregation of multiple proteins[183]. Despite the overall success of OPs as antagonists, no attention has been directed towards enhancing their antagonist activity, which is predominantly dependent on the extension of the chemical diversity of the side chains on OPs and the onus is on the tedious synthetic route for the generation of OP libraries as the synthesis requires multiple chromatography steps to add individual side chains on OPs.

We have developed a novel fragment-based approach (2D-FAST), in tandem with novel chemistry, to append a large number of side chains with a very diverse chemical space on OPs using a highly efficient synthetic method. We used this approach to modulate a dynamic and transient target, which is the self-assembly of αS, a process linked to the onset of PD. PD is the second most common neurodegenerative disorder affecting more than 10 million people worldwide and there is no cure for the disease. Therefore, there is a pressing need to identify therapeutic strategies that can prevent or slow down PD. We have used 2D-FAST approach to identify ligands that can modulate the aggregation of αS, which led to the identification of a potent antagonist of *de novo* and fibers catalyzed aggregation of αS, and *in vitro* model of the prion-like spread (PMCA) of αS fibers.

For the first time, we also demonstrated that OPs are synthetically tunable ligands with the ability to improve their cell permeability (from NS132 to NS163) without sacrificing their antagonist activity. Under matched conditions, NS163 was a better antagonist than NS132 in rescuing αS aggregation-mediated PD phenotypes in muscle cells and DA neurons in two *C. elegans* PD models, most likely due to the better cell permeability of the former. Moreover, we have developed a novel post-disease onset PD

model to study the effect of ligands on the PD phenotypes mediated by αS aggregation. Both OPs have shown remarkable rescue of the degeneration of DA neurons in this post-disease onset PD model. This study also shows a good correlation between the inhibition of *de novo* and fibers catalyzed aggregation of αS and the rescue of PD phenotypes in DA neurons in UA196 worms in both early-stage and post-disease onset models. Moreover, the inhibition of αS aggregation and prevention of PD phenotypes in *vitro and in vivo* models is a consequence of the interaction of OPs toward the N-terminal of αS and, more specifically, to the suggested aggregation-prone αS sequences[159,174]. The study further highlights the targeting of these sequences as a potential therapeutic approach for the treatment of PD.

We have also shown in the past and the current study that OPs are enzymatically stable in the biological milieu[174]. Therefore, soon, the most potent OPs will be tested for their ability to cross the blood-brain barrier and their pharmacokinetic and pharmacodynamic properties. Subsequently, we will use the most potent OPs in PD mouse models to further assess their pharmaceutical properties and the antagonist activity against PD phenotypes mediated by αS aggregation. The overall neuroprotective effect of OPs on the degeneration of DA neurons (both early and post-disease onset PD models) promises the identification of lead therapeutics for the treatment of PD.

We envision that the OP scaffold-based 2D-FAST could be used to modulate numerous pathological targets, including aPPIs and RNA-protein interactions. This approach is expandable as a greater number of side chains can be appended on OPs because of a very convenient synthetic pathway. We envisage that the novel 2D-FAST will have a broader impact as both the chemistry and the fragment-based approach could

be used for various foldamers (aromatic oligoamides, synthetic protein mimetics, and hybrid macrocycles of peptide and synthetic ligands) for the development of potent antagonists for various pathological protein and nucleic acid targets. The combination of the novel and efficient synthetic methodology and the fragment-based approach allows a systematic screening of large chemical space in a succinct time, which will aid in the identification of high affinity and specificity ligands for various pathological targets. To the best of our knowledge, this is the first example of a fragment-based approach for synthetic protein mimetics to successfully identify potent antagonists of a pathological protein target. We envision that the 2D-FAST will have a profound impact on the development of lead therapeutics for various diseases.

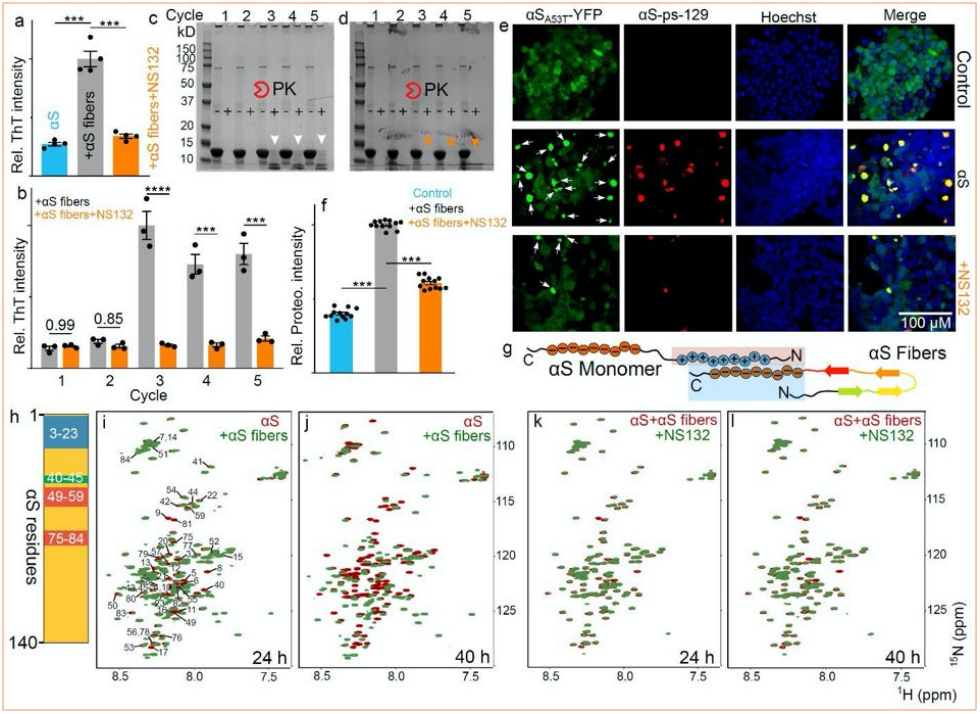

Figure 3.6 The relative ThT intensity of αS fibers (20% monomer) catalyzed aggregation of 100 μM αS in the absence and presence of NS132 at an equimolar ratio after 24 h in the aggregation conditions. The Bis-tris gels of PMCA samples from the firstto the fifth cycle in the absence (**b**) and presence (**c**) of NS132. The (-) and (+) signs indicate the amplified samples without and with the treatment of PK, respectively. The arrows

indicate the effect of PK on PMCA samples from the indicated cycles. **d**, The statistical analysis of the relative ThT intensity of various PMCA samples in the absence (grey bar) and presence (orange bar) of NS132, before treating these samples with PK. **e**, The representative confocal images of HEK cells after treatment with PMCA samples from the fifth cycle under the indicated conditions. The αSA53T-YFP (green) inclusions are indicated by white arrows. Hoechst = blue, αS-ps-129 = red, merge = Hoechst, αS-ps-129, and αSA53T-YFP. **f**, The relative intensity of Proteostat dye-stained aggregates of αSA53T-YFP inclusions in HEK cells treated with PMCA samples from the fifth cycle (2 μM αS in monomer) in the absence and presence of NS132. **g**, A model for the proposed interaction of αS monomer with αS fibers. **h**, The proposed binding interaction sites of αS fibers on the αS monomer residues. The comparison of the HSQC NMR of the 70 μM ^{15}N-labeled αS in the absence (red) and presence (green) of αS fibers after 24 h (**i**) and 40 h (**j**). The comparison of the HSQC NMR of the premixed solution of ^{15}N-labeled αS+αS fibers in the absence (red) and presence (green) of 70 μM NS132 after 24 h (**k**) and 40 h (**l**). The ThT experiments were conducted three times and the reported change in the ThT intensity was an average of three independent experiments. The Proteostat assay was conducted with at least four biological replicates and three technical replicates for each biological replicate. The data were expressed as mean and the error bars report the s.e.m. (n = 3 independent experiments and each n consisted of three technical replicates). The statistical analysis was performed using ANOVA with Tukey's multiple comparison test. *$p < 0.05$, **$p < 0.01$, ***$p < 0.001$.

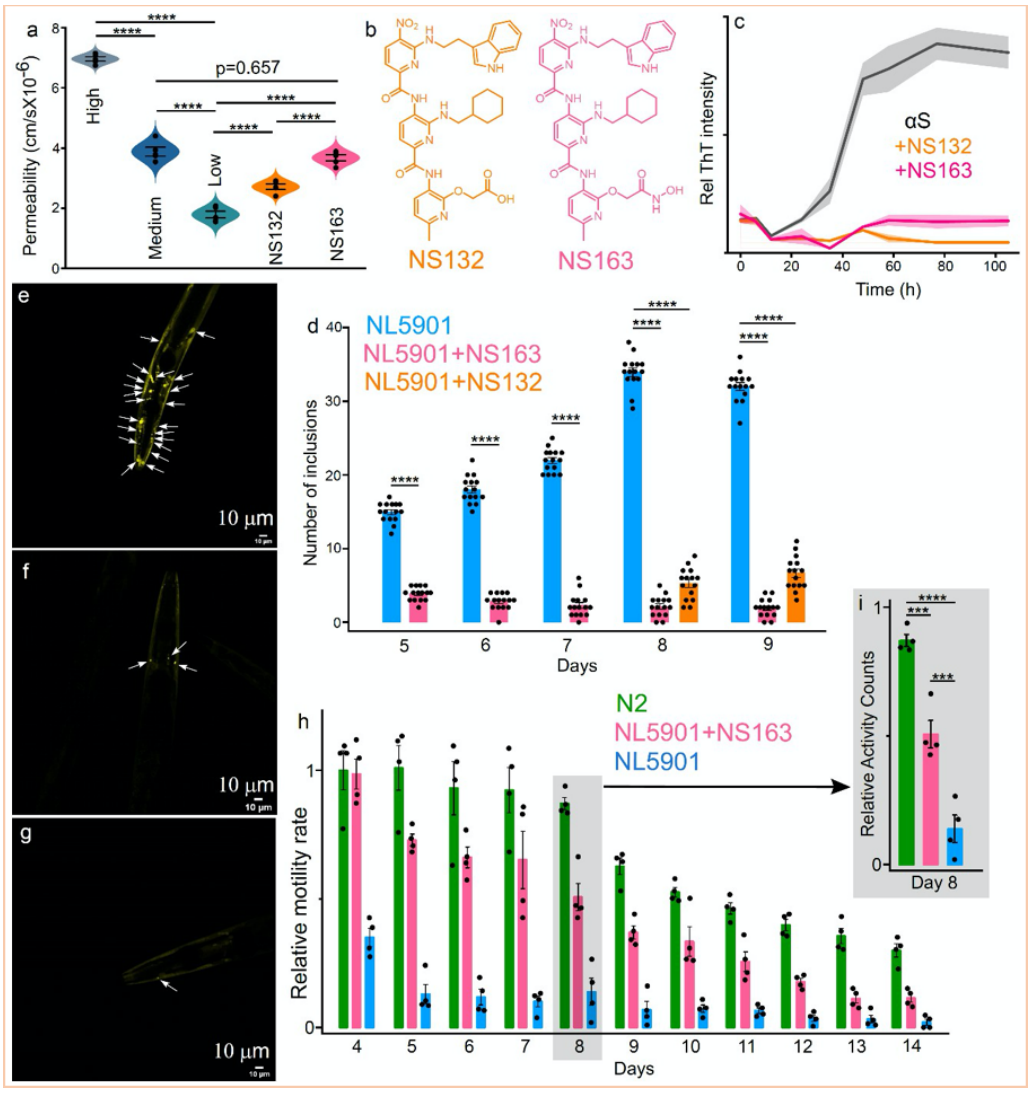

Figure 3.7 **a**, Assessment of cell permeability of the indicated ligands using the PAMPA. **b**, The chemical structures of NS132 and NS163. **c**, The ThT -based aggregation profile of 100 µM αS in the absence and presence of the indicated ligands at an equimolar ratio. **d**, The number of inclusions for experiment '**e-g**' in NL5901 in the absence and presence of NS132 and NS163 from day four to day nine of the adulthood. The representative confocal images of αS-YFP inclusions (white arrows) in the body wall muscle cells of NL5901 (Days = 8) in the absence (**e**) and presence of 50 µM NS163 (**f**) and 50 µM NS132 (**g**). **h**, The motility rate of N2 and NL5901 and statistics (Day 8, **i**) in the absence and presence of 50 µM NS163 during the aging process. For each confocal imaging experiment (e-g), at least 10 worms were used, and the inclusions were counted manually, and each condition (Each day) consisted of at least four independent experiments. For motility experiments, a total of 50 worms were used in duplicate for each experiment and each condition consisted of at least four independent experiments. The data were expressed as mean and the error bars report the s.e.m. (n = 3 or 4

independent experiments and each n consisted of a minimum of three technical replicates). The statistical analysis was performed using ANOVA with Tukey's multiple comparison test. *p < 0.05, **p < 0.01, ***p < 0.001.

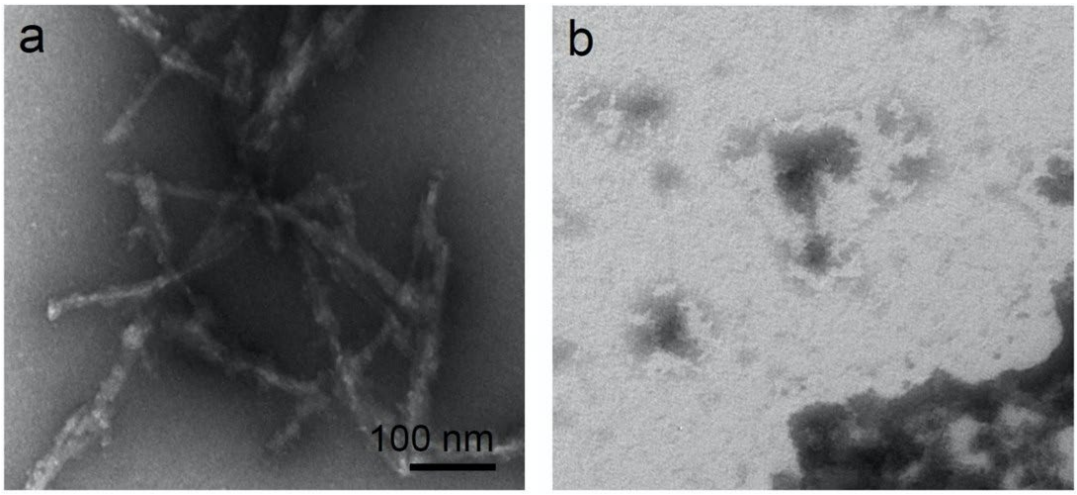

Figure 3.8 The TEM images of 100 μM αS solution aggregated for four days under aggregation conditions (1 × PBS buffer) in the absence (a) and presence (b) of NS163 at an equimolar ratio.

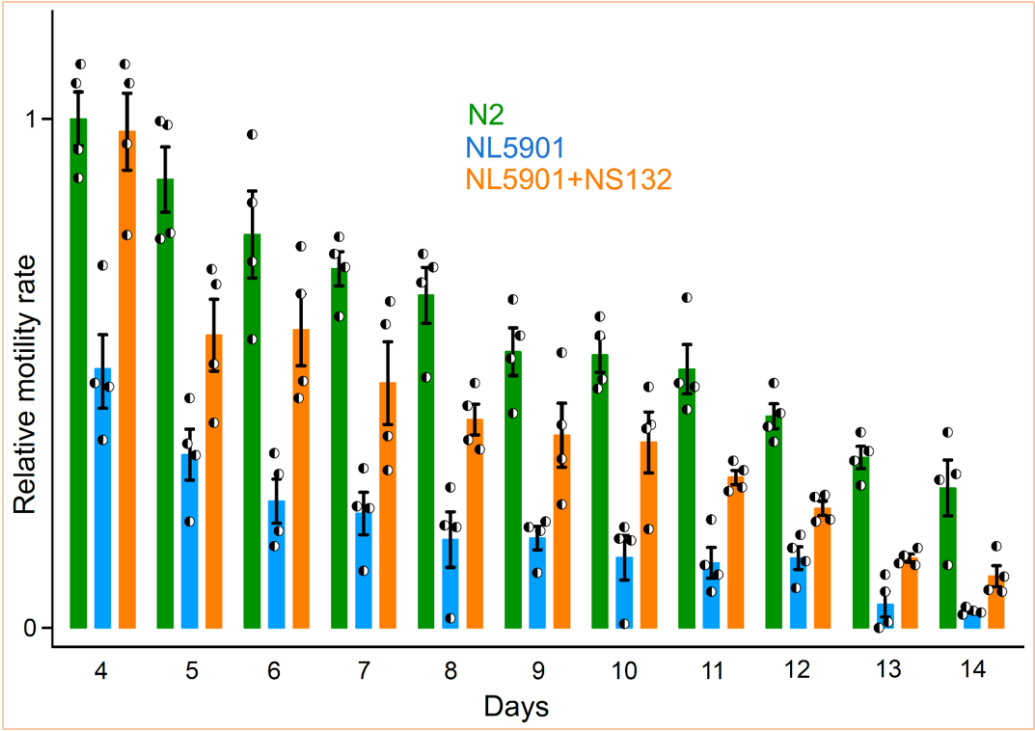

Figure 3.9 The comparison of the motility rate of N2 and NL5901 and statistics in the absence and presence of 50 μM NS132 (treatment on day two). For motility rate

experiment, a total of 50 worms were used in duplicate for each experiment and each condition consisted of at least four independent experiments. The data were expressed as mean and the error bars report the s.e.m. (n = 4 independent experiments and each n consisted of two technical replicates). The statistical analysis was performed using ANOVA with Tukey's multiple comparison test. *p < 0.05, **p < 0.01, ***p < 0.001.

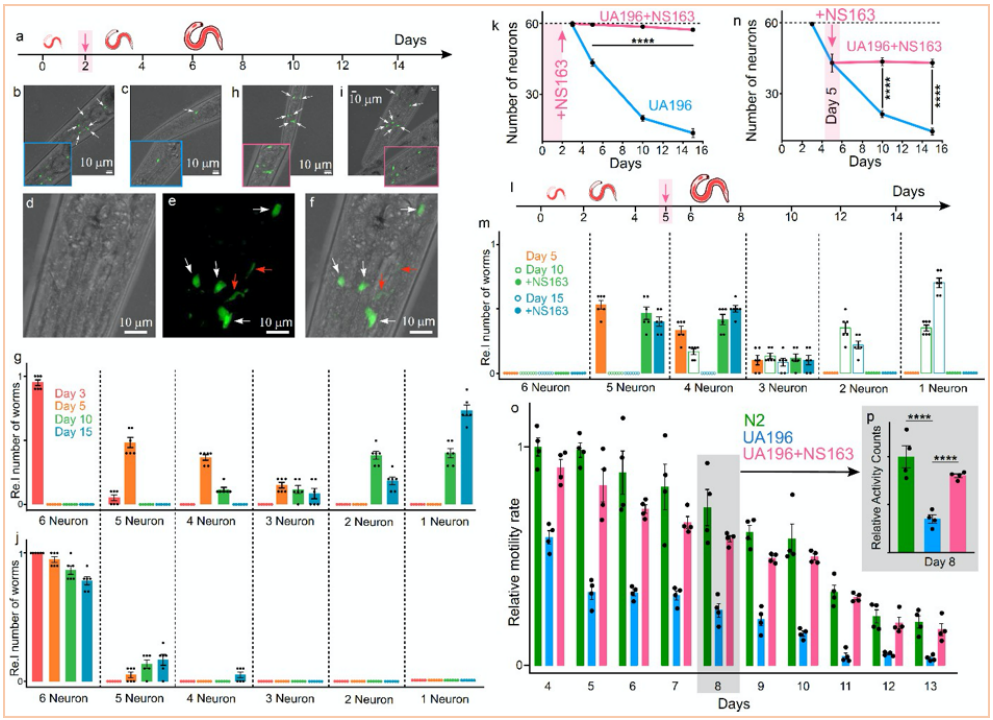

Figure 3.10 **a,** Schematic of the aging process of UA196 worms and their treatment with the ligands. Representative confocal images of UA196 worms in the absence (**b,c**) and presence (**h,i**) of 50 µM NS163 on day three and day 15. **d,e,f**, The healthy (white arrow) and degenerated (red arrow) DA neurons in UA196 worms on day five. **g,** The relative number of neurons in UA196 worms during the aging process in the absence (**g**) and presence of 50 µM NS163 (**j**). **k**, Statistics for the total number of neurons in UA196 worms during the aging process in the absence and presence of 50 µM NS163. **l**, Schematic of the aging process of UA196 worms and their treatment with the ligands in a late-onset disease model (day five). **m**, The relative number of neurons in UA196 worms during the aging process when treated on day five with 50 µM NS163. **n**, Statistics for the total number of neurons in UA196 worms when treated on day five with 50 µM NS163. **o**, The comparison of the motility rate for 13 days of N2 and UA196 and statistics (for day eight, **p**) in the absence and presence of 50 µM NS163. For each confocal imaging experiment (**b-f, h-i**), at least 10 worms were used, and the healthy neurons (GFP signal) were counted manually, and each condition (day) consisted of six independent experiments. For motility experiments, a total of 50 worms were used in duplicate for each experiment and each condition consisted of at least four independent

experiments. The statistical analysis was performed using ANOVA with Tukey's multiple comparison test. *p < 0.05, **p < 0.01, ***p < 0.001, ****p < 0.0001.

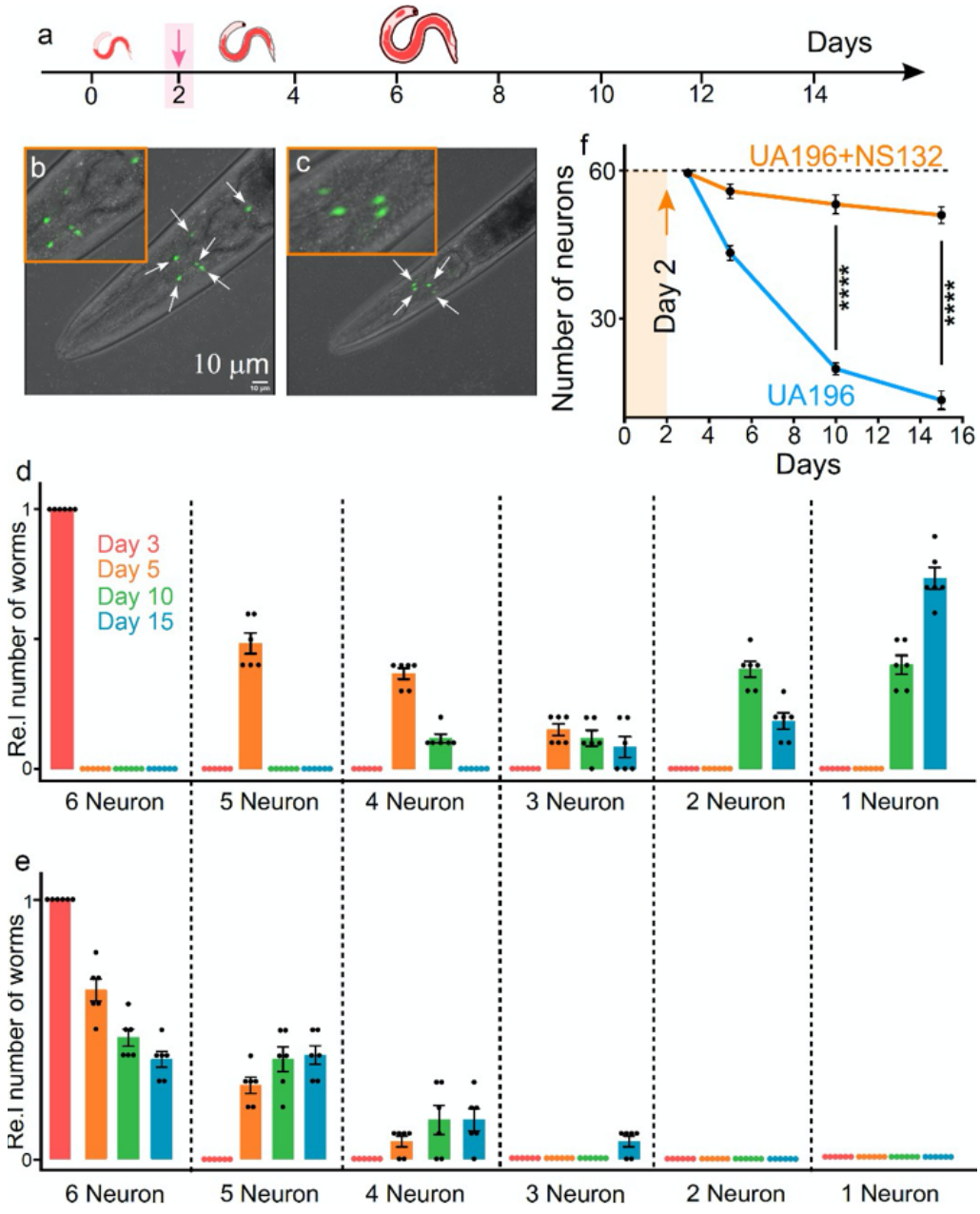

Figure 3.11 **a,** Schematic of the aging process of UA196 worms and their treatment with the ligands. Representative confocal images of UA196 worms in the presence of 50 µM NS132 on day 5 (**b**) and day 15 (**c**). The healthy DA neurons (white arrow) in UA196 worms on day 5. The relative number of neurons in UA196 worms during the aging process in the absence (**d**) and presence of 50 µM NS132 (**e**). **f**, Statistics for the total number of neurons in UA196 worms during the aging process in the absence (blue) and

presence (orange) of 50 µM NS132. For each confocal imaging experiment (**b,c**), at least 10 worms were used, and the healthy neurons were counted manually, and each condition (day) consisted of six independent experiments with freshly bleached worms. For motility rate experiment, a total of 50 worms were used in duplicate for each experiment and each condition consisted of four independent experiments with freshly bleached worms. The data were expressed as mean and the error bars report the s.e.m. (n = at least 4 independent experiments and each n consisted of at least two technical replicates). The statistical analysis was performed using ANOVA with Tukey's multiple comparison test. *p < 0.05, **p < 0.01, ***p < 0.001, ****p < 0.0001.

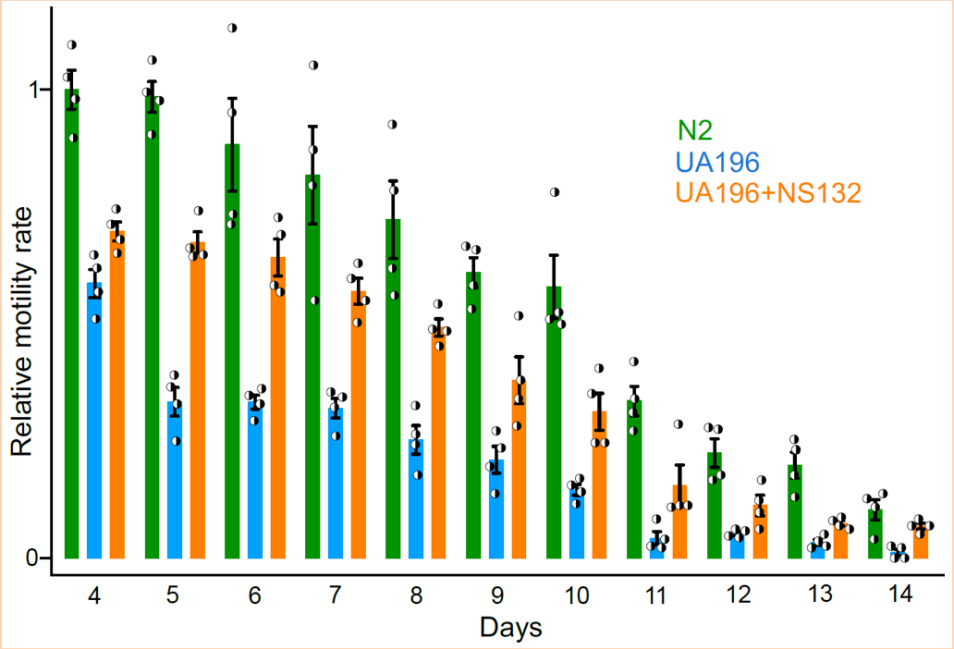

Figure 3.12 The comparison of the motility rate of N2 and UA196 in the absence and presence of 50 µM NS132 (treatment on day two). For motility rate experiment, a total of 50 worms were used in duplicate for each experiment and each condition consisted of four independent experiments. The data were expressed as mean and the error bars report the s.e.m. (n = 4 independent experiments and each n consisted of two technical replicates). The statistical analysis was performed using ANOVA with Tukey's multiple comparison test. *p < 0.05, **p < 0.01, ***p < 0.001.

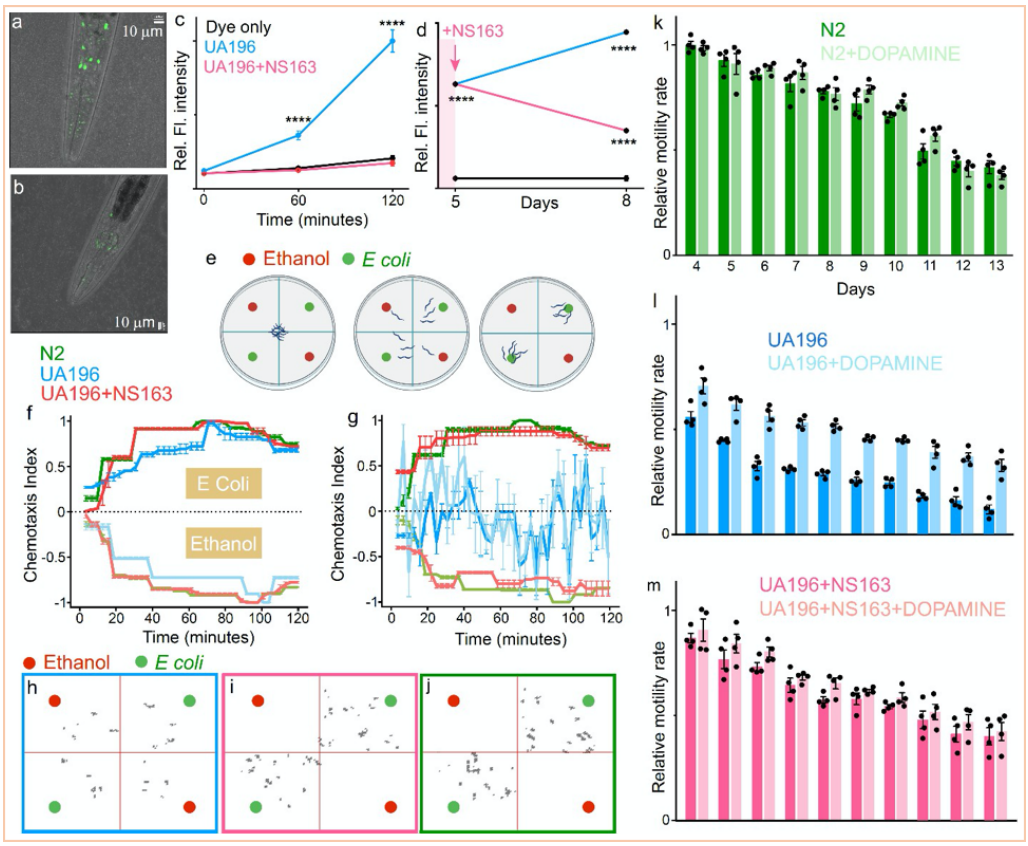

Figure 3.13 Representative confocal images of UA196 worms (day eight) treated with CM-H2DCFDA dye to quantify the ROS level (green) in the abence (**a**) and presence of 50 µM NS163 (**b**, day two treatment with NS163). **c**, Statistical analysis of the quantification of the ROS level for experiment **a-b**. **d**, Statistical analysis of the ROS level in UA196 worms when 50 µM NS163 was added on day five (arrow). **e**, Schematic to assess the behavioral deficits in UA196 worms in a petri dish in the presence of ethanol and *E. coli* as a function of time. The CI graph for N2, UA196 worms, and UA196 worms treated with 50 µM NS163 under the indicated conditions on day three (**f**) and day 10 (**g**). Snapshots at 60 min. of the animated videos collected for the CI for UA196 (**h**), UA196+50 µM NS163 (**i**), and N2 (**j**) under the indicated conditions on day 10. The motility rate for N2 (**k**), UA196 worms (**l**) and UA196 worms treated with 50 µM NS163 (**m**) in the absence and presence of 2 mM dopamine. For the ROS level quantification, at least 50 worms were used and each condition consisted of three independent experiments. For motility assay experiment, a total of 50 worms were used in duplicate for each experiment and each condition consisted of four independent experiments. For chemotaxis assays, a total of 50 worms were used for each experiment and each condition consisted of three independent experiments. The data were expressed as mean and the error bars report the s.e.m. (n = 3 or 4 independent experiments and each n consisted of a minimum of two technical replicates). For ROS assay, the data were expressed as mean and the error bars report the s.d. (n = 3 independent experiments and each n consisted of five technical replicates). The statistical analysis was performed using

ANOVA with Tukey's multiple comparison test. *p < 0.05, **p < 0.01, ***p < 0.001, ****p < 0.0001.

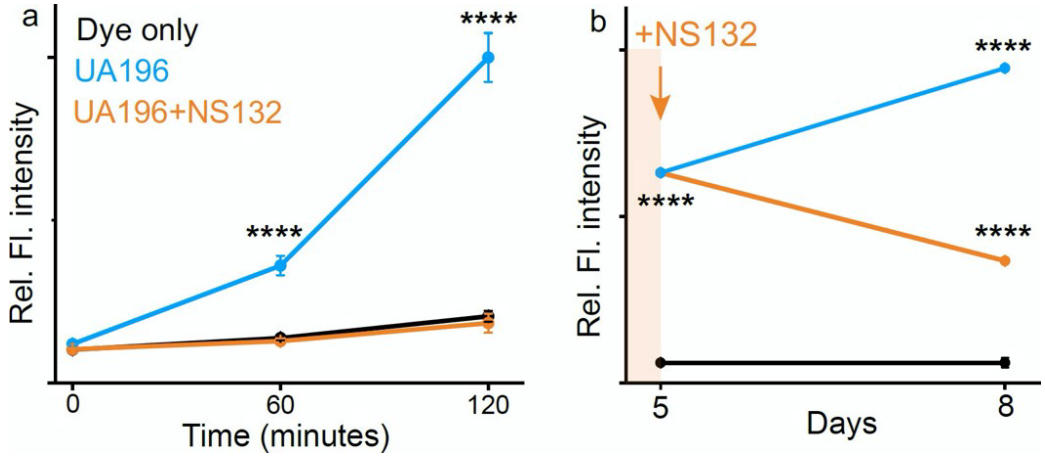

Figure 3.14 **a**, The comparison of the ROS level in UA196 worms in the absence and presence of 50 µM NS132 at the indicated time points. The UA196 worms were treated with NS132 on day 2 and the ROS level was measured on day 10. **b**, The comparison of the ROS level in UA196 worms (blue) on day 5 and day 8 when treated (orange) with 50 µM NS132 on day 5. For ROS level quantification, at least 50 worms were used and each condition consisted of three independent experiments with freshly bleached worms. The data were expressed as mean and the error bars report the s.d. (n = 3 independent experiments and each n consisted of three technical replicates). The statistical analysis was performed using ANOVA with Tukey's multiple comparison test.
*p < 0.05, **p < 0.01, ***p < 0.001, ****p < 0.0001.

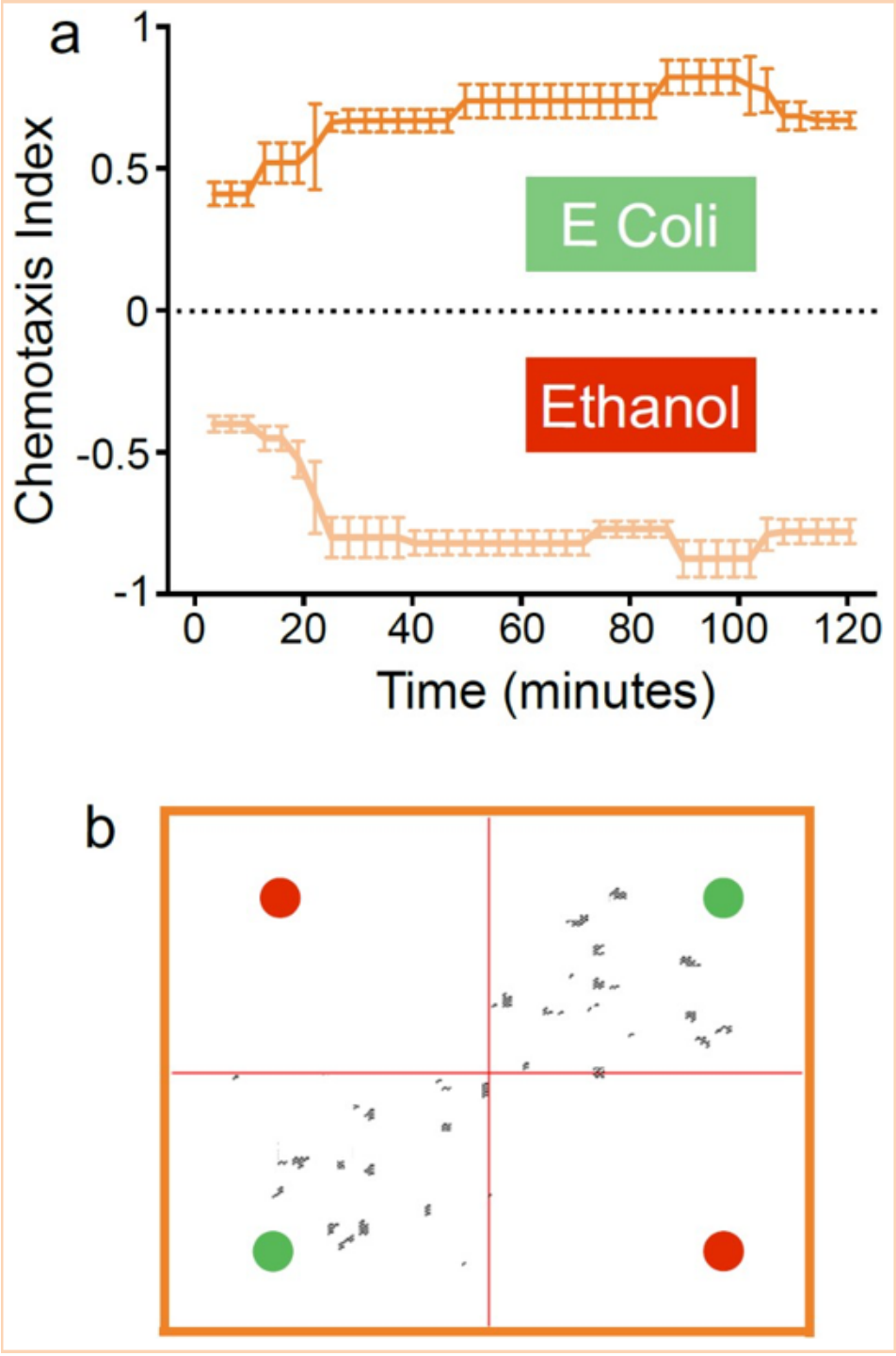

Figure 3.15 **a,** The CI graph for UA196 worms treated with 50 µM NS132 (treatment on day two) under the indicated conditions on day 10. **b**, The snapshots at 60 min. of the animated videos (Movie S8) collected for the CI for UA196+NS132 under the indicated

conditions. For chemotaxis assays, a total of 50 worms were used in duplicate for each experiment and each condition consisted of three independent experiments with freshly bleached worms. The data were expressed as mean and the error bars report the s.e.m. (n = 3 independent experiments and each n consisted of two technical replicates). The statistical analysis was performed using ANOVA with Tukey's multiple comparison test. *p < 0.05, **p < 0.01, ***p < 0.001, ****p < 0.0001.

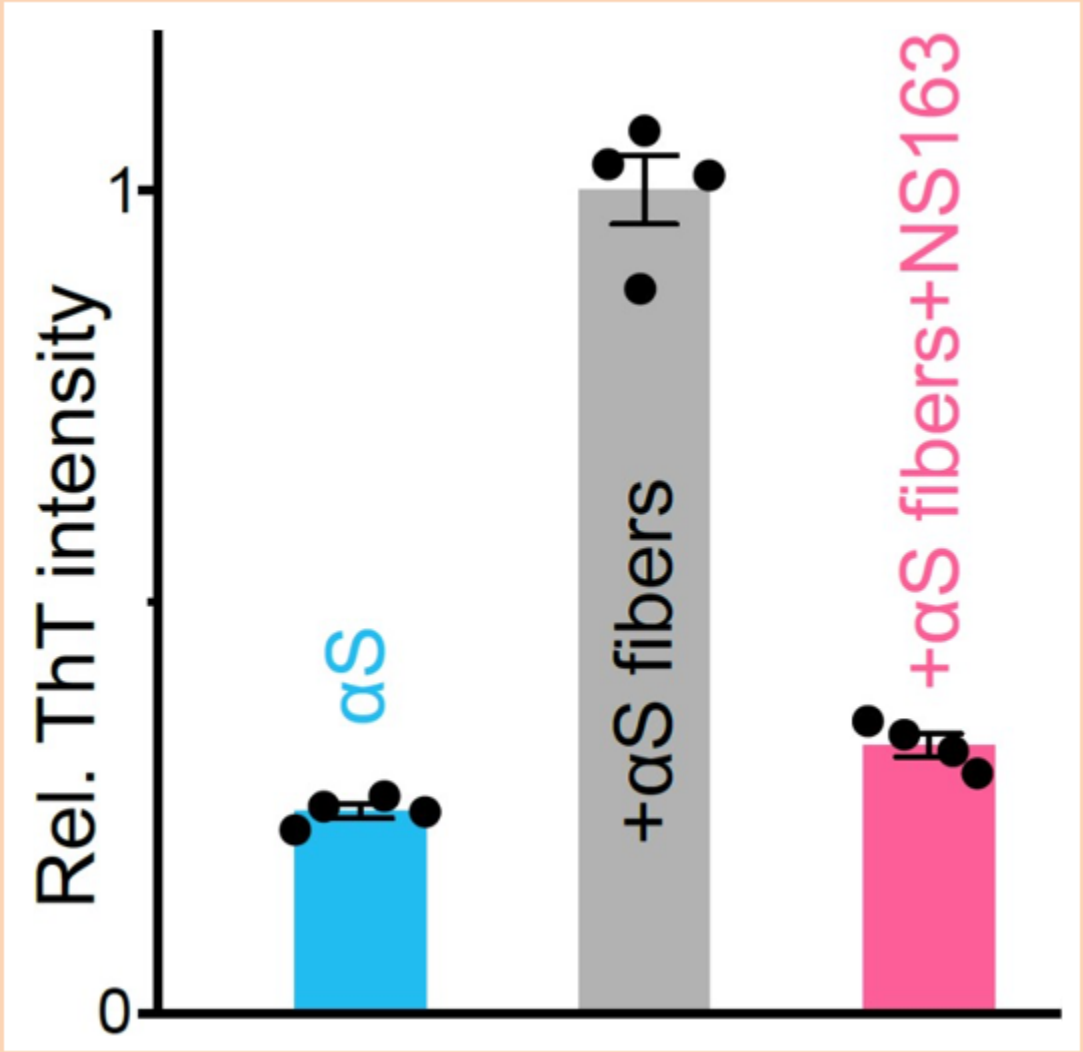

Figure 3.16 The relative ThT intensity of the aggregation of αS monomer (100 μM), αS monomer (100 μM) + αS fibers (20% monomer), and αS monomer (100 μM) + αS fibers (20% monomer) + NS163 (100 μM) after 20 h in the aggregation buffer conditions.

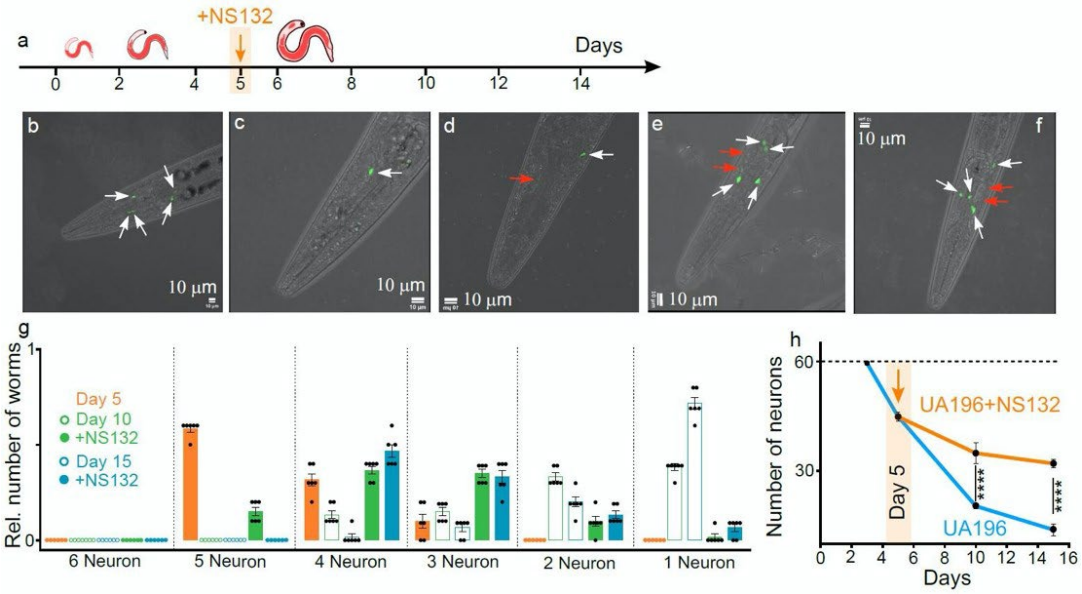

Figure 3.17 **a,** Schematic of the aging process of UA196 worms and their treatment with NS-132 at the mid-stage pathology (day 5). Representative confocal images of UA196 worms on day 5 (**b**), day 10 (**c**), and day 15 (**d**). Representative confocal images of UA196 worms on day 10 (**e**) and day 15 (**f**) when treated with 50 µM NS132 on day 5. The healthy (white) and degenerated (red) DA neurons in UA196 worms. **g**, The relative number of healthy DA neurons in UA196 worms during the aging process when treated with 50 µM NS132 on day 5. **h**, Statistics for the total number of neurons in UA196 worms during the aging process in the absence and presence of 50 µM NS132. For each confocal imaging experiment at least 10 worms were used, and the healthy neurons were counted manually, and each condition (day) consisted of six independent experiments. The data were expressed as mean and the error bars report the s.e.m. (n = 6 independent experiments and each n consisted of 10 technical replicates). The statistical analysis was performed using ANOVA with Tukey's multiple comparison test. *p < 0.05, **p < 0.01, ***p < 0.001, ****p < 0.0001.

Chapter 4: The effect of Polyamines on Alpha-Synuclein aggregation

4.1 Introduction

Polyamines (PA) are small polycation alkyl amines synthesized from decarboxylation of L- ornithine and other amino acids[192]. PA's can range in size and charge (figure 4.0), and are found in all cells at millimolar concentrations[193]. They are involved in numerous biological activities like DNA/ RNA synthesis and stability, cell signaling, transcription, translation, RNA splicing, cytoskeleton stabilization, cell differentiation and cell division[192]. PAs can be *de novo* synthesized in humans from L-methionine and L-ornithine (product of urea cycle) or absorbed from exogenous sources like diet and intestinal microbiome. The *de novo* synthesis starts when Ornithine Decarboxylase (ODC) decarboxylates ornithine forming Putrescine. Then, spermidine synthase and spermine synthase transfer aminopropyl group to putrescine and spermidine making spermine (figure 4.0).

Functional Magnetic Resonance Imaging (fMRI) and transcriptomic exploration of brain regions affected by PD revealed down regulation of membrane binding, RNA binding and metabolic proteins like Ribosomal protein L36a, lactate dehydrogenase, Spermidine spermine N1-acetyltransferase (SAT1), Heterogenous nuclear ribonuclease protein A1, Glycoprotein M6B and Syntenin[194]. SAT1 is an enzyme that acetylates PAs and its downregulation leads to higher concentrations of cellular PAs[195]. This finding established a link between PA metabolism and PD.

Another genetic link between PA and PD was established after a whole genome association study of PD patients and their siblings identified 145 Single Nucleotide Polymorphism (SNP's) of PARK9/ATP13A2 as PD risk factors[196]. Another study looked at a chilean family that has a rare early-onset form of PD called Kufor-Rakeb syndrome and found a 3057C deletion on ATP13A2 gene in the mother causing a frameshift, a 26 amino acid duplication and early termination of the gene. Additionally, the father had a G to A mutation at +5 splice site (1306 +5 G→A) reducing exon 13s splicing efficiency from 0.98 to 0.11. The reduction in splicing efficiency excludes exon 13 from the mature mRNA producing an ATP13A2 protein with a major deletion. Although the parents had these mutations, they didn't have PD, suggesting an autosomal recessive nature of ATP13A2 mutation. On the other hand, four out of 11 (36 %) of their children had early-onset PD[197]. The study also found this protein is expressed at high levels in the brain, particularly in the ventral midbrain containing substantia nigra, skeletal muscle and placenta.

ATP13A2 is an Adenosine Triphosphate (ATP) hydrolyzing transmembrane protein that transports polyamines. It localizes to late endosomes and lysosomes and translocates polyamines taken up during endocytosis into the cytosol. Disease related mutations like G504R, G533R and T12M result in an inactive ATP13A2 which can't transport PAs. This leads to lysosomal PA accumulation and alkalization and rupture[198,199]. The lysosomal dysfunction observed in ATP13A2 mutant neurons is thought to be a culprit to PD initiation[200,201]. Also, αS accumulates in lysosomes during physiological and pathological states for degradation and clearance[202–204]. Since PD associated ATP13A2 mutations cause lysosomal dysfunction, and because lysosomal

dysfunction is associated with αS aggregation, Baekelandt et al investigated the effect of ATP13A2 on αS pathology. They found ATP13A2 KD and disease mutants induce intracellular αS aggregation in SH-SY5Y cells and this effect is exacerbated when Pas are added to cell cultures[205]. This agrees with other reports demonstrating ATP13A2 deficiency cause αS aggregation and toxicity in cell cultures and animal models[206-209]. These observations stress the importance of PA in αS aggregation, thus several groups reported that PAs increase αS multimerization by binding to its C-terminus, condensing the protein conformation (cross section of 2600 $Å^2$ for αS vs 1430 $Å^2$ for αS +spermine) and increases its aggregation kinetics[210–213].

Although there has been significant progress in elucidating the mechanism of αS aggregation, our understanding of the mechanistic effect of PAs on αS aggregation is limited. Thus, our work explores different aspects of PA - αS interaction and the resulting fibrils.

4.2 Methods

4.2.1 Protein Expression and Purification

The plasmid construct pET28-HisSUMO-αS (Genscript, Piscatawa, NJ) was chemically transformed into competent BL21(DE3) cells and plated on an ampicillin selection plate. A single colony was used to inoculate a 5 mL starter culture which was kept overnight at 37 °C while shaking at 200 rpm. The following day, the starter culture was used to inoculate 4 L of autoclaved Luria Broth (LB). The culture was incubated at 37 °C and shaken at 200 rpm until the optical density (OD_{600nm}) reached 0.8. Then, protein expression was induced for 3 h by adding isopropyl β-D-thiogalactoside (IPTG) at a final

1 mM concentration. Cells were then harvested by centrifugation at 5,488 × *g* and 4 °C for 5 min. HisSUMO-αS purification was carried out using previously described methods[214]. Briefly, harvested cells were resuspended in Buffer A (20 mM Tris pH 8.0, 500 mM NaCl) and sonicated (Branson Sonifier Cell disruptor 185, Emerson, Ferguson, MO) for 15 min on ice. The lysate was centrifuged at 5776 × *g* for 10 min at 4 °C. The supernatant was loaded on an Immobilized Metal Affinity Chromatography (IMAC) resin and incubated for 3 min for optimal binding. Then, the mixture was centrifuged at 1,000 × *g* for 1 min to pellet the IMAC. The supernatant solution was removed and the IMAC was washed three times with Buffer A. HisSUMO-αS was eluted by washing the resin with increasing concentrations of Imidazole (2, 5 ,10 and 500 mM).

Pure fractions were collected, dialysed to Buffer A and cleaved with Ulp1 peptidase. Cleaved HisSUMO and Ulp1 were separated from free αS by incubating the solution with IMAC resin. Once resine was pelleted, the solution containing αS was collected, buffer exchanged to Milli-Q water using Amicon ultra 3K filters (MilliPoreSigma, Burlington, MA), before lyophilizing and storing the dried protein at -80 °C.

4.2.2 Aggregation Kinetics Measurement

Aggregation Kinetics were measured according to a previously described protocol[174]. Briefly, 70 μM αS solutions (250 μL, with or without PA) were prepared in phosphate buffer (25 mM Phosphate pH 7.3). The solutions were placed in a ThermoMixer (Eppendorf, Hamberg, Germany) at 37 °C with constant shaking at 1300 rpm. At different time points, 5 μL aliquots of each αS solution were added to 95 μL PBS containing 50 μM Thioflavin T (ThT) dye in a Costar black 96 well plate (Corning Inc., Kennebunk, ME).

ThT fluorescence intensity was measured (λ_{ex} = 450 nm and λ_{em} = 490 nm) on an Infinite M200PRO plate reader (Tecan, Männedorf, Switzerland), and plotted against time to give a sigmoidal curve typical of amyloid aggregation.

4.2.3 Proteinase K digestion (PK)

A 50 μg/ml solution of PK (IBI Scientific, Dubuque, IA) in the digestion buffer (10 mM Tris pH 8.0, 2 mM CaCl2) was diluted 10 times into 30 μL of PMCA solutions and incubated for 30 min at 37 °C. Subsequently, the sample was diluted 2 times in SDS Protein Gel Loading Dye 2 × (Quality Biological, Gaithersburg, MD) and loaded on Mini-PROTEAN TGX Stain-Free Protein Gel (BioRad, Hercules, CA). The gel was stained with Fairbanks staining method and then imaged using ChemiDoc MP (BioRad, Hercules, CA).

4.2.4 Cell culture and PFF delivery

HEK expressing αS_{A53T}-YFP (200,000 cells/ well) were plated on a 12- well cell culture plates (Celltreat, Pepperell, MA) and incubated at 37 °C and 5% CO2 (g), and allowed to adhere to the plate for 24 h in complete media (DMEM, 10% FBS, 1% pen/strep). Then, αS fibrils (control) or αS fibrils prepared with PAs were prepared for transfection by diluting the fibrils with Lipofectamine 3000 and P3000 (Lipofectamine, Thermoscientific, MA) in OptiMEM to a final 500 μL volume. The transfection solution was added to the HEK cells after removing complete media and the plate was incubated at 37 °C and 5% CO_2 (g) for 24 h. The following day, fluorescence microscopy was used to visualize intracellular seeding by locating YFP punctae.

4.2.5 Immunocytochemistry

Cells incubated with aggregates for 24 h were washed with ice cold Phosphate Buffered Saline (PBS) three times before fixing with 4 % Paraformaldehyde (PFA) prepared in PBS for 10 min. Then, the PFA was washed out with PBS and cells were incubated in 0.1 % Triton X-100 solution for 10 min for permeabilization. After removing the Triton X-100 solution, cells were blocked with 1% BSA in PBST (PBS + 0.1 % Tween 20) for 30 min. The primary antibody pS-129 was diluted 1:1000 in 1% BSA solution in PBST and incubated with the cells for 1 h at rt. The, the cells were washed with PBS and a secondary antibody (diluted 1:1000 in 1% BSA in PBST) was added and incubated for 1 h at rt. The solution was removed and replaced with PBS in preparation for fluorescent imaging.

4.2 Results

Many polyamines have been shown to initiate *in vitro* and *in vivo* αS aggregation[194,212]. Although this finding is relevant to human health as neurons cary high concentrations of PA and αS, the detailed mechanism of PA induced αS aggregation is unknown. Whether PAs interact with monomers and mediate multimerization or stabilize oligomers and increase elongation and secondary nucleation is unclear. Additionally, since the pathological hallmarks of disease brain derived αS fibril is its resistance to protease degradation, we tested the effect of different polyamines and their ability to induce protease resistant αS assemblies. In our previous work, we've observed *in vitro* aggregated αS fibrils are't resistant to proteases until they've been passed through multiple protein misfolding cyclic amplification steps[174]. We took advantage of this property and incubated αS with or without different PAs and measured Proteinase K

resistance (figure 4.0 b). We found αS aggregated alone for 2 h at pH 6.6 wasn't resistant to Proteinase K as no bands were detected after degradation (lane 2, figure 4.0 b), but in the presence of spermine, αS was found to be resistant to PK degradation (lane 7, figure 4.0 b). Bands that weren't present when αS (No PA) was treated with PK (lane 2) appeared when αS was aggregated in the presence of Spm and digested with PK (lane 7). Aggregation of αS in the presence of other PA other than Spm didn't induce PK resistant αS species observable by Coomassie blue staining (detection limit = 300 ng). The observed PK degradation pattern is commonly observed when αS fibrils amplified from disease human brains are treated with proteases[174,215]. The observation that Spm creates degradation resistant αS species – a hallmark of synucleinopathies – further implicates the role of PAs in PD initiation and pathogenesis.

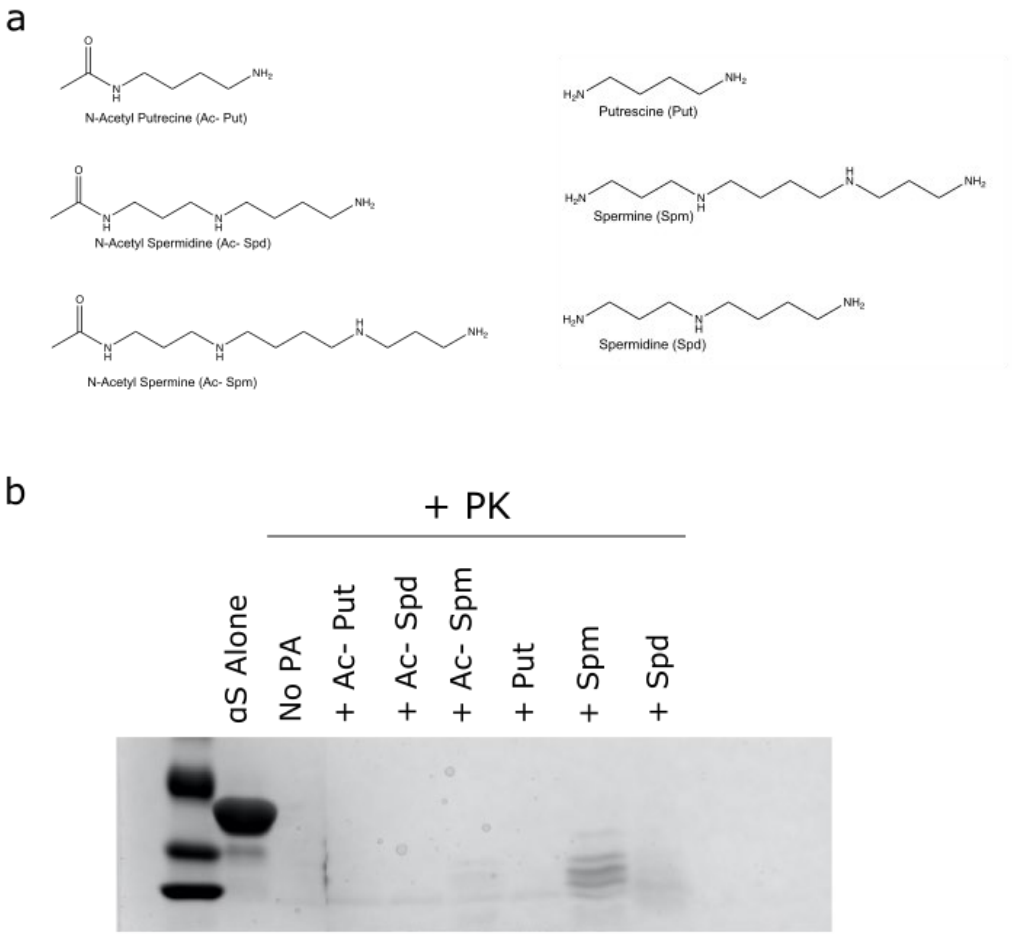

Figure 4.0 a is representation of the PAs used in this study. Since Putrescine (Put), Spermine (Spm) and Spermidine (Spd) are the most ubiquitous PAs in cellular milieu, their effect on αS aggregation was investigated[216]. Their acetylated forms (Ac-PAs) were also investigated since N1- acetylation is a downstream modification of PAs. b is a representative gel showing αS aggregated alone or with PAs and exposed to Proteinase K (PK).

To investigate if the resistance to degradation is due to Spm inactivating the protease, we incubated PK with Spm for 2 h and exposed the protease to monomeric αS (figure 4.1 a). Degrading monomeric αS with Spm-pretreated PK, left one major undegraded band (figure 4.0 a). Although there was incomplete degradation, there weren't as many bands compared to when αS was aggregated with Spm (figure 4.0 b). This adds to previous findings that PAs could interfere with protease function to some extent[217]. We speculated that aggregation conditions (37 ℃ and shaking at 12,000 rpm) are required for getting degradation resistance patterns observed in figure 4.0 b, so we incubated monomeric αS with Spm at 37 ℃ for 10 min, enough time for Spm to bind αS C-terminal region[218]. When we added PK to this solution, we didn't observe the degradation pattern seen when aggregation conditions were used (figure 4.0 b and figure 4.1 b). This suggests aggregating αS with Spm caused the degradation resistance pattern observed in figure 4.0 b and PD brain derived fibrils[174].

Since previous work has shown αS aggregation kinetics is increased in the presence of PAs, we tested if the aggregation equilibrium is also perturbed. During *in vitro* αS aggregation, monomers assemble into higher order oligomers and protofibrils which elongate to form mature fibrils. As the aggregation completes, monomers, oligomers and fibrils exist in the same solution, albeit with different concentrations[219,220]. To test if the distribution of αS assemblies change due to PAs, we aggregated αS with or without different PAs and assessed fibrillar content with Thioflavin T (ThT) fluorescence assay. The fluorescence emission of ThT dye increases when it preferentially binds cross β-sheet structures, serving as a semi-quantitative readout for fibrillization[221]. Analysis of

αS solution (70 μM) aggregated for 24 h showed significant increase in ThT fluorescence intensity compared to pre-aggregated αS solution (figure 4.1 b, $p < 0.0001$). The same was observed for αS solutions aggregated in the presence of different PAs (figure 4.1 c-h). To assess the possibility of equilibrium perturbation, we compared post-aggregation ThT intensity of the different αS solutions and found αS aggregated alone, had higher ThT intensity values compared to αS aggregated with Ac- Put, Ac-Spd, Spm and Spd, but not Ac- Spm and Put (figure 4.1 i). On average, the ThT intensity of αS aggregated alone is twice the intensity observed for αS solutions aggregated with PAs (figure 4.1 i). This observation can be due to three reasons. First, amines have a quenching effect on aromatic fluorophores confounding any fluorescence measurements in the presence of amines[222,223]. Second, ThT doesn't have equal affinity to all amyloid structures resulting in unequal limits of detection between different fibrils[224]. Third, PAs can be competing for amyloid binding sites, displacing ThT. To test if presence of PAs undermines ThT fluorescence assay, we incubated preformed fibrils with PAs and measured ThT intensity. The presence of some PAs (Ac-Spm, Put and Spm) decreased ThT intensity while the presence of other PAs (Ac- Put, Ac-Spd and Spd) didn't (figure 4.1 c). This suggests ThT fluorescence assay in the presence of PAs or other amines could be misleading.

Thus, we turned to a more rigorous method – spin-down assay – to assess if PAs perturb aggregation equilibrium[225]. Initially, we centrifuged the different solutions to separate large insoluble aggregates from small soluble assemblies and monomers, then ran denaturing gel with the different fractions (figure 4.4). Comparing insoluble and

soluble fractions from αS aggregated alone, we found more than 50 % of αS in the insoluble fraction (figure 4.4 a, lanes 2 & 3 and figure 4.4 b). Similarly, when αS was aggregated in the presence of PAs, most of the protein was found in the insoluble fraction (figure 4.4 c - h, figure 4.4 a). Then, we calculated the ratio of band intensity for insoluble to soluble fractions (Pell./Sol.) to assess the distribution of αS (figure 4.4 i). We observed aggregating αS in the presence of PAs increased the insoluble protein content, especially when Ac- Put and Spm were used (figure 4.4 i, $p < 0.005$). When αS was aggregated alone, there was ~ 1.3 times higher insoluble protein content relative to soluble protein content. In contrast, in the presence of Ac- Put and Spm, there was ~ 2 and 2.5 times higher insoluble protein content relative to soluble protein content. The increase in insoluble protein suggests PAs shift the aggregation equilibrium towards more insoluble αS assemblies.

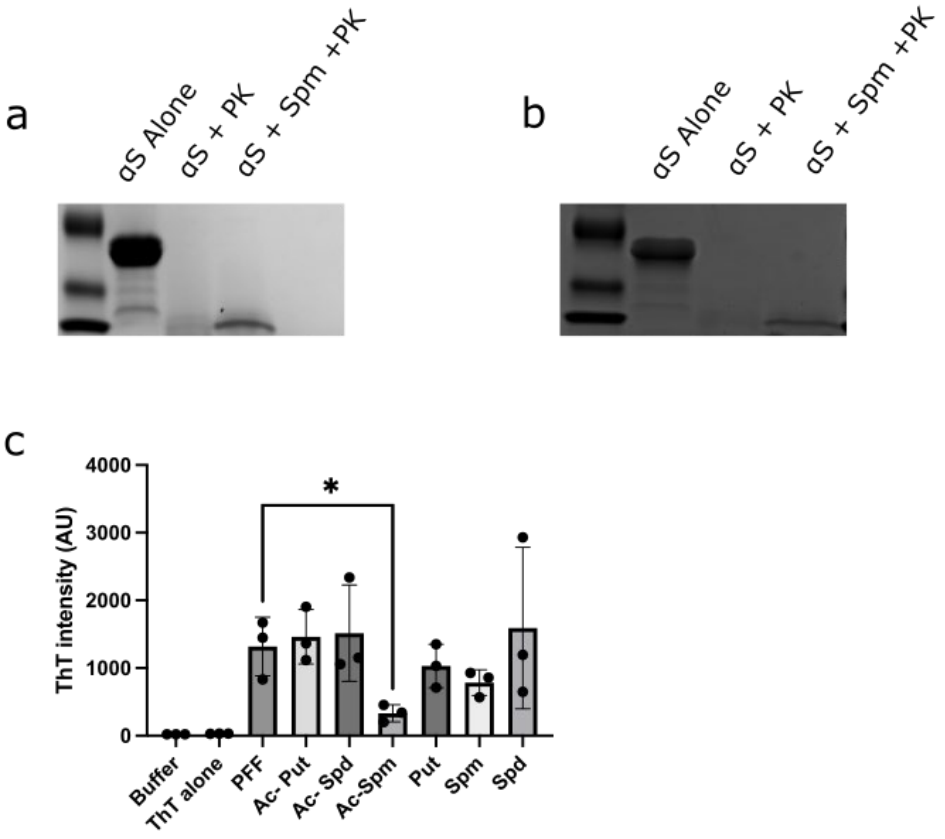

Figure 4.1 a shows a representative gel ran on αS degraded with PK incubated with Spm for 2 hrs. b shows a representative gel ran on αS degraded after incubating with Spm for 10 min. c is showing ThT intensity measured after incubating preformed fibrils with different PAs. The only significant difference is between PFF and PFF incubated with Ac-Spm (*$p < 0.05$).

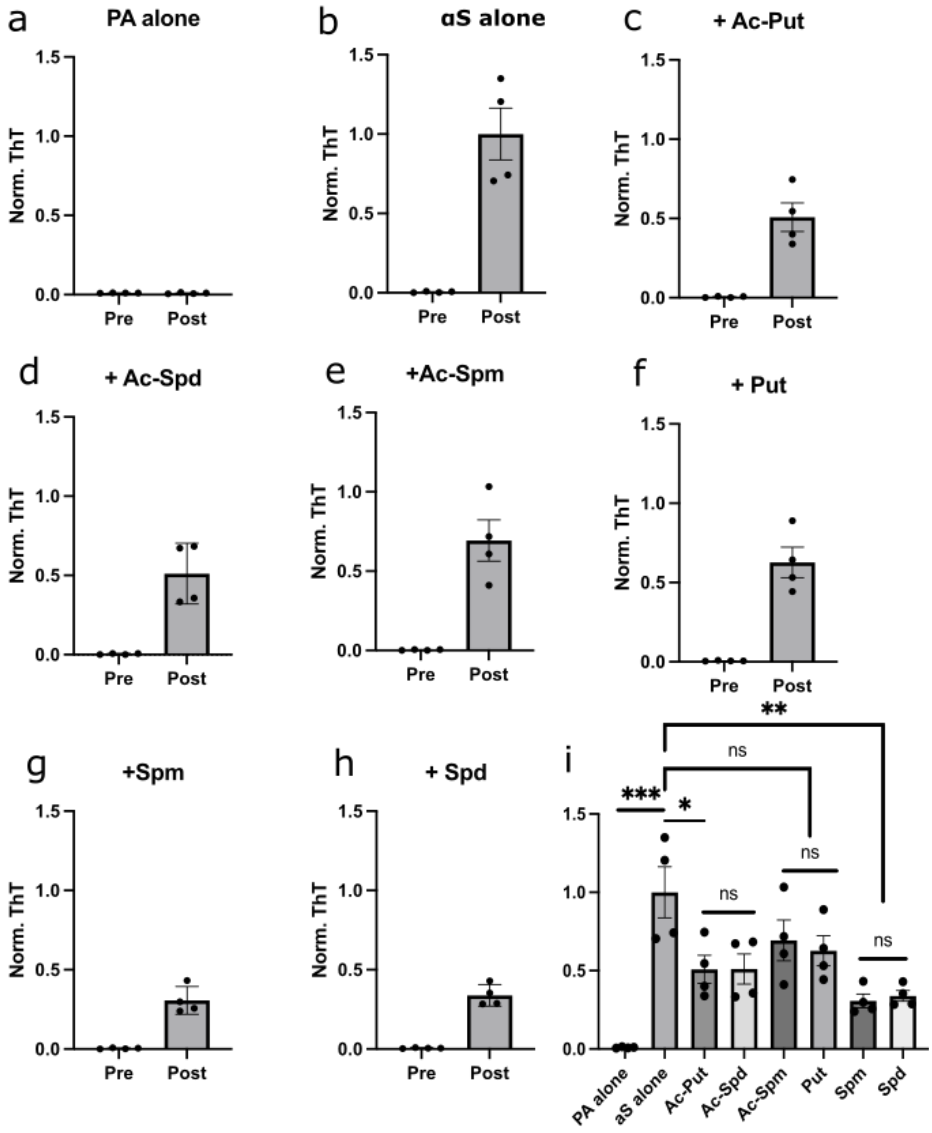

Figure 4.2 a - h show ThT values measured for αS solutions incubated with different PAs,pre-aggregation and post-aggregation. Post aggregation ThT values are compared to pre aggregated values. i shows post aggregation ThT values for αS aggregated with PAs normalized to ThT value of control aggregates (no PA). There was significant difference between PA alone vs αS alone, αS alone vs Ac-Put and αS alone vs Spm ($p = 0.0009$***,$p = 0.038$*, $p = 0.0062$**). All of the other comparisons had non-significant comparisons ($p \geq 0.5$, ns).

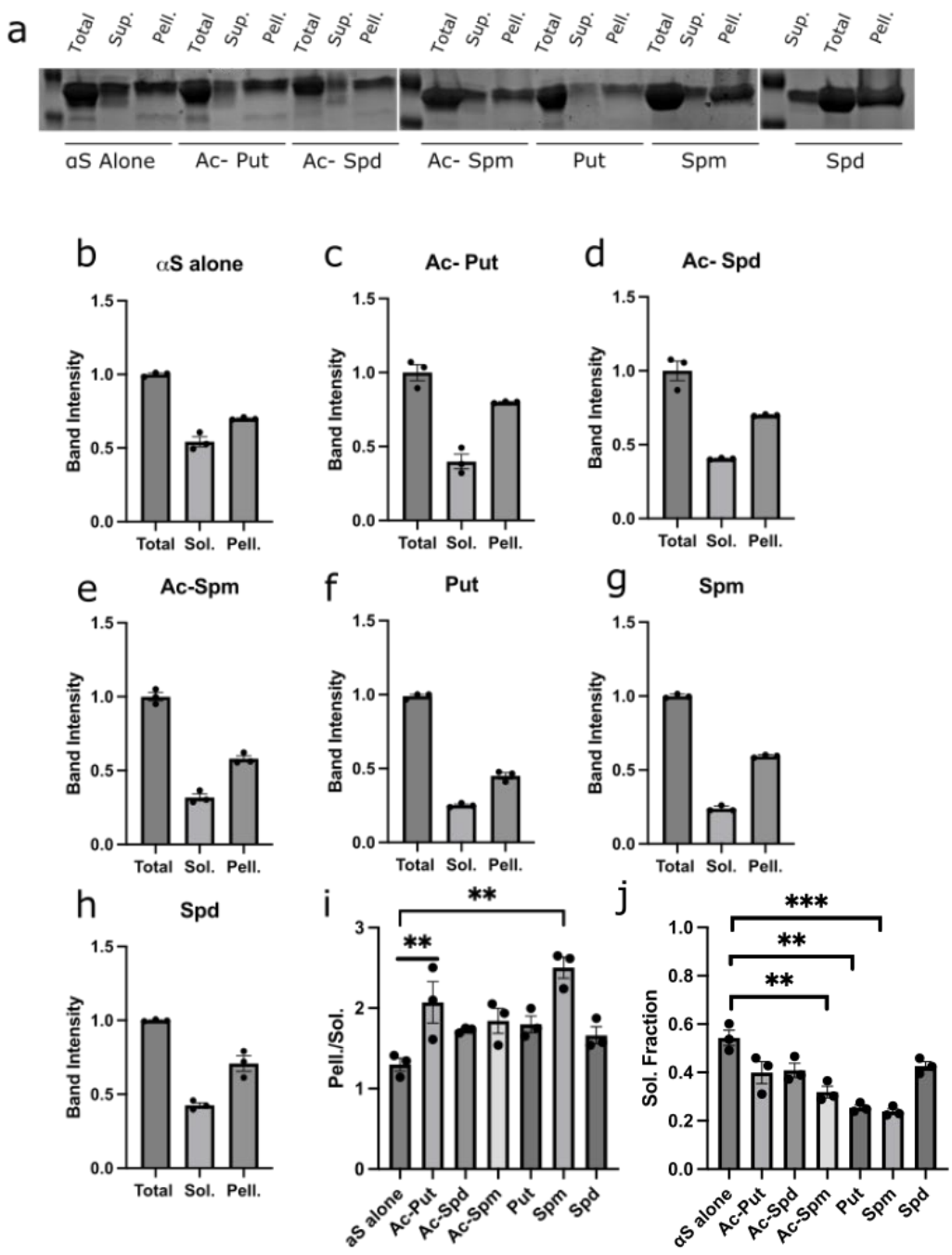

Figure 4.3 a shows a representative SDS-PAGE performed on αS solutions aggregated alone or with PAs. The solution was centrifuged at 22, 000 × g to separate insoluble aggregates from soluble protein. Then, the solution above the visible precipitate was transferred to a different tube labeled soluble fraction. The pellet was resuspended in the same volume that was removed and the tube labeled as insoluble fraction. Total, soluble and insoluble fractions were diluted in SDS-loading dye and ran on Polyacrylamide gel. B - h show band intensity of total, soluble and insoluble fractions from the SDS-PAGE

(figure 4.4 a). ImageLab software (Biorad, Hercules, CA) was used to quantify band densitometry for the different lanes corresponding to total, soluble and insoluble fractions. The intensity of soluble and insoluble bands was normalized to total band intensity and plotted in b- h. i shows the ratio of Pellet band intensity to Soluble band intensity for αS solutions aggregated alone or with PAs. Since the value of this ratio is above 1 for all the solution, it suggests more αS was found in insoluble fractions instead of soluble fractions. Comparing the Pell./Sol. ratios of control (αS alone) vs Ac- Spd showed significant difference (p = 0.0066**). The difference between control aggregates and Spm aggregates was also significant (p=0.0014***). j shows soluble fraction calculated by dividing soluble band intensity by total band intensity for all αS aggregates formed with or without PAs. Comparing control with Ac- Spm, Put and Spm shows statistically significant differences (p= 0.0048**, 0.001** and 0.0008***).

We observed that insoluble fractions were partially resistant to denaturation (2 % SDS and 95 ℃ for 10 min) and couldn't penetrate the SDS-PAGE. This can lead to incorrect quantification of the insoluble fraction. Thus, we decided to use the soluble fraction to assess equilibrium perturbation as we didn't observe any denaturation resistant bands from this solution (figure 4.4 j). We quantified the ratio between soluble protein and total protein to determine the proportion of αS remaining soluble after aggregation and used this number to compare between control (αS alone) and PA aggregated solutions (figure 4.4 j). We found αS solution aggregated with PAs had less protein in the soluble fraction compared to αS aggregated alone. The reduction in soluble αS induced by Ac-Spm, Put and Spm was statistically significant compared to αS aggregated alone ($p < 0.05$ and $p < 0.005$) (figure 4.4 j).

This data suggests presence of PAs in *in vitro* αS aggregation promote higher prevalence of insoluble αS aggregates. This corroborates our hypothesis that PAs, in addition to increasing the kinetics of αS aggregation, perturb the aggregation equilibrium to favor higher amounts of αS assemblies. Since Spm increased the concentration of PK resistant insoluble αS aggregates, we investigated if these structures can seed intracellular

αS. Therefore, we cultured Human Embryonic Kidney (HEK) 293 cells expressing αS_{A53T} - YFP and delivered the different aggregates into the cytoplasm. Although the cells express αS_{A53T}, the endogenous protein stays soluble until exogenous fibrils are introduced into the cell. Once fibrils are delivered to the cytoplasm, they seed the endogenous αS and propagate aggregation. Since the endogenous αS is labeled with a fluorophore, the resulting aggregates appear as a bright punctae observable under fluorescent microscope[226]. These cells were engineered to serve as biosensors for amyloid fibrils that can seed cellular aggregation, making them appropriate cell models to test the seeding potential of αS assemblies aggregated with Spm.

Observing the HEK αS_{A53T} - YFP control cells under fluorescent microscope, we didn't observe any punctae, suggesting absence of intracellular αS aggregates (figure 4.5). When we delivered αS aggregates prepared without Spm into the cells, we observed punctate in 2.5 % of the biosensor cells, suggesting the exogenous aggregates seeded the aggregation of αS_{A53T} - YFP9 (figure 4.5 a & b). When we delivered αS aggregates prepared with Spm, about 10 % of the biosensor cells had punctae, 4x higher than cells seeded with control aggregates (figure 4.5 b). This suggests αS aggregated in the presence of Spm can seed cellular αS.

One of the downstream events that follow cellular αS aggregation is hyperphosphorylation of the aggregated protein at serine 129 by Polo-like kinase (PLK) and Casein Kinase[227]. Serine 129 phosphorylation is observed in postmortem PD and DLB brains, mice brains injected with αS fibrils, human plasma and cerebrospinal fluid[228–230]. Although the complete effect of phosphorylated αS fibrils isn't know, Li et al

has demonstrated these fibrils have higher cellular toxicity relative to unphosphorylated α S fibrils[231]. So we tested if aggregates formed in the presence of Spm can be hyper phosphorylated.

Punctae that formed after seeding with control aggregate (without Spm) contain phosphorylated αS, as observed by pS-129 staining (an antibody specific for S129 phosphorylated αS) (figure 4.5 a). Punctae formed after seeding with αS aggregated with Spm also contained hyperphosphorylated aggregates. This suggests aggregates that formed in the presence of Spm undergo similar modification to control fibrils.

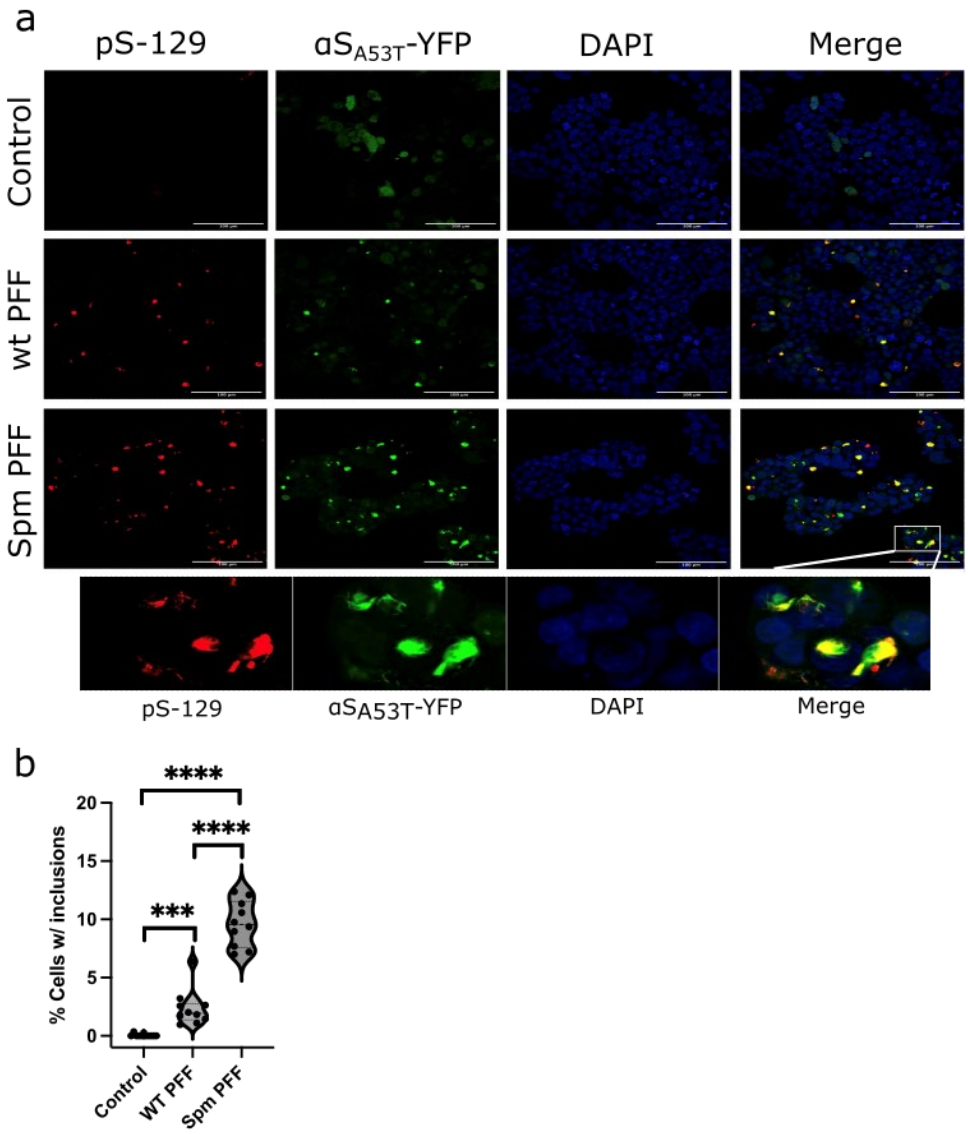

Figure 4.4 a shows a representative fluorescent image of Control cells (unseeded with aggregates), cells seeded with aggregates formed without PAs (wt PFF) and cells seeded with aggregates formed in the presence of Spm (Spm PFF). The cells were fixed with 4 % paraformaldehyde, permeabilized and stained with pS-129 antibody (binds αS phosphorylated at serine 129) and DAPI (a nuclear stain). b shows quantification of cells containing punctae in each condition. Control cells unseeded with aggregates had no intracellular aggregates, whereas cells seeded with αS fibrils aggregates alone, there was observable punctae. On average 2.5 % of the cells had intracellular aggregates (***p = 0.005). Cells seeded with αS aggregates made with Spm had higher amounts of puncta compared to control and wt PFF conditions (****p ≤ 0.0002).

4.3 Discussion

Dysregulation of PA processing proteins like ATP13A and SAT1 are implicated in PD. PAs are *in vitro* and *in vivo* agonists of αS aggregation. Several reports have demonstrated PAs increase aggregation kinetics after binding αS at the negatively charged C-terminus[218]. PD patients also have altered PA levels in their blood and cerebrospinal fluid[232,233]. These findings suggest PAs play a major role in PD pathogenesis. Hence, it is imperative to delineate the molecular interaction of PA-αS interaction. Since the histological hallmark of PD is degradation resistant αS aggregates, we speculated αS aggregated with PAs could be resistant to degradation. We tested this hypothesis by enzymatically degrading amyloid fibrils either aggregated alone or in the presence of PAs. I*n vitro* aggregated αS fibrils are generally not resistant to enzymatic degradation, but aggregates formed in the presence of Spm are resistant to degradation (figure 4.0 b)[174]. Two possible mechanisms can explain resistance to enzymatic degradation. One, certain fibril conformations/ strains are more resistant to enzymatic degradation than others[234–237]. Two, amplifying fibril concentration with protein misfolding cyclic amplification assay (PMCA) can overwhelm proteases leaving behind undegraded fragments[174,238]. So, we hypothesized Spm and the other PAs, besides increasing aggregation kinetics, can also shift the aggregation equilibrium to produce more fibrils. We tested this hypothesis by centrifuging different αS aggregates, and quantifying soluble and insoluble fractions. We found αS solutions aggregated with PAs, particularly Spm, had higher insoluble aggregates compared αS aggregated alone. Soluble protein was also significantly reduced in Spm aggregated solutions relative to control aggregates. These results suggest the resistance to degradation can be due to

increased amyloid content, although our findings don't rule out the possibility of Spm inducing a unique αS strain that is resistant to degradation.

We also tested the cellular seeding propensity of αS aggregated with Spm. These aggregates were able to seed intracellular αS at higher levels compared to control aggregates. Considering αS aggregated with Spm contains more insoluble protein fraction, it isn't surprising this solution has higher seeding propensity (figure 4.5). Although we have gained important insight into the effects of PAs on αSaggregation, we need to validate our findings using diverse experimental techniques. For example, the structures that form in the presence of Spm need to be visualized using either TEM or Atomic Force Microscopy (AFM) to confirm the aggregates are fibrillar. It is also unclear whether Spm induces unique fibrils structures, so we are performing different biophysical assays to find structural differences between control fibrils and Spm induced fibrils.

Chapter 5: Concluding Remarks

Parkinson's Disease is the second most prevalent neurodegenerative disorder after Alzheimer's Disease. The disease affects about 8.5 million people worldwide and there is no therapeutic intervention that halts or reverses the disease progression. Since PD is an aging related disorder, the incidence will increase to 12 million people by 2040 as the aging population increases. Thus, it is imperative to develop therapeutic intervention against the disease.

Since alpha-synuclein aggregates are thought to be the toxic structures that contribute to the death of dopaminergic neurons in the substantia nigra pars compacta leading to parkinsonian symptoms, preventing αS aggregation is a potential therapeutic strategy to prevent PD initiation and propagation. To that end, we developed two potent α S aggregation inhibitors – SK129 and NS163. SK129 is a tetrameric oligoquinolin foldamer functionalized with alternating propyl and carboxylic acids. It most likely interacts with amino acids 47-53 and prevents nucleation dependent aggregation. SK129 can also prevent PD brain amplified seed catalyzed aggregation. The molecule is cell permeable as demonstrated by artificial permeability assays, and its efficacy in cellular and *C.elegans* model systems.

NS163 is a trimeric oligopyridylamide foldamer functionalized with hydroxamic acid, cyclohexane and tryptophan and can bind αS at the N-terminus with 1.8 μM K_d and prevent aggregation even at sub-stoichiometric concentrations. NS163 is a hydroxamic analog of NS132, which contains carboxylic acid and has less cell permeability. Regardless, both molecules are able to permeate cells and prevent cellular αS aggregation. More importantly, NS163 works on post-onset PD model C.elegans by halting the death of dopaminergic neurons and rescuing disease related behavioral deficits.

Although NS132 and SK129 show great promise, we need to investigate the structure αS adopts after binding these molecules to get a molecular and structural understanding of how these molecules work. Additionally, the ability of these molecules to cross the blood brain barrier should be investigated. Also, since αS aggregated with NS163 and SK129 are susceptible to proteolytic degradation in vitro, it's important to investigate if they can also be degraded by cellular proteasome. Since β and γ synuclein and other proteins share sequence similarity with αS, SK129 and NS163 could bind these proteins and interfere with their function. Also, αS interacts with Processing bodies (P-bodies) using its N-terminus and associates with multiple RNA decapping proteins. At this point it's uncertain whether NS132 or SK129 binding on the N-terminus could interfere with this function[239]. Lastly, it's important to study the pharmacokinetic, dynamic and toxicity profile of SK129 and NS163.

Additionally, we explored the effect of cellular polyamines on αS aggregation and discovered Spermine, in addition to increasing aggregation kinetics, can also increase the fraction of insoluble αS after *in vitro* aggregation. The aggregates formed in the presence

of spermine are resistant to Proteinase K degradation similar to PD brain amplified aggregates. These aggregates are also able to seed intracellular αS aggregation. This stresses the role polyamines play during PD initiation and propagation. Although we know the effects Spermine has on αS aggregation, the mechanistic detail of this effect is unknown. Polyamines interact with αS's negatively charged C-terminus, and interaction with the C-terminus is thought to expose the N-terminus, accelerating aggregation.

References

1. Parkinson, J. An Essay on the Shaking Palsy. *J Neuropsychiatry Clin Neurosci* 14 (2002).
2. Hughes, A. J., Daniel, S. E., Kilford, L. & Lees, A. J. Accuracy of clinical diagnosis of idiopathic Parkinson's disease: a clinico-pathological study of 100 cases. *Journal of Neurology, Neurosurgery & Psychiatry* **55**, 181–184 (1992).
3. Heisters, D. Parkinson's: symptoms, treatments and research. *Br J Nurs* **20**, 548–554 (2011).
4. Micieli, G., Tosi, P., Marcheselli, S. & Cavallini, A. Autonomic dysfunction in Parkinson's disease. *Neurol Sci* **24 Suppl 1**, S32-34 (2003).
5. Alves, G., Forsaa, E. B., Pedersen, K. F., Dreetz Gjerstad, M. & Larsen, J. P. Epidemiology of Parkinson's disease. *J Neurol* **255**, 18–32 (2008).
6. Ascherio, A. & Schwarzschild, M. A. The epidemiology of Parkinson's disease: risk factors and prevention. *The Lancet Neurology* **15**, 1257–1272 (2016).
7. Autere, J. M., Moilanen, J. S., Myllylä, V. V. & Majamaa, K. Familial aggregation of Parkinson's disease in a Finnish population. *Journal of Neurology, Neurosurgery & Psychiatry* **69**, 107–109 (2000).
8. Kurz, M., Alves, G., Aarsland, D. & Larsen, J. P. Familial Parkinson's disease: a community-based study. *European Journal of Neurology* **10**, 159–163 (2003).
9. Chen, H., Zhang, S. M., Hernán, M. A., Willett, W. C. & Ascherio, A. Diet and Parkinson's disease: A potential role of dairy products in men. *Annals of Neurology* **52**, 793–801 (2002).
10. Kyrozis, A. *et al.* Dietary and lifestyle variables in relation to incidence of Parkinson's disease in Greece. *Eur J Epidemiol* **28**, 67–77 (2013).
11. Pouchieu, C. *et al.* Pesticide use in agriculture and Parkinson's disease in the AGRICAN cohort study. *International Journal of Epidemiology* **47**, 299–310 (2018).
12. Baldi, I. *et al.* Association between Parkinson's Disease and Exposure to Pesticides in Southwestern France. *NED* **22**, 305–310 (2003).
13. Weisskopf, M. G. *et al.* Persistent organochlorine pesticides in serum and risk of Parkinson disease. *Neurology* **74**, 1055–1061 (2010).
14. Curtin, K. *et al.* Methamphetamine/amphetamine abuse and risk of Parkinson's disease in Utah: A population-based assessment. *Drug and Alcohol Dependence* **146**, 30–38 (2015).
15. Langston, J. W., Ballard, P., Tetrud, J. W. & Irwin, I. Chronic Parkinsonism in Humans Due to a Product of Meperidine-Analog Synthesis. *Science* **219**, 979–980 (1983).
16. Olsen, J. H., Friis, S. & Frederiksen, K. Malignant Melanoma and Other Types of Cancer Preceding Parkinson Disease. *Epidemiology* **17**, 582–587 (2006).
17. Schwid, S. R. *et al.* Cancer incidence in a trial of an antiapoptotic agent for Parkinson's disease. *Movement Disorders* **25**, 1801–1808 (2010).
18. Yang, F. *et al.* Physical activity and risk of Parkinson's disease in the Swedish National March Cohort. *Brain* **138**, 269–275 (2015).
19. Hirsch, M. A., Iyer, S. S. & Sanjak, M. Exercise-induced neuroplasticity in human Parkinson's disease: What is the evidence telling us? *Parkinsonism & Related*

Disorders **22**, S78–S81 (2016).
20. Tan, L. C. *et al.* Differential Effects of Black versus Green Tea on Risk of Parkinson's Disease in the Singapore Chinese Health Study. *American Journal of Epidemiology* **167**, 553–560 (2008).
21. Driver, J. A., Logroscino, G., Lu, L., Gaziano, J. M. & Kurth, T. Use of non-steroidal anti-inflammatory drugs and risk of Parkinson's disease: nested case-control study. *BMJ* **342**, d198 (2011).
22. Hirsch, E. C. & Hunot, S. Neuroinflammation in Parkinson's disease: a target for neuroprotection? *The Lancet Neurology* **8**, 382–397 (2009).
23. Föorstl, H. & Levy, R. F. H. Lewy on Lewy bodies, parkinsonism and dementia. *International Journal of Geriatric Psychiatry* **6**, 757–766 (1991).
24. Gibb, W. R. G., Scott, T. & Lees, A. J. Neuronal inclusions of Parkinson's disease. *Movement Disorders* **6**, 2–11 (1991).
25. Gibb, W. R. G. & Lees, A. J. The Significance of the Lewy Body in the Diagnosis of Idiopathic Parkinson's Disease. *Neuropathology and Applied Neurobiology* **15**, 27–44 (1989).
26. Molecular cloning of cDNA encoding an unrecognized component of amyloid in Alzheimer disease. https://www.pnas.org/doi/10.1073/pnas.90.23.11282 doi:10.1073/pnas.90.23.11282.
27. Jakes, R., Spillantini, M. G. & Goedert, M. Identification of two distinct synucleins from human brain. *FEBS Letters* **345**, 27–32 (1994).
28. Maroteaux, L., Campanelli, J. T. & Scheller, R. H. Synuclein: a neuron-specific protein localized to the nucleus and presynaptic nerve terminal. *J Neurosci* **8**, 2804–2815 (1988).
29. Polymeropoulos, M. H. *et al.* Mapping of a Gene for Parkinson's Disease to Chromosome 4q21-q23. *Science* **274**, 1197–1199 (1996).
30. Mutation in the α-Synuclein Gene Identified in Families with Parkinson's Disease. https://www.science.org/doi/10.1126/science.276.5321.2045?url_ver=Z39.88-2003&rfr_id=ori:rid:crossref.org&rfr_dat=cr_pub%20%200pubmed.
31. Wakabayashi, K., Matsumoto, K., Takayama, K., Yoshimoto, M. & Takahashi, H. NACP, a presynaptic protein, immunoreactivity in Lewy bodies in Parkinson's disease. *Neuroscience Letters* **239**, 45–48 (1997).
32. α-Synuclein in Lewy bodies | Nature. https://www.nature.com/articles/42166.
33. Hashimoto, M. *et al.* Human recombinant NACP/α-synuclein is aggregated and fibrillated in vitro: Relevance for Lewy body disease. *Brain Research* **799**, 301–306 (1998).
34. Crowther, R. A., Jakes, R., Spillantini, M. G. & Goedert, M. Synthetic filaments assembled from C-terminally truncated α-synuclein. *FEBS Letters* **436**, 309–312 (1998).
35. Weinreb, P. H., Zhen, W., Poon, A. W., Conway, K. A. & Lansbury, P. T. NACP, A Protein Implicated in Alzheimer's Disease and Learning, Is Natively Unfolded. *Biochemistry* **35**, 13709–13715 (1996).
36. Han, H., Weinreb, P. H. & Lansbury, P. T. The core Alzheimer's peptide NAC forms amyloid fibrils which seed and are seeded by beta-amyloid: is NAC a common trigger or target in neurodegenerative disease? *Chem Biol* **2**, 163–169 (1995).

37. Fusco, G. *et al.* Direct Observation of the Three Regions in α-Synuclein that Determine its Membrane-Bound Behaviour. *Nat Commun* **5**, 3827 (2014).
38. Jarrett, J. T. & Lansbury, P. T. Seeding "one-dimensional crystallization" of amyloid: A pathogenic mechanism in Alzheimer's disease and scrapie? *Cell* **73**, 1055–1058 (1993).
39. Crespo, R., Rocha, F. A., Damas, A. M. & Martins, P. M. A Generic Crystallization-like Model That Describes the Kinetics of Amyloid Fibril Formation *♦. *Journal of Biological Chemistry* **287**, 30585–30594 (2012).
40. Mazzotti, M., Vetter, T., Ochsenbein, D. R., Maggioni, G. M. & Lindenberg, C. Nucleation. in *Polymorphism in the Pharmaceutical Industry* 261–283 (John Wiley & Sons, Ltd, 2018). doi:10.1002/9783527697847.ch9.
41. Raaij, M. E. van, Gestel, J. van, Segers-Nolten, I. M. J., Leeuw, S. W. de & Subramaniam, V. Concentration Dependence of α-Synuclein Fibril Length Assessed by Quantitative Atomic Force Microscopy and Statistical-Mechanical Theory. *Biophysical Journal* **95**, 4871–4878 (2008).
42. Rodriguez, R. A., Chen, L. Y., Plascencia-Villa, G. & Perry, G. Thermodynamics of Amyloid-β Fibril Elongation: Atomistic Details of the Transition State. *ACS Chem Neurosci* **9**, 783–789 (2017).
43. Amyloid assembly is dominated by misregistered kinetic traps on an unbiased energy landscape. https://www.pnas.org/doi/10.1073/pnas.1911153117 doi:10.1073/pnas.1911153117.
44. Zimmermann, M. R. *et al.* Mechanism of Secondary Nucleation at the Single Fibril Level from Direct Observations of Aβ42 Aggregation. *J. Am. Chem. Soc.* **143**, 16621–16629 (2021).
45. Cohen, S. I. A. *et al.* Proliferation of amyloid-β42 aggregates occurs through a secondary nucleation mechanism. *Proceedings of the National Academy of Sciences* **110**, 9758–9763 (2013).
46. Effect of allelic variation at the NACP–Rep1 repeat upstream of the α-synuclein gene (SNCA) on transcription in a cell culture luciferase reporter system | Human Molecular Genetics | Oxford Academic. https://academic.oup.com/hmg/article/10/26/3101/573521?login=true.
47. Scherzer, C. R. *et al.* GATA transcription factors directly regulate the Parkinson's disease-linked gene α-synuclein. *Proceedings of the National Academy of Sciences* **105**, 10907–10912 (2008).
48. Clough, R. L., Dermentzaki, G. & Stefanis, L. Functional dissection of the α-synuclein promoter: transcriptional regulation by ZSCAN21 and ZNF219. *Journal of Neurochemistry* **110**, 1479–1490 (2009).
49. Xia, Y. *et al.* Characterization of the human α-synuclein gene: Genomic structure, transcription start site, promoter region and polymorphisms. *Journal of Alzheimer's Disease* **3**, 485–494 (2001).
50. Koukouraki, P. & Doxakis, E. Constitutive translation of human α-synuclein is mediated by the 5′-untranslated region. *Open Biology* **6**, 160022.
51. Kahle, P. J. *et al.* Subcellular Localization of Wild-Type and Parkinson's Disease-Associated Mutant α-Synuclein in Human and Transgenic Mouse Brain. *J. Neurosci.* **20**, 6365–6373 (2000).

52. Gao, X. *et al.* Human Hsp70 Disaggregase Reverses Parkinson's-Linked α-Synuclein Amyloid Fibrils. *Molecular Cell* **59**, 781–793 (2015).
53. Bennett, M. C. *et al.* Degradation of α-Synuclein by Proteasome*. *Journal of Biological Chemistry* **274**, 33855–33858 (1999).
54. Webb, J. L., Ravikumar, B., Atkins, J., Skepper, J. N. & Rubinsztein, D. C. α-Synuclein Is Degraded by Both Autophagy and the Proteasome*. *Journal of Biological Chemistry* **278**, 25009–25013 (2003).
55. Brown, J. W. P. *et al.* β-Synuclein suppresses both the initiation and amplification steps of α-synuclein aggregation via competitive binding to surfaces. *Sci Rep* **6**, 36010 (2016).
56. Induction of de novo α-synuclein fibrillization in a neuronal model for Parkinson's disease. https://www.pnas.org/doi/10.1073/pnas.1512876113 doi:10.1073/pnas.1512876113.
57. Hashimoto, M., Rockenstein, E., Mante, M., Mallory, M. & Masliah, E. β-Synuclein Inhibits α-Synuclein Aggregation: A Possible Role as an Anti-Parkinsonian Factor. *Neuron* **32**, 213–223 (2001).
58. Rockenstein, E. *et al.* Altered expression of the synuclein family mRNA in Lewy body and Alzheimer's disease. *Brain Research* **914**, 48–56 (2001).
59. Liu, C. *et al.* The Membrane Interaction of Alpha-Synuclein. *Front Cell Neurosci* **15**, 633727 (2021).
60. Varkey, J. *et al.* Membrane Curvature Induction and Tubulation Are Common Features of Synucleins and Apolipoproteins. *J Biol Chem* **285**, 32486–32493 (2010).
61. Madine, J., Doig, A. J. & Middleton, D. A. A Study of the Regional Effects of α-Synuclein on the Organization and Stability of Phospholipid Bilayers. *Biochemistry* **45**, 5783–5792 (2006).
62. Chandra, S., Gallardo, G., Fernández-Chacón, R., Schlüter, O. M. & Südhof, T. C. α-Synuclein Cooperates with CSPα in Preventing Neurodegeneration. *Cell* **123**, 383–396 (2005).
63. Souza, J. M., Giasson, B. I., Lee, V. M.-Y. & Ischiropoulos, H. Chaperone-like activity of synucleins. *FEBS Letters* **474**, 116–119 (2000).
64. Kim, T. D., Choi, E., Rhim, H., Paik, S. R. & Yang, C.-H. α-Synuclein has structural and functional similarities to small heat shock proteins. *Biochemical and Biophysical Research Communications* **324**, 1352–1359 (2004).
65. Burré, J. *et al.* α-Synuclein Promotes SNARE-Complex Assembly in vivo and in vitro. *Science* **329**, 1663–1667 (2010).
66. Heydari, A. R., Wu, B., Takahashi, R., Strong, R. & Richardson, A. Expression of heat shock protein 70 is altered by age and diet at the level of transcription. *Mol Cell Biol* **13**, 2909–2918 (1993).
67. Erickson, R. R., Dunning, L. M. & Holtzman, J. L. The Effect of Aging on the Chaperone Concentrations in the Hepatic, Endoplasmic Reticulum of Male Rats: The Possible Role of Protein Misfolding Due to the Loss of Chaperones in the Decline in Physiological Function Seen With Age. *The Journals of Gerontology: Series A* **61**, 435–443 (2006).
68. Cuervo, A. M. & Dice, J. F. Age-related Decline in Chaperone-mediated Autophagy*. *Journal of Biological Chemistry* **275**, 31505–31513 (2000).

69. Andersson, V., Hanzén, S., Liu, B., Molin, M. & Nyström, T. Enhancing protein disaggregation restores proteasome activity in aged cells. *Aging* **5**, 802–812 (2013).
70. Reduced proteasome activity in the aging brain results in ribosome stoichiometry loss and aggregation. *Molecular Systems Biology* **16**, e9596 (2020).
71. Rimal, S. *et al.* Inefficient quality control of ribosome stalling during APP synthesis generates CAT-tailed species that precipitate hallmarks of Alzheimer's disease. *Acta Neuropathologica Communications* **9**, 169 (2021).
72. Bjorklund, G. *et al.* Metals and Parkinson's Disease: Mechanisms and Biochemical Processes. *Curr Med Chem* **25**, 2198–2214 (2018).
73. Xu, B. *et al.* Manganese promotes α-synuclein amyloid aggregation through the induction of protein phase transition. *J Biol Chem* **298**, 101469 (2021).
74. Harischandra, D. S. *et al.* Manganese promotes the aggregation and prion-like cell-to-cell exosomal transmission of α-synuclein. *Sci Signal* **12**, eaau4543 (2019).
75. Andruska, K. M. & Racette, and B. A. Neuromythology of Manganism. *Curr Epidemiol Rep* **2**, 143–148 (2015).
76. Li, Y. *et al.* Amyloid fibril structure of α-synuclein determined by cryo-electron microscopy. *Cell Res* **28**, 897–903 (2018).
77. Alam, M. M. *et al.* Alpha synuclein, the culprit in Parkinson disease, is required for normal immune function. *Cell Reports* **38**, 110090 (2022).
78. Kim, S. *et al.* Transneuronal Propagation of Pathologic α-Synuclein from the Gut to the Brain Models Parkinson's disease. *Neuron* **103**, 627-641.e7 (2019).
79. Vasili, E., Dominguez-Meijide, A. & Outeiro, T. F. Spreading of α-Synuclein and Tau: A Systematic Comparison of the Mechanisms Involved. *Frontiers in Molecular Neuroscience* **12**, (2019).
80. Tardivel, M. *et al.* Tunneling nanotube (TNT)-mediated neuron-to neuron transfer of pathological Tau protein assemblies. *Acta Neuropathologica Communications* **4**, 117 (2016).
81. Freundt, E. C. *et al.* Neuron-to-neuron transmission of α-synuclein fibrils through axonal transport. *Ann Neurol* **72**, 517–524 (2012).
82. Toba, S. *et al.* Alpha-synuclein facilitates to form short unconventional microtubules that have a unique function in the axonal transport. *Sci Rep* **7**, 16386 (2017).
83. Lee, J.-G., Takahama, S., Zhang, G., Tomarev, S. I. & Ye, Y. Unconventional secretion of misfolded proteins promotes adaptation to proteasome dysfunction in mammalian cells. *Nat Cell Biol* **18**, 765–776 (2016).
84. DnaJ/Hsc70 chaperone complexes control the extracellular release of neurodegenerative-associated proteins. *The EMBO Journal* **35**, 1537–1549 (2016).
85. Tanik, S. A., Schultheiss, C. E., Volpicelli-Daley, L. A., Brunden, K. R. & Lee, V. M. Y. Lewy Body-like α-Synuclein Aggregates Resist Degradation and Impair Macroautophagy*♦. *Journal of Biological Chemistry* **288**, 15194–15210 (2013).
86. Xie, Y. X. *et al.* Lysosomal Exocytosis Releases Pathogenic α-Synuclein Species from Neurons. 2021.04.10.439302 Preprint at https://doi.org/10.1101/2021.04.10.439302 (2021).
87. Mao, X. *et al.* Pathological α-synuclein transmission initiated by binding lymphocyte-activation gene 3. *Science* **353**, aah3374 (2016).
88. Grey, M. *et al.* Acceleration of α-Synuclein Aggregation by Exosomes. *J Biol Chem*

290, 2969–2982 (2015).
89. Freeman, D. *et al.* Alpha-Synuclein Induces Lysosomal Rupture and Cathepsin Dependent Reactive Oxygen Species Following Endocytosis. *PLoS One* **8**, e62143 (2013).
90. Fusco, G., Sanz-Hernandez, M. & De Simone, A. Order and disorder in the physiological membrane binding of α-synuclein. *Current Opinion in Structural Biology* **48**, 49–57 (2018).
91. Fusco, G. *et al.* Structural basis of membrane disruption and cellular toxicity by α-synuclein oligomers. *Science* **358**, 1440–1443 (2017).
92. Jambrina, E. *et al.* Calcium Influx through Receptor-operated Channel Induces Mitochondria-triggered Paraptotic Cell Death*. *Journal of Biological Chemistry* **278**, 14134–14145 (2003).
93. Di Maio, R. *et al.* α-Synuclein binds to TOM20 and inhibits mitochondrial protein import in Parkinson's disease. *Science Translational Medicine* **8**, 342ra78-342ra78 (2016).
94. Mahul-Mellier, A.-L. *et al.* The process of Lewy body formation, rather than simply α-synuclein fibrillization, is one of the major drivers of neurodegeneration. *Proc Natl Acad Sci U S A* **117**, 4971–4982 (2020).
95. Winslow, A. R. *et al.* α-Synuclein impairs macroautophagy: implications for Parkinson's disease. *Journal of Cell Biology* **190**, 1023–1037 (2010).
96. Martinez-Vicente, M. *et al.* Dopamine-modified α-synuclein blocks chaperone-mediated autophagy. *J Clin Invest* **118**, 777–788 (2008).
97. Hinault, M.-P. *et al.* Stable α-Synuclein Oligomers Strongly Inhibit Chaperone Activity of the Hsp70 System by Weak Interactions with J-domain Co-chaperones. *J Biol Chem* **285**, 38173–38182 (2010).
98. Kim, C. *et al.* Neuron-released oligomeric α-synuclein is an endogenous agonist of TLR2 for paracrine activation of microglia. *Nat Commun* **4**, 1562 (2013).
99. Harms, A. S. *et al.* α-Synuclein fibrils recruit peripheral immune cells in the rat brain prior to neurodegeneration. *Acta Neuropathologica Communications* **5**, 85 (2017).
100. Dufek, M., Rektorova, I., Thon, V., Lokaj, J. & Rektor, I. Interleukin-6 May Contribute to Mortality in Parkinson's Disease Patients: A 4-Year Prospective Study. *Parkinsons Dis* **2015**, 898192 (2015).
101. Mogi, M. *et al.* Tumor necrosis factor-alpha (TNF-alpha) increases both in the brain and in the cerebrospinal fluid from parkinsonian patients. *Neurosci Lett* **165**, 208–210 (1994).
102. Jara, J. H., Singh, B. B., Floden, A. M. & Combs, C. K. Tumor necrosis factor alpha stimulates NMDA receptor activity in mouse cortical neurons resulting in ERK-dependent death. *J Neurochem* **100**, 1407–1420 (2007).
103. Neniskyte, U., Vilalta, A. & Brown, G. C. Tumour necrosis factor alpha-induced neuronal loss is mediated by microglial phagocytosis. *FEBS Lett* **588**, 2952–2956 (2014).
104. Moss, D. W. & Bates, T. E. Activation of murine microglial cell lines by lipopolysaccharide and interferon-gamma causes NO-mediated decreases in mitochondrial and cellular function. *Eur J Neurosci* **13**, 529–538 (2001).
105. Cui, G. *et al.* Concurrent activation of striatal direct and indirect pathways during

action initiation. *Nature* **494**, 238–242 (2013).
106. Chiken, S. *et al.* Dopamine D1 Receptor-Mediated Transmission Maintains Information Flow Through the Cortico-Striato-Entopeduncular Direct Pathway to Release Movements. *Cerebral Cortex* **25**, 4885–4897 (2015).
107. Lin, M. *et al.* In Parkinson's patient-derived dopamine neurons, the triplication of α-synuclein locus induces distinctive firing pattern by impeding D2 receptor autoinhibition. *Acta Neuropathologica Communications* **9**, 107 (2021).
108. Kravitz, A. V. *et al.* Regulation of parkinsonian motor behaviors by optogenetic control of basal ganglia circuitry. *Nature* **466**, 622–626 (2010).
109. Chiken, S. & Nambu, A. Mechanism of Deep Brain Stimulation. *Neuroscientist* **22**, 313–322 (2016).
110. Benabid, A. L., Pollak, P., Louveau, A., Henry, S. & Rougemont, J. de. Combined (Thalamotomy and Stimulation) Stereotactic Surgery of the VIM Thalamic Nucleus for Bilateral Parkinson Disease. *SFN* **50**, 344–346 (1987).
111. Charvin, D., Medori, R., Hauser, R. A. & Rascol, O. Therapeutic strategies for Parkinson disease: beyond dopaminergic drugs. *Nat Rev Drug Discov* **17**, 804–822 (2018).
112. Beckers, M., Bloem, B. R. & Verbeek, M. M. Mechanisms of peripheral levodopa resistance in Parkinson's disease. *npj Parkinsons Dis.* **8**, 1–9 (2022).
113. Chu, Y. *et al.* Intrastriatal alpha-synuclein fibrils in monkeys: spreading, imaging and neuropathological changes. *Brain* **142**, 3565–3579 (2019).
114. Shimozawa, A. *et al.* Propagation of pathological α-synuclein in marmoset brain. *Acta Neuropathologica Communications* **5**, 12 (2017).
115. Schwab, K. *et al.* A Protein Aggregation Inhibitor, Leuco-Methylthioninium Bis(Hydromethanesulfonate), Decreases α-Synuclein Inclusions in a Transgenic Mouse Model of Synucleinopathy. *Front Mol Neurosci* **10**, 447 (2018).
116. Price, D. L. *et al.* The small molecule alpha-synuclein misfolding inhibitor, NPT200-11, produces multiple benefits in an animal model of Parkinson's disease. *Sci Rep* **8**, 16165 (2018).
117. Underwood, R. *et al.* 14-3-3 mitigates alpha-synuclein aggregation and toxicity in the in vivo preformed fibril model. *Acta Neuropathologica Communications* **9**, 13 (2021).
118. A Double-Blind, Placebo-Controlled, Multiple Dose Study to Evaluate Safety, Tolerability, and Pharmacokinetics of UCB0599 in Healthy Study Participants and Patients With Parkinson's Disease (PD) - AdisInsight. https://adisinsight.springer.com/trials/700307811.
119. Eskandari, H. *et al.* Inhibitors of α-Synuclein Fibrillation and Oligomer Toxicity in Rosa damascena: The All-Pervading Powers of Flavonoids and Phenolic Glycosides. *ACS Chem. Neurosci.* **11**, 3161–3173 (2020).
120. Zhao, J. *et al.* (−)-Epigallocatechin-3-gallate (EGCG) inhibits fibrillation, disaggregates amyloid fibrils of α-synuclein, and protects PC12 cells against α-synuclein-induced toxicity. *RSC Adv.* **7**, 32508–32517 (2017).
121. EGCG remodels mature α-synuclein and amyloid-β fibrils and reduces cellular toxicity | PNAS. https://www.pnas.org/doi/10.1073/pnas.0910723107?url_ver=Z39.88-2003&rfr_id=o

ri%3Arid%3Acrossref.org&rfr_dat=cr_pub++0pubmed.
122. Legeay, S., Rodier, M., Fillon, L., Faure, S. & Clere, N. Epigallocatechin Gallate: A Review of Its Beneficial Properties to Prevent Metabolic Syndrome. *Nutrients* **7**, 5443–5468 (2015).
123. Schantz, M., Erk, T. & Richling, E. Metabolism of green tea catechins by the human small intestine. *Biotechnol J* **5**, 1050–1059 (2010).
124. Pervin, M. *et al.* Blood brain barrier permeability of (−)-epigallocatechin gallate, its proliferation-enhancing activity of human neuroblastoma SH-SY5Y cells, and its preventive effect on age-related cognitive dysfunction in mice. *Biochem Biophys Rep* **9**, 180–186 (2017).
125. Lopresti, A. L. The Problem of Curcumin and Its Bioavailability: Could Its Gastrointestinal Influence Contribute to Its Overall Health-Enhancing Effects? *Advances in Nutrition* **9**, 41–50 (2018).
126. Membrane surface charge dictates the structure and function of the epithelial Na+/H+ exchanger. *The EMBO Journal* **30**, 679–691 (2011).
127. Sumioka, A., Yan, D. & Tomita, S. TARP Phosphorylation Regulates Synaptic AMPA Receptors through Lipid Bilayers. *Neuron* **66**, 755–767 (2010).
128. Limbocker, R. *et al.* Squalamine and trodusquemine: two natural products for neurodegenerative diseases, from physical chemistry to the clinic. *Natural Product Reports* **39**, 742–753 (2022).
129. Pineda, A. & Burré, J. Modulating membrane binding of α-synuclein as a therapeutic strategy. *Proceedings of the National Academy of Sciences* **114**, 1223–1225 (2017).
130. Sangwan, S. *et al.* Inhibition of synucleinopathic seeding by rationally designed inhibitors. *eLife* **9**, e46775 (2020).
131. An engineered monomer binding-protein for α-synuclein efficiently inhibits the proliferation of amyloid fibrils | eLife. https://elifesciences.org/articles/46112.
132. Wrasidlo, W. *et al.* A de novo compound targeting α-synuclein improves deficits in models of Parkinson's disease. *Brain* **139**, 3217–3236 (2016).
133. Neuropore Therapies Inc. *A Phase 1, Randomized, Double-Blind, Single Ascending Dose Trial of the Safety, Tolerability and Pharmacokinetics of NPT200-11 in Healthy Subjects*. https://clinicaltrials.gov/ct2/show/NCT02606682 (2016).
134. Jones, S. & Thornton, J. M. Principles of protein-protein interactions. *Proc. Natl. Acad. Sci. USA* 8 (1996).
135. Mabonga, L. & Kappo, A. P. Peptidomimetics: A Synthetic Tool for Inhibiting Protein–Protein Interactions in Cancer. *Int J Pept Res Ther* **26**, 225–241 (2020).
136. Eliezer, D., Kutluay, E., Bussell, R. & Browne, G. Conformational properties of α-synuclein in its free and lipid-associated states11Edited by P. E. Wright. *Journal of Molecular Biology* **307**, 1061–1073 (2001).
137. Apetri, M. M., Maiti, N. C., Zagorski, M. G., Carey, P. R. & Anderson, V. E. Secondary structure of alpha-synuclein oligomers: characterization by raman and atomic force microscopy. *J Mol Biol* **355**, 63–71 (2006).
138. Hill, D. J., Mio, M. J., Prince, R. B., Hughes, T. S. & Moore, J. S. A Field Guide to Foldamers. *Chem. Rev.* **101**, 3893–4012 (2001).
139. Burré, J., Sharma, M. & Südhof, T. C. Cell Biology and Pathophysiology of

α-Synuclein. *Cold Spring Harb Perspect Med* **8**, a024091 (2018).
140. Izawa, Y. *et al.* Role of C-terminal negative charges and tyrosine residues in fibril formation of α-synuclein. *Brain and Behavior* **2**, 595–605 (2012).
141. Guichard, G. & Huc, I. Synthetic foldamers. *Chemical Communications* **47**, 5933–5941 (2011).
142. Kumar, S. *et al.* Foldamer-mediated manipulation of a pre-amyloid toxin. *Nat Commun* **7**, 11412 (2016).
143. Marafon, G. *et al.* Photoresponsive Prion-Mimic Foldamer to Induce Controlled Protein Aggregation. *Angewandte Chemie International Edition* **60**, 5173–5178 (2021).
144. Kumar, S., Henning-Knechtel, A., Chehade, I., Magzoub, M. & Hamilton, A. D. Foldamer-Mediated Structural Rearrangement Attenuates Aβ Oligomerization and Cytotoxicity. *J. Am. Chem. Soc.* **139**, 17098–17108 (2017).
145. Huang, C., Ren, G., Zhou, H. & Wang, C. A new method for purification of recombinant human alpha-synuclein in Escherichia coli. *Protein Expr Purif* **42**, 173–177 (2005).
146. Powers, A. E. & Patel, D. S. Expression and Purification of Untagged α-Synuclein. in *Alpha-Synuclein: Methods and Protocols* (ed. Bartels, T.) 261–269 (Springer, 2019). doi:10.1007/978-1-4939-9124-2_20.
147. Sangwan, S. *et al.* Inhibition of synucleinopathic seeding by rationally designed inhibitors. *eLife* **9**, e46775 (2020).
148. Galvagnion, C. *et al.* Lipid vesicles trigger α-synuclein aggregation by stimulating primary nucleation. *Nat Chem Biol* **11**, 229–234 (2015).
149. Shahnawaz, M. *et al.* Development of a Biochemical Diagnosis of Parkinson Disease by Detection of α-Synuclein Misfolded Aggregates in Cerebrospinal Fluid. *JAMA Neurology* **74**, 163–172 (2017).
150. Dickson, D. W. *et al.* Neuropathological assessment of Parkinson's disease: refining the diagnostic criteria. *The Lancet Neurology* **8**, 1150–1157 (2009).
151. Minckley, T. F. *et al.* Sub-nanomolar sensitive GZnP3 reveals TRPML1-mediated neuronal Zn2+ signals. *Nat Commun* **10**, 4806 (2019).
152. Brenner, S. THE GENETICS OF CAENORHABDITIS ELEGANS. *Genetics* **77**, 71–94 (1974).
153. Chaudhuri, J., Parihar, M. & Pires-daSilva, A. An introduction to worm lab: from culturing worms to mutagenesis. *J Vis Exp* 2293 (2011) doi:10.3791/2293.
154. Garcia-Moreno, J. C., Porta de la Riva, M., Martínez-Lara, E., Siles, E. & Cañuelo, A. Tyrosol, a simple phenol from EVOO, targets multiple pathogenic mechanisms of neurodegeneration in a C. elegans model of Parkinson's disease. *Neurobiol Aging* **82**, 60–68 (2019).
155. Kumar, S. & Miranker, A. D. A foldamer approach to targeting membrane bound helical states of islet amyloid polypeptide. *Chem Commun (Camb)* **49**, 4749–4751 (2013).
156. Levine III, H. Thioflavine T interaction with synthetic Alzheimer's disease β-amyloid peptides: Detection of amyloid aggregation in solution. *Protein Science* **2**, 404–410 (1993).
157. Xicoy, H., Wieringa, B. & Martens, G. J. M. The SH-SY5Y cell line in Parkinson's

disease research: a systematic review. *Molecular Neurodegeneration* **12**, 10 (2017).
158. Sanders, D. W. *et al.* Distinct tau prion strains propagate in cells and mice and define different tauopathies. *Neuron* **82**, 1271–1288 (2014).
159. Doherty, C. P. A. *et al.* A short motif in the N-terminal region of α-synuclein is critical for both aggregation and function. *Nat Struct Mol Biol* **27**, 249–259 (2020).
160. Ulmer, T. S., Bax, A., Cole, N. B. & Nussbaum, R. L. Structure and Dynamics of Micelle-bound Human α-Synuclein*. *Journal of Biological Chemistry* **280**, 9595–9603 (2005).
161. A natural product inhibits the initiation of α-synuclein aggregation and suppresses its toxicity | PNAS. https://www.pnas.org/doi/abs/10.1073/pnas.1610586114?url_ver=Z39.88-2003&rfr_id=ori:rid:crossref.org&rfr_dat=cr_pub%20%200pubmed.
162. Shahnawaz, M. *et al.* Discriminating α-synuclein strains in Parkinson's disease and multiple system atrophy. *Nature* **578**, 273–277 (2020).
163. Small molecule inhibits α-synuclein aggregation, disrupts amyloid fibrils, and prevents degeneration of dopaminergic neurons | PNAS. https://www.pnas.org/doi/10.1073/pnas.1804198115.
164. Guerrero-Ferreira, R. *et al.* Two new polymorphic structures of human full-length alpha-synuclein fibrils solved by cryo-electron microscopy. *eLife* **8**, e48907 (2019).
165. Luk, K. C. *et al.* Exogenous alpha-synuclein fibrils seed the formation of Lewy body-like intracellular inclusions in cultured cells. *Proc Natl Acad Sci U S A* **106**, 20051–20056 (2009).
166. Currey, H. N., Malinkevich, A., Melquist, P. & Liachko, N. F. ARENA-based activity profiling of tau and TDP-43 transgenic C. elegans. *microPublication Biology* **2020**, (2020).
167. Structure of the toxic core of α-synuclein from invisible crystals | Nature. https://www.nature.com/articles/nature15368.
168. Regulation of α-synuclein by chaperones in mammalian cells | Nature. https://www.nature.com/articles/s41586-019-1808-9.
169. Sargent, D. *et al.* 'Prion-like' propagation of the synucleinopathy of M83 transgenic mice depends on the mouse genotype and type of inoculum. *J Neurochem* **143**, 126–135 (2017).
170. Mass spectrometry-based protein–protein interaction networks for the study of human diseases. *Molecular Systems Biology* **17**, e8792 (2021).
171. Vabulas, R. M. & Hartl, F. U. Aberrant protein interactions in amyloid disease. *Cell Cycle* **10**, 1512–1513 (2011).
172. Arkin, M. R., Tang, Y. & Wells, J. A. Small-Molecule Inhibitors of Protein-Protein Interactions: Progressing toward the Reality. *Chemistry & Biology* **21**, 1102–1114 (2014).
173. Pujols, J., Peña-Díaz, S., Pallarès, I. & Ventura, S. Chemical Chaperones as Novel Drugs for Parkinson's Disease. *Trends in Molecular Medicine* **26**, 408–421 (2020).
174. Ahmed, J. *et al.* Foldamers reveal and validate therapeutic targets associated with toxic α-synuclein self-assembly. *Nat Commun* **13**, 2273 (2022).
175. Oh, M. *et al.* Potential pharmacological chaperones targeting cancer-associated MCL-1 and Parkinson disease-associated α-synuclein. *Proceedings of the National*

Academy of Sciences **111**, 11007–11012 (2014).
176. Kumar, S. & Hamilton, A. D. α-Helix Mimetics as Modulators of Aβ Self-Assembly. *J. Am. Chem. Soc.* **139**, 5744–5755 (2017).
177. Palanikumar, L. *et al.* Protein mimetic amyloid inhibitor potently abrogates cancer-associated mutant p53 aggregation and restores tumor suppressor function. *Nat Commun* **12**, 3962 (2021).
178. Murray, C. W. & Rees, D. C. The rise of fragment-based drug discovery. *Nat Chem* **1**, 187–192 (2009).
179. Scott, D. E. *et al.* Using a Fragment-Based Approach To Target Protein–Protein Interactions. *ChemBioChem* **14**, 332–342 (2013).
180. Hebda, J. A., Saraogi, I., Magzoub, M., Hamilton, A. D. & Miranker, A. D. A peptidomimetic approach to targeting pre-amyloidogenic states in type II diabetes. *Chem Biol* **16**, 943–950 (2009).
181. Bavinton, C. E. *et al.* Rationally designed helical peptidomimetics disrupt α-synuclein fibrillation. *Chem. Commun.* **58**, 5132–5135 (2022).
182. Kautu, B. B., Carrasquilla, A., Hicks, M. L., Caldwell, K. A. & Caldwell, G. A. Valproic Acid Ameliorates C. elegans Dopaminergic Neurodegeneration with Implications for ERK-MAPK Signaling. *Neurosci Lett* **541**, 116–119 (2013).
183. Kumar, S., Birol, M. & Miranker, A. D. Foldamer scaffolds suggest distinct structures are associated with alternative gains-of-function in a preamyloid toxin. *Chem. Commun.* **52**, 6391–6394 (2016).
184. Saraogi, I. *et al.* Synthetic alpha-helix mimetics as agonists and antagonists of islet amyloid polypeptide aggregation. *Angew Chem Int Ed Engl* **49**, 736–739 (2010).
185. Peduzzo, A., Linse, S. & Buell, A. K. The Properties of α-Synuclein Secondary Nuclei Are Dominated by the Solution Conditions Rather than the Seed Fibril Strain. *ACS Chem. Neurosci.* **11**, 909–918 (2020).
186. Structural insights into α-synuclein monomer–fibril interactions | PNAS. https://www.pnas.org/doi/full/10.1073/pnas.2012171118.
187. Harrington, A. J., Yacoubian, T. A., Slone, S. R., Caldwell, K. A. & Caldwell, G. A. Functional Analysis of VPS41-Mediated Neuroprotection in Caenorhabditis elegans and Mammalian Models of Parkinson's Disease. *J Neurosci* **32**, 2142–2153 (2012).
188. Ray, A., Martinez, B. A., Berkowitz, L. A., Caldwell, G. A. & Caldwell, K. A. Mitochondrial dysfunction, oxidative stress, and neurodegeneration elicited by a bacterial metabolite in a C. elegans Parkinson's model. *Cell Death Dis* **5**, e984–e984 (2014).
189. Ezcurra, M., Tanizawa, Y., Swoboda, P. & Schafer, W. R. Food sensitizes C. elegans avoidance behaviours through acute dopamine signalling. *EMBO J* **30**, 1110–1122 (2011).
190. Margie, O., Palmer, C. & Chin-Sang, I. C. elegans chemotaxis assay. *J Vis Exp* e50069 (2013) doi:10.3791/50069.
191. Mor, D. E. *et al.* Metformin rescues Parkinson's disease phenotypes caused by hyperactive mitochondria. *Proceedings of the National Academy of Sciences* **117**, 26438–26447 (2020).
192. Sagar, N. A., Tarafdar, S., Agarwal, S., Tarafdar, A. & Sharma, S. Polyamines: Functions, Metabolism, and Role in Human Disease Management. *Med Sci (Basel)* **9**,

44 (2021).
193. Pegg, A. E., Lockwood, D. H. & Williams-Ashman, H. G. Concentrations of putrescine and polyamines and their enzymic synthesis during androgen-induced prostatic growth. *Biochemical Journal* **117**, 17–31 (1970).
194. Lewandowski, N. M. *et al.* Polyamine pathway contributes to the pathogenesis of Parkinson disease. *Proceedings of the National Academy of Sciences* **107**, 16970–16975 (2010).
195. Tate, P. M., Mastrodomenico, V. & Mounce, B. C. Ribavirin Induces Polyamine Depletion via Nucleotide Depletion to Limit Virus Replication. *Cell Reports* **28**, 2620-2633.e4 (2019).
196. Maraganore, D. M. *et al.* High-Resolution Whole-Genome Association Study of Parkinson Disease. *Am J Hum Genet* **77**, 685–693 (2005).
197. Hereditary parkinsonism with dementia is caused by mutations in ATP13A2, encoding a lysosomal type 5 P-type ATPase | Nature Genetics. https://www.nature.com/articles/ng1884.
198. Yang, X. & Xu, Y. Mutations in the ATP13A2 gene and Parkinsonism: a preliminary review. *Biomed Res Int* **2014**, 371256 (2014).
199. van Veen, S. *et al.* ATP13A2 deficiency disrupts lysosomal polyamine export. *Nature* **578**, 419–424 (2020).
200. Dehay, B. *et al.* Lysosomal dysfunction in Parkinson disease. *Autophagy* **8**, 1389–1391 (2012).
201. Wallings, R. L., Humble, S. W., Ward, M. E. & Wade-Martins, R. Lysosomal Dysfunction at the Centre of Parkinson's Disease and Frontotemporal Dementia/Amyotrophic Lateral Sclerosis. *Trends in Neurosciences* **42**, 899–912 (2019).
202. Lee, H.-J., Khoshaghideh, F., Patel, S. & Lee, S.-J. Clearance of α-Synuclein Oligomeric Intermediates via the Lysosomal Degradation Pathway. *J. Neurosci.* **24**, 1888–1896 (2004).
203. Mak, S. K., McCormack, A. L., Manning-Boğ, A. B., Cuervo, A. M. & Di Monte, D. A. Lysosomal Degradation of α-Synuclein in Vivo*. *Journal of Biological Chemistry* **285**, 13621–13629 (2010).
204. Tunneling nanotubes spread fibrillar α-synuclein by intercellular trafficking of lysosomes. *The EMBO Journal* **35**, 2120–2138 (2016).
205. Si, J. *et al.* ATP13A2 Regulates Cellular α-Synuclein Multimerization, Membrane Association, and Externalization. *Int J Mol Sci* **22**, 2689 (2021).
206. Schultheis, P. J. *et al.* Atp13a2-deficient mice exhibit neuronal ceroid lipofuscinosis, limited α-synuclein accumulation and age-dependent sensorimotor deficits. *Hum Mol Genet* **22**, 2067–2082 (2013).
207. Lopes da Fonseca, T., Pinho, R. & Outeiro, T. F. A familial ATP13A2 mutation enhances alpha-synuclein aggregation and promotes cell death. *Human Molecular Genetics* **25**, 2959–2971 (2016).
208. Usenovic, M., Tresse, E., Mazzulli, J. R., Taylor, J. P. & Krainc, D. Deficiency of ATP13A2 Leads to Lysosomal Dysfunction, α-Synuclein Accumulation, and Neurotoxicity. *J. Neurosci.* **32**, 4240–4246 (2012).
209. Dirr, E. R. *et al.* Exacerbation of sensorimotor dysfunction in mice deficient in

Atp13a2 and overexpressing human wildtype alpha-synuclein. *Behav Brain Res* **343**, 41–49 (2018).
210. Grabenauer, M. *et al.* Spermine Binding to Parkinson's Protein α-Synuclein and its Disease-Related A30P and A53T Mutants. *J Phys Chem B* **112**, 11147–11154 (2008).
211. Goers, J., Uversky, V. N. & Fink, A. L. Polycation-induced oligomerization and accelerated fibrillation of human α-synuclein in vitro. *Protein Science* **12**, 702–707 (2003).
212. Antony, T. *et al.* Cellular Polyamines Promote the Aggregation of α-Synuclein *. *Journal of Biological Chemistry* **278**, 3235–3240 (2003).
213. NMR of α-synuclein–polyamine complexes elucidates the mechanism and kinetics of induced aggregation. *The EMBO Journal* **23**, 2039–2046 (2004).
214. Spriestersbach, A., Kubicek, J., Schäfer, F., Block, H. & Maertens, B. Chapter One - Purification of His-Tagged Proteins. in *Methods in Enzymology* (ed. Lorsch, J. R.) vol. 559 1–15 (Academic Press, 2015).
215. Tanudjojo, B. *et al.* Phenotypic manifestation of α-synuclein strains derived from Parkinson's disease and multiple system atrophy in human dopaminergic neurons. *Nat Commun* **12**, 3817 (2021).
216. Park, M. H. & Igarashi, K. Polyamines and Their Metabolites as Diagnostic Markers of Human Diseases. *Biomol Ther (Seoul)* **21**, 1–9 (2013).
217. Kaur-Sawhney, R., Shih, L., Cegielska, T. & Galston, A. W. Inhibition of protease activity by polyamines. *FEBS Letters* **145**, 345–349 (1982).
218. Fernández, C. O. *et al.* NMR of α-synuclein–polyamine complexes elucidates the mechanism and kinetics of induced aggregation. *EMBO J* **23**, 2039–2046 (2004).
219. Lorenzen, N. *et al.* The Role of Stable α-Synuclein Oligomers in the Molecular Events Underlying Amyloid Formation. *J. Am. Chem. Soc.* **136**, 3859–3868 (2014).
220. Dusa, A. *et al.* Characterization of Oligomers during α-Synuclein Aggregation Using Intrinsic Tryptophan Fluorescence. *Biochemistry* **45**, 2752–2760 (2006).
221. Xue, C., Lin, T. Y., Chang, D. & Guo, Z. Thioflavin T as an amyloid dye: fibril quantification, optimal concentration and effect on aggregation. *Royal Society Open Science* **4**, 160696.
222. Deepa, H. R., Thipperudrappa, J. & Suresh Kumar, H. M. A study on fluorescence quenching of a laser dye by aromatic amines in alcohols. *Can. J. Phys.* **93**, 469–474 (2015).
223. Van, S.-P. & Hammond, G. S. Amine quenching of aromatic fluorescence and fluorescent exciplexes. *J. Am. Chem. Soc.* **100**, 3895–3902 (1978).
224. McGlinchey, R. P., Ni, X., Shadish, J. A., Jiang, J. & Lee, J. C. The N terminus of α-synuclein dictates fibril formation. *Proceedings of the National Academy of Sciences* **118**, e2023487118 (2021).
225. Litberg, T. J., Docter, B., Hughes, M. P., Bourne, J. & Horowitz, S. DNA Facilitates Oligomerization and Prevents Aggregation via DNA Networks. *Biophys J* **118**, 162–171 (2020).
226. Kaufman, S. K. *et al.* Tau prion strains dictate patterns of cell pathology, progression rate, and regional vulnerability in vivo. *Neuron* **92**, 796–812 (2016).
227. Waxman, E. A. & Giasson, B. I. Characterization of kinases involved in the phosphorylation of aggregated α-synuclein. *J Neurosci Res* **89**, 231–247 (2011).

228. Schmitz, M. *et al.* Cerebrospinal Fluid Total and Phosphorylated α-Synuclein in Patients with Creutzfeldt–Jakob Disease and Synucleinopathy. *Mol Neurobiol* **56**, 3476–3483 (2019).
229. Chen, W. R. *et al.* Phosphorylated α-synuclein in diluted human serum a biomarker for Parkinson's disease. *Biomed J* S2319-4170(21)00182–7 (2021) doi:10.1016/j.bj.2021.12.010.
230. Saito, Y. *et al.* Accumulation of phosphorylated alpha-synuclein in aging human brain. *J Neuropathol Exp Neurol* **62**, 644–654 (2003).
231. Ma, M.-R., Hu, Z.-W., Zhao, Y.-F., Chen, Y.-X. & Li, Y.-M. Phosphorylation induces distinct alpha-synuclein strain formation. *Sci Rep* **6**, 37130 (2016).
232. Gomes-Trolin, C., Nygren, I., Aquilonius, S.-M. & Askmark, H. Increased Red Blood Cell Polyamines in ALS and Parkinson's Disease. *Experimental Neurology* **177**, 515–520 (2002).
233. Paik, M.-J. *et al.* Polyamine patterns in the cerebrospinal fluid of patients with Parkinson's disease and multiple system atrophy. *Clin Chim Acta* **411**, 1532–1535 (2010).
234. Candelise, N. *et al.* Seeding variability of different alpha synuclein strains in synucleinopathies. *Annals of Neurology* **85**, 691–703 (2019).
235. Frare, E. *et al.* Identification of the core structure of lysozyme amyloid fibrils by proteolysis. *J Mol Biol* **361**, 551–561 (2006).
236. Schönfelder, J. *et al.* Protease resistance of ex vivo amyloid fibrils implies the proteolytic selection of disease-associated fibril morphologies. *Amyloid* **28**, 243–251 (2021).
237. Lambeth, T. R. & Julian, R. R. Proteolysis of Amyloid β by Lysosomal Enzymes as a Function of Fibril Morphology. *ACS Omega* **6**, 31520–31527 (2021).
238. Johnson, C. J. *et al.* Degradation of the Disease-Associated Prion Protein by a Serine Protease from Lichens. *PLoS One* **6**, e19836 (2011).
239. Hallacli, E. *et al.* The Parkinson's disease protein alpha-synuclein is a modulator of processing bodies and mRNA stability. *Cell* **185**, 2035-2056.e33 (2022).